

H24/3835

No Restrictions.

MONASH UNIVERSITY
THESIS ACCEPTED IN SATISFACTION OF THE
REQUIREMENTS FOR THE DEGREE OF
DOCTOR OF PHILOSOPHY

ON..... 17 August 2004.....

.....
Sec. Research Graduate School Committee

Under the Copyright Act 1968, this thesis must be used only under the normal conditions of scholarly fair dealing for the purposes of research, criticism or review. In particular no results or conclusions should be extracted from it, nor should it be copied or closely paraphrased in whole or in part without the written consent of the author. Proper written acknowledgement should be made for any assistance obtained from this thesis.

ERRATA & ADDENDUM

p 21, beneath Equation 1.18, line 3. The sentence should read "More recently, from extrapolation of data to 0 K, the Mn spins were found to flop at 4.5T."

p 24 The second sentence should read "For FePS₃, the five-fold degeneracy of the d-orbitals is lifted, splitting into a triply degenerate..."

p 30, para 1. The fourth sentence should read "In a crystallographic unit cell, the iron and phosphorus each occupy only one point location while the sulphur has..."

p 32, In the sixth line from the bottom, "this data" should be changed to "these data".

p 40, para 2, line 6. Insert "at" between "be around".

p 50, para 3. In the sixth sentence replace "Heisneberg" with "Heisenberg". Also insert the word "show" after the words "Heisenberg magnets do not".

p 53, Figure 3.1 caption. Insert at the end of caption: "The absorption lines in a magnetically ordered spectrum with negligible quadrupole splitting are generally labelled 1-6 for increasing energy transfer between the ground and excited states. The lines maintain the same numbering even though they may not be in numerical order in the spectrum, such as when a magnetic field is applied to the sample."

p 58, line 1. Replace "represent" with "represents"

p 68, para 3. The second sentence should read "Neutrons interact predominantly with the nucleus of an atom and magnetically with unpaired electrons rather than with the entire cloud of electrons as x-rays do."

p 69 para 2. Replace "it rotates with a frequency of precession called the Larmor frequency" with "it precesses at a frequency called the Larmor frequency."

p 69, para 3, line 5. Replace "diffraction" with "scattering".

p 71, para 5. The final sentence should read "The scattering length for scattering from a single fixed nucleus can be related to the differential cross section by the following equation,"

p 72, para 1. The second sentence should read "Coherent scattering occurs when the neutron beam interacts in the same way with each of the nuclei in the material and consequently the wave fronts of the scattered beam are in phase."

p 72, para 1, line 5. Insert "for spatially correlated samples," after "That is,"

p 73, sect 3.7, para 1. The final sentence should be omitted.

p 77, para 2, line 2. The words "to oscillate" should be removed.

p 79, para 2, line 10. The words "single domain" should be inserted before "ferromagnets".

p 83, para 3. Omit the first and last sentences and then after line 8, insert: "The translation between the fundamental reciprocal lattice positions and the magnetic reflections can therefore be defined as a magnetic-order wavevector."

p 83, para 3, line 10. Replace the term "propagation vector" with "magnetic-order wavevector"

p 83, para 4. In the fourth line, change "this data" to "these data"

p 84, line 1. Replace "propagation vector" with "magnetic-order wavevector as defined above"

p 84, line 5. Remove "the effective magnetic propagation vector would be 0,0,0"

p 84, line 6. Replace the final sentence with "So for MnPS_3 the propagation vector is 0,0,0 as stated by Kurosawa et al., (1983), but due to absences in the magnetic peaks, the effective magnetic-order wavevector that can describe the magnetic peaks is 1,1,0."

p 86, line 3. Replace "10 cm" with "10 mm"

p 95, para 3. Sentence 3 should read "The supermirror devices polarise the incident neutron beam and analyse the polarisation state of the scattered beam before it is registered in one of 8 detectors."

p 96, Figure 4.9 caption. Replace "LONPOL" with "LONGPOL"

p 96, line 2. Insert the word "on" after "negligible effect"

p 97, para 2. In the sixth sentence, replace the word "remanent" with "remanent"

p 104, line 4. After "... supporting this proposition." Add, "The materials also displaying this feature were the antiferromagnetic alloys, MnNi and MnCu. MnCu is a well-investigated material that has only shown evidence of this low temperature feature in measurements taken with the Teflon sample rod."

p 104, para 2. Delete the final two sentences "At these paramagnetic ... *ab*-plane".

p 127, para 1. In sentence 2, replace the word "filed" with "field"

p 131, para 2. In the fourth sentence, replace "effect" with "affect"

p 136, para 1. In sentence 3, change "was" to "were".

p 140. In the fourth line from the bottom, change "know" to "known"

p 147, final para. In the first sentence, change "spherically" to "spherical"

p 150, para 3, lines 1 and 3. The words "data was" needs to be replaced with "data were".

p 153, para 2. Insert after the final sentence: "Any spin waves that might have been present in the structure may become visible if the spectrum in Figure 6.9 was plotted as a function of energy, however the current analysis was sufficient to indicate that the bulk of the scattering from the diffuse region was magnetic and elastic."

p 162, line 2. The words "data was" needs to be replaced with "data were".

p 163, para2, line 1. The words "this data" should be replaced with "these data".

p 164, para 1. Insert after sentence four, "The relatively constant magnitude of the low temperature magnetic moment seems to contradict the conclusions drawn earlier (on page 116) stating that the effective moment decreases with temperature. This indicates that the observed ferrimagnetism in FePS_3 does not necessarily occur from the flipping of exactly half of the antiparallel moments to be parallel with a strong applied field. The ferrimagnetic phase may instead occur as a canting of the antiparallel moments. The ferrimagnetic phase may not be perfectly collinear and the tendency to non-collinearity may increase with temperature."

p 168, para 2, line 8. The words "data was" needs to be replaced with "data were".

p 170, line 9. Change "iron precession frequency" to "⁵⁷Fe nuclear precession frequency"

p 170, para 2. Replace the final sentence with "If the magnetic arrangement was dynamic, the rotational frequency of the moment component in the *ab*-plane may change as a field was applied along *c**. This would mean that the observed hyperfine field might not be entirely along *c**. If the rotational frequency in the *ab*-plane were reduced below the nuclear Larmor precession frequency, then there would be a component of the moment that would appear to be stationary in the *ab*-plane. Thus a small component of lines 2 and 5 should be seen in the spectra. As this was not observed, it is not likely that FePS₃ has a dynamical helical moment arrangement."

p 172, Fig 7.2. In the caption replace "makers" with "markers"

p 177, after para 2. "It was shown in figure 5.1 that the susceptibility of FePS₃ had some field history dependence below approximately 80 K. It is not entirely obvious why this field dependence exists, however it does not indicate long-range order in the *c**-direction as the neutron diffraction results are still broad at 5K."

p 180, after para 3. "Another factor which may decrease the accuracy of this simulation is the line shapes. Although Gaussian line shapes have been used to fit the long-range Bragg peaks, Lorentzian line shapes may better fit the peaks with larger scattering vectors along *l*. The use of Gaussians allowed for a simple variation of the peak width about *l*, which was important to the simulation. The multiplicity of the Lorentzian fit may also influence the relative intensities of the peaks. It was noticed in Table 6.3 that not all equivalent *l* positions have an observed peak. Thus the difference between the relative peak intensities of Figures 7.6 and 7.7 may be attributed to these factors. Improvement of the simulation would better determine this."

p 184, para 3. The third sentence should be replaced with "In the paramagnetic phase, this model predicts peaks at all positions of the low temperature structures. In a low temperature structure, only certain peaks are chosen according to the magnetically ordered structure. Often, all of the paramagnetic structures can be present at low temperatures, but spatially separate in domains. Assumptions were made to simplify this model, one of which involved an approximation of the monoclinic tilt in the crystal structure. As all Brillouin zones are equivalent, the model can be used to predict all the observed magnetic peaks."

p 189, Figure 7.12 caption. The words "This data" should be replaced with "These data".

p 207, para 4, line 2. The words "data was" needs to be replaced with "data were".

Comment: The phrase "true two dimensional magnet" was used throughout this dissertation to describe the absence of three dimensional order in FePS₃. The short-range order is always present in FePS₃, as it is in any paramagnetic material. The term "true two dimensional magnet" was used to differentiate between FePS₃ and "very good approximations of a two dimensional magnet" like MnPS₃ which eventually order in the third dimension.

MAGNETIC ORDERING IN THE
TWO DIMENSIONAL
ANTIFERROMAGNET,
FEPS₃

A thesis submitted for the degree of
Doctor of Philosophy

By
Kirrily Rule
B. A., B. Sc. (Hons.)

School of Physics and Materials Engineering
Monash University
Australia

February 2004

CONTENTS

Acknowledgments.....	3
Declaration	4
Summary.....	5
Introduction to Magnetism	7
Introduction to Iron Thiophosphate.....	29
Experimental Techniques	52
Sample Preparation	86
4.1 Crystal Growth.....	86
4.2 Initial Crystallographic Analysis	87
4.3 Experimental Procedures	88
4.4 SQUID Magnetometry.....	89
4.5 High Field Magnetisation Measurements	90
4.6 Mössbauer Spectroscopy	90
4.7 Neutron Diffraction	93
Results and Discussion of Magnetometry and Mössbauer Spectroscopy	101
5.1 Magnetic Susceptibility of FePS ₃	101
5.2 Exchange Integrals in FePS ₃	106
5.3 The Landé splitting factor.....	110
5.4 High field magnetization measurements.....	112
5.5 Mössbauer Spectroscopy of the Single Crystal Sample	118
5.6 Mössbauer Spectroscopy of the Powder sample.....	122
5.7 Applied Magnetic Fields.....	126
5.8 The Goldanskii-Karyagin Effect.....	130
5.9 Search for the EFG direction	133
5.10 Conclusions.....	141
Results and Discussion of Neutron Diffraction Techniques	142
6.1 Powder Diffraction of FePS ₃	142
6.2 Energy Analysis of FePS ₃ using LONGPOL.....	147
6.3 Maximum Entropy Analysis.....	152
6.4 Laue neutron diffraction	157
6.5 D19 Observations	160
6.6 Conclusion	165
The Magnetic Structure of FePS ₃	167
7.1 Initial magnetic structures of FePS ₃	167
7.2 Low Dimensional Magnetic Structure	174

7.3 Simulations	178
7.4 Temperature dependence of the 2D magnetic Bragg peaks.....	185
7.5 Comparisons with other magnetic structures.....	190
7.6 Conclusions.....	194
Spin Diffusion through FePS_3	195
8.1 Conventional Spin Diffusion	195
8.2 Spin Diffusion in FePS_3	198
8.3 Experimental Set Up.....	199
8.4 Results of FePS_3	200
8.5 Analysis of the Spin Diffusion Results.....	201
8.6 Conclusions.....	204
Conclusions and Further work	205
Bibliography.....	208
Supporting Publications.....	216

ACKNOWLEDGMENTS

First, acknowledgements must go to the various sources of funding received for the duration of this experiment. I greatly appreciate the Australian Postgraduate Award offered by the Australian government as well as the supplement award from the Australian Institute of Nuclear Science and Engineering (AINSE) for the funding to support myself throughout this PhD. Thanks must also go to the School of Physics and Materials Engineering and Monash University for the financial support to attend local and international conferences. The funding for this research was supported with an ARC grant as well as support for international research from the Access to Major Research Facilities fund.

I would like to sincerely thank my "doctor-father", Trevor Hicks, for his unyielding support and encouragement in everything I attempted during this candidature. Without his advice, patience and our many discussions I would not have maintained my focus on the problem at hand.

I would also like to thank my co-supervisors in this work – Shane Kennedy for his generous donation of time and effort with everything neutron related and John Cashion for his wise guidance and experience with everything Mössbauer related.

Others that have offered insightful discussions related to the project include A. M. Mulders and D. J. Goossens, as well as G. J. McIntyre who also assisted with experimentation and analysis of my single crystal sample at the ILL in France. Thanks also to A. Studer, T. Ersez and Y. Fei for their assistance with setting up and taking neutron measurements at the Lucas Heights Research Reactor in Sydney.

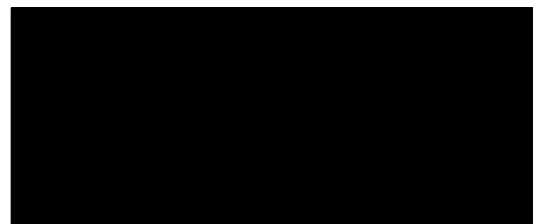
Rod Mackie, Alan Holland and the entire School of Physics and Materials Engineering workshop also have my gratitude for their creativity, and wealth of experience, which have provided me with technical assistance in the XRD, furnace and Mössbauer labs.

I would also like to thank a variety of people for providing an environment rich with discussions and ideas. The properties-of-materials discussion group including A. E. Smith offered new perspectives to my research and calculations. I would also like to thank my office partner and friend, (soon to be Dr.) Tamar Greaves, for keeping me sane and fit!

Finally to my family and friends to whom this is dedicated: My grandparents who have been waiting for this day for 9 years and my parents who knew not to ask when I would ever finish. Thank you all for your support and love throughout.

DECLARATION

I declare that this thesis contains no material, which has been accepted for the award of any other degree or diploma at any university. To the best of my knowledge and belief this thesis contains no material published or written by another person, except where due reference is made in the text.



Kirriily C. Rule

February 2004

SUMMARY

The purpose of this thesis was to investigate the low dimensional, antiferromagnetic material FePS_3 . This material belongs to the thiophosphate family of compounds; a group of quasi-two dimensional magnetic materials which exhibit strong intraplanar exchange interactions and only weak interplanar interactions. These materials are formed by transition metal ions in a honeycomb lattice, which are flanked by phosphorus dumbbells and sulphur layers. The quasi-two dimensional nature arises from Van der Waals gaps separating each honeycomb layer along the z -direction.

Initial powder neutron diffraction studies revealed that the previously accepted magnetic structure model was in fact incorrect, and thus much of the work contained in this thesis was focused on discovering the true magnetic structure of FePS_3 . The main experimental techniques used include magnetometry, Mössbauer spectroscopy and neutron scattering from both single crystal and powdered samples.

Single crystals of FePS_3 were grown via vapour transport, and appeared as thin, shiny-grey crystals reaching volumes of around $10 \times 10 \times 0.1$ mm. Susceptibility measurements exhibited a broad maximum indicative of low dimensional magnetic materials with a Néel temperature measured at approximately 120 K. High, applied field measurements taken with a pulsed field of up to 38 T revealed a metamagnetic phase change from antiferromagnetic to ferrimagnetic to paramagnetic as the applied field and temperature were increased.

Mössbauer spectra were taken both above and below the magnetic ordering temperature with the γ -ray oriented perpendicular to the ab -plane. Single crystal measurements indicated that the moments were oriented parallel and antiparallel with the γ -ray direction, via the absence of lines 2 and 5 in the hyperfine split spectrum. Applied field measurements indicated that the internal hyperfine field was 9.75 ± 0.06 T at 10 K. Mössbauer spectra were used to investigate the degree of lattice vibrational anisotropy (known as the Goldanskii-Karyagin Effect). By orienting a single crystal absorber at the 'magic angle' of 54.7° to the γ -ray direction, the sample was completely randomised. From the resulting asymmetry in the quadrupole split lines, it was found

that there was greater vibrational anisotropy along the z -direction of the crystal. Investigations into the electric field gradient (EFG) indicated that it was oriented close to the c^* -direction.

Powder neutron diffraction scans revealed diffuse magnetic peaks at low scattering angles, which were found to be diffuse Bragg peaks. Elastic scattering from polarised neutron analysis eliminated the possibility that the diffuse peaks were caused by magnons in the lattice. These measurements were taken with the Medium Resolution Powder Diffractometer (MRPD) and the LONG wavelength POLarisation analysis spectrometer (LONGPOL) respectively, at the High Flux Australian Reactor (HIFAR) in Sydney.

Single crystal neutron scattering measurements were taken using the Laue diffractometer, VIVALDI, and the four-circle diffractometer, D19, at the Institut Laue-Langevin (ILL) in France. These measurements indicated that the magnetic unit cell structure was twice as large as the crystallographic cell in both the a - and b -directions and around three times as large along the c -direction. The magnetic intensity from both measurements appeared to be smeared along the c -direction indicating rod like scattering profiles in reciprocal space. This was considered similar to the diffuse magnetic Bragg peaks observed in the MRPD data as an indication of incomplete long-range order perpendicular to the ab -plane.

Comparisons between the known two-dimensional Ising antiferromagnet, Rb_2CoF_4 , and FePS_3 revealed very similar traits and observations from neutron diffraction studies. Thus it was concluded that FePS_3 has no long-range magnetic order along c , and may not repeat exactly every third layer. The in-plane magnetic structure that best fit the data was in fact that described by Le Flem et al., (1982) and consists of ferromagnetic chains of moments, at an angle of 60° to the crystallographic a -axis, which are coupled antiferromagnetically.

Paramagnetic spin diffusion studies were also conducted, using LONGPOL, to investigate the rate at which the spin state on one site will percolate through a two-dimensional, paramagnetic lattice. At temperatures close to the Néel temperature, the inelastically scattered neutrons followed a distribution similar to a Lorentzian profile, which would indicate an exponential rate of diffusion as dictated by the conventional theory of spin diffusion. At temperatures much larger than the Néel temperature, the neutrons followed a distribution that may have resembled a square wave. This would indicate a different diffusion rate, such as a *sinc* function or something similar.

CHAPTER ONE

1: Introduction to Magnetism

The discovery and usage of magnetic materials can be traced back thousands of years to the naturally occurring mineral, magnetite (Fe_3O_4), whose properties of magnetising iron were well known to the ancient Greeks around 800 B.C. (Mattis, 1965). A deeper understanding of magnetism and magnetic materials was not realised until more recently by William Gilbert whose book, *De Magnete* (translated as "On the Magnet") was published in 1600, detailing a picture of the earth's magnetic field (Cullity, 1972). Although the theories of magnetism have spread from this work by the likes of Hans Christian Oersted, Michael Faraday, Pierre Curie, Pierre Weiss, and Van Vleck, there is still much to be learnt about many materials. As our knowledge of magnetism increases, the significance of magnetic materials becomes more evident in every day life. As research progresses, even more information about magnetism is revealed and more magnetic materials and devices are discovered, providing the basis for technological advances such as transformers for power and communications, recording media and superconducting devices, to name just a few.

1.1 FUNDAMENTAL MAGNETISM

On an atomic scale, the magnetic moment, μ , of an atom contributes to the magnetic behaviour of the material. Atomic magnetic moments originate from the total angular momentum, J , of an atom. Angular momentum is produced by the motion of the electrons about the nucleus and classically about their own axis, and contains both an orbital, L , and spin, S , component. For each of these angular momentum terms, J , L and S are the respective quantum numbers that describe the state of the ion. The orbital angular momentum, L , describes the rotation of electrons around a nucleus. Each electron also has a spin angular momentum, s ; the sum of which forms the total spin component of the magnetic moment, S . The total angular momentum of an atom is therefore the vector sum of the two components.

$$J = L + S \quad (1.1)$$

The values of J must be integers or half integers, due to the allowed values for both L and S . For a given orbital angular momentum, L , there are $(2L + 1)$ levels of L_z where L_z takes on integer values between $\pm L$. The spin of each electron has two possible states for each value of L ; $S_z = +\frac{1}{2}$ and $S_z = -\frac{1}{2}$ for parallel and antiparallel spin respectively. Each of the total number of electrons, n , can occupy any one of these states, which are considered to be degenerate if the electrons do not interact with each other. The degeneracy of these states can be mostly removed via a combination of Coulomb and spin-orbit interactions between electron-electron pairs.

The values of the spin and orbital quantum numbers vary depending on the occupancy of the available electron states in an atom. This variation is determined by a set of constraints, which were devised for energy minimisation and can be used to calculate L , S and J for an atom. These constraints are known as Hund's rules and are as follows (Smart, 1966; Ashcroft & Mermin, 1976):

- i) *Electrons will couple for a maximum total atomic spin, S , while remaining within the limits of the Pauli exclusion principle.* This implies that electrons prefer to fill all of the electron shells first, rather than pair. For the transition metal Mn^{2+} , the 5 electrons in the 3d shell will fill each shell with parallel electron spins, resulting in a maximum spin quantum number of $\frac{5}{2}$. Fe^{2+} , which has six electrons in the 3d-shell, will have one pair of electrons while 4 remain unpaired. Thus the spin quantum number for Fe^{2+} is $S = \frac{4}{2} = 2$.
- ii) *The total orbital angular momentum, L , will also be maximum value, consistent with the constraint of the 1st rule.* This implies that the electrons will occupy states with the largest orbital angular momentum first. The Mn^{2+} ion has an orbital angular momentum of zero while for Fe^{2+} , $L = 2$ as an electron goes into the highest available orbital state.
- iii) It can be seen that for electron shells less than half full, the total angular momentum is equal to $|L - S|$, while for shells that are more than half full, $J = |L + S|$, and for shells that are exactly half full, $L = 0$ and $J = S$. Thus for Mn^{2+} , $J = S = \frac{5}{2}$ while for Fe^{2+} , $J = 4$.

The spin and orbital motion of the electron will both contribute to the overall magnetic moment of the atom. The orbital and spin magnetic moments for an electron can be defined according to the following equations.

$$\begin{aligned}\mu_L &= \mu_B \sqrt{L(L+1)} \\ \mu_S &= 2\mu_B \sqrt{S(S+1)}\end{aligned}\quad (1.2)$$

In both terms above, the units of the atomic magnetic moment are in Bohr magnetons, μ_B . This is the quantum of magnetic moment associated with the orbital angular momentum of an electron in an atom as seen in Equation 1.2 (Cracknell, 1975). In CGS units, the Bohr magneton is defined as

$$\mu_B = \frac{|e|\hbar}{2m_e c} \quad (1.3)$$

where m_e and e are the mass and charge of the electron, \hbar is Planck's constant divided by 2π and c is the speed of light. In SI units, the factor of c is removed from Equation 1.3 and μ_B is equal to 9.274×10^{-24} J T⁻¹ (Kittel, 1986). Thus the net magnetic moment of an atom, also known as the effective moment, can be defined below in terms of the spectroscopic splitting factor, g_J , and the total angular momentum, J . This value is measured in the paramagnetic state, where the spins are thermally disordered.

$$\mu_{\text{eff}} = g_J \mu_B \sqrt{J(J+1)} \quad (1.4)$$

The spectroscopic splitting factor, g_J , is equal to 1 for purely orbital motion ($S = 0$) and 2.0023 for spin ($L = 0$), although this is often approximated as 2 (Abragam & Bleaney, 1986). This factor is also known as the Landé splitting factor and can be defined as in Equation 1.5 when both orbital and spin components interact. A contribution from both orbital and spin motion will often give a g -factor slightly greater than 2 (Cullity, 1972). For rare earths, g_J can often be greater than 2.

$$g_J = 1 + \frac{J(J+1) + S(S+1) - L(L+1)}{2J(J+1)} \quad (1.5)$$

Equation 1.4 can be evaluated simply, but only represents isolated atoms. Three-dimensional atoms or ions in a solid can be better represented by the equation for spin only (Equation 1.2).

This implies that there is no orbital contribution to the moment from the ions bound in a solid – the orbital component is said to be “quenched” (Cullity, 1972; Kittel, 1986). This comes from the influence of the crystal field, which affects the orbits of the electrons on atoms in the lattice. The orbits become bound to the crystal lattice in a relatively strong orbit-lattice coupling which is much stronger than the loosely bound spin-orbit coupling within the lattice. As an example, free Fe^{2+} has an effective moment calculated as $\mu_{\text{eff}} = 6.70\mu_B$ but a spin only moment of $\mu_{\text{spin}} = 2\mu_B\sqrt{S(S+1)} = 4.90\mu_B$ which is closer to the average measured value for Fe^{2+} of $5.40\mu_B$ (Kittel, 1986). As spin-orbit coupling becomes more prominent in a solid material, the effective moment deviates from the spin-only component.

1.2 MAGNETIC ANISOTROPY

Magnetic anisotropy is an indication of preferred moment orientation – that is, the moments prefer to align along one axis rather than another. This can be influenced by a number of factors including crystal anisotropy. The preferred direction of alignment is often called the “easy direction” while the other orientations are called “hard directions”. As an example, a ferromagnetic material can become magnetised at a low applied field directed along the easy direction yet require a higher applied field perpendicular to this to become magnetised along the hard direction.

Crystal anisotropy arises mostly from spin-orbit coupling within a lattice and describes the interaction between the spin and orbital motion of the electrons (Cullity, 1972). The spin-orbit coupling of a free ion, is different from an ion in a lattice due to the changes in the orbital moment. For example, free Fe^{2+} has an orbital moment due to the 6th electron in the *d*-shell, which is coupled to the spin by the spin-orbit coupling. However, within a crystal structure, the total moment is less than that for the free atom. In a crystal structure, the orbital moment is partially quenched, leading to an effective moment that is somewhat less for an atom bound in a solid than a free atom. Thus in a solid, the orbital direction is fixed to the lattice, which also fixes the spin via the spin-orbit coupling.

The energy of a system is lowest when the moments align along a direction called the easy magnetic direction. To rotate the moments to a harder direction requires an applied field with

enough energy to overcome the anisotropy. Thus the energy required is called the anisotropy energy, which is large enough to overcome the spin-orbit coupling. Spin-spin coupling involves an exchange interaction between two spins that keep their relative alignment constant (i.e. parallel or antiparallel). This exchange energy relies only on the relative angle between the spins and not the alignment within the crystal. Orbit-lattice coupling involves fixing the orbital component of the magnetic moment within the lattice.

Long-range magnetic order can be described by a combination of three interactions. These include exchange interactions, magnetic dipole interactions and single ion anisotropy interactions. Exchange interactions between neighbouring atoms can be described by the exchange coupling constant, J , as defined in Equation 1.6 where the exchange constant is closely related to the magnetic ordering temperature, T_c and the spin angular momentum, S . By considering only the z nearest neighbours with all other interactions negligible, the interaction can be defined by the following equation (Kittel, 1986).

$$J = \frac{3k_B T_c}{2zS(S+1)} \quad (1.6)$$

These exchange interactions are often approximated using the mean field theory (MFT) of solids developed by Pierre Weiss. This model approximates all of the exchange interactions within a lattice and replaces them with an overall, equivalent magnetic field, H_m . Thus every moment, no matter how remote, contributes to the overall molecular field. This field acts on each moment just as an external field would, such that H_m is said to be proportional to the magnetization of the sample (Mattis, 1965). The exchange constants tend to be highly isotropic which is responsible for producing magnetic order in the mean field approximation. The MFT indicates that both the exchange and anisotropy fields will affect an antiferromagnetic material in an applied field. The exchange field can be written as

$$H_E = \frac{-2Jz\langle S \rangle}{g\mu_B} \quad (1.7)$$

where $\langle S \rangle$ is the average value of the spin angular momentum value, S , along the direction of magnetic order and z is the number of nearest neighbours of a given spin, coupled together. Similarly, the anisotropy field is

$$H_A = \frac{2K\langle S \rangle}{g\mu_B} \quad (1.8)$$

where K is the anisotropy constant which is different for different materials.

The interaction between two spins, across all pairs of ions in the material, can be described by a model known as the spin Hamiltonian. In its most simple form it is known as the Heisenberg Hamiltonian. The Heisenberg Hamiltonian involves isotropic exchange interactions that depend only upon the angle between the spins on nearest neighbours as in Equation 1.9 below.

$$\mathcal{H}^{spin} = -\sum_{i,j} J_{ij} \underline{S}_i \cdot \underline{S}_j \quad (1.9)$$

Here, J_{ij} is known as the exchange-coupling constant representing the exchange forces between two magnetic atoms at sites, i and j . When the exchange constant is negative, it implies that the interaction between the nearest neighbours is antiferromagnetic. Ferromagnetic materials have positive exchange constants. The spin Hamiltonian can also be written in its extended form, as described by the MFT, which contains three major interaction terms (Okuda et al., 1983).

$$\mathcal{H} = -2J \sum_{i,j} S_i S_j - K \sum_i S_i^2 + g\mu_B H_0 \sum_i S_i \quad (1.10)$$

The first term in Equation 1.10 is the simple exchange interaction between two magnetic atoms within a lattice from Equation 1.9. The second term takes into account the axial distortion from the single-ion anisotropy and involves the crystal field parameter, K also known as the anisotropy constant from Equation 1.8. This term arises from the effects of spin-orbit splitting and crystal field effects. That is, the orbital overlap of the electrons allow the magnetisation of the crystal to "see" the crystal lattice and the spin interacts with the orbital motion via spin-orbit coupling. It has been found to be temperature dependent, reducing to zero around the critical temperature (Cullity, 1972). For Fe^{2+} in the compound FePS_3 , the K -term arises from the splitting due to the large octahedral crystal field as well as the smaller trigonal field (Jernberg et al., 1984). The final term in this equation is the Zeeman term and represents the interaction with the external field, H_0 , applied to the material.

The MFT is ideal for describing three-dimensional magnetic lattices as it treats all the interactions between spins equally. Thus the magnetic exchange field is taken as an average

across all S in the material. The MFT is not good for modelling systems with long-range order, as these materials tend to have short-ranged interactions. The MFT does not account for variation in the dimensionality of either the magnetic lattice or the spins themselves, and so does not adequately model low energy excitations.

The dimensions of a magnetic lattice can be described according to the interactions that take place between moments. Some magnetic materials may be restricted to exchange interactions between planar spins only, which would imply that the interactions are 2-dimensional (2D). The 2D nature of the exchange may originate from a 2D crystal structure, with physical distance reducing the possibility of interplanar magnetic exchange. This event is not taken into consideration by the MFT model.

Mathematical models can be used to describe the spin orientations as a function of temperature and applied field. These are often depicted as various forms of the spin Hamiltonian. A spin arrangement, with only one defined spin direction, can be described by an $S = 1/2$ Ising system. An Ising system is divided into two states – spin up and spin down, along one axis, when the uniaxial anisotropy constrains the spin to lie in one crystal direction or when the interaction only depends on the z-component of the spin. Each moment is given a spin state in the Ising model and the interactions between spins can form 1D chains, 2D planar interactions or 3D interactions throughout the lattice. The interactions are commonly restricted to nearest neighbour and second nearest neighbour interactions to simplify the model. A planar spin arrangement can be modelled by the XY-model, which implies that the spins are constrained by the uniaxial anisotropy to lie in the plane, or that the interactions depend only on the xy -components of the spin. Finally, the Heisenberg model can be used to describe an isotropic spin system. In this model, the spins are not restricted to any plane or axis. The spin dimensionality, and therefore the magnetic system, can be determined by expanding Equation 1.9.

$$\mathcal{H} = - \sum \left\{ J_{\perp} (S_{ix} S_{jx} + S_{iy} S_{jy}) + J_{\parallel} (S_{iz} S_{jz}) \right\} \quad (1.11)$$

When either $J_{\perp} = 0$ or $J_{\parallel} = 0$, the equation represents either the Ising model or XY model respectively, and when $J_{\perp} = J_{\parallel}$ the equation represents the isotropic Heisenberg Hamiltonian.

1.3 MAGNETIC MATERIALS

The MFT can be used to predict the magnetic susceptibility of a material at high temperatures. Magnetic materials can be classified according to their bulk susceptibility – the magnetization of a material, M at a particular applied field, H . Here, the magnetisation can be defined as the magnetic moment per unit volume of a material. This can be described by the equation below, which is an indication of how susceptible the magnetic moments are to align within an applied magnetic field.

$$\chi = \frac{M}{H} \quad (1.12)$$

Ferromagnets are defined by their ability to become magnetised with all magnetic moments aligned in one preferred direction (Figure 1.1a). Widely known ferromagnetic elements include Fe, Ni and Co. These materials have large, positive susceptibilities, greater than 1 with typical values between 50 and 10 000 (Jiles, 1991). The units of χ are dimensionless.

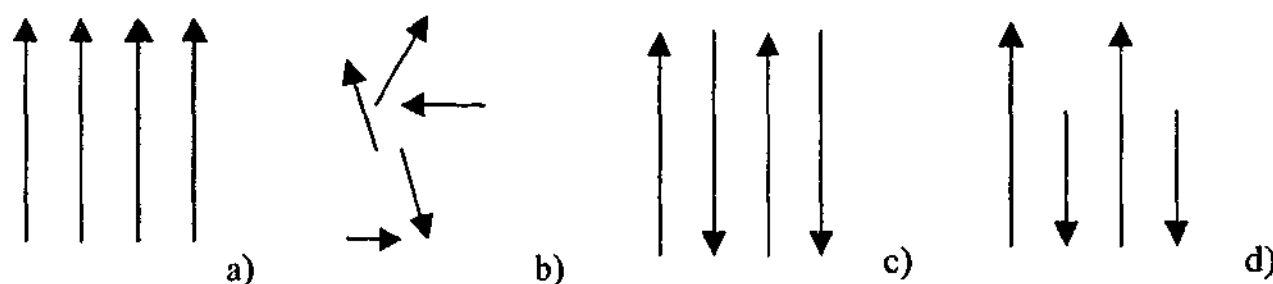


Figure 1.1: Magnetic Ordering can be defined by the ordered arrangement of the electronic spins. a) a simple ferromagnet, b) paramagnet, c) antiferromagnet and d) ferrimagnet

Paramagnetic materials have no intrinsic magnetic order. That is, their magnetic moments are non-zero but aligned randomly throughout the sample such that the overall magnetisation of the material is zero. However when a paramagnetic material is aligned within an applied field, the magnetisation aligns weakly along the direction of the field. General susceptibilities for these materials are $\chi \approx 10^{-3}$ to 10^{-5} (Jiles, 1991). Increasing the temperature in a paramagnetic material will increase thermal vibrations between atoms, which therefore increase the randomisation of the moments, thus lowering the susceptibility. A simplified diagram of a paramagnetic arrangement can be seen in Figure 1.1b.

Antiferromagnetic materials have a small positive susceptibility that varies with temperature. These materials are considered to have zero overall magnetisation and for a long while they were considered to be paramagnetic. However, neutron diffraction studies on MnO (Shull & Smart, 1949) indicated a strong magnetic order below a critical temperature, the Néel temperature. The only difference between paramagnetic and antiferromagnetic susceptibilities can be seen when measurements are taken over a range of temperatures above and below the Néel temperature. Collinear antiferromagnetic materials, when magnetically ordered, have two magnetic moment sublattices within which the moments are parallel, but between which they are antiparallel. This results in zero overall magnetisation and can be seen in Figure 1.1c. There are different types of antiferromagnetism – the simplest being collinear antiferromagnetism. This case looks at quantised moments, with only two possible moment directions at low temperatures in the ground state; up or down. Other possible antiferromagnetic structures involve canted moments, or helical or screw arrangements, where the moments rotate about a given axis with an overall magnetisation of zero.

Ferrimagnetic materials have similar properties to both ferromagnetic materials and antiferromagnetic materials. The moments form two sublattices as in antiferromagnets, yet the size of the moment in each sublattice is different such that the overall magnetisation in the material is ferromagnetic. This can be seen in Figure 1.1d.

1.4 CURIE'S LAW OF MAGNETIC SUSCEPTIBILITY

Magnetic materials can undergo various magnetic phase changes that are temperature dependent, with the most common phase change being that between magnetic order and disorder. The susceptibility of a material is temperature dependent and changes in susceptibility highlight the magnetic phase changes. Susceptibility was measured extensively by Pierre Curie (Cullity, 1972) in 1895 when he found that a material's magnetisation changes according to the temperature at which it is used. For instance at very high temperatures, most materials are paramagnetic, due to the random, thermal motions of the moments. A ferromagnetic material becomes magnetically ordered below its Curie temperature, T_C while an antiferromagnetic material orders below the critical temperature called the Néel temperature, T_N . This can be seen in Figure 1.2 (Kittel, 1986).

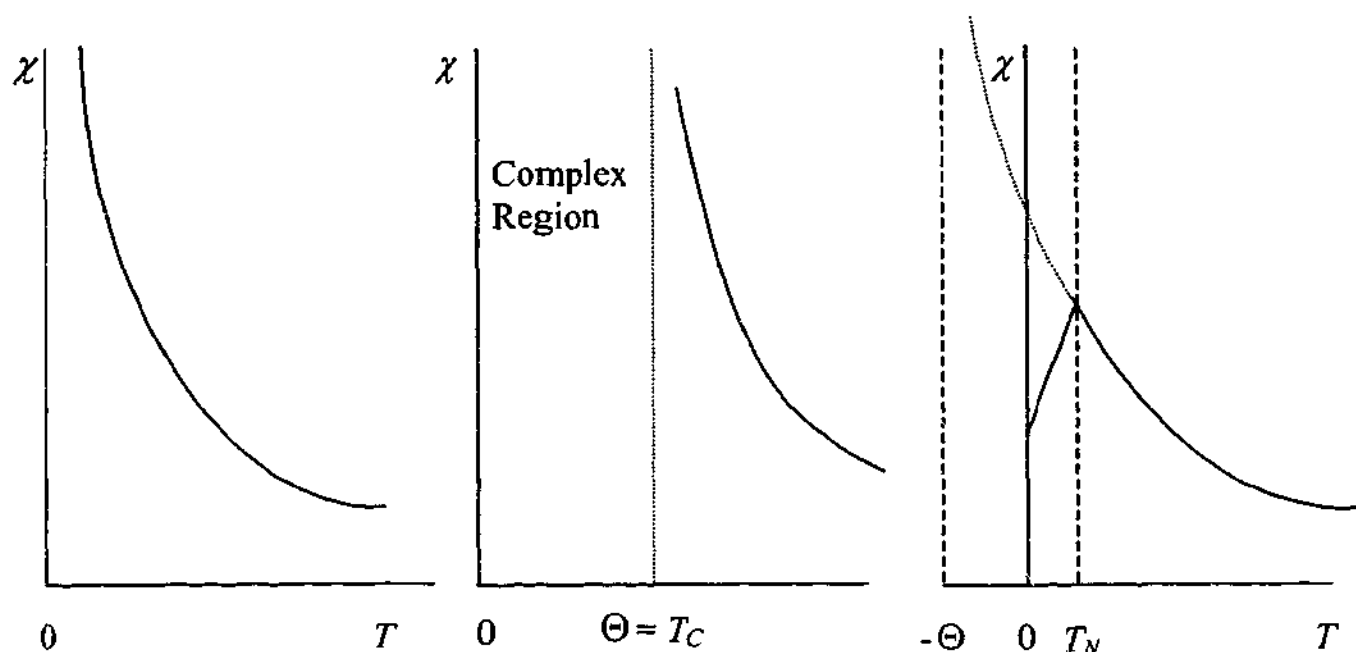


Figure 1.2: Temperature dependence of the magnetic susceptibility for a paramagnet, a ferromagnet and a powder averaged antiferromagnet. Above the transition temperature, each follows the Curie-Weiss law in Equation 1.13 (Kittel, 1986). For a powdered antiferromagnetic sample, the susceptibility falls to approximately $2/3$ of the maximum value below the Néel temperature.

Curie found that susceptibility varies inversely with temperature in the paramagnetic phase, which is indicated in the Curie-Weiss law in Equation 1.13 (Jiles, 1991)

$$\chi = \frac{C}{T - \Theta} \quad (1.13)$$

Here Θ is the Weiss characteristic temperature and C is the Curie constant. As the temperature is reduced, the susceptibility goes to infinity at the critical temperature when $T = \Theta$. Infinite susceptibility indicates that for zero applied field, the material will have a finite magnetisation (Cullity, 1972). When $\Theta > 0$, the susceptibility describes a material that will undergo a phase transition from paramagnetic to ferromagnetic at the ordering temperature, defined as the Curie temperature, $\Theta = T_C$. Materials that can be described by $\Theta < 0$ in the equation above, undergo a transition from paramagnetic to antiferromagnetic at the ordering temperature which is usually (but not always) the Néel temperature, $|\Theta| = T_N$.

In a simple collinear antiferromagnet, the value of Θ is negative since the magnetic moments are strongly coupled together by the exchange interaction which is negative between

nearest neighbours (Smart, 1966). For a paramagnet, Θ is equal to zero. The Curie constant, C , is given by

$$C = \frac{Ng^2\mu_B^2S(S+1)}{3k_B} \quad (1.14)$$

where N is the number of magnetic atoms per volume, and k_B is Boltzman's constant (Abragam & Bleaney, 1986). Thus by combining Equations 1.13 and 1.14, the high temperature susceptibility can be given by Equation 1.15 below (Niira & Oguchi, 1954). A value of the spectroscopic splitting factor, g , can be measured with this law. When looking at the plot of $1/\chi$ versus temperature for temperatures well above the ordering temperature, the gradients of the parallel and perpendicular inverse susceptibility lines should differ, however the temperature intercept should be the same for both plots (Figure 1.3). The gradients will give the value of the g -factor, while the intercept will be the Θ value in the Curie Weiss law:

$$\chi = \frac{Ng^2\mu_B^2S(S+1)}{3k_B(T+\Theta)}, \quad \text{so} \quad (1.15)$$

$$\frac{1}{\chi} = \frac{3k_B T}{Ng^2\mu_B^2S(S+1)} + \frac{3k_B\Theta}{Ng^2\mu_B^2S(S+1)}$$

The parallel and perpendicular susceptibilities are different primarily due to the strength of the anisotropy in each direction. If the field is applied parallel to the preferred direction of moment orientation, then a small applied field is required for alignment, however, a much larger applied field is required to overcome the anisotropy if the preferred moment orientation is perpendicular to the applied field direction.

An example of this is the antiferromagnet FeF_2 , which can be seen in Figure 1.3, in which the susceptibility is greatest for the applied field parallel to the antiferromagnetic direction (Niira & Oguchi, 1954). The parallel susceptibility was taken for an applied field parallel to the z direction, which is also the preferred direction of moment alignment.

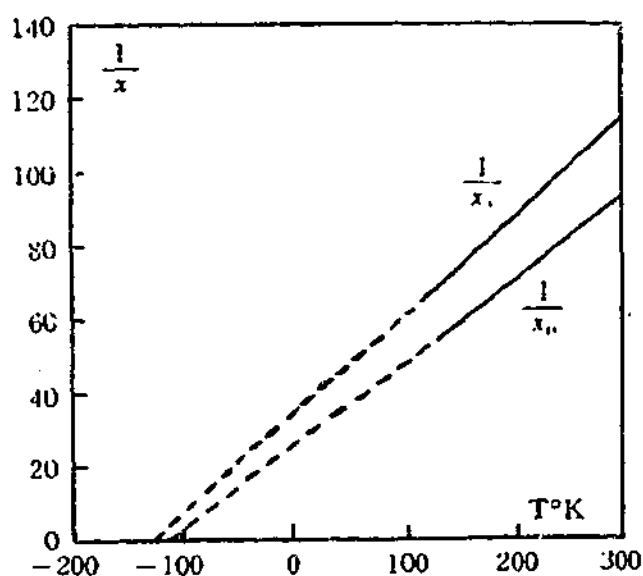


Figure 1.3: Plot of inverse molar susceptibility for FeF_2 (Niira & Oguchi, 1954). The top line represents the inverse susceptibility for an applied field perpendicular to the preferred direction of moment orientation, while the lower line represents the inverse susceptibility for an applied field parallel to the preferred moment direction.

The high temperature susceptibility for an antiferromagnet can also be written as a series expansion,

$$\chi(T) = \frac{N (g\mu_B)^2}{V 3k_B T} S(S+1) \left[1 + \frac{\Theta}{T} + O\left(\frac{\Theta}{T}\right)^2 \right] \quad (1.16)$$

$$\Theta = \frac{S(S+1)}{3} \frac{J_0}{k_B}, \quad J_0 = \sum_R J(R)$$

where Θ is directly proportional to the exchange interactions, J_0 between nearest neighbours separated by R . Here, V is the volume (Ashcroft & Mermin, 1976). This is simply another form of the Curie-Weiss law (Equation 1.15) with a factor of $[1 + \Theta/T]$, where the value of this factor is greater than unity for ferromagnetic coupling and less than unity for antiferromagnetic coupling. Thus higher order expansions of this equation can be used to determine the nature of ordering below the critical point, even for susceptibility measurements taken above the ordering temperature. The magnitude of Θ is determined by the strength of the exchange interactions from the sum of the first, second and more distant nearest neighbours according to the MFT. This

can be seen in the different forms of the susceptibility curves for ferromagnets and antiferromagnets in Figure 1.2.

At temperatures around the transition temperature, such as the Néel temperature for an antiferromagnet, a phase change occurs and the bulk magnetic properties of the material change. This region is known as the critical point of the material. Other properties such as specific heat, thermal expansion and magnetoresistance also go through critical changes around the transition temperature. By applying a strong external magnetic field to a material, magnetic phase changes can be induced at temperatures close to the critical point (de Groot & de Jongh, 1986). A phase change does not always refer to the change from order to disorder as it does when discussing the spontaneous magnetisation of an antiferromagnetic material. The phase change at the critical point could also indicate a change from one type of order to another.

The Curie-Weiss law does not hold true for materials below the magnetic ordering temperatures. Below the Néel temperature of an antiferromagnet, the susceptibility curve tends to diverge, depending on whether the field, B , is applied parallel or perpendicular to the direction of magnetisation in a single crystal sample, as in Figure 1.4.

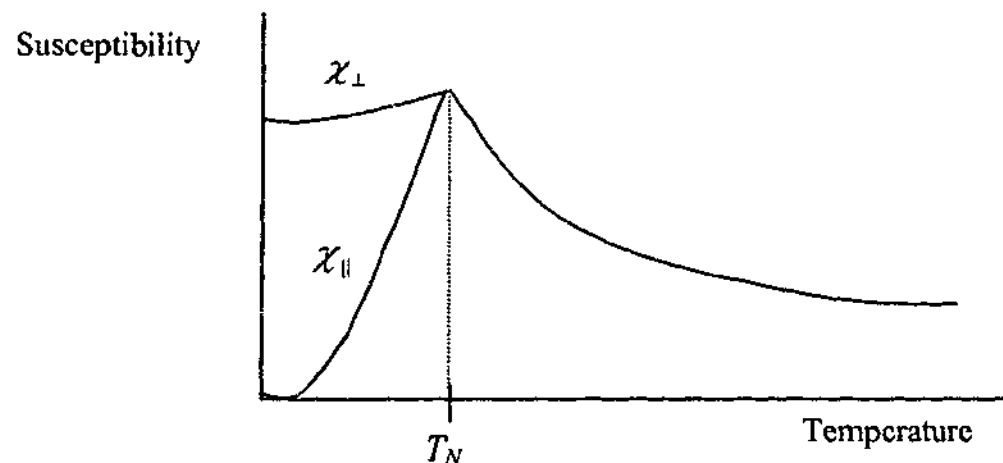


Figure 1.4: Magnetic susceptibility curve for a simple antiferromagnetic material. For a simple antiferromagnetic material the susceptibility reaches a maximum at the Néel temperature, T_N . Applied fields parallel and perpendicular to the moment direction give remarkably different susceptibility curves.

The observed orientation dependence is due to the anisotropy of the moments within the crystal lattice. Magnetic susceptibility measurements of an antiferromagnet shows that parallel susceptibility ($\chi_{||}$) goes to zero at zero temperature, while the perpendicular susceptibility (χ_{\perp}) goes to some non-zero value at zero temperature (Niira & Oguchi, 1954). The susceptibility of a

powder-averaged sample will decrease to around $2/3$ of the peak height, which corresponds to twice as many crystallites with a magnetisation perpendicular with the applied field, as parallel to it. This was displayed in the furthest right plot in Figure 1.2.

At $T = 0$ K, the antiferromagnetic moments remain strongly coupled together in a single crystal sample, such that applying a small field parallel to one sublattice will not be sufficient to shift the other sublattice from its antiparallel position. An example of this type of phenomenon is the spin-flop phase transition, which can occur in antiferromagnets like MnPS_3 . This results in zero susceptibility, as the exchange field between the moment sublattices at low temperatures is much stronger than the applied magnetic field. When the moments are perpendicular to the applied field at zero temperature, even small amounts of field can begin to rotate both moment sublattices, giving a finite susceptibility at low temperatures.

Heisenberg antiferromagnets, with moderate anisotropy, often exhibit a bi-critical point around the Néel temperature. At this position, there is a phase change between antiferromagnetic, paramagnetic and the spin flop phases as in Figure 1.5. However it must be noted that phase changes occur across the boundaries of each line. The bi-critical point is unique in that it is the distinction between two phase changes from the antiferromagnetic phase.

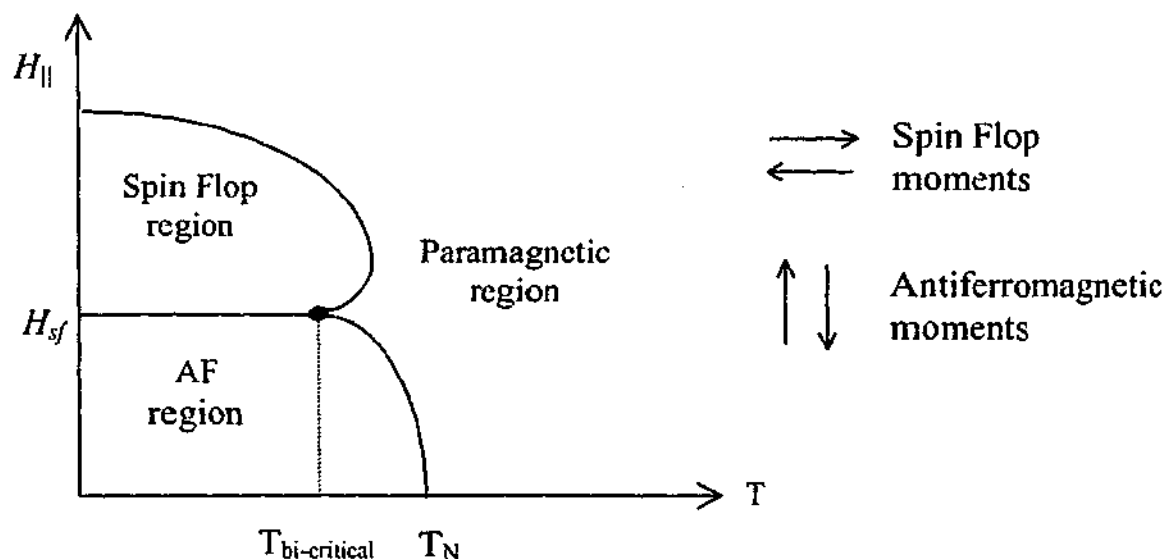


Figure 1.5: Possible phase diagram to illustrate the boundaries for the antiferromagnetic (AF), paramagnetic and spin flop phases. The field is applied parallel to one moment sublattice. The bi-critical temperature indicates the parameters where two phase-changes occur. (Landau & Binder, 1981)

In an antiferromagnetic material, the moments from the two sublattices are often so strongly bound to each other via exchange interactions, that an applied field parallel to one of the sublattice directions will not result in the antiparallel moments flipping parallel with the applied field. Instead, it has been found that the moments remain coupled and flop approximately perpendicular to the applied field. This rotation of paired moments is called a spin flop and occurs at a critical field H_{sf} , which is nearly temperature independent. In this case, the energy required to turn the antiparallel moments parallel to the field is much greater than the energy required to flip both moment sublattices perpendicular to the applied field (de Groot & de Jongh, 1986). The spin flop critical field can be viewed schematically in Figure 1.5 and is given by

$$H_{sf} = \sqrt{(2H_E H_A - H_A^2)} \quad (1.17)$$

which can be simplified by the approximation for small anisotropy when $H_E \gg H_A$ (Okuda et al., 1983).

$$H_{sf} \cong \sqrt{(2H_E H_A)} \quad (1.18)$$

where H_E is the exchange field and H_A is the anisotropy field as defined in Equations 1.7 and 1.8. This can be observed as a phase transition similar to Figure 1.5. For MnPS_3 , the spin flop field at 4.2 K was around 3.7 ± 0.3 T (Okuda et al., 1986). More recently the Mn spins were found to flop at 4.5 T at 0 K (Goossens & Hicks, 1998). The discrepancy between these values of approximately 20 % was deemed to be a fault in the earlier work, due to the highly accurate reproducibility of the later value (Goossens & Hicks, 1998).

1.5 ANISOTROPY DUE TO CRYSTAL FIELD EFFECTS

Another quantity related to the susceptibility and anisotropy of the material, is the spin-orbit coupling coefficient, λ . This parameter describes the degree of the coupling between the electronic spin and orbital angular momenta for an ion within a material. Defined in Hund's third rule, the lowest energy for a single electron will be achieved when the spin and orbital angular momentum of that electron are antiparallel (Kittel, 1986). When the spin angular momentum vector is oriented directly opposite to the magnetic moment vector, the value of λ is positive. A free transition metal ion will have one electron ground state in the 3d level which is 5-fold

degenerate (see Figure 1.7). However when the same ion is bound within a crystal lattice, the energy levels of the electrons will be split as the degeneracy is lifted. A large spin-orbit coupling would be related to a large splitting of the degenerate spin states, such that only the lowest energy state would be occupied. Alternatively, if the spin-orbit coupling coefficient was very small, the electrons would require less energy to be in each of the degenerate states, thus rendering them similar in energy level.

The value of the spin-orbit coefficient for a free ion is different to an ion embedded within a lattice, due to the shielding effects of the ligand electrons. This coefficient, λ , is usually negative for electron shells that are *more* than half full and positive for those that are *less* than half full (Abragam & Bleaney, 1986). An ion that has a half full electron shell, such as manganese, which is spherically symmetric, will not experience spin-orbit coupling. It has been evaluated by Griffith (1971) that for a free ion of Fe^{2+} , the spin-orbit coupling coefficient is -92 cm^{-1} and it has been found to be -101 cm^{-1} by Abragam and Bleaney (1986).

The spin-orbit coupling constant has been related to the spectroscopic splitting factor, g , according to the following equation (Joy & Vasudevan, 1992a).

$$g_i^2 = \frac{3(kT)^2}{\mu_B^2 S(S+1)} \frac{\partial^2}{\partial H^2} (\ln Z_i) \quad (1.19)$$

where $i = \parallel$ or \perp , Z_i is the partition function $\sum \exp(-E_j/kT)$ and E_j are the energies of the accessible states. From this the parallel and perpendicular g factors can be found (Joy & Vasudevan, 1992a). Thus the Weiss temperature, Θ , is dependent on the exchange parameter, J , and the spin-orbit coupling constant, λ . The different excited states in the material are directly related to the different states of the spin-orbit coupling.

Both spin-orbit coupling and crystal fields can affect the susceptibility of the transition metal ions, just as they can affect their magnetic moments. The $3d$ electrons in the transition metal ions experience an inhomogeneous electric field from the neighbouring ions in the crystal lattice. This crystal field forces a reduction in the spin-orbit interaction from the free ion value. The orbital angular momentum can then couple strongly with the crystal lattice field, which splits the $(2L + 1)$ degenerate orbital sublevels into different energies. For instance, if $L = 1$, then the levels $m_L =$

$\pm 1, 0$ each have the same energy in a free atom situation. In a solid lattice, affected by the crystal field, these levels form three separate and discrete energy levels.

The magnetic susceptibility is highly dependent on the magnetic anisotropy of the magnetic ion. Thus the degree of anisotropy can be determined by investigating the splitting of the ground state electron levels and the distribution of the electrons in the crystal structure. The electric field within a lattice is also known as the crystal field and is produced by the surrounding electrons and nuclei in the structure. A spherically symmetric charge distribution about a metal ion will produce no crystal field effects in the lattice as there is no preferred orientation of the ion. If the charge distribution is anything other than spherical, the crystal field will align along the easy axis for the lowest energy state. Upon excitation to a higher energy state, the symmetry in the lattice will not necessarily follow the same symmetry. Manganese, with its spherically symmetric charge distribution, will show minimal anisotropy, and therefore little crystal field splitting.

The compound FePS_3 can be considered as a cubic close-packed array of sulphur atoms with FeP_2 groups sitting on trigonally distorted octahedral sites (Taylor et al., 1973). An octahedral arrangement of point charges around an Fe^{2+} ion will look like Figure 1.6 below.

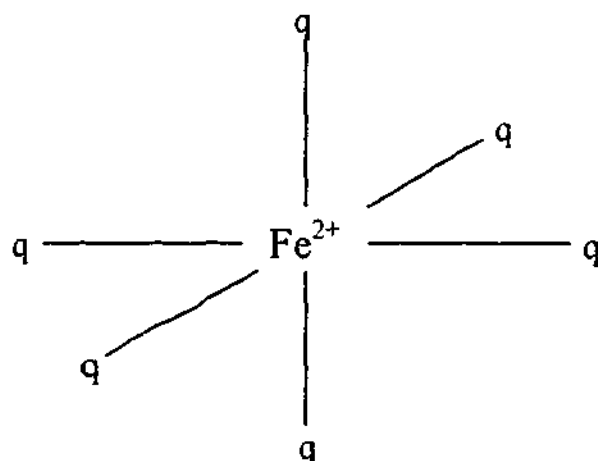


Figure 1.6: Ligand point charges surrounding an Fe^{2+} ion

A non-distorted octahedral crystal field will produce an orbital triplet and doublet with the triplet level lowest in energy (Ingalls, 1971). Inducing distortion will remove the degeneracy and produce a further crystal field splitting. Tetragonal distortion corresponds to a compression along the $[100]$ axis, while trigonal distortion involves the compression along the $[111]$ direction.

The trigonal distortion splits the degeneracy of the octahedral symmetry as can be seen in the following energy diagram. For FePS_3 , the d -orbitals are five fold degenerate, splitting into a triply degenerate T_{2g} and a doubly degenerate E_g level as seen in Figure 1.7. The $3d$ states in transition metal compounds are more easily described by the weak field limit of the crystal field theory rather than a strong field (Joy & Vasudevan, 1992a).

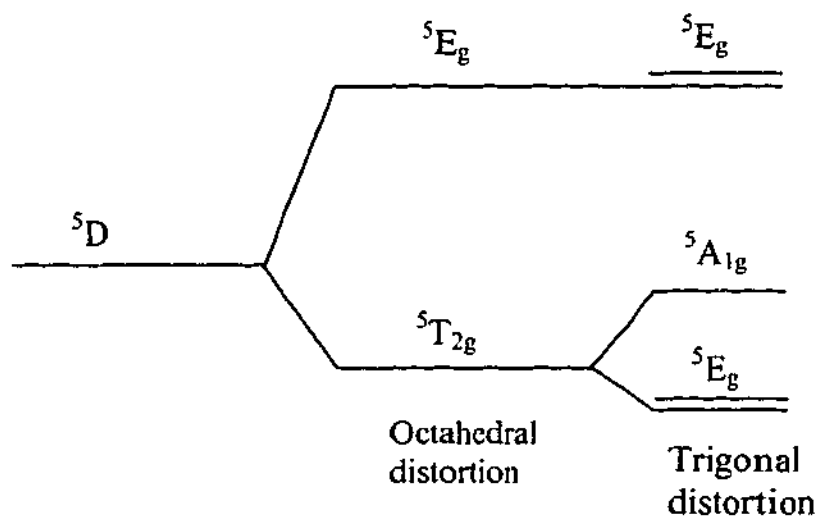


Figure 1.7: Splitting of energy levels in FePS_3 due to distortion of the crystal field. The single line represents the electron energy level of a free ion. The next lines represent the splitting of orbital states caused by octahedral and trigonal fields.

The susceptibility measured in the paramagnetic region can also be used to determine the spin structure of the metal ions (Joy & Vasudevan, 1992a). The most common situation for the divalent metal ions is in fact a high spin configuration, which is an indication that all the $3d$ levels are occupied (Figure 1.8a). This follows Hund's rules and for Fe^{2+} gives a quantum spin number of $S = 2$ due to the unpaired electrons. A low spin state would indicate that the splitting between the $^5T_{2g}$ ground state and the 5E_g energy level is larger than the pairing energy and so the electrons prefer to pair in the $^5T_{2g}$ (Figure 1.8b). The spin of this system is $S = 0$.

The high and low spin-orbital diagram in Figure 1.8 shows that the splitting of the energy levels is defined by the cubic field splitting parameter, Dq , which for a free, unbound ion of Fe^{2+} is 1000 cm^{-1} (Abragam & Bleaney, 1986). The splitting of the energy levels can also be described by the term Δ , which is equivalent to $10Dq$. This value is typically taken from the optical absorption data and has been found for FePS_3 to be $\Delta = 8700 \text{ cm}^{-1}$ by Joy and Vasudevan

(1992b). The difference in these values is due to the different environments of the Fe^{2+} ion; either as a free ion, or bound within a solid with crystal field effects from the P and S ions.

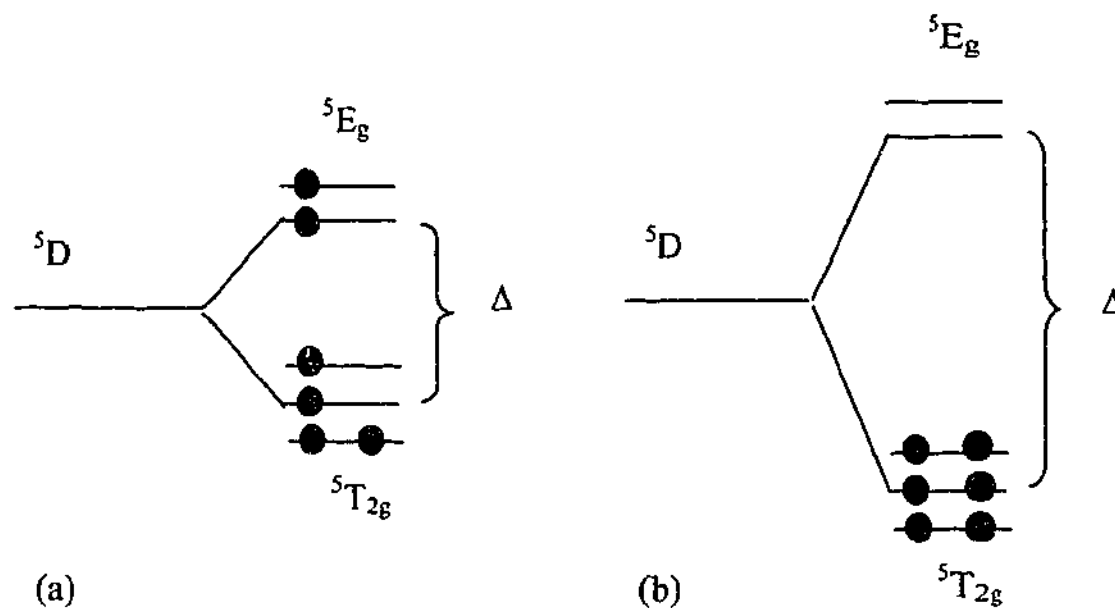


Figure 1.8: High spin state (a) for an Fe^{2+} ion and a low spin state (b) showing the difference in energy required to pair the electrons. For a low spin state, the value of Δ is greater than the pairing energy of the electrons.

1.6 MAGNETIC EXCITATIONS AND SPIN WAVES

The classical model of a magnetic moment will find it fixed and aligned with one particular direction, say the z -direction, at zero temperature. For simplicity, this model describes the magnetic moments at an atomic site as static with the direction dictated by the local anisotropy. However, the spin of a moment can also be defined as a vector quantity by quantum mechanics, with three angular momentum components in a dynamic environment. In this case, the z component is less than the magnitude of the classical angular momentum. In addition to the vector model of the atom, the spins fluctuate about the average spin direction (z), causing the measured spin on the ion to be less than that predicted by Hund's rules. This difference in the value of the spin for antiferromagnets is known as the spin defect and is dependent upon the exchange interactions at low temperatures in an ordered state. As the spins are connected by the exchange interactions, collective vibrations are set up in the lattice as spin waves. Quantum mechanically, the lowest energy of these vibrations is not zero, thus oscillations remain at $T = 0$

K which results in the spin defects in antiferromagnets. However the higher the spin quantum number, S , the closer the system is to the classical model, and the smaller the spin defect.

Reducing the temperature of a magnetic material to zero temperature will ensure that it is in its ground state. Classically this means that the magnetic moment on each atom will align in a fixed position. For simplicity, consider the alignment for a simple ferromagnet, such that there is only one magnetisation direction. The ground state of a ferromagnet occurs when all spins are aligned in the same directions (Figure 1.9a). For temperatures above $T = 0$ K, the thermal energy within the lattice increases, and the moments are free to move and vibrate into excited states. The simplest concept of an excited magnetic state is when one moment becomes aligned antiparallel to the direction of magnetisation (Figure 1.9b). This is not necessarily the lowest energy level excited state. Spin waves, otherwise known as magnons, occur when the moments rotate about a common axis (Figure 1.9c). Each moment is related to its neighbour by an angular phase difference, such that the moments appear as waves through the lattice. Tilting all of the moments to an angle of θ with respect to each other requires much less energy than rotating one moment antiparallel to the magnetisation direction (Jiles, 1991). The angle θ can also change by small increments giving a continuum of excited energy levels, which cannot be realised by flipping individual spins.

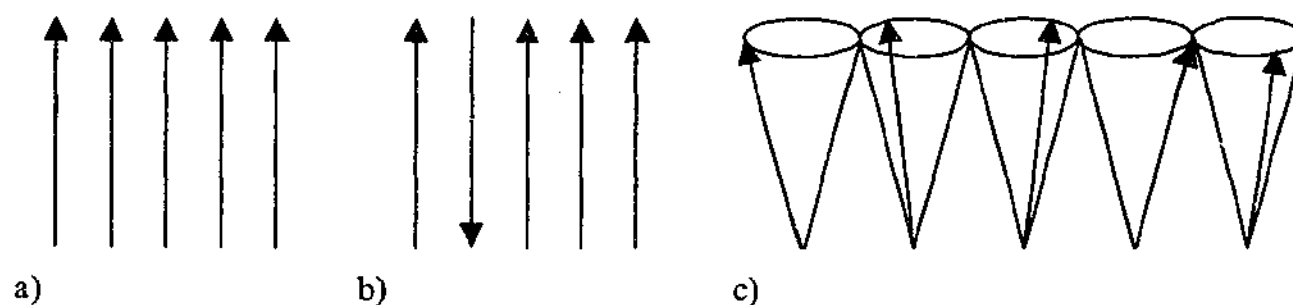


Figure 1.9: a) Ground state ferromagnet with two excited states; b) a single, antiparallel moment and c) spin waves

The energy of a spin wave can be described by Equation 1.20 in which q is the wave number and D is a stiffness constant controlled by the strength of the interactions that stabilize the magnetic order (Crangle, 1991).

$$E = \hbar\omega = Dq^2 + E_0 \quad (1.20)$$

Here E_0 is the static energy of the spin proportional to the total field at the atom, which is produced by the applied and anisotropy fields.

1.7 LOW DIMENSIONAL MAGNETISM

Low dimensional magnetic materials have come under much scrutiny over the last few decades due to interesting properties observed about the critical region. Low dimensional magnetism indicates that the magnetic ordering may be restricted to one or two dimensions. For instance, two-dimensional magnetic materials have strong coupling with nearest neighbour ions in two dimensions, but little to no exchange interactions in the third. Two-dimensional (2D) magnetic systems are often referred to as *quasi*-two dimensional, indicating that the ordering is actually 3-dimensional and long-ranged, however the interactions along one direction are much weaker than the other two. A true 2D magnetic material may have incomplete long-range order along at least one axis.

Two-dimensional magnetic materials tend to exhibit a much broader critical region about the ordering temperature than 3D materials. Thus critical behaviour can be investigated in more detail in these materials. Two-dimensional materials have also been found to display short-range order between moment spins at high temperatures (Joy & Vasudevan, 1992a). A lot of the materials that fall into the low dimensional category are not crystallographically 2D, but have non-magnetic elements separating the magnetic ions. Thus the 2D material takes on layered magnetic characteristics with a magnetic dimensionality of 2.

One such family of compounds that is considered to be two-dimensional both structurally and magnetically is the transition metal thiophosphate group MPS_3 (where $M = Mn, Fe, Ni$ etc.). These materials were first investigated by Klingenberg *et al.*, (1968) and have been studied consistently for the last three decades. Unlike many 2D magnetic systems, the transition metal ions are separated by a van der Waals gap parallel to the *ab*-plane, rather than non-magnetic species.

Manganese thiophosphate has been studied extensively as a two dimensional magnetic material due to the low anisotropy of the Mn ions. In the Mn^{2+} ion, the *d*-shell electrons occupy half the shell such that the manganese ions have a spherically symmetric distribution of electrons

about the nucleus. This leads to a very low anisotropy. It is best described by the isotropic Heisenberg Hamiltonian (Joy & Vasudevan, 1992a).

The purpose of this research was to investigate low-dimensional materials, specifically FePS₃. This thesis investigates primarily the magnetic properties of this material in both the ordered and paramagnetic states. Although this material has been studied extensively for the past 4 decades, the investigation is by no means complete. Thus it is an aim to collect all the information currently available and complete the picture of FePS₃ as a low-dimensional antiferromagnetic material.

Throughout this thesis, FePS₃ has been compared with the closely related compound, MnPS₃, as they both show remarkably different characteristics. Although the structures of these crystals are very similar, the magnetic properties remain very different. For instance MnPS₃ has been grouped as a Heisenberg antiferromagnet whereas FePS₃ has been considered as an Ising type antiferromagnet. This distinction shall be investigated further in this thesis. The most significant difference between Fe²⁺ and Mn²⁺ is the single extra electron in the 3*d*-shell of iron. It is intriguing to consider that just one extra electron can make such vast differences to the crystallographic and magnetic properties of FePS₃.

An original purpose of this investigation was to observe spin glass behaviour in the composite structure Zn_xFe_{1-x}PS₃ beyond the critical concentration for antiferromagnetism. By replacing the magnetic Fe²⁺ with the non-magnetic Zn species, the crystals could be diluted magnetically. This would have produced a 2D Ising spin glass, which is interesting to study as the lower critical dimension of an Ising spin glass is 2. However, the antiferromagnet structure of FePS₃ was found to be different to the previously accepted model and thus the direction of this work was focused on determining a correct magnetic structure.

CHAPTER TWO

2: Introduction to Iron Thiophosphate

Iron thiophosphate belongs to the family of thiophosphates with the generic formula MPS_3 , where M is a transition metal (eg. Mn, Ni, Fe, Zn). These compounds exhibit antiferromagnetic behaviour, with weakly connected layers and are thought to be good examples of quasi two-dimensional magnetism (Joy & Vasudevan, 1992a). The crystal structure of these compounds can be seen below in Figure 2.1. The transition metal ions form a honeycomb structure within the ab -plane, which is flanked by phosphorus pairs. The bond length between the P-P pairs has been found to be 2.2 \AA parallel to the c -axis (Khumalo & Hughes, 1981). Two layers of sulphur atoms, which are in turn separated by van der Waals gaps, separate each Fe-P layer. This can also be viewed along the c -axis as in Figure 2.2.

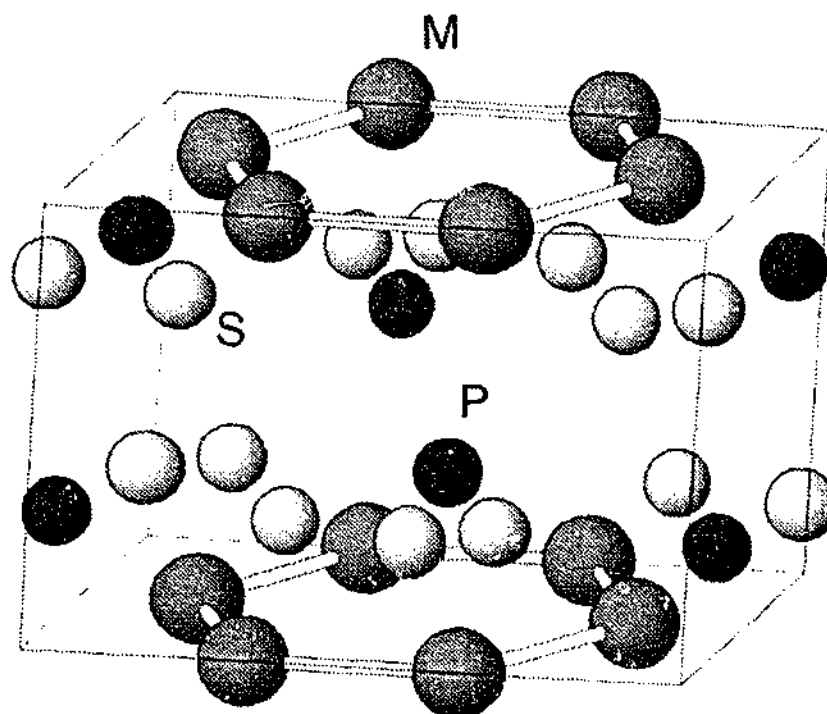


Figure.2.1: Relative positions of the transition metal (M), sulphur (S) and phosphorus (P) atoms.

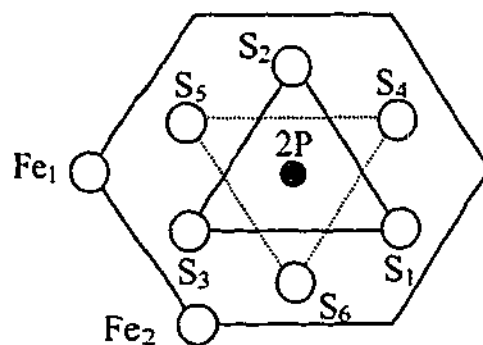


Figure 2.2: The formula unit of FePS₃ consisting of a basis of 2 Fe atoms, 2 P atoms and 6 S atoms. This cell is viewed along the *c*-axis (Bernasconi et al., 1988).

2.1 STRUCTURAL CHARACTERISTICS OF FePS₃.

First produced in 1965 (Hahn & Klingen, 1965), the structure of FePS₃ was investigated and assigned a triclinic symmetry due to the apparent regularity along the *c*-axis. It was only three years later that this family of compounds was re-assigned with a monoclinic symmetry, from the space group of *C2/m*. The cell parameters were measured as $a = 5.93 \text{ \AA}$, $b = 10.28 \text{ \AA}$, $c = 6.72 \text{ \AA}$ with an angle of $\beta = 107.1^\circ$ (Klingen et al., 1968). In a crystallographic unit cell, iron and phosphorus occupy one formula unit each, while the sulphur has two different positions (see Table 2.1). This crystal structure has a 2-fold rotation symmetry along the *b*-axis which passes through the Fe atoms (Chandra & Ericsson, 1979). The atomic structure repeats after approximately 3 monoclinic layers, however as this is not an exact multiple, the system cannot be considered triclinic.

Table 2.1: Atom positions from the monoclinic space group of *C2/m* (Klingen et al., 1970). Positions in unit cell length. Point locations in Wyckoff notation.

Atom	Point location	x	y	z
Fe	4g	0	0.333	0
P	4i	0.057	0	0.171
S(1)	4i	0.751	0	0.247
S(2)	8j	0.248	0.166	0.248

The lattice parameters of FePS_3 have been observed to deviate from the room temperature values as the temperature was decreased below the ordering temperature (Bjarman et al., 1983). At temperatures above 115 K, the lattice parameters appeared to follow a linear expansion expected from increased thermal motion as can be seen in Figure 2.3 below. As the temperature dropped to below 115 K, a step-wise variation was apparent, with the a -axis deviating more from the linear variation than the b -axis. However it must be noted that the maximum deviation from the linear trend was about 0.5% (Bjarman et al., 1983).

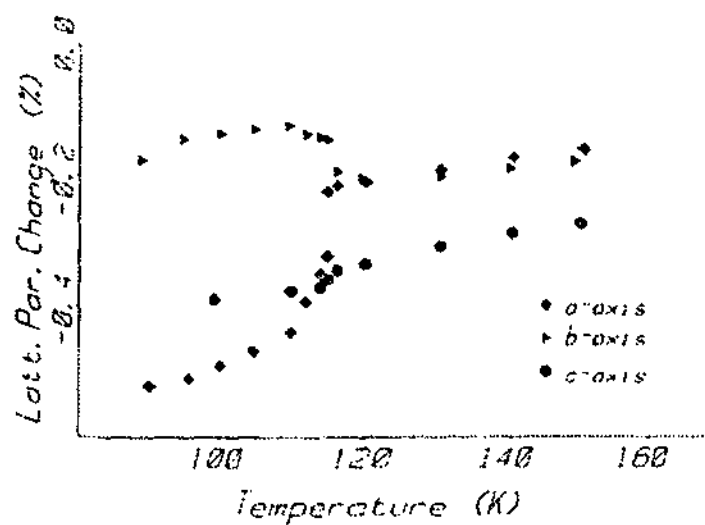


Figure 2.3: The deviation of the lattice parameters as a function of temperature (Bjarman et al., 1983).

The materials were originally made by the chemical vapour deposition technique with iodine acting as a transport agent for the high purity powdered materials (Nitsche & Wild, 1970). However it was later found that higher quality crystals were formed when excess sulphur was substituted as the transport agent (Klingen et al., 1973b; Brec et al., 1980). Thin films of FePS_3 have also been produced using a flash evaporation method from crystalline starting materials (Gledel et al., 1989). The films were amorphous and the study concentrated on comparing the crystalline and amorphous properties of each form as well as to look at evaporation as a technique for producing the FePS_3 . The structural characteristics were identical in both forms of FePS_3 . The density of the material has been found to be around 3.10 g/cm^3 (Klingen et al., 1973b; Taylor et al., 1973).

Most studies performed on FePS₃, have used either powdered samples or single crystal samples. Due to their two dimensional nature, the single crystal samples were often cleaved *in-situ* to produce a clean surface upon which to take measurements (Khumalo & Hughes, 1981; Ohno & Nakai, 1985; Grasso et al., 1986). Some studies have investigated FePS₃ by using stacked crystals, however the alignment of these crystals has led to controversial results (Kurosawa et al., 1983).

2.2 COVALENT VERSUS IONIC BONDING

There has been much debate about the electronic structure of FePS₃, focusing on the possible interactions between Fe²⁺ and the (P₂S₆)⁴⁻ subgroup. Some believe the bonding is covalent (Kamata et al., 1996), and others believe it to be ionic (Piacentini et al., 1982a; Piacentini et al., 1982b; Piacentini et al., 1984), while some conceded to a combination of the two effects (Scagliotti et al., 1987).

The ionic model treats the Fe²⁺ separately from the (P₂S₆)⁴⁻ cluster. The Fe²⁺ ion is viewed with localized 3*d* orbitals that do not interact with the anionic cluster. The covalent model involves a mixing of the electron states, combining the effects of both the metal and ligand on the electronic structure. The splitting of these energy levels is largely due to the formation of bonding and anti-bonding pairs between the iron 3*d* levels and the sulphur 3*p* levels (Choi et al., 1994).

Ultra-violet (UV) reflectivity has been used to investigate the localisation of the 3*d* orbitals of the metal ions in the thiophosphate family. The spectra for Mn, Fe and Ni were very similar, prompting the theory that the band structures are also similar (Khumalo & Hughes, 1981). It was concluded from this data that the *d* orbitals were localised and electrons from these bands did not take part in the optical transitions, thus explaining the similarities between spectra (Khumalo & Hughes, 1981).

A possible electron band structure for FePS₃ was set out by (Khumalo & Hughes, 1981) according to the reflectivity data they obtained. This can be seen in Figure 2.4 with the observed energies required to promote an electron into a higher band.

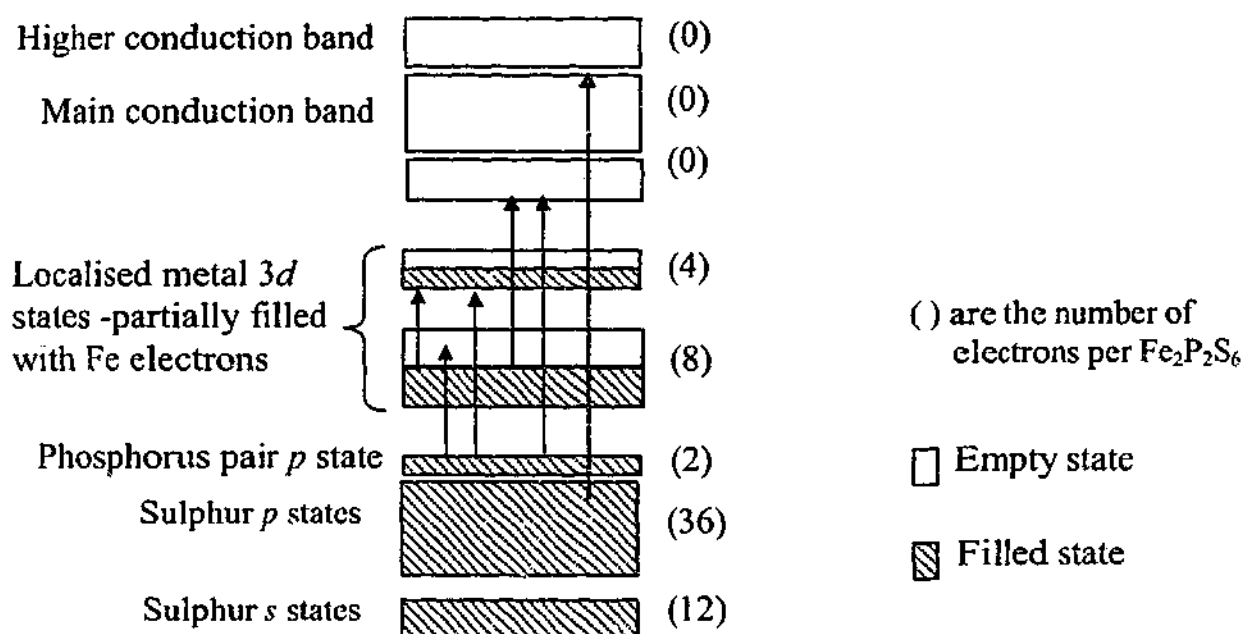


Figure 2.4: Possible electron band structure for $FePS_3$. The general interband transitions are responsible for the optical properties of these materials. From left to right the transitions have a maximum energy of 1.5 eV, 3.0 eV, 4.0 eV, 5 eV, an energy near the UV region, and an energy within the UV region (Khumalo & Hughes, 1981).

Band gap calculations performed by Kurita and Nakao (1989) began with an ionic model and were compared with the x-ray photoemission data from (Brec et al., 1979). The transition metal 3d bands of $FePS_3$ were observed to lie near the Fermi energy level. This implied that interactions between the Fe^{2+} and the ligand were possible, thus rendering the ionic model inappropriate to describe the electronic structure.

Piacentini et al. (1982a) used x-ray photoemission spectra to observe the optical properties of $FePS_3$ and concluded that an ionic model of $Fe_2^{2+}(P_2S_6)^{4-}$ could be used to describe most of the electronic properties of the material. However, it was also suggested that a certain degree of covalency was present between the Fe and S, as satellite structures were observed around the main photoemission peak. These satellite structures were derived from a possible overlap between the iron 3d and sulphur 3s electrons (Piacentini et al., 1982a). A low conduction band was observed in UV inverse photoemission results, which supported a covalent electronic model as the 3d states of the metal were mixed with the anion ligand states (Puppin et al., 1991). A later

experiment involving resonant and angle-resolved photoemission, also indicated that some components of the Fe 3*d* level were significantly delocalised with interactions evident between these electrons and those from the 3*p* sulphur levels (Choi et al., 1994). X-ray absorption data of single crystal samples also exhibited multiplet structures which led to similar conclusions about the electronic structure (Piacentini et al., 1984; Ohno & Nakai, 1985).

Single crystal Raman spectroscopy has also been used to study the electronic configuration of *FePS₃*. Measurements indicate the presence of a weak ionic interaction, coupled with some covalent bonding (Scagliotti et al., 1987). The Raman peaks have most widely been assigned to either the normal modes of the (*P₂S₆*)⁴⁻ anions, or to phonons from the vibrational modes of the iron. The paramagnetic spectra of both *NiPS₃* and *ZnPS₃* exhibited similar features to that of *FePS₃*, implying that the scattering from the crystal lattice may have been induced by the common (*P₂S₆*)⁴⁻ subgroup, similar to UV reflectivity data. This could indicate a primarily ionic interaction (Sourisseau et al., 1983; Balkanski et al., 1987).

Optical absorption spectra revealed that the localised 3*d* orbitals of Fe in *FePS₃* were atomic-like, which indicated an ionic nature (Joy & Vasudevan, 1992b). Calculations of the crystal field parameters within *FePS₃* were very similar to the observed transition energies. Features in the Infrared (IR) measurements were correlated to the inter-atomic distances between the metal and sulphur atoms (Joy & Vasudevan, 1993). From this it was suggested that ionic bonding was stronger than covalent, as covalent interactions would produce a greater metal dependence in the spectra.

Constant initial-state spectroscopy (CIS) measurements were performed on single crystal samples with photoemitted synchrotron electrons oriented to the normal of the sample surface. Results indicated that almost all of the valence band structures had some contribution from both the (*P₂S₆*)⁴⁻ clusters and the Fe²⁺ ions (Miyazaki et al., 1995). Thus orbital mixing between the Fe²⁺ and (*P₂S₆*)⁴⁻ groups was considered responsible for these results. More recent polarised absorption experiments also indicated that there was a significant mixing of the Fe *d*-orbitals with the sulphur valence states as well as mixing between the phosphorus and sulphur *p*-states (Kamata et al., 1996). These most recent results both supported the covalent bonding model for *FePS₃*.

The phonon dispersion curves calculated by Bernasconi et al. (1988) assumed that the interactions were covalent between the iron and the ligand. The calculations of the FePS₃ electronic band structure relied on the tight-binding scheme and the experimental results of Whangbo, Brec, Ouvrard and Rouxel (1985) (Whangbo et al., 1985) also found strong covalent interactions between iron and sulphur, contrary to many experimental results and the expected weak-interaction model favoured by Piacentini et al. (1982a, b, 1984).

With all this evidence, it is most likely that the true model of bonding is not entirely covalent or ionic, but a mixture of each with crystal field effects and electron correlations both influencing the structure.

2.3 OPTICAL PROPERTIES OF FePS₃.

Optical absorption measurements from 33 – 4 Å showed that FePS₃ has an optical absorption edge with a band gap of around 1.5 – 1.6 eV (Brec et al., 1979; Foot et al., 1980; Aruchamy et al., 1988). The size of the band gap found from ultraviolet photoemission spectra (UPS) was much lower than this value; around 1.0 eV (Miyazaki et al., 1995). The discrepancy between these measurements was attributed to the differences in experimental conditions. UPS involves the transitions of all electrons, including the *d*-electrons, while the method of optical absorption is based only on the strong optically allowed transitions between bands that originated from the (P₂S₆)⁴⁻ clusters. It was indicated from this study, that a mixing of electrons between the Fe²⁺ atoms and the (P₂S₆)⁴⁻ clusters would result in a smaller band gap, and therefore a larger conductivity, which was definitely the case when FePS₃ was compared with NiPS₃ (Miyazaki et al., 1995).

Reflectivity measurements were also conducted on the thiophosphate group. The refractive index was determined from measurements taken with cleaved single crystal samples. For FePS₃ this value was found to be 2.49 (Piacentini et al., 1982a).

It has also been shown that at ambient temperatures, FePS₃ shows no photoconductivity, and it has thus been ruled out as a possible photocell material (Foot et al., 1980; Aruchamy et al., 1988).

2.4 ELECTRICAL PROPERTIES OF FePS₃.

Investigations into the electronic structure of FePS₃ have also revealed some interesting electronic properties of this compound. This information is important for understanding the intercalation chemistry, and how this material may act as a battery cathode.

FePS₃, like all the transition metal thiophosphates, has been observed as a broadband semiconductor with p-type charge carriers at temperatures below 430 K (Brec et al., 1979; Foot et al., 1980; Byvik et al., 1982; Aruchamy et al., 1988). However, above 430 K, the charge carriers have been observed as electrons hopping between the localised 3d states (Grasso et al., 1990).

These semiconductor properties prompted investigations of FePS₃ as a possible photo-electrode in liquid-junction photo-electrochemical cells (Byvik et al., 1982; Aruchamy et al., 1988). In these studies, the indirect band gap was found to be around 2.2 eV. This implies that the energy gap between the valence band and the conduction band is 2.2 eV, while the optical band gap energy of 1.6 eV is a measure of the transition energy from the valence band to the *d*-orbital E_g energy levels in Fe²⁺ (Figure 2.5).

This appears to contradict the UPS results in which the presence of the *d*-shell electrons in the Fe²⁺ indicated a reduced band gap energy. These materials did not make good cells as they were only stable in acidic solutions of around pH 2 with very low energy efficiencies, despite an open circuit voltage of around 0.06 V (Aruchamy et al., 1988).

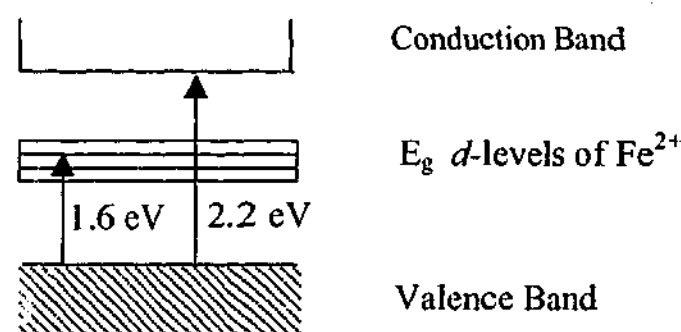


Figure 2.5: Schematic diagram indicating the difference between the direct and indirect band gaps in FePS₃ (Aruchamy et al., 1988). The direct band gap was discovered by light excitation processes.

The key to using these materials as batteries is for the process of Li intercalation to be electrochemically reversible. For this use, the electron band structure in these materials must be known. The resistivity of $FePS_3$ was found to be of the order of 10^4 - $10^5 \Omega \text{ cm}$, with no significant temperature dependence (Brec et al., 1979; Foot et al., 1980). After intercalation, the resistivity was noticed to decrease by about 3 orders of magnitude, changing the system from a p-type semiconductor to an n-type.

2.5 CRYSTAL FIELD EFFECTS IN $FePS_3$

The magnetocrystalline anisotropy of a material arises from a combination of crystal field effects within the lattice structure. These effects include the spin-orbit coupling in the Fe^{2+} ion, and the trigonal distortions of the FeS_6 octahedra (Figure 2.6) (Joy & Vasudevan, 1992a). When the anisotropy is large ($g_{\parallel}^2 > g_{\perp}^2$), there is a strongly preferred direction of moment orientation. In $FePS_3$, the Ising model best describes this preferred moment direction (Joy & Vasudevan, 1992a).

The angle θ in Figure 2.6 is a measure of the trigonal distortion of the FeS_6 octahedra. This value indicates a deviation from the true octahedral value of 54.75° where a decrease in this angle represents an elongation and an increase represents a trigonal compression (Joy & Vasudevan, 1992a). The change in angle is brought about by the change in proximity of the S layers with respect to the Fe layer.

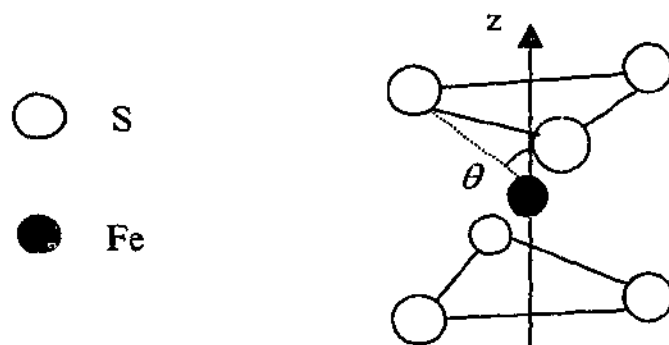


Figure 2.6: The FeS_6 octahedra under a trigonal distortion about the z-axis (Joy & Vasudevan, 1992a). The angle θ represents the deviation from the true octahedral value of 54.75° .

The metal ions in each of the MPS_3 compounds are octahedrally coordinated with the transition metal ion in a high spin electronic configuration (Le Flem et al., 1982; Joy & Vasudevan, 1992a). This suggests that the electrons prefer to remain unpaired and fill all of the d -orbitals before pairing, as suggested by Hund's rules. This was described by Figure 1.8 in Chapter 1. For the electrons to remain unpaired in $FePS_3$, the energy of the trigonal splitting parameter, Δ , in Figure 1.8 is less than the pairing energy in the high spin case. The Fe^{2+} ions in $FePS_3$ are octahedrally coordinated with the sulphur, as in Figure 2.6, such that the 5D state is split by the crystal field. The study by Joy and Vasudevan (1992a) concluded that a weak field limit to crystal field theory was appropriate to describe the interactions between the iron and sulphur systems. This was due to the high spin state of the Fe^{2+} ion. In the weak-field limitation, the crystal field is considered weak in comparison to the electron-electron repulsions. This is a common model for many compounds involving first order transition metals (Griffith, 1971).

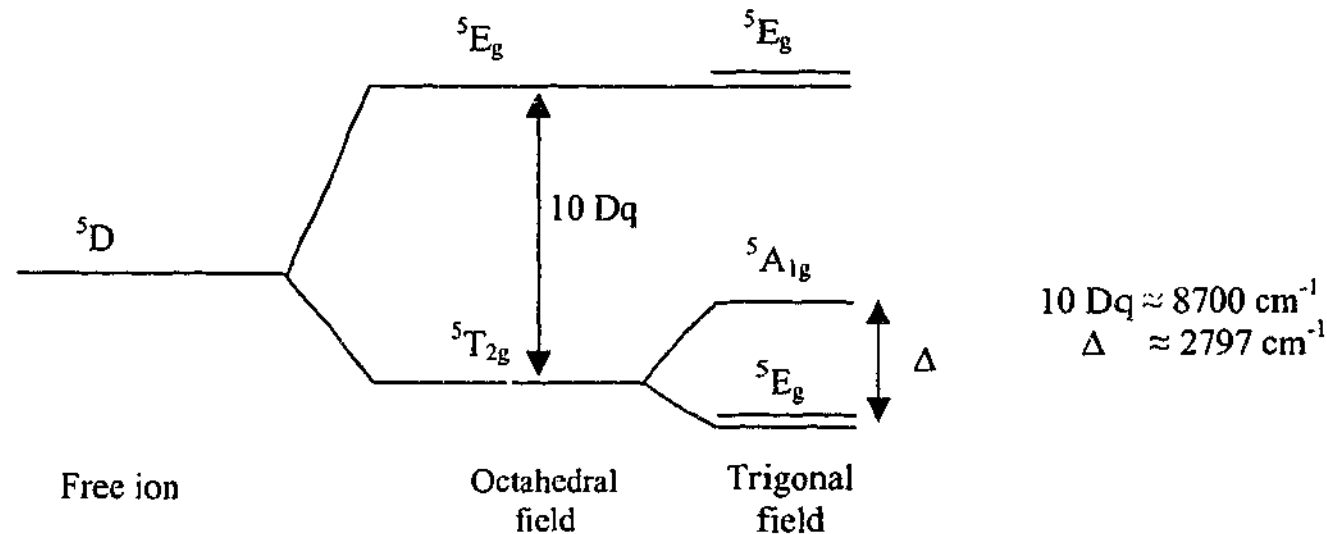


Figure 2.7: Splitting of energy levels in $FePS_3$ due to distortion of the crystal field. The 5D level is split by crystal field and ligand distortion (Rao & Raychaudhuri, 1992).

The splitting of the ground level of Fe^{2+} into the doubly degenerate E_g state and the triply degenerate T_2 state can be seen in Figure 2.7. In the weak-field limit, this splitting was calculated to be $Dq = 870 \text{ cm}^{-1}$ while the transition metal d -shell electrons were considered to be localised (Joy & Vasudevan, 1992a). This splitting is slightly less than the splitting of a free Fe^{2+} ion of $Dq = 1000 \text{ cm}^{-1}$ (Abragam & Bleaney, 1986).

Fe²⁺ has a ground state of ⁵T_{2g} in a weak field limit with a ligand field splitting, $10 Dq \leq 1.8$ eV. The first excited state for this is the ⁵E_g level (Piacentini et al., 1982a). Satellite structures around the absorption edge of FePS₃ in the x-ray photoemission data can be attributed to the crystal field effects of Fe²⁺, as they occur at energies very similar to other Fe²⁺ compounds (Piacentini et al., 1982a).

The degenerate ⁵T_{2g} ground state for FePS₃ can be split into an orbital doublet, ⁵E_g level and a singlet ⁵A_{1g} level by the trigonal field. The crystal field forces the spins to align parallel with the trigonal axis, even in the paramagnetic region (Rao & Raychaudhuri, 1992). The anisotropy of the spins along the trigonal axis arises from the splitting of the orbital degeneracy by the trigonal field. The uniaxial anisotropy, which can be seen by the relatively large energy gap of the trigonal splitting parameter, $\Delta = 2797 \text{ cm}^{-1}$ between the ground state and the ⁵A_{1g} state, categorises FePS₃ as an Ising type system (Joy & Vasudevan, 1992b; Rao & Raychaudhuri, 1992).

The spin-orbit coupling constant, λ , for a free ion of Fe²⁺ is around -100 cm^{-1} (Griffith, 1971; Abragam & Bleaney, 1986). Raman spectroscopy results have been used to calculate the spin-orbit coupling constant for FePS₃ to be $\lambda = -85 \text{ cm}^{-1}$ (Sanjuán et al., 1992). From susceptibility data, the constant was found to be $\lambda = -89.8 \text{ cm}^{-1}$ measured perpendicular to the moment direction and -92.8 cm^{-1} measured parallel to the moment direction (Joy & Vasudevan, 1992a). Although these values are very similar, they should be the same, as λ is constant for a material irrespective of the direction of measurement. It appears as though Joy and Vasudevan (1992a) calculated this value twice, to obtain a sufficiently accurate fit to their parallel and perpendicular susceptibility data. They also calculated the first nearest neighbour exchange parameter, J_1 , twice with varying results. This inferred that there were two first nearest neighbour interactions which represents an unphysical situation for FePS₃. This fact was later realised in the study by Chandrasekharan and Vasudevan (1994) who revealed that only by forcing the unphysical solution could the Mean Field Theory analysis fit the data. The implications of the different exchange parameters and the study by Joy and Vasudevan (1992a) will be discussed further in Section 2.6. The spin-orbit coupling constant has also been determined for a randomised, powder sample to be around $\lambda = -166 \text{ K}$ (Jernberg et al., 1984; Chandrasekharan & Vasudevan, 1994; Chatterjee, 1995) which corresponds to an energy of 115 cm^{-1} . Thus, the

experimental methods appear to exhibit a lower spin-orbit coupling parameter when compared to the free ion case, while calculations indicated a slightly larger value.

2.6 MAGNETIC PROPERTIES OF FePS₃.

The magnetic properties of FePS₃ are often compared with other members of the thiophosphate family, as the different metal species are responsible for the different magnetic interactions in each compound. ZnPS₃, for instance, is a non-magnetic species as zinc has no moment. At room temperature, all thiophosphates are paramagnetic while antiferromagnetic ordering is observed below the Néel temperature for each magnetic member. The Néel temperature has been found to be around 120 K for FePS₃ with different susceptibility studies giving a range of values from 111 K (Rao & Raychaudhuri, 1992) to 126 K (Taylor et al., 1973). This variation could be a result of slight imperfections from crystal to crystal. From susceptibility measurements, the magnetic moments were found to be directed perpendicular to the *ab*-plane, and the maximum susceptibility was found to be 126 K (Okuda et al., 1983).

Taylor et al., (1973) found the effective magnetic moment of FePS₃ to be $5.43 \pm 0.06 \mu_B$. This value is less than the calculated effective moment of $6.70 \mu_B$ for Fe²⁺ and more than the spin only moment of $4.90 \mu_B$, suggesting the presence of spin-orbit coupling. It was later found by Brec et al., (1979) that the effective magnetic moment of FePS₃ was $5.0 \mu_B$. This moment was determined from powder susceptibility data taken well above the Néel temperature between 300 and 500 K, to ensure that the compound followed the Curie-Weiss law. The earlier investigation by Taylor et al., (1973) was performed at temperatures below 300 K and therefore may have deviated somewhat from the Curie-Weiss law. The value obtained by Brec et al., (1979) is much closer to the spin-only moment, indicating that the effect of spin-orbit coupling may be less significant than previously thought. More recently the magnetic moment for FePS₃ was found to be clustered about the calculated spin-only moment with experimental results given as $4.94 \mu_B$ (Le Flem et al., 1982), $4.8 \pm 0.1 \mu_B$ /Fe²⁺ (Okuda et al., 1983), and $5.1 \pm 0.6 \mu_B$ (Kurosawa et al., 1983).

Calculations of the magnetic moment based on the electronic band structure were found to be much lower than the experimental value. The magnetic moment due to spin only contributions was calculated to be $3.95 \mu_B$ and $3.72 \mu_B$ in two different studies (Kurita & Nakao, 1989; Zhukov et al., 1996). These results imply that there must be an orbital contribution to make up the difference between the spin only moment and the observed magnetic moment of close to $5 \mu_B$ for FePS₃.

From Equation 1.4, it can be seen that the effective magnetic moment is dependent on the spectroscopic splitting factor, g . However, from Joy and Vasudevan (1992a) it was shown that g is temperature dependent. Therefore the effective moment is also temperature dependent. In each of the above investigations, this effect was not recognised. The main ramification of this is that it may produce two different Weiss constants from the parallel and perpendicular susceptibilities.

The magnetic structure in real space was first proposed by Le Flem et al. (1982) and consisted of ferromagnetic chains of Fe ions, coupled antiferromagnetically within the plane. Each plane was also antiferromagnetically coupled. Each iron ion was coupled ferromagnetically with two of its nearest neighbours and antiferromagnetically with the third. This structure can be seen below in Figure 2.8 where the moments are parallel to the c^* -axis.

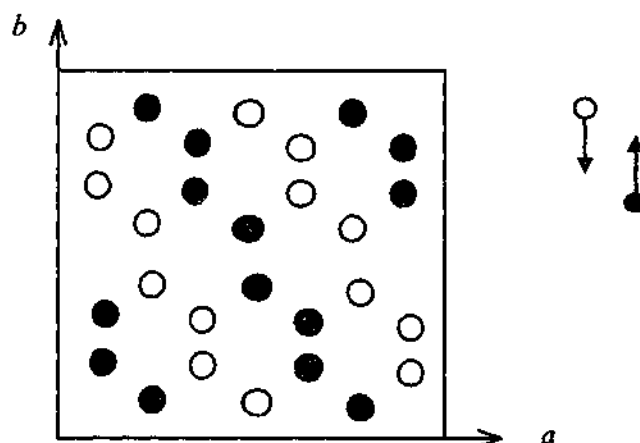


Figure 2.8 Proposed magnetic structure from (Le Flem et al., 1982).

Later, this same structure was tested with results of a neutron diffraction study of FePS₃ however, within this paper another in-plane structure was selected as the best representation of

the moments in FePS₃ (Kurosawa et al., 1983). This can be seen in Figure 2.9 and is a rotation of the above structure by 60° in the *ab*-plane. The results published in this paper were questionable and will be discussed at length in Chapter 3.

After comparing the Mössbauer spectra of FePS₃ and FePSe₃, Jernberg et al., (1984) decided that the similar hyperfine fields implied a magnetic structure within the iron layers that was most likely to be the same for both compounds. Other magnetic properties such as the Néel temperature, and the magnitude of the effective moment were also very similar between compounds, which may also indicate similar magnetic structures. The magnetic structure for FePSe₃ was well defined from previous neutron diffraction data (Wiedenmann et al., 1981) and is similar to that of Le Flem in the plane. The crystal structure of FePSe₃ has rhombohedral symmetry with a space group of *R*3̄. The unit cell is three times that of FePS₃ along the *c*-direction. Magnetically, the structure repeats after 2 nuclear unit cells along *a* and *c*, which corresponds to a repetition of 6 nuclear layers along the *c*-axis in the FePS₃ structure. Thus the FePSe₃ magnetic structure has three parallel layers of Fe atoms followed by three antiparallel layers (Wiedenmann et al., 1981).

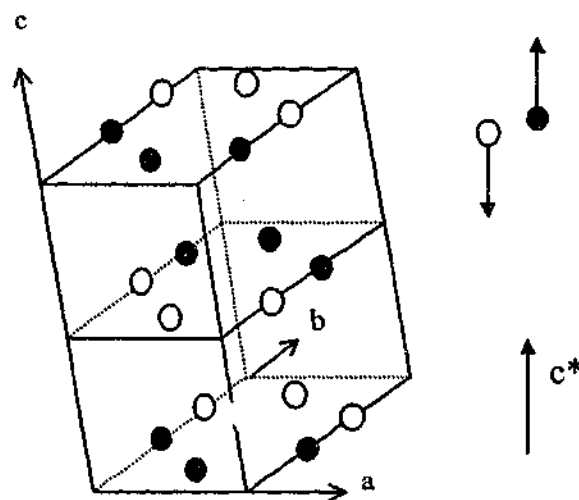


Figure 2.9: Magnetic structure favoured by Kurosawa et al. (1983)

From phonon dispersion data, a third magnetic structure was proposed for FePS₃ (Bernasconi et al., 1988). In this structure, the magnetic unit cell was considered to be four times as large as the nuclear unit cell corresponding to a doubling of the cell in the *z*-direction as well as the *ab*-plane. No in-plane moment structure was set out for this magnetic cell.

The Weiss temperature has also been found from susceptibility measurements using polycrystalline samples. The results varied between research groups, and have been found as 14 K (Taylor et al., 1973), 65 K (Brec et al., 1979), 104 K (Le Flem et al., 1982), 15 K (Kurosawa et al., 1983) and -15 K (Okuda et al., 1983). This vast range can be attributed to the extreme differences in preferred orientation of the plate-like material in powdered form. Single crystal susceptibility measurements revealed two Weiss characteristic temperatures for measurements taken parallel and perpendicular to the crystal z-axis (Joy & Vasudevan, 1992b). These were $\Theta_{\parallel} = 53$ K and $\Theta_{\perp} = -54$ K. They maintained that the difference in sign indicated the direction of measurement with respect to the moments and the magnitude was influenced by both exchange interactions and single-ion anisotropy. Crystal field effects from the trigonal distortion were suggested as an explanation for the extreme difference in Θ . Figure 2.10 below shows the magnetic susceptibility plots from a single crystal sample of FePS₃ with the applied field parallel and perpendicular to the moment direction (Joy & Vasudevan, 1992a). The broadness of the peak is an indication of the short-range order present in FePS₃, while the intensity difference between the two plots is an indication of anisotropy.

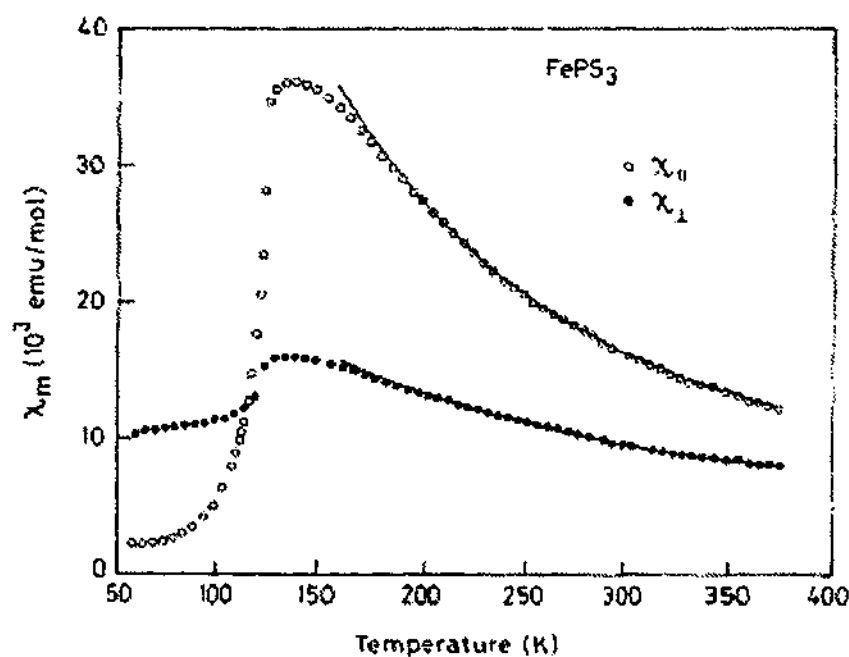


Figure 2.10: Susceptibility measurements taken with the applied field parallel and perpendicular to the c^* -direction (Joy & Vasudevan, 1992a).

Various models have been devised to describe the susceptibility of an antiferromagnet in the paramagnetic region. These models can be used to determine certain parameters such as the spectroscopic splitting factor, g , and the spin-orbit coupling coefficient λ . During a review of various models, Chandrasekharan and Vasudevan (1994) compared the high temperature susceptibility data with the respective fits of the High Temperature Series Expansion (HTSE) model, the Correlated Effective Field (CEF) model, the Mean Field Approximation (MFA) and the Oguchi method. Results from this suggested that the HTSE was the most accurate model to fit the high temperature susceptibility of 2D Heisenberg antiferromagnets such as MnPS₃. This relation can be seen in Equation 2.1 for a 2D Heisenberg antiferromagnet where C_n represents the expansion coefficients, which are dependent on the magnetic lattice (Lines, 1970).

$$\chi_m = \frac{Ng^2 \mu_B^2 S(S+1)}{3kT} \cdot \frac{1}{\sum_{n=1}^{\infty} C_n \left(\frac{JS(S+1)}{kT} \right)^{n-1}} \quad (2.1)$$

The exchange interaction between the Mn ions in MnPS₃ was measured to be approximately 400 times greater within the plane than between planes (Wildes et al., 1998). Exchange constants have also been calculated for FePS₃ by numerous investigators. The MFT values obtained by Jernberg et al. (1984) were 14.6 K for the intra-sublattice exchange constant, and 20.6 K for the inter-sublattice exchange constant. Okuda et al. (1983) obtained exchange parameters for the first, second and third nearest neighbours as $J_1/k = 19.6$ K, $J_2/k = -10.3$ K and $J_3/k = 2.2$ K, which do not correspond directly with the range of values for each parameter, found by Kurosawa et al., (1983). Kurosawa approximated the interlayer exchange with the third nearest neighbour value in the plane, and it was thought that slight deviations in atom spacing might have resulted in the discrepancies. The intraplanar distances between first, second and third nearest neighbour iron atoms are 3.4 Å, 5.9 Å and 6.8 Å respectively while between the layers the nearest neighbour distance is equal to the crystallographic c axis, 6.72 Å.

The magnetic exchange parameters were also calculated from the high temperature susceptibility measurements by taking a Mean Field Approximation analysis (Joy & Vasudevan, 1992a). However two different values for the first nearest neighbour exchange parameter, J_1 , were found. Due to the differences between the parallel and perpendicular susceptibility, different values of J_1 were needed to form a reasonable fit to the data. This gave the nearest neighbour exchange as ferromagnetic when the applied field was perpendicular to the

magnetisation direction, and antiferromagnetic when the applied field was parallel with the magnetisation axis. Thus both the exchange constants and the spin-orbit coupling constants were set to impossible values for a good fit.

By using the CEF model, the values found by Chandrasekharan and Vasudevan (1994) for the first and second nearest neighbour interactions within the plane were 27.2 K and -2.3 K respectively. These values were considered an improvement on the initial MFA exchange calculations of Joy and Vasudevan (1992a). The CEF model simplifies the problem of many-body magnetism to a single bodied, non-interacting ensemble form. It is useful for describing systems for which the exchange energy (J) is comparable to the size of the thermal energies (kT) and the crystal field splitting (Lines, 1974). It was noted that in this case, the CEF approximation fitted the low temperature data in the ordered phase much better than the paramagnetic phase. This model was also able to account for the low dimensionality of the magnetic structure, incorporating spontaneous fluctuations, which are completely ignored in the MFT approach. Both methods of obtaining the first and second nearest neighbour interactions indicated that the nearest neighbours interacted ferromagnetically and the next nearest neighbour interactions were antiferromagnetic.

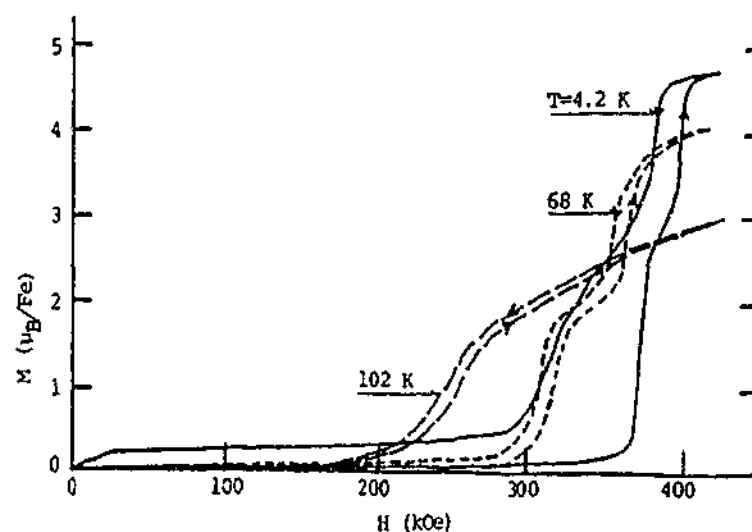


Figure 2.11: Magnetization curves for $FePS_3$ with the field applied parallel to the z -direction at temperatures 4.2 K, 68 K and 102 K (Okuda et al., 1983).

High field magnetisation measurements have been conducted along the z -direction of a single crystal of FePS₃ (Okuda et al., 1983). Two magnetic phase changes were observed as the applied field was increased to 45 T, corresponding to the transitions from antiferromagnetic to ferrimagnetic and then to paramagnetic. This can be seen in Figure 2.11.

The transition fields decreased with increasing temperature, until $T = T_N$, above which the crystal remained paramagnetic at all applied fields. It was suggested that the free energy is lowest for the antiferromagnetic case and greatest for the paramagnetic state, which would suggest that when the material goes through the transition into the ferrimagnetic state, the antiparallel moments are nearest neighbours (Okuda et al., 1983).

FePS₃ falls into the category of an Ising type antiferromagnet. The anisotropy of these materials is determined from the degree of crystal field influences, which are dependent upon the occupation of the d -shell electrons. Susceptibility measurements performed on single crystals indicate a considerable anisotropy parallel to the applied field direction where χ_{\parallel} is about twice that of χ_{\perp} (Jernberg et al., 1984; Joy & Vasudevan, 1992a). This leads to anisotropic g factors such that $g_{\parallel} > g_{\perp}$ suggesting the possibility of significant spin-orbit coupling (Joy & Vasudevan, 1992a). This is consistent with the description of FePS₃ in terms of the Ising Hamiltonian, rather than the Heisenberg model.

The anisotropy of FePS₃ has been attributed to effects from both single ion anisotropy and magnetic dipole anisotropy. However the effect of the single ion anisotropy dominates the overall anisotropy, creating a strong, uniaxial anisotropy almost entirely due to the single-ion anisotropy, which is much larger than for MnPS₃. The anisotropy in MnPS₃ is governed by the dipole interactions due to the spherical symmetry of the Mn²⁺ ion, and is much weaker than the anisotropy of FePS₃.

It has been suggested by some that line intensity enhancement in Raman spectra can be attributed to the folding of Brillouin zones about Γ . The folding of these zones, occurring in the low temperature regions, indicated that the magnetic structure had a larger unit cell than the crystallographic structure (Balkanski et al., 1987; Scagliotti et al., 1987). Low temperature, single-phonon Raman scattering revealed new structures that were attributed to the magnetic ordering, as well as enhancement of the original nuclear peaks (Scagliotti et al., 1987).

Bemasconi et al. (1988) produced phonon dispersion curves, which suggested that the antiferromagnetic unit cell is double the crystallographic unit cell in both the z direction and in the ab plane. This reduces the Brillouin zone to a quarter of its original size with folding occurring about Γ similar to the Raman spectroscopy results. This does not support the original magnetic structure proposed by Le Flem et al. (1982).

Raman spectroscopy has also played an important role in the observation of magnons in many structures, including FePS_3 . When magnons are present in the magnetic lattice, they will cause a frequency shift of certain magnetic peaks, as the temperature is changed. The single crystal measurements taken at 21 K indicated the presence of a magnon at 122 cm^{-1} (Sekine et al., 1990b). This corresponds to a band gap energy of 15 meV for the magnon at 21 K. As the temperature of the sample was increased to 85 K, the frequency of the band was reduced to around 116 cm^{-1} . This corresponds to an energy gap of 14.4 meV and can be seen at the position of the arrow in Figure 2.12.

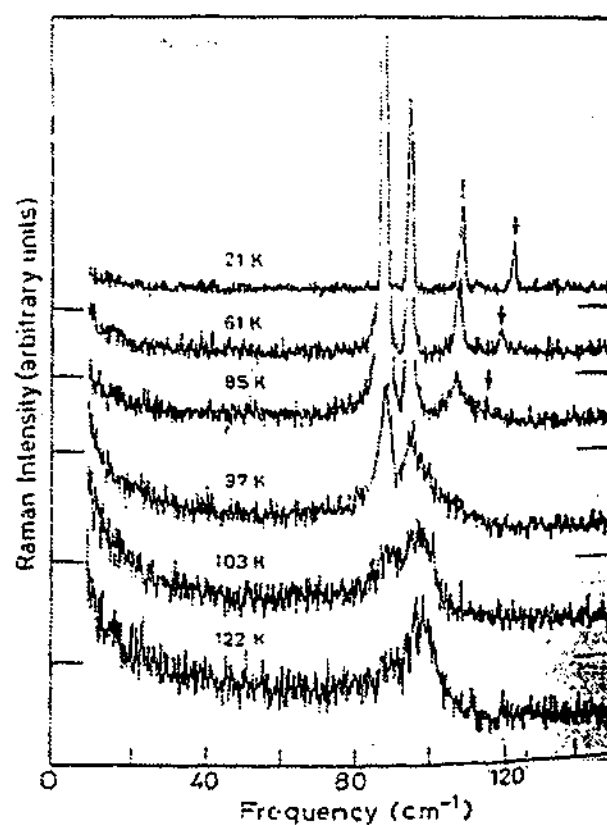


Figure 2.12: Raman spectra indicating the shift in frequency of the one-magnon peak from 122 cm^{-1} to 116 cm^{-1} as the temperature increased (Sekine et al., 1990b). The arrow indicates the magnon peak.

Above 85 K, the one-magnon Raman peak became unresolved as the intensity decreased. The presence of magnon bands has not been observed in previous Raman spectra (Scagliotti et al., 1985; Scagliotti et al., 1987).

2.7 INTERCALATION PROPERTIES OF $FePS_3$

MPS_3 members have been studied extensively due to their interest as cathodic materials in high energy-density rechargeable lithium batteries. It is the characteristic two dimensionality of their lamella crystal structure which has led to investigations into their intercalation chemistry (Gledel et al., 1989). Metal disulphides such as TiS_2 were previously favoured for rechargeable lithium batteries, as Li was easily intercalated into the van der Waals gaps between the sulphur layers. Lithium intercalation in the thiophosphate family was also investigated, due to the similar layered structure it shared with TiS_2 . It was noted however, that thiophosphates could absorb up to three times more lithium than TiS_2 , with no noticeable parameter expansion (Thompson & Whittingham, 1977; Brec et al., 1979).

A significant charge transfer has been observed between many intercalated materials and their host species. The process of lithium intercalation into $FePS_3$ involves lithium entering the van der Waals gaps as a positive ion, donating its electron to the host band structure (Silipigni et al., 1996). This has led to an understanding that a suitable host material should have some vacant conduction electron levels. Thus the intercalation capacity of the host material is determined by the nature of the electron accepting levels in the metal (Kurita & Nakao, 1989). This implies that the band-gap energy of the host material plays an important role in determining the best materials for fuel cell reactions (Foot et al., 1980). The electronic bands formed from overlapping iron $3d$ and sulphur $3p$ levels may contribute to the lithium intercalation process by acting as acceptor levels (Bernasconi et al., 1988). The results from these studies implied that both $MnPS_3$ and $ZnPS_3$ make poor cathode materials in this type of battery (Brec et al., 1979; Kurita & Nakao, 1989).

It has been found that although $FePS_3$ is capable of absorbing a considerable concentration of Li into its van der Waals gaps, $NiPS_3$ can absorb the most, yielding a better cathodic material (Kurita & Nakao, 1989). Crystals of $FePS_3$ showed a decrease in resistivity as the concentration of the Li solution and exposure time increased. The decrease in resistivity corresponds to an

increase in the electrical charge carriers, which for $FePS_3$ is highest at low temperatures. The degree of conductivity of these intercalates has been attributed to the distribution of the electrons from the ionised Li. In $FePS_3$, these electrons lie close to the conduction band and are therefore not free, whereas for $NiPS_3$, the donated electrons lie within the conduction band, which leads to an increase in conductivity (Brec et al., 1979).

When intercalating other materials into the crystal cell, some parameter expansion has been observed. The crystal field effects from the intercalated species can cause intralayer deformation by altering the trigonal distortion angle θ (Silipigni et al., 1996). Intercalating larger species such as N-methylstilbasoliums showed a remarkable increase in the c -axis from 2 to 3 times the original length for 16% to 18% addition of the intercalate material (Chen et al., 2001).

Intercalation has also been responsible for altering the magnetic structure of the host species, $FePS_3$. The Fe^{2+} in $FePS_3$ has been observed in Mössbauer spectra to undergo reduction upon intercalation of lithium (Fatseas et al., 1987). Although the localised magnetic moment of Fe remained the same, the conductivity decreased noticeably. Some studies have shown that after intercalation, there is evidence of two different types of iron site in the lattice. This can lead to different electronic and magnetic interactions within the compound, such as superparamagnetism (Leaustic et al., 1996). In the pure intercalated materials, it has been observed that low dimensionality is retained; however upon oxidation, the intercalated species was shown to exhibit 3-dimensional characteristics. This feature has been implicated in the poor cathodic performance of $FePS_3$ when compared with $NiPS_3$ (Ouvrard et al., 1991). When intercalated with 1,10-phenanthroline monohydrate (Phen), the resulting compound exhibited a weak yet significant internal ferromagnetic signal of 197 G (Köseoglu et al., 2003).

Another way to alter the magnetic and electric properties of $FePS_3$ is through the process of dilution. Dilution is different from intercalation in that some of the metal ions are replaced with an alternative element. Different amounts of a substitute element, such as cadmium or zinc, will affect the properties in different ways (Sakai et al., 1997). Dilution of the host compound to form $Fe_{1-x}Ni_xPS_3$ has shown that the strong anisotropy of the Fe^{2+} will influence the magnetic order such that with only 20% Fe, the moments orient perpendicular to the ab -plane, rather than along the ab -plane as is the case for pure $NiPS_3$ (Rao & Raychaudhuri, 1992). Similarly, mixing cadmium with the iron did not result in a random distribution of elements. Instead, the Fe^{2+} ions were observed to clump together in nano-sized domains, with ferromagnetic interactions

(Leaustic et al., 1999). These two examples indicate how strongly the iron atoms influence the mixed species, due to its anisotropy. In general, as the lattice is expanded from the iron replacement, the conductivity decreases, suggesting that cation-cation distance may be a significant factor affecting the electrical properties (Manríquez et al., 2000).

Dilution of the Fe with 50% Cd changed the structure such that two iron sites were present in a room temperature Mössbauer spectrum, which have been attributed to high and low spin Fe^{2+} sites (Bhowmick et al., 1992). This implies that the process of dilution does not reduce the iron atom. In the mixed compound, an increased quadrupole splitting indicated an increase in the trigonal distortion of the crystal lattice (Bhowmick et al., 1992). The presence of both iron sites has been attributed to a strong competition between ferromagnetic and antiferromagnetic interactions in the magnetic lattice. These interactions are related to the change in nearest neighbour distances brought about by the insertion of Cd into the lattice.

2.8 PURPOSE OF THIS INVESTIGATION

The purpose of this study was to investigate FePS_3 as a two-dimensional material, however in doing this, the magnetic structure was also investigated and re-evaluated. Although the magnetic structure of this compound has been studied and accepted for 20 years, it was found to be incorrect, and steps were taken to fully discover the nature and arrangement of the magnetic moments. FePS_3 has also proven a suitable material for investigating the paramagnetic spin diffusion mechanism in 2D materials. Results indicate that the rate of diffusion changes as the degree of magnetic order decreases. The dilution of Fe in FePS_3 was also to be investigated with an aim to observe possible spin glass behaviour. The spin glass ordering temperature for a 2D Ising antiferromagnets is around 0 K, whereas 2D Heisenberg magnets do not long-range order above 0 K. Thus, FePS_3 , as a 2D Ising antiferromagnet may show ordering at some finite temperature as opposed to a structure like MnPS_3 which did not order in its spin glass state. However this study was not possible due to unforeseen circumstances such as determining the magnetic structure of FePS_3 and difficulty with growing the diluted crystals.

The main techniques that have been employed to investigate FePS_3 are Mössbauer spectroscopy and neutron diffraction, utilising both powdered and single crystal samples. These techniques are outlined in Chapter 3 with results in Chapters 5 and 6. Other preliminary

investigation techniques include X-ray diffraction and SQUID magnetometry, the results of which will also be presented in Chapters 4 and 5.

CHAPTER THREE

3: Experimental Techniques

3.1 MÖSSBAUER SPECTROSCOPY

Mössbauer spectroscopy investigates the manner in which nuclei absorb and emit gamma radiation in a resonant and recoil free manner. First discovered in 1957 by Rudolf Mössbauer, this technique provides sensitive information about the electric and magnetic interactions surrounding the absorbing nucleus.

Mössbauer spectra come in the form of one or more recoil-free absorption dips which indicate that the γ -rays have been resonantly absorbed by nuclei. In the harmonic approximation, the atomic recoil-free fraction in a sample can be denoted by f where

$$f = \exp\left(-k^2 \langle x^2 \rangle\right) \quad (3.1)$$

Here k is $2\pi/\lambda$ (where λ is the wavelength of the γ -ray) and $\langle x^2 \rangle$ is the mean square vibrational amplitude of the resonating atom propagating along the x direction. Increasing the recoil-free fraction, f will provide clearer Mössbauer spectra and give more reliable data. The recoil-free fraction decreases with increased k , suggesting that higher energy γ -rays reduce the intensity of the absorption dips. The recoil-free fraction can also be made larger as $\langle x^2 \rangle$ is made small. This is often achieved by reducing the temperature of the absorber, as it reduces the thermal motion of the absorbing nuclei.

3.2 HYPERFINE PARAMETERS

The hyperfine parameters are a measure of the splittings and shifts in the ground state and excited state of the absorber nuclei. They involve a coupling between the nuclear multipole

moments and the electrons surrounding the nuclei. These parameters include the isomer shift, electric quadrupole coupling and magnetic hyperfine interactions.

3.2.1 Isomer Shift

The isomer shift provides information about the electron density at the nucleus and is observed as the difference in transition energies between the source and absorber. It is a measure of the Coulomb interaction between the electron cloud and the absorbing nucleus. As the s -shell electrons can penetrate the nuclear region, they can interact electrostatically with the nucleus. This results in a small shift in the nuclear energy levels. The interaction between the s -electrons and the nucleus is sensitive to the valence state of the absorbing nuclei and is observed as a shift in the absorption line position in an energy spectrum without a change in the degeneracy. This is shown in Figure 3.1 below.

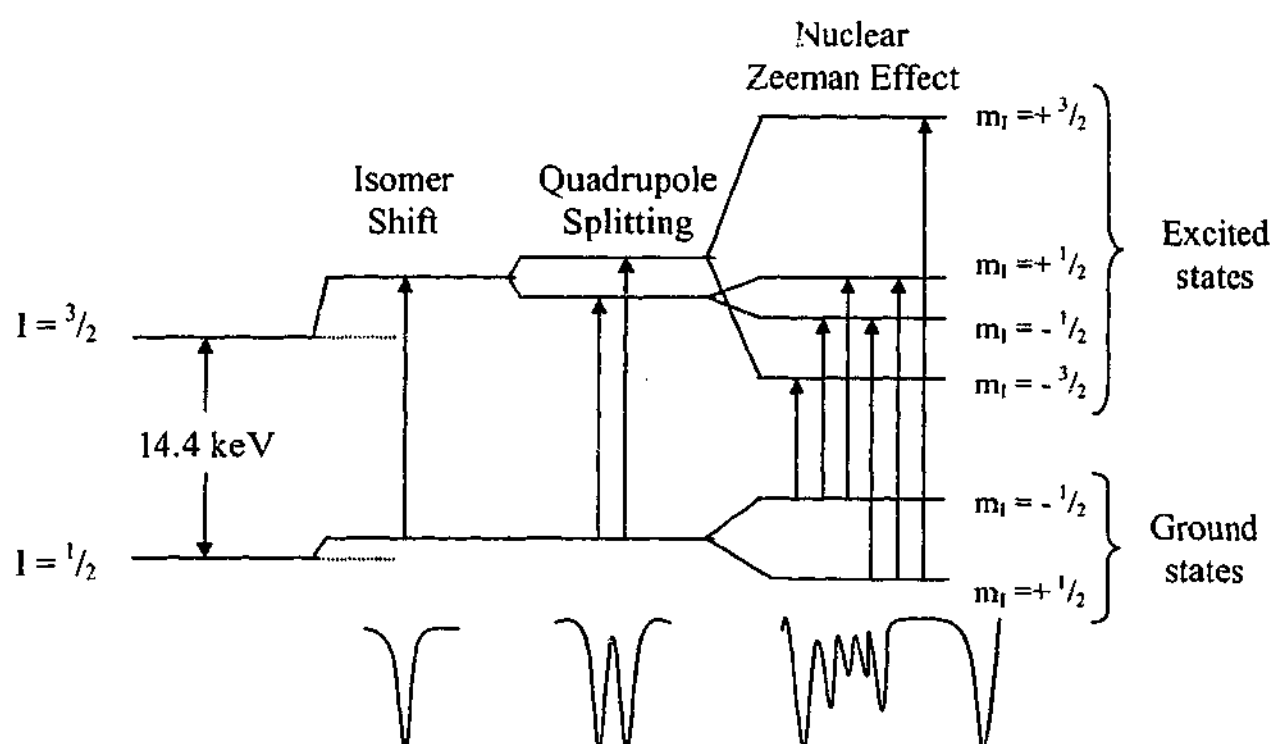


Figure 3.1: Energy level diagram for Fe^{57} showing the energy differences attributed to the Isomer shift, Quadrupole splitting and Hyperfine magnetic splitting.

The isomer shift can be described by the following expression, which relates the change in position of the absorption line to the difference between the electron density of the source and the absorber.

$$I.S. = \left(\frac{4\pi}{5} \right) Z e^2 R \delta R \left[|\Psi_a(0)|^2 - |\Psi_s(0)|^2 \right] \quad (3.2)$$

where R is the nuclear radius which is a uniformly charged sphere and δR is equal to the difference in the nuclear radius between the ground and excited states, $R_{\text{excited}} - R_{\text{ground}}$. The value of δR is usually very small and is negative for ^{57}Fe . The $|\Psi(0)|^2$ represents the relativistic density of the s -electrons inside the nucleus, where $R = 0$, and the subscripts a and s refer to the absorber and source respectively. This relativistic correction is usually only needed for heavy atoms.

One way that the electron density can affect the isomer shift is if the absorber nucleus valency is different to that of the source by the addition or subtraction of s -electrons. A secondary mechanism that can alter the isomer shift occurs when there is a change in the number of electrons from the outer d or f shells. The removal of an outer d -shell electron will lead to a stronger attraction between the s -shell electrons and the nucleus, corresponding to an increase in the electron density $|\Psi(0)|^2$ at the nucleus (Cohen, 1976). For instance, a small positive isomer shift for Fe, with respect to α -Fe, may indicate the presence of Fe^{3+} whereas a slightly larger positive isomer shift can be attributed to Fe^{2+} (Ingalls, 1971). This is due to the removal of a d -shell electron. The isomer shift can also give information about the oxidation state and bond properties of the absorber nucleus (Vértes et al., 1979). The isomer shift is expected to become more positive with increasing electronegativity of the ligands surrounding the metal ion (Gütlich, 1975).

3.2.2 Quadrupole Splitting and EFG

When considering the isomer shift above, it was assumed that the Mössbauer nucleus was spherical with a uniform charge distribution. If the absorber nucleus was distorted from this spherical symmetry, the charge would be distributed such that a quadrupole moment would be

felt at the nucleus. The nuclear quadrupole moment, Q , is a measure of the deviation from spherical symmetry of the nuclear charge and is given by Equation 3.3.

$$Q = \frac{1}{e} \int \rho r^2 (3 \cos^2 \theta - 1) d\tau \quad (3.3)$$

Here, the integral is over the entire nuclear volume. The sign of Q is related to the shape of the distortion. If Q is positive, the nucleus is elongated, while when Q is negative, the nucleus is flattened (Gütlich, 1975).

The electric field gradient (EFG) can be described as the non-symmetric electric field surrounding the absorber nucleus, created by the electrons in the solid. The valence electrons from the absorber nuclei, and the ligand field effects from the surrounding atoms also contribute to the non-symmetric charge distribution (Travis, 1971). The electric field felt at the absorber nucleus is the gradient of the electrostatic potential, V while the electric field gradient is found by taking the derivative of the electric field. Mathematically this can be written as a 3×3 matrix with the nine components expressed in terms of the directions x , y , and z as seen in Equation 3.4.

$$EFG = - \begin{bmatrix} V_{xx} & V_{xy} & V_{xz} \\ V_{yx} & V_{yy} & V_{yz} \\ V_{zx} & V_{zy} & V_{zz} \end{bmatrix} \quad (3.4)$$

These tensor components can be defined in Equation 3.5 below

$$V_{ij} = \left(\frac{\partial^2 V}{\partial i \partial j} \right)_N ; \quad i, j = x, y, z \quad (3.5)$$

where V is the electrostatic potential taken along a set of orthogonal axes x , y and z , at the nuclear site N . The three diagonal components that can describe the EFG, V_{xx} , V_{yy} , and V_{zz} form an orthogonal set where $V_{xx} = \partial^2 V / \partial x^2$, $V_{yy} = \partial^2 V / \partial y^2$, and $V_{zz} = \partial^2 V / \partial z^2$.

This tensor can be diagonalised such that only the three diagonal elements are necessary to describe the EFG. These diagonal values are the eigenvalues of the EFG, where $|V_{zz}| \geq |V_{yy}| \geq |V_{xx}|$ and these are referred to as a new set of principal axes (Bancroft, 1973). The eigenvalues are obtained using three eigenvectors during the process of diagonalisation. These values satisfy

Laplace's equation, where the sum of the three elements V_{xx} , V_{yy} , and V_{zz} , is equal to zero. Thus only two parameters are independent.

The crystallographic axes of the material may not correspond to the orthogonal axes of the EFG, and thus a rotation matrix must be used to relate the principal axes of the EFG, defined in setting up the EFG matrix, to the crystal axes. From the EFG tensor, the two independent parameters are usually chosen to be V_{zz} and η , the latter defined in Equation 3.6. This parameter is called the asymmetry parameter and is a measure of the difference of the EFG in the x and y directions.

$$\eta = \frac{|V_{xx} - V_{yy}|}{V_{zz}} \quad (3.6)$$

Thus the asymmetry parameter is limited to $0 \leq \eta \leq 1$. When $V_{xx} = V_{yy}$ the asymmetry parameter is zero, and the EFG is axially symmetric (Greenwood, 1971; Gülich, 1975).

The interaction between the electric quadrupole moment and the EFG can be described by the electric quadrupole Hamiltonian,

$$\mathcal{H}_Q = \frac{eQV_{zz}}{4I(2I-1)} [3I_z^2 - I(I+1) + \eta(I_x^2 + I_y^2)] \quad (3.7)$$

where I represents the nuclear spin quantum number and I_x , I_y and I_z are the components of the angular momentum operator \hat{I} . ^{57}Fe has a nuclear ground state with spin $1/2$ and an excited state with spin $3/2$ at 14.4 keV. The nuclear quadrupole moment is only non-zero for the $I = 3/2$ state. Thus the EFG affects only the excited state, removing the degeneracy between the $m_1 = \pm 1/2$ and $m_1 = \pm 3/2$. A positive EFG corresponds to a predominance of negative charge in the xy -plane around the nucleus. As it is energetically more favourable for a positive quadrupole moment to lie near the xy -plane than the z -axis, the $m_1 = \pm 1/2$ has a lower energy than the $m_1 = \pm 3/2$ spin state (Travis, 1971).

The interaction between the nuclear quadrupole moment and the EFG is known as the quadrupole splitting. The single absorption line in a ground state Mössbauer spectrum may therefore be split into two peaks corresponding to the non-spherical charge distribution about the excited state nucleus (Figure 3.1). This corresponds to a splitting in the $I = 3/2$ level. Thus the

splitting of the peaks in a Mössbauer spectrum can give a measure of the degree of distortion in the electronic system.

The magnitude of the quadrupole splitting is directly related to the z component of the EFG tensor, and η according to Equation 3.8. This electric quadrupole splitting is for the first nuclear excited state of the ^{57}Fe nucleus ($I = 3/2$) as can be seen in Figure 3.1. E_Q is the quadrupole coupling energy and the energy difference of the measured quadrupole splitting is equal to twice E_Q .

$$E_Q = \pm \frac{eQV_z}{4} \left(1 + \frac{\eta^2}{3} \right)^{\frac{1}{2}} \quad (3.8)$$

The quadrupole split lines occur when the ligands are distorted from a purely cubic symmetry about the absorber nucleus (Travis, 1971). The valence contribution to the quadrupole splitting comes from the asymmetrical distribution of valence shell electrons.

3.2.3 Magnetic Hyperfine Interactions

The magnetic hyperfine interaction (nuclear Zeeman effect) is an indication of the local magnetic field experienced by the nuclei due to both magnetic properties of the material and externally applied fields. This can be seen as a further splitting of the absorption lines into usually 6 transitions for ^{57}Fe (Figure 3.1). The energy of the nuclear Zeeman effect can be described by the following equation (Gonser, 1975):

$$E_m = -g_N \mu_N B m_I = \frac{-\mu B m_I}{I} \quad (3.9)$$

Here m_I is the magnetic quantum number and ranges between $\pm I$, μ_N is the nuclear magneton which is equal to $5.05 \times 10^{-27} \text{ J/T}$, and g_N is the nuclear Landé splitting factor. B is the magnetic field and μ is the dipole moment of the nucleus. The Hamiltonian can therefore be written as,

$$\mathcal{H}_M = -g_N \mu_N B(0) [I_z \cos \theta + (I_x \cos \phi + I_y \sin \phi) \sin \theta] \quad (3.10)$$

In this equation, the value of θ represent the angle of the γ -ray with respect to the direction V_{zz} , and ϕ is the projection of the γ -ray direction onto the $V_{xx} - V_{yy}$ plane as seen in Figure 3.2 below. The value α represents the angle between the principal direction of the EFG and the magnetic field, while β is the planar angle from V_{xx} to the magnetic field. This equation describes how the internal hyperfine field, an applied field and the angular momentum of the nuclear levels will affect the splitting of the sextet.

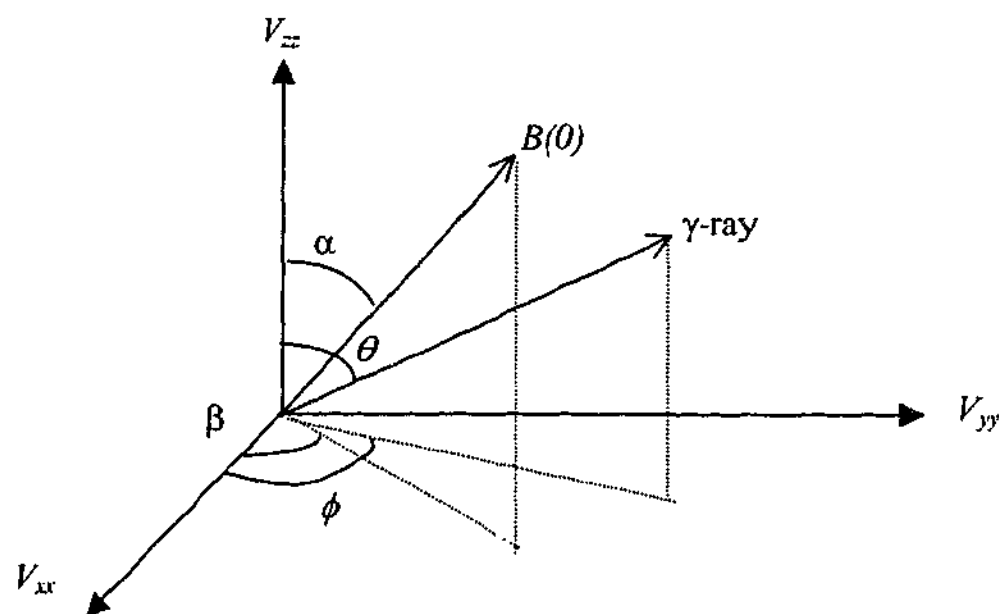


Figure 3.2: Cartesian system representing the principal axes of the EFG, and the orientation of the internal hyperfine field and the γ -ray with respect to the EFG.

3.3 RELATIVE LINE INTENSITIES

The relation that describes the relative intensities of the lines of a magnetic hyperfine split spectrum is shown below in Equation 3.11. The symbol x is the angle between the γ -ray propagation direction and the quantisation axis – in this case the magnetic field experienced by the nucleus. This implies that there is an angular dependence for the intensity of each transition. The first term represents the relative intensity of the outer lines of a hyperfine split spectrum with an energy transition from the $\pm 3/2$ level to the $\pm 1/2$ level ($\Delta m = \pm 1$). The second and third terms

are the middle and inner line intensities respectively. These represent the transitions from $\pm 1/2$ to $\pm 1/2$ ($\Delta m = 0$) and $\mp 1/2$ to $\pm 1/2$ energy levels ($\Delta m = 0$).

$$3(1 + \cos^2 x) : 4\sin^2 x : (1 + \cos^2 x) \quad (3.11)$$

Thus the relative line intensities for a completely random magnetic material are 3:2:1:1:2:3. An α -Fe foil measured at room temperature with no applied field displays a line intensity ratio closely resembling this ratio. For the situation where the magnetic field direction is perpendicular to the γ -ray ($x = 90^\circ$), the ratio is 3:4:1:1:4:3, while parallel components result in a ratio of 3:0:1:1:0:3.

The relative intensities of the absorption lines in a Mössbauer spectrum can give an observer useful information about a material that the positions of the lines can't provide. These can range from information about preferred orientation effects, to relaxation effects and saturation effects.

It is important when measuring the intrinsic properties of an absorber that external influences are minimised. The geometric arrangement of the transmission Mössbauer experiment is one such external influence that has to be controlled. External effects that can be corrected include texture problems within the sample, optimising the thickness of the absorber and source to sample distance (Gonser & Pfannes, 1974; Kreber & Gonser, 1974). By reducing these external conditions, the intrinsic factors can be measured.

3.3.1 The Thin Absorber Approximation

The thin absorber approximation is commonly used to simplify transmission Mössbauer spectra. By making the absorber sufficiently thin, the line broadening due to thickness effects is small enough to allow the line shapes to be fitted with Lorentzian profiles. However the sample must also remain thick enough that the most accurate results can be obtained in the shortest time possible (Long et al., 1983).

An absorber that is too thick will reduce the flux of γ -rays detected, resulting in line-width broadening and decreased resolution of a multiple line spectrum (Greenwood, 1971). If an absorber is too thin, it will reduce the amount of resonant absorption that takes place. For

optimal absorption with minimal line broadening, the percentage dip in a Mössbauer spectrum must be less than around 8 %.

3.3.2 Polarisation effects

As single crystal absorbers are rarely thin enough to avoid saturation effects, steps must be taken to include these effects during analysis. Most single crystal absorbers will be influenced by polarisation effects to some degree, which in turn effects the saturation of the absorber (Housley et al., 1969). Polarisation in Mössbauer spectroscopy can relate to either a polarised source, or polarisation of the absorber. For instance, a completely polarised absorber can only absorb γ -rays for half of the incoming unpolarised beam, thus altering the line intensities from those of an un-polarised absorber (Housley, 1969).

For a completely un-polarised, random absorber, a 6 line, magnetically ordered spectrum would have relative intensities of 3:2:1:1:2:3. If the absorber is completely polarised by a magnetic field applied parallel to the γ -ray direction, then the relative line intensities are 3:0:1:1:0:3 and similarly for an applied field perpendicular to the γ -rays, the intensities are 3:4:1:1:4:3 (Williams & Brooks, 1975). Normalising for the partial strength of each line, the un-polarised spectrum would yield $3/12:2/12:1/12$ for the outer middle and inner lines, while for magnetization parallel and perpendicular, the intensities would be $3/4:0:1/4$ and $3/8:4/8:1/8$ respectively (Williams & Brooks, 1975). For a longitudinal polarisation, lines 3 and 6 require absorption of right-hand circularly polarised γ -rays as these follow the $\Delta m = +1$ transitions, while for lines 1 and 4 it is left-hand circularly polarised γ -rays as these are the $\Delta m = -1$ transitions. Thus it is observed that the lines of opposite transition energy absorb oppositely handed polarised γ -rays. Similarly, the relative intensities of lines 2 and 5 are affected by linearly polarised γ -rays as the transition for these lines is $\Delta m = 0$.

One difficulty with correcting for polarisation occurs in the progressive polarisation of the γ -ray beam as it passes through an absorber. As the γ -ray becomes polarised, there is a reduced fraction of the beam that is available for absorption, and this may also affect the relative line intensities (Housley et al., 1969). Sample thickness may also combine with polarisation effects to

influence the absorption of the γ -rays. As the γ -ray beam passed through a thick sample, there are less γ -rays available for absorption. Thickness effects will influence the entire beam incident on the sample, while polarisation effects alone will only affect half the beam.

In an asymmetric quadrupole split Mössbauer spectrum, polarisation effects will alter the ratio of the line intensities. The dip with the largest intensity may be affected most by polarisation due to a greater recoil free fraction absorbing gammas in that line. However, angular effects such as changing the tilt of the sample may also affect the recoil free fraction. For a thin sample, the polarisation may reduce the transitions such that they have a lower flux around the rear of the crystal sample. This reduces the intensity of the strongest dip more than the smaller intensity dip, and therefore alters the overall intensity ratio.

3.3.3 Texture and the Goldanskii-Karyagin effect

The Goldanskii-Karyagin effect (GKE) is observed as a change in the spectrum due to the effect of an atom's thermal vibration within the lattice having a larger amplitude in one preferred direction. Above absolute zero temperature, atoms within a solid vibrate with a mean squared displacement from an equilibrium position. In some situations, an atom will vibrate with a greater mean squared displacement in one direction when compared with another. According to Equation 3.1, this suggests that the different crystallographic directions of vibration have different recoil-free fractions, f , producing different absorption probabilities (Ericsson & Wäppling, 1976).

For a single crystal sample, the GKE does not affect the relative line intensities of a quadrupole split spectrum, as there is only one orientation of the atomic structure with respect to the γ -ray direction. Thus any anisotropic lattice vibrations affect each absorption line equally such that the asymmetry in the quadrupole split lines is due purely to the texture of the single crystal absorber. Texture is the term given to a group of crystals, molecules, or spins within a sample that orient themselves along a common direction (Gonser & Pfannes, 1974). A completely randomised polycrystalline sample with no GKE and no texture will follow a quadrupole split intensity ratio of the $\Delta m = \pm 1$ and $\Delta m = 0$ transitions of 1:1. However those un-textured polycrystalline samples with GKE present will exhibit an asymmetry between the $\Delta m = \pm 1$ and $\Delta m = 0$ transition intensities. The degree of vibrational anisotropy is strongly

temperature dependent, such that increased temperature results in a more pronounced asymmetry (Cohen, 1976).

The asymmetry of the Mössbauer line intensities is sometimes attributed to the GKE without complete consideration of the sample environment (Pfannes & Gonser, 1973; Ericsson & Wäppling, 1976). Preferred orientation can remain in a polycrystalline sample even after efforts to randomise the sample. This often leads to incorrect classification, as the effect of the GKE on the relative line intensities is often less pronounced than the texture effects. At room temperature, a lattice vibrational anisotropy three times greater in one crystallographic direction has been found to result in a 5% asymmetry in the line intensities (Ericsson & Wäppling, 1976). However, a misalignment of the randomised sample by a few degrees can give asymmetries larger than 5% that completely obscure the GKE.

Care must be taken to remove all traces of texture from a Mössbauer absorber in order to obtain a truly random sample and accurately measure the intrinsic effects. One method involves combining the textured material with an inert powder such as boron nitride so that the textured particles are held in suspension (Chandra & Ericsson, 1979). This method fails if small amounts of pressure are applied to the sample as this can force the crystallites to re-align within the sample holder, thus destroying the randomness (Pfannes & Gonser, 1973). This follows the assumption that the most common direction of alignment is perpendicular to the direction of compression, which is parallel to the direction of the γ -ray. Another method for removing the effects of texture has been labelled as the "magic angle" technique (Ericsson & Wäppling, 1976). From Equation 3.11 it can be shown that if the angle between the γ -ray and the normal of the absorber was 54.7° , the intensities of the $\Delta m = 0$ and $\Delta m = \pm 1$ lines are equal. This method has been extended to remove the texture effects from any preferred orientation, provided that the hyperfine interaction remains axial (Grenèche & Varret, 1982). In this method, four spectra should be taken at 90° intervals about the 54.7° plane and superimposed to remove planar texture effects.

Another way to confirm the presence of GKE, is by conducting multiple temperature experiments. The texture of a sample will not change with temperature, but the recoil free fraction and therefore the GKE will. As the temperature is reduced, the lattice becomes frozen, reducing vibrations. Thus it must be the GKE that is responsible for any change of asymmetry with temperature.

3.3.4 EFG direction

The relative line intensities in a quadrupole split, randomised sample can give information about the orientation of the lattice vibrational anisotropy. In a similar way, the relative line intensities of a single crystal spectrum, related to the orientation of the crystal in the γ -ray beam, can be used to determine the angular dependence of the principal axis of the EFG. Both V_{zz} and the preferred axis of vibration are therefore usually expressed in terms relative to the direction of the γ -ray. The ratio of the line intensities from the transitions $\Delta m = 0$ and $\Delta m = \pm 1$ can be seen in Equation 3.12. Here, θ is the angle between the γ -ray and the principal axis of the EFG and ϕ is the angle in the xy plane.

$$\frac{I_{(\Delta m=\pm 1)}}{I_{(\Delta m=0)}} = \frac{I_{\pm 3/2}}{I_{\pm 1/2}} = \frac{\left(1 + \frac{\eta^2}{3}\right)^{\frac{1}{2}} + (3 \cos^2 \theta - 1 + \eta \sin^2 \theta \cos 2\phi)/4}{\left(1 + \frac{\eta^2}{3}\right)^{\frac{1}{2}} - (3 \cos^2 \theta - 1 + \eta \sin^2 \theta \cos 2\phi)/4} \quad (3.12)$$

For completely random samples, this ratio is 1 as $\langle \cos^2 \theta \rangle = \langle \sin^2 \theta \rangle = \frac{1}{3}$. When the sample is a single crystal and $\theta = 0$, then the relative line intensities of the two quadrupole split absorption dips are 3:1 and 3:5 when $\theta = 90^\circ$ (Gonser & Pfannes, 1974). Thus the relative line intensities of a quadrupole split spectrum have an angular dependence with respect to the γ -ray propagation direction and the EFG (Kündig, 1967). Kündig (1967) has evaluated the ^{57}Fe Hamiltonian to find the transition energies and relative line intensities for a Mössbauer spectrum. This Hamiltonian is the sum of the quadrupole Hamiltonian and the magnetic Hamiltonian (Equations 3.7 and 3.10 respectively) where values of θ and ϕ represent the angles as defined in Figure 3.2. Using this Hamiltonian and Equation 3.12, the line positions and intensities can be calculated for varying combinations of the parameters $B(0)$, $eQ V_{zz}$, θ_q , η and ϕ .

3.4 PREVIOUS MÖSSBAUER SPECTROSCOPY RESULTS WITH FePS_3 :

^{57}Fe Mössbauer spectroscopy has proven to be a popular technique for studying FePS_3 and its intercalated compounds; however, the analysis is by no means complete. Taylor, et al., (1973) first performed Mössbauer spectroscopy on a single crystal sample of FePS_3 in 1973. The γ -ray direction was oriented along the c^* axis and measurements were taken at room temperature and 77 K. Their results can be seen in Figure 3.3, with a quadrupole split doublet at room temperature, and 5 visible lines in the magnetically ordered spectrum.

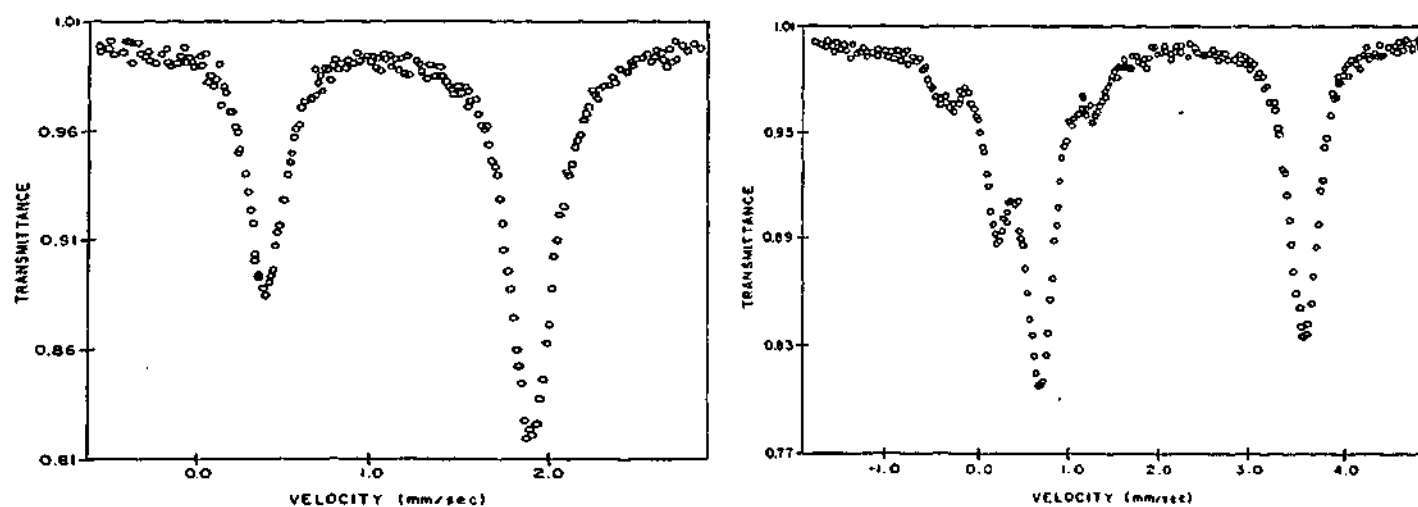


Figure 3.3: Mössbauer spectroscopy data taken with a pseudo-single crystal at 296 K (left) and 77 K (right) (Taylor et al., 1973).

This same group also performed Mössbauer spectroscopy with FePSe_3 crystals with similar results (Taylor et al., 1974). This is an indication that although the crystallographic unit cells are different for each compound (FePSe_3 has a rhombohedral cell), the iron sites have similar environments.

3.4.1 Single crystal and powder sample measurements

Although no Lorentzian profiles were published with the FePS_3 data, the hyperfine parameters were given as follows. For the room temperature data, the isomer shift was $1.13 \pm$

0.02 mm/s, the quadrupole splitting was 1.525 ± 0.009 mm/s and the intensity ratio of the right line over the left was 1.78 (Taylor et al., 1973). Although a hyperfine split spectrum was presented, no hyperfine field was published in this data. The presence of only 5 lines rather than the characteristic 6 lines of a magnetically ordered spectrum was explained in terms of degeneracy between the transition energies of lines 1 and 4. The FePSe₃ parameters taken at room temperature were 1.05 ± 0.01 mm/s for the chemical shift and 1.449 ± 0.001 mm/s for the quadrupole splitting. The intensity ratio was 2.70 and the internal hyperfine field for magnetically ordered FePSe₃ was 9.5 ± 0.2 T at 77 K. From this it can be seen that the intensity ratio of the quadrupole split lines for FePSe₃ was close to 1:3, as opposed to that for FePS₃ of around 1:1.8.

Bjarman et al. (1983) and Jernberg et al. (1984) have studied the temperature dependence of the relative line intensities in both single crystal and powdered samples of FePS₃. They took multiple Mössbauer measurements above and below the ordering temperature, and their single crystal spectra demonstrated the gradual shift from an asymmetric doublet to a five line, magnetically ordered spectrum. A powdered sample of FePS₃ was pressed into a disk with boron nitride, and thus the supposedly random sample spectra show considerable preferred orientation. Between 110 K and 120 K, they observed both antiferromagnetic and paramagnetic phases co-existing in each of the single crystal and powdered samples. They concluded that at temperatures above the ordering temperature, V_{zz} was parallel to the c^* -direction and the asymmetry parameter, η , was zero. The analysis assumed that the direction of V_{zz} was parallel to the hyperfine field within the lattice.

The quadrupole splitting and isomer shifts were similar to those obtained by Taylor et al. (1973), however they also obtained an internal hyperfine field of 9.69 ± 0.01 T at 5 K, which reduced to 8.23 ± 0.01 T at 100 K. The paramagnetic intensity ratio appeared to be very similar to the previous study, although, using Equation 3.12, Bjarman et al. (1983) made the assumptions that $\theta = 0$ (i.e. V_{zz} parallel to the γ -ray direction), and the asymmetry parameter, η , was close to zero. Following from this data, they assumed that the moment direction was parallel to the gamma ray direction, however the appearance of lines 2 and 5 in their spectra and that of Taylor et al. (1973) did not support this.

The large quadrupole splitting in the Mössbauer spectra suggests that there is a large crystal field splitting between the ground and excited states. This implies that the trigonal field is significantly larger than the spin-orbit interaction in FePS₃ (Jernberg et al., 1984).

Mössbauer spectra for powdered samples of FePS₃ have not been consistent, largely due to the strong preferred orientations of the powdered samples. Figure 3.4 shows the most recent room temperature and magnetically ordered spectra of powdered FePS₃ taken by Sakai et al., (1999b). The difference between this and the single crystal data is obvious in the significant intensities of lines 2 and 5 in the magnetically ordered spectrum. The internal magnetic field was found from this data to be 9.0 T. The asymmetry of the quadrupole split lines was approximately 1.14, which is slightly larger than the expected ratio of a randomised sample of 1. This was attributed to preferred orientation within the sample (Sakai et al., 1999b).

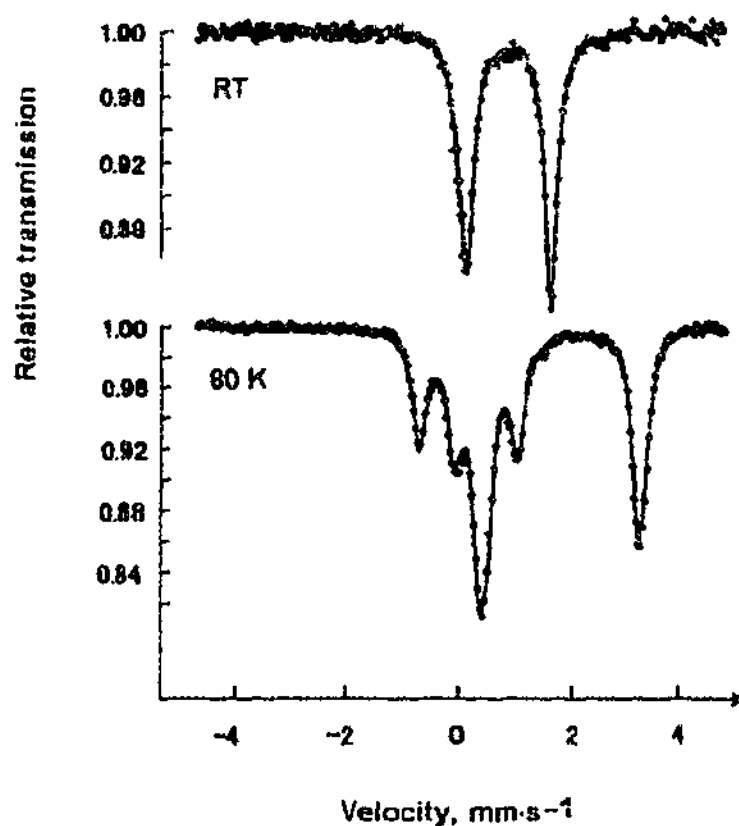


Figure 3.4: Powder Mössbauer spectra taken at room temperature and 80 K (Sakai et al., 1999b).

3.4.2 Goldanskii-Karyagin effect in FePS_3

One group has performed GKE measurements on FePS_3 (Chandra & Ericsson, 1979), using a powdered cube of material. FePS_3 was chosen for the GKE study, as its direction of asymmetry in the quadrupole split lines due to the GKE was opposite that caused by the texture of the material. To prove the absence of texture, a 1 cm cube of crushed FePS_3 mixed with Boron Nitride was measured from all three mutually perpendicular directions. Result taken at room temperature gave similar line intensity ratios (within 5%). Spectra taken at increasing temperatures showed increased asymmetry in the lines as seen in Figure 3.5. The line intensity ratio at room temperature was found to be 0.97, which dropped to 0.92 at 400 K (Chandra & Ericsson, 1979). The largest amplitude of vibration was stated as parallel to V_{zz} , which was assumed to be oriented along the c^* -axis. From this it was deduced that the f -factor was larger in the ab -plane than along the c^* -direction. The Debye temperature was also calculated from the relation between the peak area and temperature and found to be 226 ± 10 K (Chandra & Ericsson, 1979).

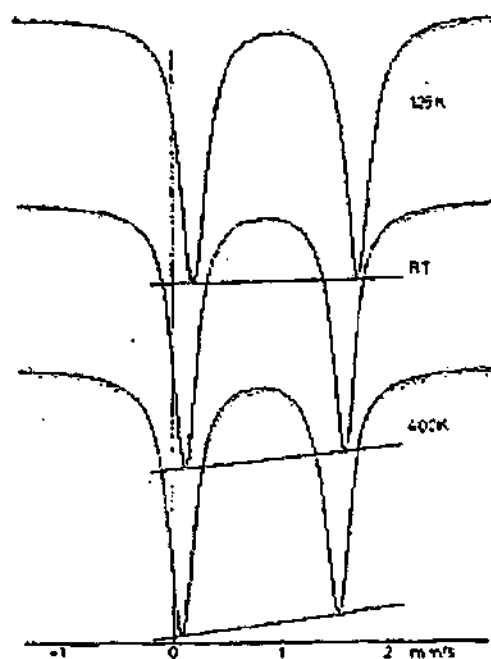


Figure 3.5: GKE measurements of powdered FePS_3 taken at varying temperatures from 125 K to 400 K (Chandra & Ericsson, 1979). The change in asymmetry due to temperature is denoted by the change in gradient of the lines.

3.5 NEUTRON SCATTERING

Neutrons were first discovered in 1932 by James Chadwick, and described as a particle similar in mass to a proton but with no electric charge. The neutron with a mass of 1.675×10^{-27} kg, solved many of the problems relating to atomic mass (Squires, 1978). Neutrons have a spin of $1/2$ and a net magnetic moment of $5.4 \times 10^{-4} \mu_B$ (Jiles, 1991). Thermal neutrons have energies in the meV range, which gives them wavelengths suitable for studying the lattice spacings of solids (Dachs, 1978).

Both neutron and x-ray diffraction give similar results for structural investigations, however there are various advantages and disadvantages to each technique. X-ray diffraction involves the scattering of short wavelength radiation from an electron cloud within a target material. As x-ray diffraction relies on the interactions with electrons, heavy elements with high-density electron clouds, scatter x-rays well. On the other hand, elements such as oxygen and hydrogen with relatively few electrons are not easily detected as the x-rays pass right through the sample with little or no scattering (Bacon, 1975). X-ray beams tend to have fluxes typically 10^{13} times greater than for neutron beams, which reduces counting time and increases the resolution of detection (Pynn, 1990). They are also relatively cheap and convenient to use, with lab-based x-ray diffraction devices readily available.

Neutrons possess no electric charge while thermal neutrons have a momentum approximately equal to a phonon. Neutrons tend to interact with the nucleus of an atom rather than the cloud of electrons surrounding it as x-rays do. These interactions between neutrons and atoms occur via nuclear forces that are short-range compared with the electric forces for x-rays, which have a long-range. As inter-atomic distances can be up to 10^6 times larger than the actual nuclei, a neutron can penetrate deeply into a material before it is scattered (Pynn, 1990). This makes neutron diffraction a useful tool for investigating the bulk properties of a sample, rather than just the surface regions.

Scattering amplitudes also differ between x-rays and neutrons – sometimes an element is “seen” better by x-rays and sometimes by neutrons. As the neutron has no electric charge, it is able to scatter equally well off heavy and light elements. Lattice structures for materials with a high proportion of lighter elements are best investigated with neutrons. Hydrogen is an example of an element that is practically invisible to x-rays but scatters neutrons strongly (Squires, 1978).

Different isotopes of certain elements can also be distinguished relatively easily by neutron scattering whereas x-rays scatter equally from different isotopes (Bacon, 1975). This makes isotopic labelling useful in samples for neutron diffraction studies.

Neutrons have a spin quantum number of $1/2$, which implies a spin angular momentum of $1/2\hbar$. Despite the fact that a neutron has no net charge, it is the spin of the neutron that produces a nuclear magnetic moment. An applied magnetic field will influence a spinning neutron such that it rotates with a frequency of precession called the Larmor frequency. This is equal to $2\mu B/h$ where B is the applied external field, h is Planck's constant and μ is the magnetic moment of the neutron. The accepted value of the neutron moment, μ_n is $-1.913 \mu_N$, where μ_N is the nuclear magneton (otherwise equal to $e\hbar/2m_p = 5.051 \times 10^{-27} \text{ JT}^{-1}$) (Bacon, 1969; Squires, 1978). This property makes neutrons perfect for investigating the magnetic properties of materials.

Neutrons are also observed to scatter quite weakly, so a lot more time, neutrons and sample are needed for a reasonable spectrum when compared with x-rays. Neutron sources are also not as common as x-ray sources and often investigators are required to travel to a reactor to carry out research. The energy of a neutron is typically 10^5 times smaller than x-ray energies, which makes neutron diffraction useful for observing excitations in solids. Thus neutron scattering is an important tool for examining crystallographic structures and lattice vibrations as well as magnetic properties and excitations.

3.6 THERMAL NEUTRON SCATTERING

The wavelength, λ , of a neutron, with a velocity, v , can be described by the de Broglie relation:

$$\lambda = \frac{h}{m_n v} \quad (3.13)$$

where h is Planck's constant and m_n is the mass of the neutron. A typical velocity for thermal neutrons is around 2.20 km s^{-1} at room temperature (Squires, 1978). From this, the energy of the neutrons can be found, in units of meV, according to Equation 3.14.

$$E_n = \frac{1}{2} m_n v^2 = \frac{h^2}{2m_n \lambda^2} \quad (3.14)$$

In a scattering experiment, three quantities can be determined; the scattered intensity of the neutron, the energy change of the neutron and the momentum change of the neutron. The final two are a measure of the velocity difference between incident and scattered neutrons. A simplified diagram of a beam of neutrons scattering from a sample can be seen in Figure 3.6.

The wave vector k describes the incident beam of neutrons and has a magnitude of $2\pi/\lambda$. When the incident neutron with a wave vector, k , hits the sample, it is scattered with a wave vector, k' . The difference between the incident and scattered wave vectors is known as the scattering vector, κ .

$$\kappa = k - k' \quad (3.15)$$

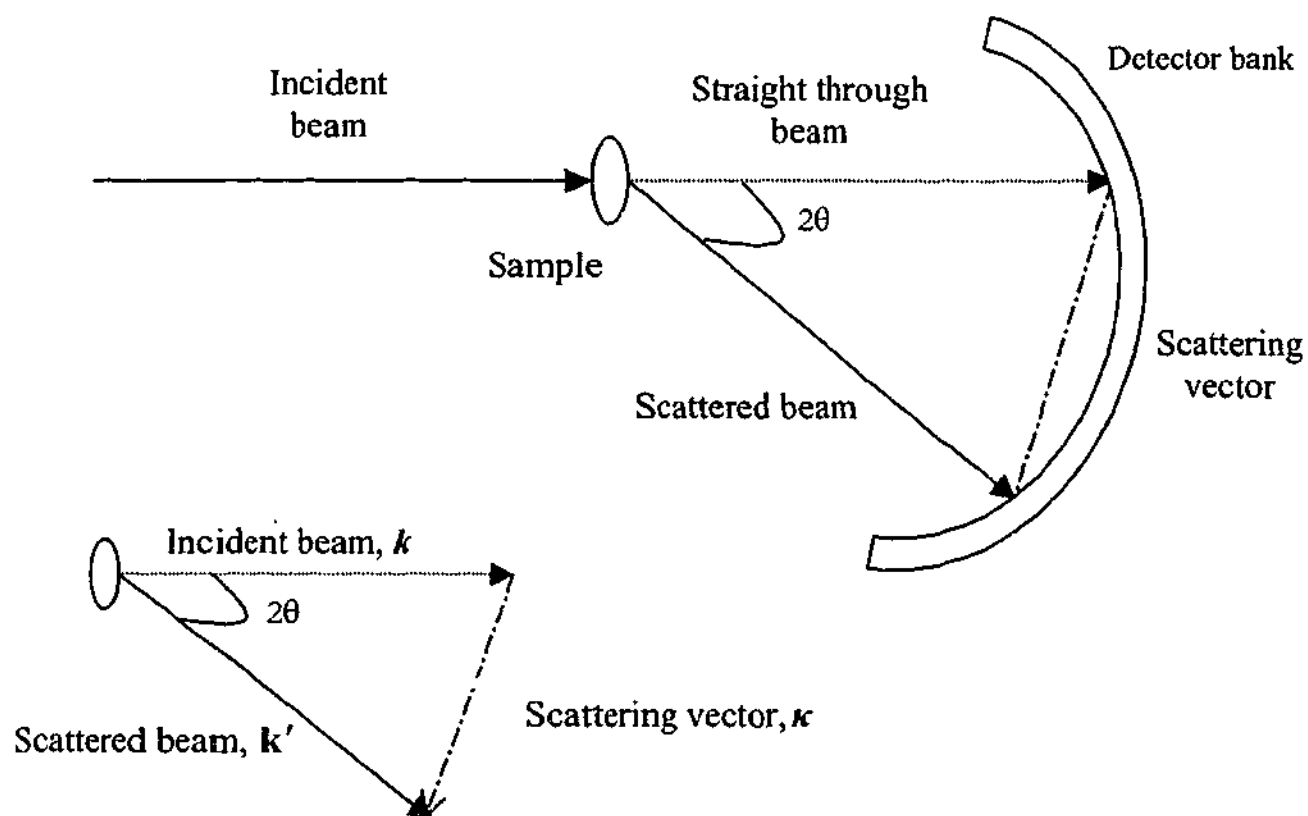


Figure 3.6: Neutron scattering geometry and the equivalent scattering vectors in reciprocal space.

The scattering vector, κ , (also known as Q), is an indication of the momentum transfer vector between the incident and diffracted neutrons. This can be seen in Equation 3.16.

$$p = \hbar\kappa \quad (3.16)$$

The angle between the incident and scattered wave vectors is 2θ , and the scattering vector is related to the neutron wavelength by

$$\kappa = \frac{4\pi \sin \theta}{\lambda} \quad (3.17)$$

The intensity of Bragg peaks is influenced by both constructive and destructive interference of the scattered rays due to the wave-like characteristics of the neutron beam. The incident neutrons can be described by a plane wave, while the resulting scattered wave is spherical with a wave function

$$\Psi = -\left(\frac{b}{r}\right)e^{ikr} \quad (3.18)$$

Here b is the scattering length and r is the distance from the centre of the scattering nucleus to the wave front. The scattering length is a complex quantity, which varies greatly between nuclei within the material of investigation. The values of b vary randomly with mass number and different isotopes and can be found from experimental results. The imaginary part of the scattering length is related primarily to the absorption of the neutron and is usually small enough to disregard in the case of scattering nuclei. It does become increasingly important for materials that absorb neutrons strongly such as boron or cadmium (Bacon, 1975). The scattering length is also dependent on the spin state of the nucleus-neutron system, with each spin state (for both the nucleus and the interacting neutron) associated with its own b . Nuclei with a spin state of zero are limited to one scattering length associated with the spin $1/2$ neutron (Squires, 1978).

The differential scattering cross section ($d\sigma/d\Omega$) is a representation of the scattered neutron as it changes state from k to its final wave vector, k' . It can be defined as the total number of neutrons scattered per second into the solid angle, $d\Omega$, per unit of incident beam intensity. The symbol σ represents the scattering cross-section, which measures the scattering power of a nucleus. It can be defined as $4\pi b^2$. The scattering length can be related to the differential cross section by the following equation (Squires, 1978).

$$\frac{d\sigma}{d\Omega} = b^2 \quad (3.19)$$

The cross section can be separated into two parts – one from the coherent scattering and the other from the incoherent. Coherent scattering (elastic diffraction) occurs when the incident neutrons interact the same way with each of the nuclei in the material. Thus, the scattered beams can constructively and destructively interfere with one another. Constructive interference will only occur at values of the scattering vector that are equal to the reciprocal lattice vectors. That is

$$\kappa = ha^* + kb^* + lc^* \quad (3.20)$$

The coherent part of the differential cross section is the square of the average amplitude and can be written as

$$\left(\frac{d\sigma}{d\Omega}\right)_{\text{coherent}} = \left| \bar{b} \sum_j \exp(i\kappa \cdot \mathbf{R}_j) \right|^2 \quad (3.21)$$

where \mathbf{R}_j defines the positions of the nuclei in the sample with scattering lengths b_j (Williams, 1988).

Incoherent scattering occurs when each nucleus interacts with the neutron differently, so there is no periodic interference between the scattered waves as the phase differences are random. In this case, the resulting pattern is just the superposition of the scattered intensities from each atom. Incoherent scattering is zero for samples with only one isotope and with a nuclear spin of zero. The incoherent term in the differential cross section is given by

$$\left(\frac{d\sigma}{d\Omega}\right)_{\text{incoherent}} = N \overline{|b - \bar{b}|^2} \quad (3.22)$$

where N is the number of scattering nuclei in the sample and the \bar{b} represents the average value of the scattering length over all isotope distributions and for all nuclear spin orientations in the scattering sample.

During a thermal neutron scattering experiment, the primary feature measured is the partial differential scattering cross section, which describes the total number of neutrons scattered per second across a certain solid angle $d\Omega$ with a range of energies between E_q and E_q (Squires, 1978; Balcar & Lovesey, 1989). The partial differential scattering cross section contains

information about the shape, size and interactions between scattering centres within a sample, where the scattering centres are the nuclei and molecules that interact with the incident neutrons. The partial differential cross section can be defined by the following expression (Lovesey, 1984).

$$\frac{d^2\sigma}{d\Omega dE'} = \frac{k'}{k} \left(\frac{m}{2\pi\hbar^2} \right)^2 \sum_{q'} \sum_q P_q \left| \langle \mathbf{k}'s'q' | \hat{V}(\boldsymbol{\kappa}) | \mathbf{k}s q \rangle \right|^2 \delta(\hbar\omega + E_q - E_{q'}) \quad (3.23)$$

where $\hat{V}(\boldsymbol{\kappa})$ is the interaction potential. The neutron spin state goes from s to s' as the wave vector goes from state \mathbf{k} to \mathbf{k}' and the sample states go from q to q' . The primed values represent the final state of the neutron.

When $|\mathbf{k}| = |\mathbf{k}'|$, the energy of the incident neutron is conserved, and the neutron is said to be elastically scattered. If $|\mathbf{k}| \neq |\mathbf{k}'|$, the scattered neutron may have either gained or lost energy and is inelastically scattered.

3.7 NEUTRON SCATTERING PROFILES

The interaction potential between the nucleus and the incident neutron can be defined for nuclear, coherent scattering, by the Equation 3.24 where \mathbf{R} represents the position of the nucleus and \mathbf{r} the position of the neutron. The delta function implies that when $\mathbf{R} = \mathbf{r}$ the neutron interacts with the nucleus via a collision.

$$\hat{V} = \frac{2\pi\hbar^2}{m} \sum_{\mathbf{R}} b(\mathbf{R}) \delta(\mathbf{r} - \mathbf{R}) \quad (3.24)$$

By substituting this into Equation 3.23, the nuclear structure factor is revealed. The structure factor, F_{hkl} , indicates the extent to which interference of the scattered waves from identical ions in a basis can affect the intensity of the corresponding Bragg peak. This is dependent on the degree of local order in the sample. The structure factor is the sum over the contributions from each atom in the unit cell. The scattering lengths, b_m , from each atom in the unit cell may be different, which allows for a different contribution to the structure factor from each atom.

$$F_{nucl}^2 = \left| \sum_n b_n \exp \left\{ 2\pi i \left(\frac{hx_n}{a_0} + \frac{ky_n}{b_0} + \frac{lz_n}{c_0} \right) \right\} \right|^2 \quad (3.25)$$

F_{nucl}^2 is the squared structure factor for each separate nuclear reflection (hkl) and is taken as the sum over all the atoms, n , in the unit cell (Bacon, 1975). The structure factor is directly related to the intensity of the peak such that no peak will be observed for reflections with zero structure factor. Multiplicity is another influence that may affect the relative amplitudes of the nuclear peaks in a powder diffraction pattern. All the different reflections that have the same scattering vector magnitude, will contribute to the peak intensity at the same scattering angle in powder diffraction.

3.8 MAGNETIC NEUTRON SCATTERING

Neutrons make an excellent tool for investigating magnetic structures. Many materials have an ordered arrangement of magnetic moments that exist primarily due to the unpaired electrons. These moments are affected by the influence of internal magnetic fields created by the neighbouring moments, and by external fields that can be applied to the material. The neutron is scattered via the interaction between its own magnetic moment and the magnetic field in the sample in such a way as to give rise to magnetic Bragg reflections, similar to nuclear Bragg reflections. This interaction can be described by the interaction potential, where $\gamma = -1.913$ is the neutron gyromagnetic ratio and $\hat{\sigma}$ represents the neutron spin operator, which can be expressed in terms of the Pauli spin matrices for spin $1/2$ particles (Balcar & Lovesey, 1989).

$$\hat{U} = -\gamma\mu_N\hat{\sigma} \cdot \hat{B} \quad (3.26)$$

The magnetic neutron scattering for paramagnetic materials will be largely incoherent. Only those materials with an ordered magnetic structure will exhibit magnetic neutron scattering in the form of magnetic Bragg peaks. Magnetic scattering depends on the orientation of the magnetic moments relative to the scattering vector. If the orientation of the incident and scattered neutrons produce a scattering vector that is parallel to the magnetic moment of the scattering atom, the amplitude of the scattered neutron is zero. In this situation, the sum of the internal magnetic fields perpendicular to the scattering vector vanishes. This is as a result of the divergence of \mathbf{B}

being zero, $\nabla \cdot \mathbf{B} = 0$. The second arrangement involves a scattering vector that is perpendicular to the moment direction. This case will give a maximum scattering amplitude proportional to the dipole moment in the sample (Dachs, 1978). The scattering length for a magnetic atom with atomic spin S_n is

$$p_n = S_n f_n \left(\frac{e^2 \gamma}{m_e c^2} \right) \quad (3.27)$$

where e and m_e are the charge and mass of an electron, γ is the gyromagnetic ratio of the neutron c is the speed of light and f_n is the magnetic form factor.

Similar to nuclear scattering, the magnetic peak intensities are governed by magnetic structure factors and form factors, which are dependent on the moment direction. The magnetic structure amplitude factor can be seen below, where α_n is the angle between κ and the magnetic moment on the n^{th} atom (Bacon, 1975).

$$F_{\text{magn}}^2 = \left| \sum_n \sin(\alpha_n) p_n \exp \left\{ 2\pi i \left(\frac{hx_n}{a_0} + \frac{ky_n}{b_0} + \frac{lz_n}{c_0} \right) \right\} \right|^2 \quad (3.28)$$

Thus the total structure factor for each (hkl) reflection is given by the sum of the nuclear and magnetic structure factors. This is for randomly polarised neutrons only.

$$|F_{hkl}|^2 = |F_{\text{nucl}}|^2 + |F_{\text{magn}}|^2 \quad (3.29)$$

Magnetic structures can be described by the periodic repetition of a magnetic unit cell, where a propagation vector, τ , can define the relationship between the nuclear and magnetic unit cells. The propagation vector relates the magnetic atoms in the nuclear unit cell to the orientations of the moments on those atoms. The magnetic period can be the same as the nuclear period, as in the case of a single domain ferromagnet, or it can be larger than the nuclear unit cell. In general, a propagation vector will refer to any position on or within the surface of the first Brillouin zone. This allows the possibility of two general classes of magnetic structures; commensurate and incommensurate.

A commensurate magnetic structure relates the magnetic unit cell to the nuclear unit cell via a simple, exact multiple. For instance, a propagation vector of $\tau = 0, 0, 1/3$ implies that the

magnetic unit cell is commensurate and exactly three times as large as the nuclear unit cell along the c -axis. An incommensurate structure is one in which there is no simple relationship between the nuclear and magnetic unit cells. For instance, a propagation vector of $\tau = 0,0,0.32$ suggests that the magnetic unit cell is not quite triple the nuclear cell in the c -direction. Thus a propagation vector with either integer or simple fractional components defines a commensurate structure, while an incommensurate structure does not have a simple multiple relationship with the crystal cell. A helical magnetic structure in which the orientation of the magnetic moments changes by a constant angle, α , is one example of an incommensurate system.

3.9 DIFFUSE SCATTERING

Bragg scattering is observed from highly ordered materials with a well-defined lattice periodicity. A delta function can be used to approximate Bragg scattering from an ideal material with long-range order. Therefore, this type of scattering is highly dependent on the scattering vector, κ . However not all materials are perfect and certain impurities or structure defects in a material can reduce the order sufficiently that diffuse scattering appears in the diffraction pattern. Diffuse scattering from a structure with little or no order will be independent of κ and appears as a broadening of the neutron scattering profile. Bragg peaks from a well-ordered material do not contain any diffuse scattering, however they are often superimposed over diffuse peaks, giving the impression that the Bragg reflections have diffuse baselines. The diffuse scattering coupled to Bragg reflections is often so low in intensity that it is beyond the detection resolution of the instrumentation, and can therefore be disregarded.

Diffuse magnetic scattering can be observed during the transition from order to disorder. As the interactions between the magnetic scattering centres decrease with increased temperature, the intensity of the magnetic Bragg peaks decrease with increasing temperature, and disappear completely at the ordering temperature. Thus close to the ordering temperature, the diffuse scattering becomes more easily observed. Diffuse magnetic scattering can also reveal information about the short-range magnetic correlations of the sample.

3.10 POLARISED NEUTRONS

The physical state of a beam of neutrons can hold two pieces of information about the neutrons – the momentum state and the spin state. In regular neutron experiments the spin state of the neutron is considered to be random, or un-polarised. If the spin state of the incident neutrons is given a specific orientation, then the spin state of the scattered beam can provide extra information about the sample. Polarised neutrons are commonly used to investigate magnetic materials, as the polarisation of the neutrons can distinguish between magnetic and nuclear scattering. Polarisation analysis is particularly good for investigating short-range order in magnetic and atomic lattices.

A randomly oriented beam of neutrons can be polarised by restricting the polarisation vector to oscillate in one plane. Initial neutron polarising experiments used magnetised iron plates to separate the neutron polarisation states. However, by reducing the polarisation state to one plane the intensity of the beam was also reduced by around half (Williams, 1988). More recent methods of polarisation utilise supermirrors, which reflect neutrons with only one polarisation spin state. These consist of multi-layered thin films with alternating ferromagnetic and non-magnetic materials that are arranged such that only one of the neutron spin states, say “up”, has a non zero critical angle from the material. Thus the supermirrors absorb the “down” spins and the reflected beam is polarised.

By applying a guide field to the polarised neutrons, the quantisation axis of the spins can be defined and this can be used to maintain the direction of the polarisation. These guide fields are usually small enough to maintain the neutron spins without influencing the sample magnetization, yet large enough to negate the effect of the Earth’s field and other stray fields. To rotate the polarised neutrons successfully, the guide field must vary adiabatically such that the length used for turning the neutron spins is longer than the distance travelled by the neutron in one Larmor precession (Schweika, 2002).

When investigating materials using polarised neutrons, the polarisation of the incident neutrons and the polarisation state of the scattered neutrons must be considered. The scattered beam’s polarisation state is measured according to the state of the spin flippers located in the incident beam of a polarised neutron device. If the spin flippers are switched off, only non-spin flip (NSF) neutrons can be detected, while spin flip (SF) scattering events are recorded when one flipper is on. A sequence can be produced which turns the flipper on and off in time. The result

of this will appear in the detectors at a later time and thus the neutron time of flight can be measured.

The polarisation vector, \mathbf{P} , can describe the polarisation of an incident neutron beam, while \mathbf{P}' defines the polarisation of the scattered neutrons. The polarisation vector can be defined as the expectation value of the spin operator $\langle \hat{s}' \rangle$ divided by the spin of the neutron, $1/2$ (Williams, 1988).

$$\mathbf{P} = \frac{\langle \hat{s}' \rangle}{0.5} = 2(\langle \hat{s}'_x \rangle \mathbf{i}_x + \langle \hat{s}'_y \rangle \mathbf{i}_y + \langle \hat{s}'_z \rangle \mathbf{i}_z) \quad (3.30)$$

where the polarisation ranges from $0 < |\mathbf{P}| < 1$ (0 = unpolarised and 1 = completely polarised). The polarisation vector can also be equated to the expectation value of Pauli spin matrices, $\langle \sigma \rangle$. Although the axis of polarisation can be in any direction as defined by the guide field, it is convenient to consider the polarisation, \mathbf{P} , to follow one of two orientations – either parallel to the scattering vector ($\mathbf{P} \parallel \boldsymbol{\kappa}$) or perpendicular to the scattering vector ($\mathbf{P} \perp \boldsymbol{\kappa}$) as seen in Figure 3.7.

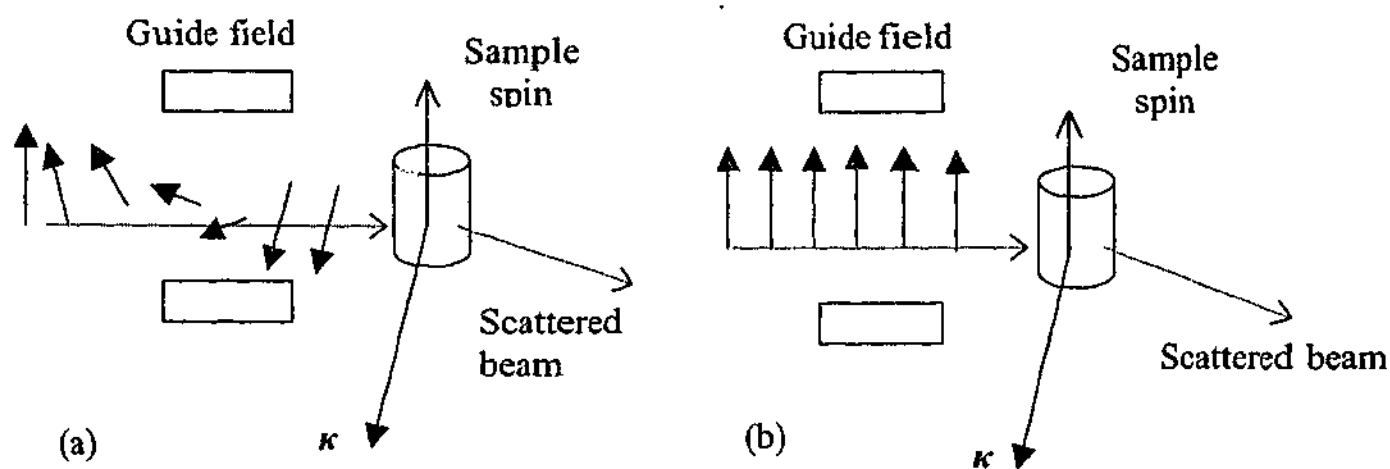


Figure 3.7: Two orientations of the polarisation vector \mathbf{P} , parallel with the scattering vector (a) and perpendicular with the scattering vector (b).

Paramagnetic materials can be investigated with polarised neutron scattering, to determine the relative proportions of nuclear spin incoherent scattering (NSIS) and coherent scattering.

Nuclear coherent scattering is always non-spin flip (NSF) and gives rise to the Bragg peaks in a diffraction pattern with a scattering amplitude of b . NSIS is independent of the polarisation directions but will be $2/3$ NSF and $1/3$ spin flip (SF) scattering.

Taking measurements with the neutron polarisation parallel and perpendicular to the scattering vector can also be used to isolate magnetic scattering. For magnetic Bragg peaks, the scattering of the neutrons depends on the initial polarisation direction with respect to the moment orientation. Magnetic scattering is only possible for the components of the moments that are perpendicular to the scattering vector, κ . Thus, when there is a component of the magnetic moment oriented perpendicular to the neutron polarisation direction, SF scattering will occur (Schweika, 2002). From this it can be seen that when the polarisation is along the scattering vector all the magnetic scattering is SF. By investigating a sample using polarised neutrons oriented both parallel and perpendicular to the scattering vector, it is possible to separate the purely nuclear from the purely magnetic scattering cross sections for ferromagnets, as well as an interference term between the nuclear and magnetic scattering (Lovesey, 1984). In the case of nuclear spin scattering the same is true except that components of the nuclear spin parallel to the scattering vector also scatter.

The nuclear spin incoherent scattering can interfere with polarised neutron scattering studies of magnetic materials (Bacon, 1975). If a sample has a nuclear spin and therefore an incoherent scattering cross section, then $2/3$ of the scattered neutrons will be spin flipped. This means that the two components of the nuclear spin perpendicular to the polarisation give SF scattering and the component parallel to the polarisation gives NSF scattering. This is independent of the polarisation direction for nuclear spin scattering, which makes separating the nuclear and magnetic cross sections difficult. Thus for magnetic polarisation analysis, it is important to determine the nuclear spin of each scattering element. The sulphur nucleus has been found to have zero nuclear spin indicating that the nuclear spin incoherent cross section is also zero (Bacon, 1975). Most Fe isotopes also have zero nuclear spin, however, ^{57}Fe has a non-zero nuclear spin, which gives a very small incoherent nuclear cross section. Phosphorus has a nuclear spin of a half, which also gives a very small nuclear spin incoherent scattering. From this it can be seen that FePS_3 has very little nuclear spin incoherent scattering. Thus any spin flip event in a polarised neutron spectrum of FePS_3 may be considered as magnetic. NSIS scattering does not form either Bragg peaks or diffuse peaks because the nuclear spins are randomly oriented with no

correlation between them. Diffuse peaks might occur in the spectrum of FePS₃ due to short-range correlations between the atomic magnetic moments due to the electrons.

3.11 ANALYSIS TECHNIQUES

Powder neutron diffraction scans can be analysed using the Rietveld method which fits a Gaussian line shape to the Bragg reflections via least squares minimisation. The two programs used for analysing the powder diffraction scans in this work include Rietica (Howard, 1982) and FullProf (Rodriguez-Carvajal, 1998). Rietica was found preferable for non-magnetic refinements, while FullProf was capable of adding magnetic phases to ordered spectra.

Rietveld refinement is based on a model that calculates each possible reflection using Bragg's law. It also calculates the structure factor so that the intensity of each reflection, as well as the position, is modelled. The process of this technique involves modelling the structure and composition of the sample material as well as the characteristics of the diffractometer to generate a diffraction pattern (Bacon, 1975). Variables related to lattice parameters, occupancy, thermal variations and preferred orientation in the sample could be altered to change the modelled pattern until it matches the experimental pattern. Diffractometer parameters to be varied include the neutron wavelength, the zero point of the detectors as well as non-linearities in the measurements of the scattering angle, 2θ . This refinement technique, for investigating powdered samples, fits all the reflections simultaneously.

Atomic scattering information is determined from this method by calculating the structure factor for each Bragg reflection in the space group. The integrated intensity of the observed reflection is proportional to the square of the magnitude of the structure factor $|F_{magn}|^2$. Peak shapes can be modelled by common functions such as Gaussian, Lorentzian, Pseudo-Voigt and Voigtians. Rietveld can also account for asymmetry in each of these line shape functions. Half widths of the lines may give information about particle size and the degree of imperfection in the sample. From the crystallographic information, accurate atom coordinates can be determined, along with site occupancy information and thermal vibration information.

Powder diffraction assumes random orientation of crystallites, and the Rietveld analysis method assumes crystallites to be spherical, such that there is no texture or preferred orientation

in a completely randomised sample. This however may not be true in actual samples, where materials may cleave along a certain axis and platelets form rather than spherical particles. Thus a 'powdered' sample may actually have a preferred direction and some peaks may not be observed in the data collection process. Rietveld analysis can be altered for preferred direction, however an easier solution would be to ensure accurate sample preparation. Another flaw that may affect the data includes large particles imbedded in the powder. This has the effect of making the intensities of some reflections too large, overshadowing the other peaks. Again care must be taken to eliminate such flaws. Background should also be reduced in data collection as a high signal to noise ratio can lead to poor sensitivity of results.

One limitation of each of these programs however, is in their inability to model low-dimensional and incommensurate structures. Both programs assume that the order is long-ranged in the material and that the magnetic unit cell is an integer multiple of the nuclear unit cell. Thus the fits displayed in this work have a certain degree of uncertainty from this factor.

Maximum entropy is a Bayesian method of data analysis that can be used for neutron diffraction data (Schweizer, 2002). Contrary to the Rietveld method of powder diffraction analysis, the maximum entropy method (MEM) does not attempt to fit a "model" to the set of data. Instead, this method of MEM relies on instrumental uncertainties to calculate a fit to the reconstructed data. Most other data fitting techniques use a well-defined model to fit an expected pattern to the data. Any points that do not appear to fit the model are then disregarded. This assumes that there is only one model to fit the data, whereas MEM does not start with a model, and only fits the data that is there. It calculates the probability that the fit is correct by considering certain conditions imposed by the instrumental limitations.

MEM can also be used to account for the physical scenario of less than infinite counts to find a distribution (Ables, 1974). Used widely in the field of astronomy, the maximum entropy method of analysis uses all of the data available to remove the instrumental uncertainties. One application of this is for reconstructing time of flight data. Information from an un-scattered neutron beam can be used to define the instrumental uncertainties, which may affect the interpretation of results using other analysis methods. A beam of neutrons that has not deviated from its original path will hold information about the spread of neutron velocities in the beam, the dead time spent in the spin flipper and the time spent in the detector before being detected.

The maximum entropy method of fitting data has been found from maximizing the thermodynamic entropy function, S , to solve the problem of assigning probability distributions with certain constraints (Ables, 1974). This mathematical form describes the measure of ignorance that the program follows in comparing the data with the assigned fit.

$$S = -\sum_i p_i \log p_i \quad (3.31)$$

Here, p_i is equal to the occupancy of a cell number i (N_i) divided by the configuration of a number of particles (N) (Schweizer, 2002). Originally this was introduced by Boltzmann to express the probability of a certain configuration in 6 dimensional phase-space, but it can just as easily be translated to any space. This value of p_i is then maximized according to the constraints that $0 \leq p_i \leq 1$ and $\sum_i p_i = 1$ as well as any other constraints observed in the data (Ables, 1974).

Each configuration does not have the same probability of occurring, however the most probable will maximize the above equation. This approach relies only on the maximisation of entropy rather than any dynamical laws.

3.12 NEUTRON DIFFRACTION STUDIES OF FePS_3

Previously, only one group has performed neutron diffraction experiments on FePS_3 , and their results have been accepted for 20 years (Kurosawa et al., 1983). In their study, they stacked multiple single crystals together with a common c^* -direction (within 3°) to form a pseudo-single crystal. By rotating the sample in the neutron beam, both nuclear and magnetic Bragg reflections were observed. Magnetic reflections became visible below 120 K, but were sharpest at 5 K.

The reduced magnetic moment was found to deviate from the temperature dependent Brillouin function. The strong anisotropy of iron was considered responsible for the deviation from this Brillouin function for $S = 2$. However the square-shaped trend for FePS_3 was similar to that observed in the neutron diffraction study of FePSe_3 (Wiedenmann et al., 1981). The crystallographic structure of the selenide compound is somewhat different to that of FePS_3 in that the former has rhombohedral symmetry. The propagation vector for FePSe_3 was found from the neutron diffraction study to be $\frac{1}{2} 0 \frac{1}{2}$. As the nuclear unit cell contains three layers of iron, the magnetic unit cell is 2 times as large along the z -direction. The magnetic structure in FePSe_3 was

found to be collinear from the powder neutron diffraction data, with a magnetic moment of $4.9 \mu_B$ oriented parallel to the c-axis (Wiedenmann et al., 1981).

In the neutron diffraction study by Kurosawa et al. (1983), the observed Bragg peaks for FePS₃ were compared with the calculated values. The magnetic peaks were indexed according to each of the crystallographic peaks translated via the propagation vector of $\tau = [0, 0, 1/2]$. However during a more recent inspection of this data, the magnetic peaks with significant intensity did not appear to follow this pattern (Rule et al., 2002). For instance, the magnetic peak labelled (0 1 3/2) was observed to have a maximum intensity. Taking the relation, $hkl_{\text{nucl}} \pm \tau = hkl_{\text{mag}}$, the nuclear reflections responsible for this magnetic peak were calculated to be (011) and (012). According to the crystallographic selection rules for this monoclinic system of $h + k = 2n$ (where n is an integer), these nuclear reflections are forbidden. If this were the correct labelling for the magnetic peak, then the propagation vector would have to be either $\tau = [0, 1, 1/2]$ or $\tau = [1, 0, 1/2]$ such that the related nuclear reflections followed the selection rules.

Also in this study, the theory of the propagation vector was incorrectly identified. For the monoclinic space group of $C 2/m$, the two iron atoms that form the basis are at the positions (000) and $(1/2, 1/2, 0)$ in the primitive unit cell. Because the basis of the honeycomb lattice is two, two types of reciprocal lattice point are produced. The selection rules for a non-zero structure factor for this monoclinic system are $h + k = 2n$ where n is an integer. The fundamental positions at the centre of the Brillouin zones for this system are defined as the reciprocal lattice positions where k is a multiple of 3 times any integer. Thus for positions where k takes on any other value, the reflection is considered to arise from the superlattice positions located elsewhere in the zones. The magnetic reflections for FePS₃ can therefore be defined as the sum of the fundamental reciprocal lattice vector with the propagation vector. Kurosawa et al. (1983) made the assumption that the magnetic peaks occur at each nuclear reflection $\pm \tau$, rather than from the fundamental reciprocal lattice point.

The lack of distinction between the types of nuclear lattice positions is obvious upon viewing the data collected for MnPS₃ in the same study. The magnetic unit cell for MnPS₃ has the same dimensions as the nuclear unit cell, and so Kurosawa et al., (1983) proposed a propagation vector of $[0, 0, 0]$. This propagation vector implies that the lattice periodicity is the same as the magnetic periodicity and that magnetic peaks fall on nuclear peaks. While the magnetic reflections for MnPS₃ do lie at the same scattering angles as nuclear peaks, they do not fall on every nuclear

peak. The effective propagation vector to describe the magnetic structure would be $[1,1,0]$. That is, the magnetic reflections occur at scattering angles that correspond to superlattice reciprocal lattice positions rather than the fundamental reciprocal lattice positions. There are magnetic reflections only at these reciprocal lattice points simply because if there were magnetic reflections at all points the effective magnetic propagation vector would be $0,0,0$ and the structure would be ferromagnetic. So, for MnPS_3 the magnetic propagation vector is $1,1,0$ (and $-1,-1,0$; $1,-1,0$; $-1,1,0$).

For FePS_3 , Kurosawa took the same approach as above, and assumed that if the interaction between layers of iron was antiferromagnetic then the propagation vector must indicate the doubling of the nuclear unit cell. From this, they proposed a propagation vector of $[0,0,1/2]$, despite the difference in the in-plane structures of FePS_3 and MnPS_3 . What Kurosawa failed to see was that when there are two types of point in reciprocal space, the propagation vector follows from the fundamental reciprocal lattice position at $0,0,0$.

From this data, Kurosawa et al. (1983) proposed a number of magnetic moment structures. The configuration most favored can be seen in Figure 3.8a below and resembles the proposed magnetic moment arrangement derived by Le Flem et al. (1982).

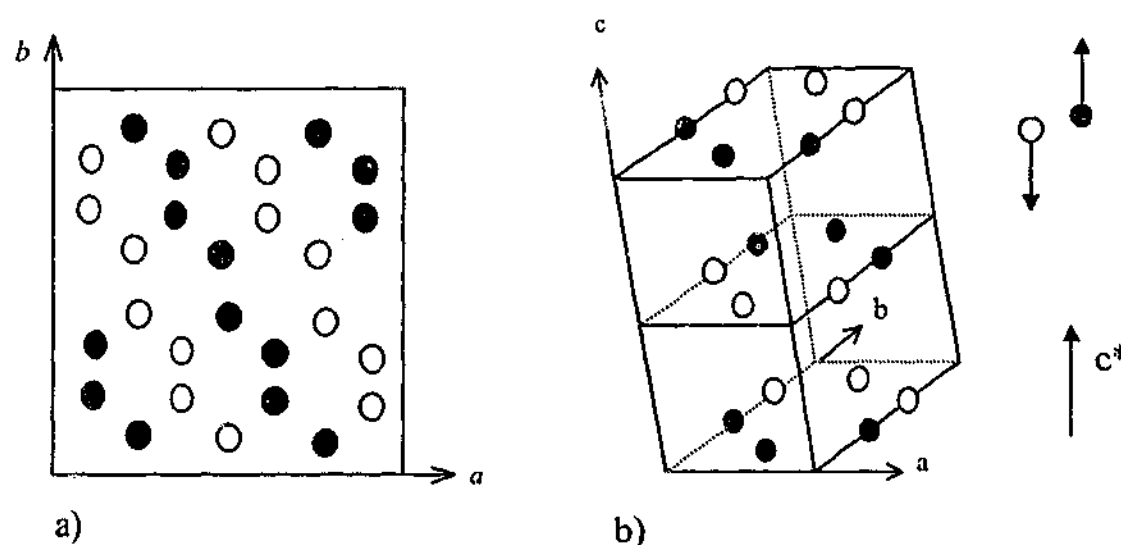


Figure 3.8: Magnetic structures of FePS_3 as determined from neutron diffraction studies. a) shows the in-plane structure of Le Flem et al. (1982) and Wiedenmann et al. (1981), while b) shows the structure of Kurosawa et al. (1983).

The in plane propagation vector for Kurosawa's structure appears to be $(hk) 0l$ and by doubling the crystallographic unit cell in the c^* -direction the full propagation vector should have been $[0,1,1/2]$ rather than the published value of $[0,0,1/2]$. It appears as though the propagation vector of $[0,0,1/2]$ was chosen to correspond with the structure proposed by Le Flem et al. (1982), which is double the nuclear unit cell along the c^* -direction. This arrangement of moments in the plane is the same as that observed for FePSe_3 by Wiedenmann et al. (1981) except for the difference between the a and b directions in the rhombohedral FePSe_3 structure compared with the monoclinic FePS_3 structure.

However, the magnetic structure that was finalised by Kurosawa et al. (1983) is seen in Figure 3.8b, which is slightly different to the in-plane structure of Le Flem et al. (1982). This is the structure that corresponds to a propagation vector of $[0,1,1/2]$, and is a 60° rotation from Le Flem's in-plane structure of ferromagnetic chains coupled antiferromagnetically with each other in the plane, with planes coupled antiferromagnetically to each other.

So although Kurosawa et al. (1983) performed calculations investigating the magnetic form factor and the magnitude of the magnetic moment using the structure of Le Flem et al. (1982), a slightly different structure was finally attributed to FePS_3 , and it is this structure that has been accepted by many research groups for some time. It is the discovery of these inconsistencies mentioned previously that has led the current work investigating the magnetic structure of FePS_3 more carefully.

CHAPTER FOUR

4: Sample Preparation

4.1 CRYSTAL GROWTH

For high purity crystals, ultra high purity starting materials were obtained. Stoichiometric quantities of 99.999% Fe, 99.995% P and 99.99% S powders were measured by weight, and mixed in a quartz ampoule of length 30 cm, with an internal diameter of 10 cm. Samples were created from typically 3-6 g of starting material with around 5-10% extra sulphur added as transport agent (Brec et al., 1980). All residual air was removed from the ampoule via a vacuum pump, which reduced the interior atmosphere to around 10^{-6} torr. The tube was flushed with argon 3-5 times to reduce the amount of oxygen in the tube. Finally the ampoule was sealed such that a vacuum of 10^{-6} torr remained.

The method of chemical vapour transport was used to create crystals of FePS_3 . The quartz ampoule was placed in a 2-zone furnace with the powdered sample at the hot end, which was set to 690°C (Figure 4.1). The cool end was set to 630°C such that the temperature gradient was 2° per cm of quartz. The sample was left for two weeks and then cooled gradually.

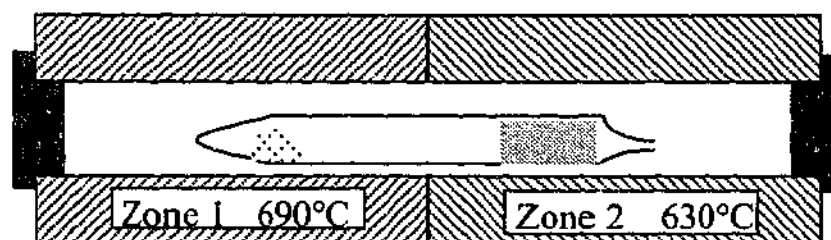


Figure 4.1: Two zone furnace used for crystal growth. The powdered sample began at the hotter end (Zone 2), and crystal nucleation occurred on the inside wall of the quartz tube at the cooler end (Zone 1).

Very thin, platelet samples formed around the inner edges at the cool end of the tube. These were removed by breaking the tube. Crystal sizes ranged from tiny, almost powdered pieces, to around $20 \times 20 \times 0.1$ mm. Many of the larger crystals were partly shaped like a hexagon in the

xy-plane, with an angle of approximately 120° between segments. Observations with an optical microscope revealed a lined texture parallel to the edges of the crystal, such that it appeared as though many hexagons were drawn on the surface. Similar sketches have been drawn in an earlier paper detailing the structure of FePS_3 (Klingen et al., 1973a).

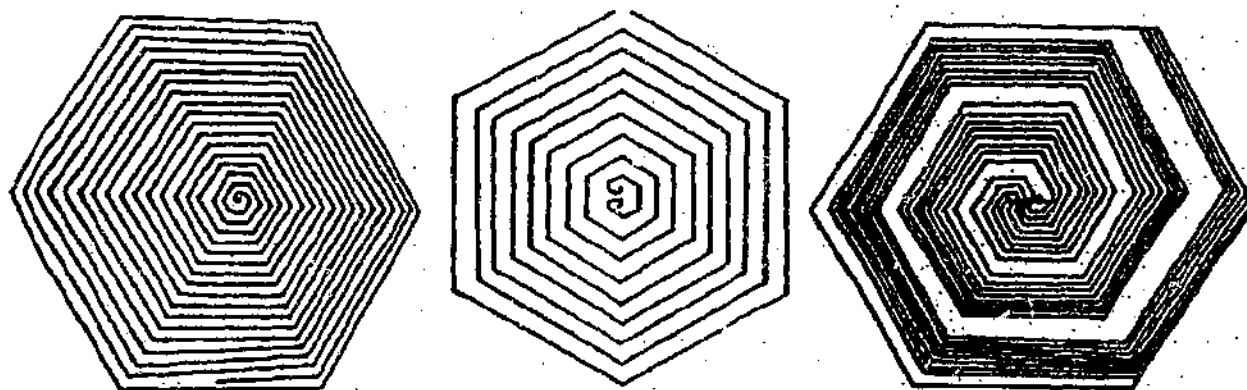


Figure 4.2: Diagram of the hexagonal structures on the surface of the crystals (Klingen et al., 1973a).

4.2 INITIAL CRYSTALLOGRAPHIC ANALYSIS

Preliminary x-ray diffraction measurements were conducted on crushed crystals from each sample set using a Scintag Pad5 high resolution x-ray diffractometer. This was to confirm that the correct phase had been obtained with no extra phases or contaminants. Crystals were placed onto a specimen holder, which was scanned at 2° per minute with step lengths of 0.03° . A typical x-ray diffraction spectrum can be seen in Figure 4.3.

As can be seen, two slightly different templates were found to describe each of the peaks in the powdered sample pattern; FePS_3 and $\text{Fe}_2\text{P}_2\text{S}_6$. Both, however, represent the same phase and are identical in their crystallographic structures. The only difference in the observed reflections between these templates lies in the form of the sample and preferred orientation in FePS_3 . The first template of FePS_3 , was produced from powder diffraction (Taylor et al., 1973; Brec et al., 1980) while the second template was classified as $\text{Fe}_2\text{P}_2\text{S}_6$ from single crystal studies (Klingen et al., 1970, 1973a; Brec et al., 1979). The second template is the more detailed and includes almost all of the peaks observed in the first structure. The discrepancy between the number and intensity of the peaks could be due to strong preferred orientation of platelets in the powdered samples. As this particular compound is tightly bound in the *ab*-plane and less tightly bound along the *z*-axis,

the compound forms platelets which, when compacted would prefer to stack along the *ab*-plane rather than randomly. In both templates the crystallographic unit cell was determined to be exactly the same size, which is another indication that the two templates describe the same structure.

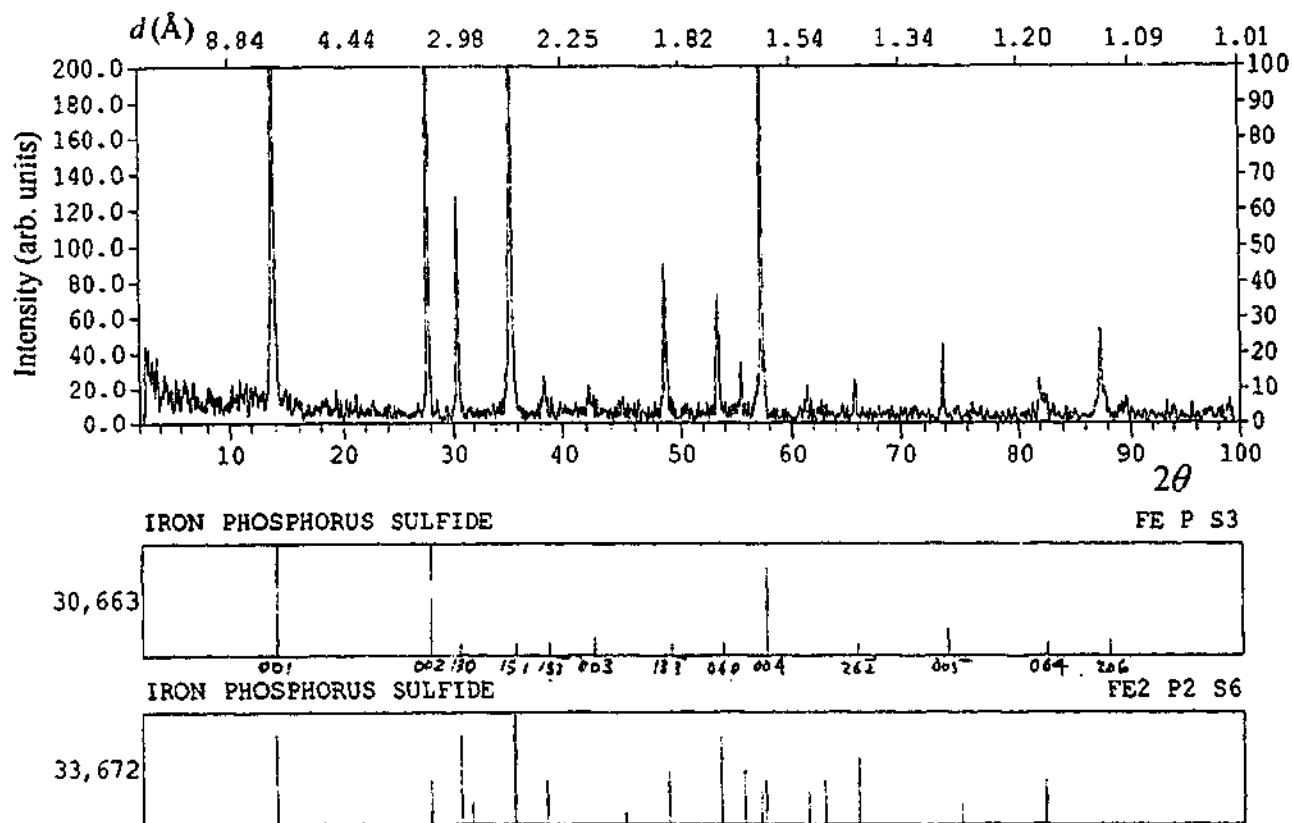


Figure 4.3: A typical x-ray diffraction spectrum for FePS₃. The vertical markers below the pattern indicate where the expected peaks for this compound should lie.

4.3 EXPERIMENTAL PROCEDURES

A variety of experimental techniques were used to characterise the crystals. In some situations, powdered samples were needed, and in others, a single crystal was used. The smaller flakes that grew around the edge of the quartz tube were used for the crushed samples. These were ground between a pestle and mortar until a reasonably fine powder was obtained. Single crystals were chosen from the larger samples, with care taken to select samples that were not bent or damaged. Crystals that showed a high degree of hexagonal structure were also considered preferable over crystals with rough edges.

4.4 SQUID MAGNETOMETRY

The SQUID (Superconducting QUantum Interference Device) magnetometer was used to investigate the magnetic properties of a sample under magnetic fields of varying strength and direction. One of the most sensitive devices for measuring magnetic fields, the SQUID takes measurements by moving a sample through superconducting detection coils (Mc Elefresh, 1994). Temperature is a controllable variable in the SQUID, and can thus be used to determine the susceptibility of certain materials (usually within the range of 5K to 300K).

A single crystal with a diameter around 5 mm was chosen for use in the SQUID magnetometer. To take measurements both parallel and perpendicular to the moment direction, two Teflon sample holders were made to accommodate the crystal (Figure 4.4). The sample holders were cylindrical and fit snugly within a drinking straw at the end of the sample rod, such that the sample was within the detection region at the bottom of the SQUID.

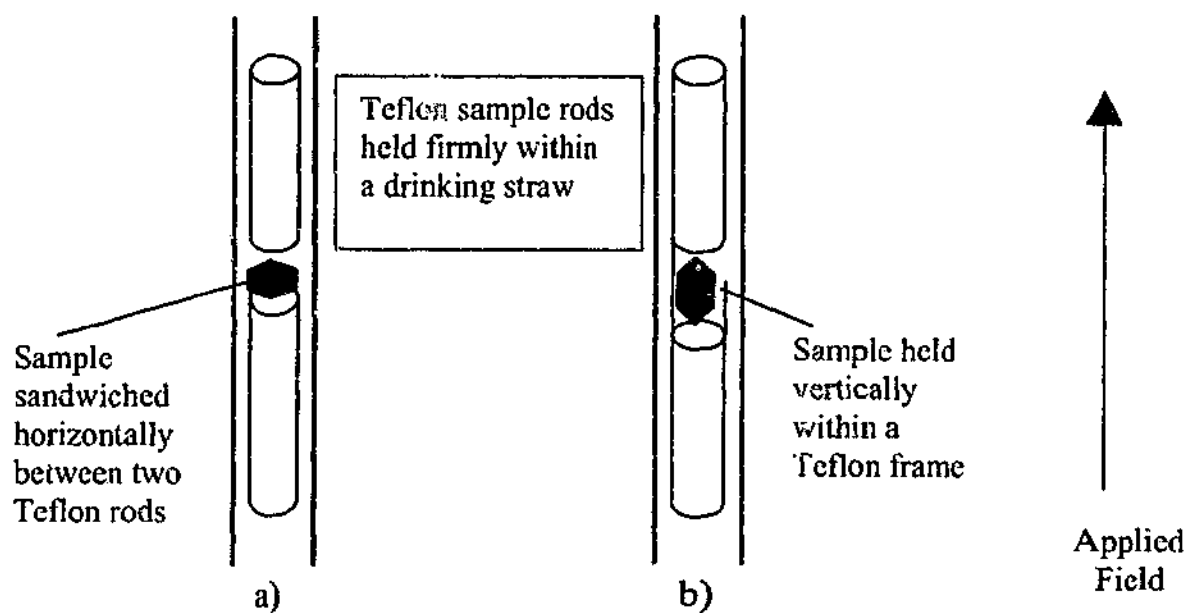


Figure 4.4: Sample holders for the SQUID magnetometer. The crystal sample was aligned with its c^* -axis parallel (a) and perpendicular (b) to the applied field direction.

The Quantum Design MPMS-7 SQUID magnetometer was filled with liquid helium to produce a base temperature of 4.2 K. The sample was inserted with the ab -plane both parallel and perpendicular to the applied field direction, and the susceptibility was measured over the temperature range of 5-300 K. Samples were either cooled to 5K with an applied field (Field

Cooled) or in the absence of an applied field (Zero-Field Cooled). The applied field ranged between 0.06 T and 0.6 T between successive measurements but remained constant throughout each measurement.

4.5 HIGH FIELD MAGNETISATION MEASUREMENTS

Small single crystal samples were cut to a diameter of around 3mm and stacked together to create a large enough sample for use in the pulsed-field magnetometer. The sample was oriented such that the field was applied along the common c^* -direction of each of the crystals. The magnetization was measured using a pulsed magnetic field at the University of Amsterdam with a semi-continuous magnetic field of up to 40 T. This field was pulsed for a total duration of several hundreds of milliseconds with field levels constant to within around 20 mT of the set value (Amsterdam, 2000).

The temperature of the sample remained constant for each measurement in which the applied field was increased from 0 T to 38 T. The temperatures for each run ranged from 5.5 K to 147 K. Magnetisation measurements were taken to observe the change in magnetisation with respect to the applied field. This was used to determine the magnetisation at which the metamagnetic phase changes occurred in FePS_3 , as reported by Okuda et al. (1983). This experiment was also conducted to determine if a spin-flop transition would be observed in applied fields of up to 38 T.

4.6 MÖSSBAUER SPECTROSCOPY

A variety of samples were made for Mössbauer spectroscopy data collection. One absorber was prepared by mixing crushed crystals with boron nitride powder. This mixture was placed into a 13 mm diameter, Perspex sample holder for use in the Mössbauer rigs. The thickness of this absorber was around 0.5 mm.

A single thickness of FePS_3 with a diameter less than 13 mm was chosen for single crystal Mössbauer measurements. The crystal was oriented in two different ways – flat within the sample holder such that the face of the crystal could be aligned perpendicular to the γ -ray

direction, and on a Perspex wedge such that the normal to the crystal face was aligned 17° from the γ -ray direction (Figure 4.5).

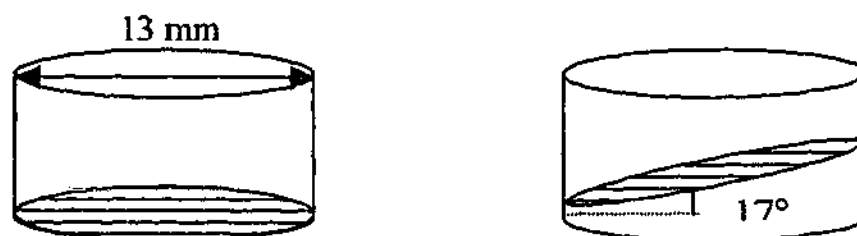


Figure 4.5: Single crystal sample orientations in 13 mm diameter sample holders for Mössbauer spectroscopy experiments. Left is the usual orientation, and right is the tilted orientation.

An oscillating $^{57}\text{CoRh}$ source, of between 13 and 50 mCi, was used for each experiment, emitting 14.4 keV γ -radiation. The velocity of the source was calibrated with an α -iron foil at room temperature. The velocity waveform was triangular shaped (constant acceleration) and the spectra were collected across 512 channels for a folded spectrum. Typical counting times were between 1 and 5 days.

Three different Mössbauer experiments were conducted using transmission geometry. The source oscillated either vertically or horizontally, depending on the experimental set up. Low temperature and room temperature measurements were taken, in which the face of the sample holder (and therefore the ab -plane of the single crystal) was perpendicular to the gamma ray direction. The second of the experiments involved the same orientation of the samples in applied magnetic fields of 10 T and 14 T. The third set of experiments explored the effects of a tilted sample on the Mössbauer hyperfine parameters. This included a study of the Goldanskii-Karyagin Effect (GKE) and an investigation into the direction of the EFG with respect to the gamma ray direction.

Both powdered and single crystal samples were investigated at room temperature, as well as temperatures below the Néel temperature, including 96 K and 10 K. These temperatures were reached by loading the sample into a cryostat filled with liquid nitrogen and liquid helium respectively. The source to sample distance was calculated to optimise the intensity of the beam without line broadening effects. In room temperature samples with a 6 mm source diameter, and a 7.6 mm sample diameter, the typical source to sample distance was around 78 mm.

These same samples were also measured in a cryostat surrounded by a variable magnetic field aligned parallel to the γ -ray direction. As a superconducting magnet was responsible for the applied field, all magnetic field measurements were taken at 10 K.

GKE measurements were conducted using a sample-frame oriented at the "magic angle" of 54.7° . The sample was aligned with the oscillating source such that the centre of the γ -ray beam was directed through the centre of the vertical component of the sample. Between each of four successive spectra, the sample was rotated by 90° . Care was taken to ensure that each spectrum had the same number of counts and could thus be added together.

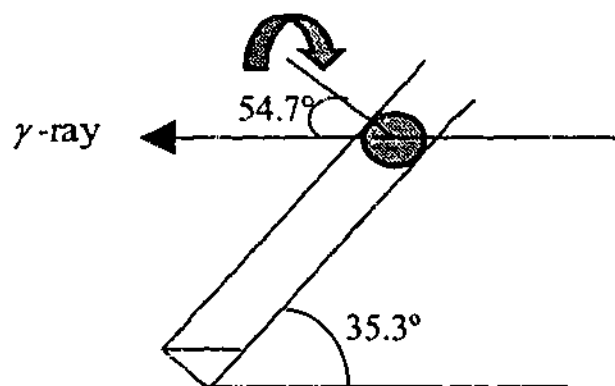


Figure 4.6 Sample set-up for the GKE Mössbauer spectroscopy experiment

To investigate the GKE completely, multi temperature measurements could be taken. These were not performed due to lack of instrumentation. By heating a sample, the asymmetry of the lines would change, as the atoms were forced to vibrate more. Texture effects are not temperature dependent, so any variation in the asymmetry with changes in temperature would indicate the presence of GKE in the sample.

The direction of the principal axis of the EFG was investigated using a single crystal sample mounted on a 17° wedge. The sample was oriented such that the crystallographic a -axis was aligned directly up or down the wedge, such that there was a variation in the c -axis. The wedge angle of 17° was chosen as this was the angle between the c and c^* axes. Thus in one sample position, the γ -ray was parallel to the crystallographic c -direction.

4.7 NEUTRON DIFFRACTION

Two different samples were required for neutron diffraction experiments. The first was used in the experiments conducted at the Lucas Heights Research Laboratories in Sydney, Australia, and was essentially a randomised powdered sample. Effort was made to reduce the effects of the preferred orientation in the sample. Pressing the crushed crystals into pellets, three cylinders were made. Each cylinder had a diameter of 10 mm and a length of around 12 mm. The mass of material in each cylinder was 1.67 ± 0.05 g.

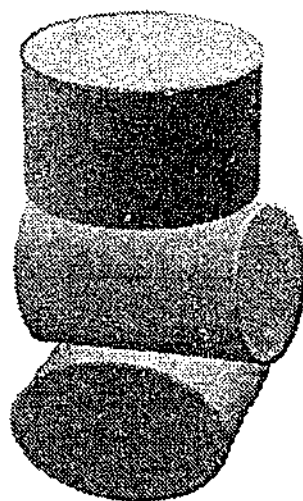


Figure 4.7: Stacking of the crushed FePS_3 crystal for MRPD data collection.

Due to the stacking nature of the pressed FePS_3 platelets, it was assumed that each cylinder had a significant proportion of crystallites aligned with their z-axis vertical. Thus, to average the orientation effects, the cylinders were stacked with their axes mutually perpendicular. These can be seen in Figure 4.7 above.

4.7.1 Medium Resolution Powder Diffractometer (MRPD)

The MRPD, at the Lucas Heights Research Reactor in Sydney, Australia was used for initial powder diffraction experiments of FePS_3 . This device consists of eight germanium monochromator crystals, which restrict the white neutrons from the reactor to a single, monochromatic wavelength for experiments. The wavelengths for this device range from 1.06 \AA

to 5.0 Å, and the detectors can register the intensity variation of the scattered neutrons through an angular 2θ range of 4° to 138° . The sample environment within the MRPD can also be changed, by adding devices to control the temperature, pressure or magnetic field at the sample position. A schematic aerial view of the MRPD can be seen in Figure 4.8 below.

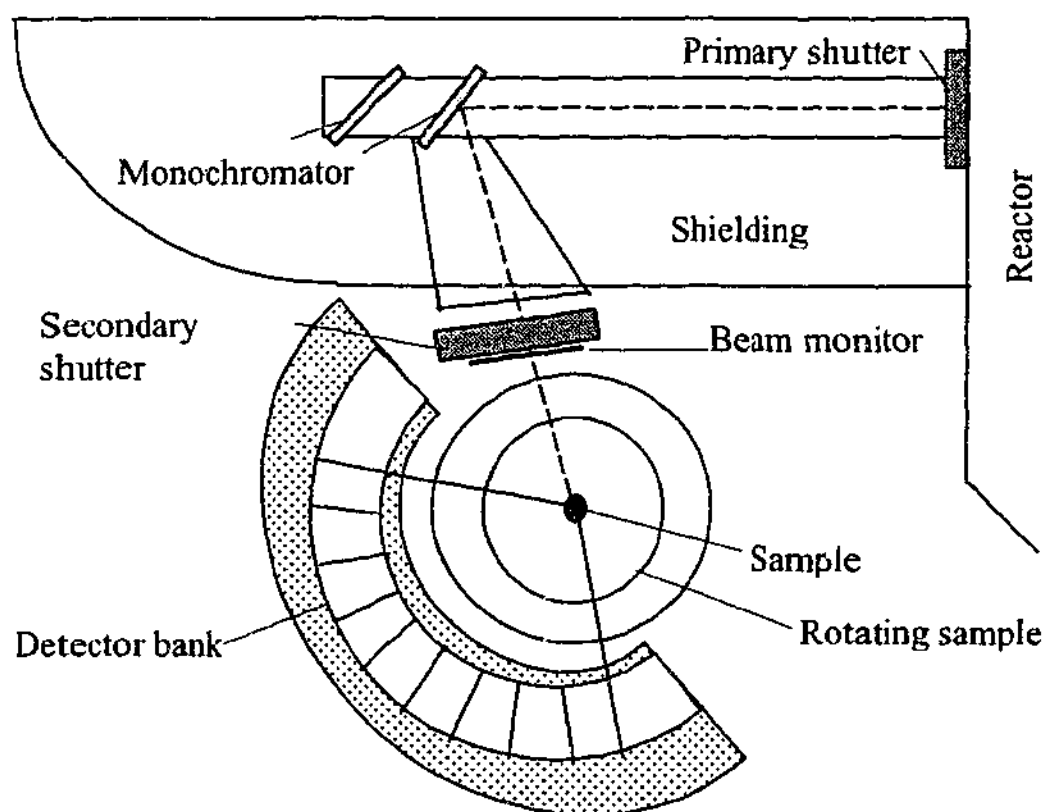


Figure 4.8: Schematic diagram of MRPD located at the Lucas Heights Laboratories, Australia.

The MRPD is located around the shell containing the HIFAR reactor, which is short for the High Flux Australian Reactor. The HIFAR reactor at Lucas Heights has a flux of neutrons with up to 1×10^{14} neutrons/cm²/second, with the intensity of the beam on the MRPD being 4×10^5 neutrons/cm²/second (ANSTO, 2003). Thus the MRPD is used to obtain medium resolution scans in relatively short collection times.

The neutron wavelength was initially adjusted to 1.666 Å. Room temperature experiments were conducted with the three pellets encased in a vanadium sleeve, and rotated on the sample stage throughout data collection. For low temperature experiments, the sample was held together

with a thin sheath of aluminium foil and mounted in a Heliplex cryo-refrigerator. Scans were taken at temperatures between 4 K and 130 K to observe the phase change between the antiferromagnetic and paramagnetic states. The cryo-fridge was rotated during data collection such that an average signal from all regions of the sample was obtained. This involved taking shorter scans at different incident angles and summing them to achieve an overall randomisation similar to the room temperature scans. Each temperature scan took around 10 hours.

Scans were also taken at different wavelengths up to 5.0 Å. Increasing the wavelength increased the resolution of the low scattering angle magnetic peaks. Each of these scans was taken at 4 K for maximum magnetic intensity.

4.7.2 LONG Wavelength POLarisation-Analysis Spectrometer (LONGPOL)

LONGPOL is another device at the Lucas Heights Research Reactor that was used to investigate FePS₃. As suggested by the name, LONGPOL uses long wavelength neutrons of 3.6 Å, which are polarised via supermirror devices with over 94% polarisation efficiency (ANSTO, 2003). This spectrometer has eight supermirror detectors that can register the polarisation state of the scattered neutrons. LONGPOL is used as a time-of-flight (TOF) spectrometer, and incorporates a spin-flipper to control the polarisation direction of the incident neutrons. These devices allow LONGPOL to be used in experiments involving changes in momentum, polarisation and energy of the neutrons after interaction with the sample. A birds-eye view of LONGPOL can be seen in Figure 4.9.

Two experiments were conducted using LONGPOL. The first was an energy analysis of the low scattering angle magnetic peaks, and the second involved a study of magnetic spin diffusion in the paramagnetic state.

For the initial energy analysis experiment, two FePS₃ pellets were stacked vertically, perpendicular to the scattering plane. The sample holder was placed in a cryo-fridge and measurements were taken at temperatures ranging from 13 ± 1 K to room temperature. The polarisation of the neutrons was rotated adiabatically such that the spin polarisation was parallel to the scattering vector for the middle of the eight detectors in the ³He detector bank (Figure 4.10).

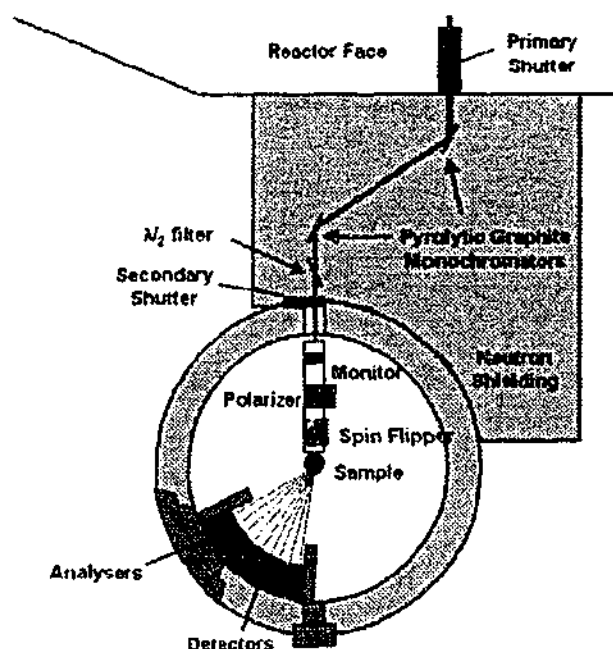


Figure 4.9: Schematic diagram of LONPOL (ANSTO, 2003)

The magnetic field used to rotate the neutron spin was approximately 0.02 T – strong enough to maintain the neutrons, yet weak enough to have negligible effect on the sample. The effect of this field can be seen in Figure 4.10, where it is applied parallel to the scattering vector and perpendicular to the polarisation direction. The detector bank was rotated between scans to collect a range of magnetic and nuclear intensities between Q values of 0 and 1.8 \AA^{-1} .

Only magnetic moments perpendicular to the scattering vector will scatter the neutrons. Magnetic moments perpendicular to the polarisation axis will result in a spin flip of the neutrons, while nuclear scattering will not flip the spins. Thus, when the polarisation axis was arranged parallel to the scattering vector, all the magnetically scattered neutrons were spin-flipped; while the nuclear scattered neutrons remained in the original orientation.

Energy analysis was conducted at temperatures below the Néel temperature, to observe magnons within the sample. As the energy of the incident neutrons was 6.3 meV, it was more appropriate to register an energy gain for the time of flight measurements. For this reason a maximum number of magnons were required within the lattice such that the energy was transferred to the scattering neutrons. Thus the temperature was maintained within 1 K of 100 K, so that the sample was magnetically ordered, yet energetic enough for a maximum occupancy of magnons. Therefore the neutrons could scatter with an energy gain.

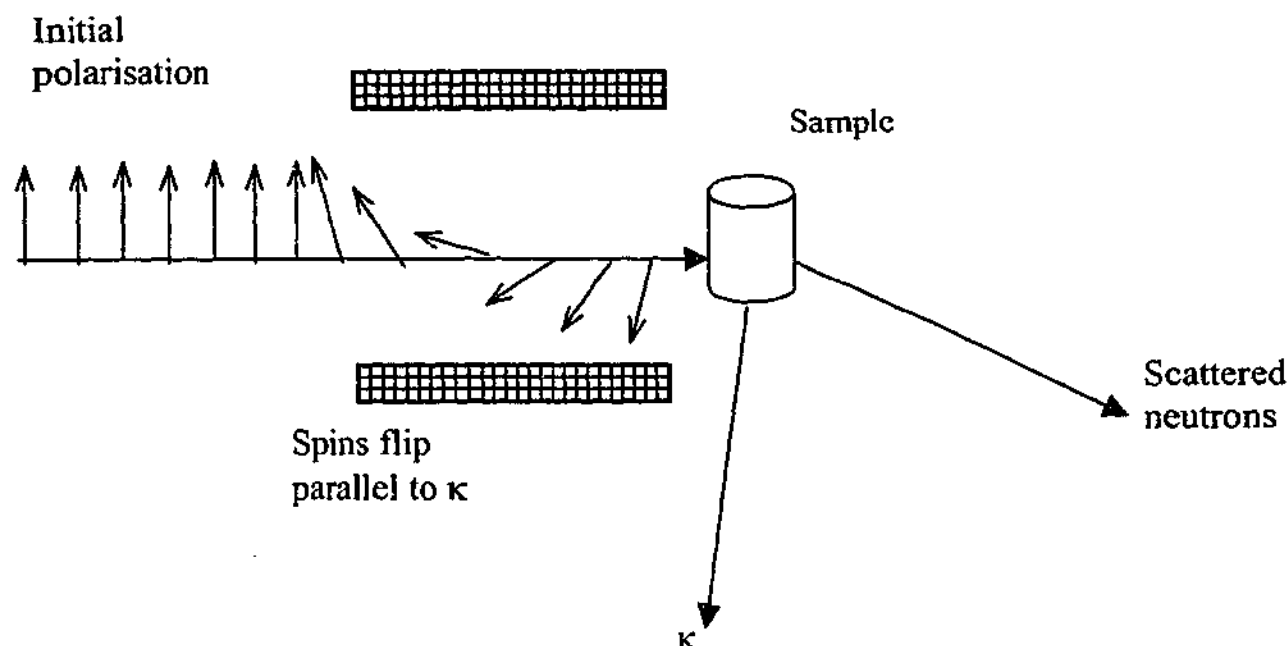


Figure 4.10: Rotation of the polarisation axis to align parallel with the scattering vector, κ .

Each scan was analysed according to its time of flight spectrum by performing a cross correlation between the spin flipper state and the detected neutron intensity. From this investigation, significant peaks could be classified as spin flip (magnetic) or non-spin flip (nuclear) and elastic or inelastic.

The spin diffusion experiment involved a similar experimental set up to that mentioned previously. In this experiment, measurements were taken with the polarisation axis aligned either parallel or perpendicular to the scattering vector so that the ratio of the spin-flipped and non spin-flipped neutrons in each orientation could be compared. Initially the sample, consisting of three FePS_3 pellets, was mounted in the centre of a small four-coil electromagnet. This was placed in the beam of neutrons with a small field applied for the parallel polarisation and the field removed for the perpendicular. However, preliminary tests indicated that the electromagnet did not produce a field over sufficient path length to rotate the polarisation axis adiabatically. The magnet was also found to retain a remanent field when the current was removed. Due to these inconsistencies, the applied field was produced by a permanent magnet and only two pellets formed the sample. Therefore only the parallel part of the experiment was conducted. The applied field was around 0.03 T and measurements were taken at 150 K, 200 K and 250 K.

Results taken below the Néel temperature in the elastic region were analysed using a maximum entropy package to determine the energy width of the magnetic Bragg peaks. This

program fitted the data by removing all instrumental uncertainties rather than applying a model of predetermined line shape. The LONGPOL data taken above the Néel temperature was initially analysed using cross-correlation and the observed peak distribution was then calculated via Fourier transforms to ascertain the diffusion rate of moments through the lattice. The maximum entropy package could not be used to reconstruct inelastic data, as it does not accurately calculate errors from the data.

4.7.3 Very Intense Vertical Axis Laue Diffractometer (VIVALDI)

VIVALDI is the newly built vertical axis Laue diffractometer at the Institut Laue-Langevin (ILL) in Grenoble, France.

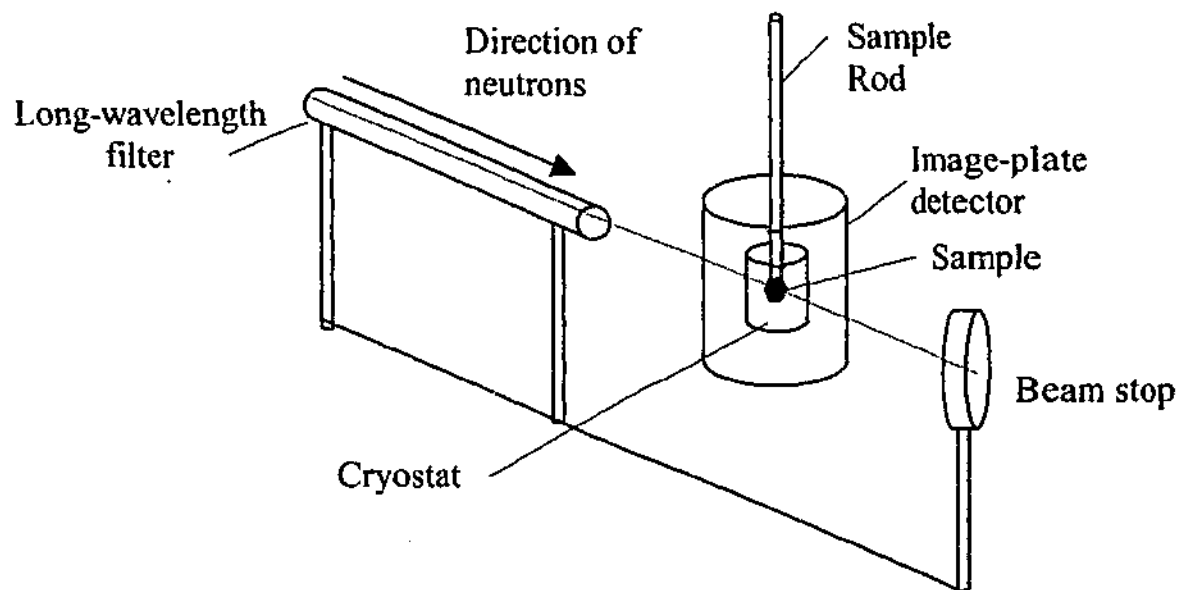


Figure 4.11: A schematic view of VIVALDI

VIVALDI consists of a white thermal beam of neutrons with a wavelength range between 0.8 - 4.5 Å (ILL-VIVALDI, 2003). This device is used primarily for single crystal diffraction. A single crystal sample of FePS_3 was attached to a vertical sample rod, which was inserted into the cryostat for data collection (Figure 4.11).

The sample used at the Institut Laue-Langevin was in fact a large single crystal chosen for its visible hexagonal structure. The approximate size of this crystal was 10×7 mm in the *ab*-plane. This was attached to a small specimen pin for the duration of all experiments on both VIVALDI (the Very Intense Vertical Axis Laue Diffractometer) and D19 (a 4 circle, single crystal diffractometer). An aluminium sleeve was placed around the sample before it was placed into the cryostat.

For each crystal position, Laue images were recorded at two temperatures, 5 K and 140 K. The crystal was rotated between each data set to obtain different families of reflections and therefore to assist in fitting a monoclinic model to the diffraction patterns. The fitting program Lauegen from CCLRC, Daresbury (Campbell, 1995) was used to fit the nuclear peaks to the data. The magnetic peaks observed in the 5 K patterns were also modelled, by assuming that the magnetic unit cell was a direct multiple of the nuclear unit cell.

4.7.4 D19 – The four circle diffractometer

D19 at ILL is a single crystal diffractometer with a working wavelength range of 1.0 to 2.4 Å. It comprises a banana shaped position sensitive detector set symmetrically about the straight through beam position as seen in the side view of Figure 4.12.

This detector measures 2D areas from the sample and is particularly good at investigating crystals with large unit cells, typically larger than 20 Å. D19 is located at the reactor face and utilizes high flux monochromatic neutrons with a flux of up to 10^7 neutrons/cm²/second (ILL-D19, 2003).

The sample rod containing the single crystal sample was placed within the rotating sample stage on D19. The strong intensity nuclear peaks were found and the peak assignments from the VIVALDI plots were used to calibrate the crystal in reciprocal space. The crystal was then cooled to 20 K and the *hkl* positions of possible magnetic peaks were scanned. Due to time constraints, only some magnetic peaks were found. These were located in the vicinity of the strongest magnetic peaks found and labelled with VIVALDI and Lauegen. The intensity of these reflections along the crystallographic *c**-axis was recorded.

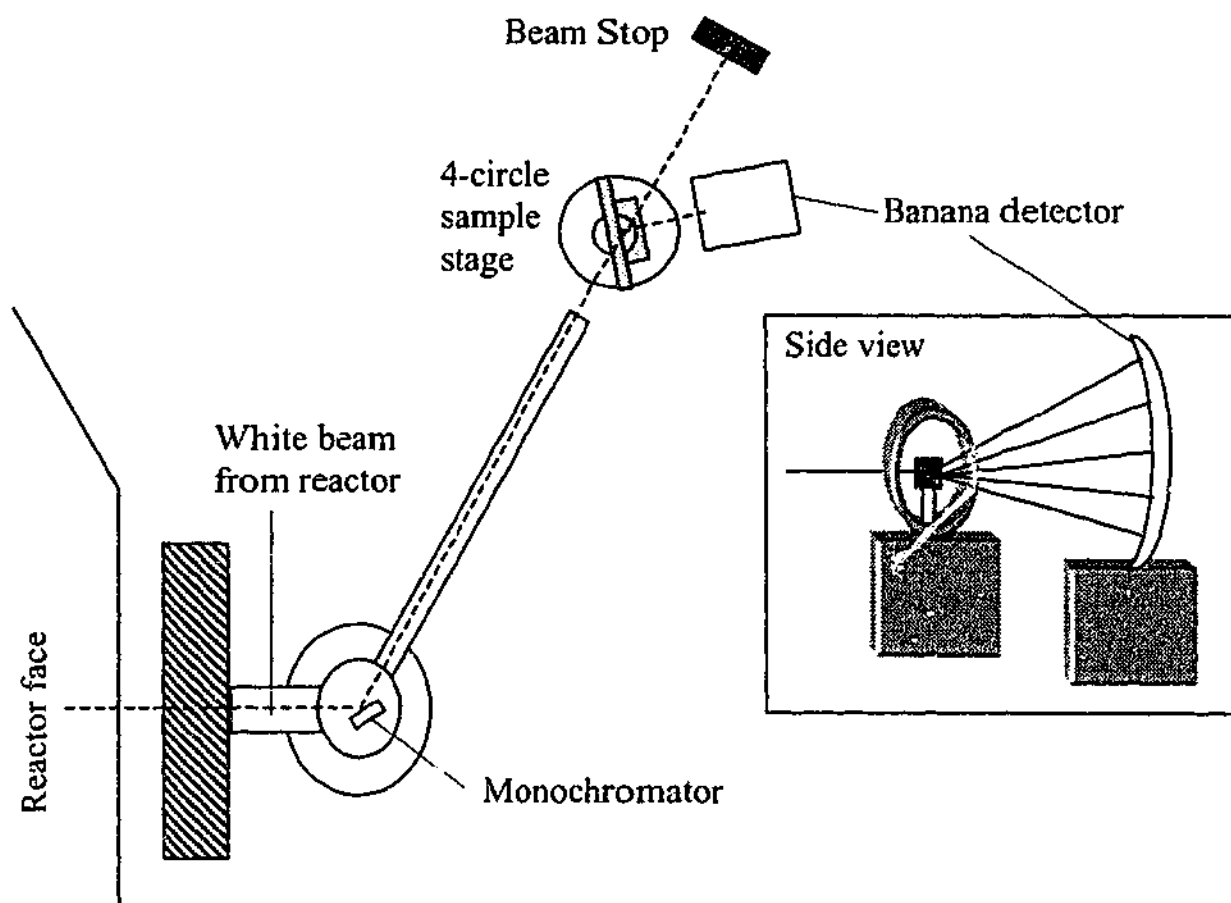


Figure 4.12: Birds-eye view of D19, the four-circle monochromatic diffractometer.

CHAPTER FIVE

5: Results and Discussion of Magnetometry and Mössbauer Spectroscopy

SQUID magnetometer results such as susceptibility measurements were used to analyse the bulk magnetic properties of a single crystal of FePS_3 . By changing the sample orientation within the SQUID, the applied field could be varied relative to the crystallographic and magnetic axes. Using the sample holders in Figure 4.4, the applied field could be oriented either parallel or perpendicular to the crystallographic c^* -direction; that is, parallel or perpendicular to the plane of the crystal. The c^* -axis is an important reference as it corresponds to the previously reported magnetic moment direction (Le Flem et al., 1982; Okuda et al., 1983). Susceptibility measurements taken with the sample in either of the above orientations could reveal information about the behaviour of the moment sublattices in an applied field. Susceptibility measurements can be used to map out phase transitions in magnetic materials. Phase transitions occur when the magnetic moment structure is affected by changes in the applied field or sample temperature.

For antiferromagnetic materials, the strength of the interactions between the moment sublattices can be investigated from the analysis of susceptibility data. This can reveal information about the anisotropy energies and exchange parameters of a material. Thus susceptibility measurements from the SQUID can give much information about the magnetization and bulk magnetic properties of FePS_3 .

5.1 MAGNETIC SUSCEPTIBILITY OF FePS_3

Susceptibility measurements of a single crystal sample were performed from 5 – 300 K with applied fields ranging from 0.06 – 0.6 T. The susceptibility, taken with a field of 0.06 T applied perpendicular (\perp) to the c^* -direction, can be seen in Figure 5.1. The circles represent the susceptibility taken for zero-field cooled data (ZFC) while the squares represent the field cooled

(FC) results. Marked on the graph in Figure 5.1 are the temperature at which there is a maximum susceptibility, T_{max} , and the magnetic ordering temperature, T_N .

The FC sample was cooled to 5 K in a constant applied field of 0.06 T and both FC and ZFC measurements were taken with increasing temperature. The ZFC and FC observations were similar around the ordering temperature of 120 K suggesting that the susceptibility in this region was independent of the sample's history. Above 150 K, the FC susceptibility remained consistently lower than the ZFC, while below 80 K, the FC was greater than the ZFC. Thus, cooling the crystal below its ordering temperature, in the presence of an external field induced a slightly larger susceptibility. This suggests that cooling in the presence of a field may cause the moments to freeze with some alignment along the direction of the applied field (perpendicular to the c^* -direction), away from their easy axis. This means that a metastable state has been retained in the ordering of the third dimension. This indicates that the magnetic sublattices are possibly not as strongly correlated as for $MnPS_3$, in which the FC and ZFC susceptibilities were identical (Goossens, 1999).

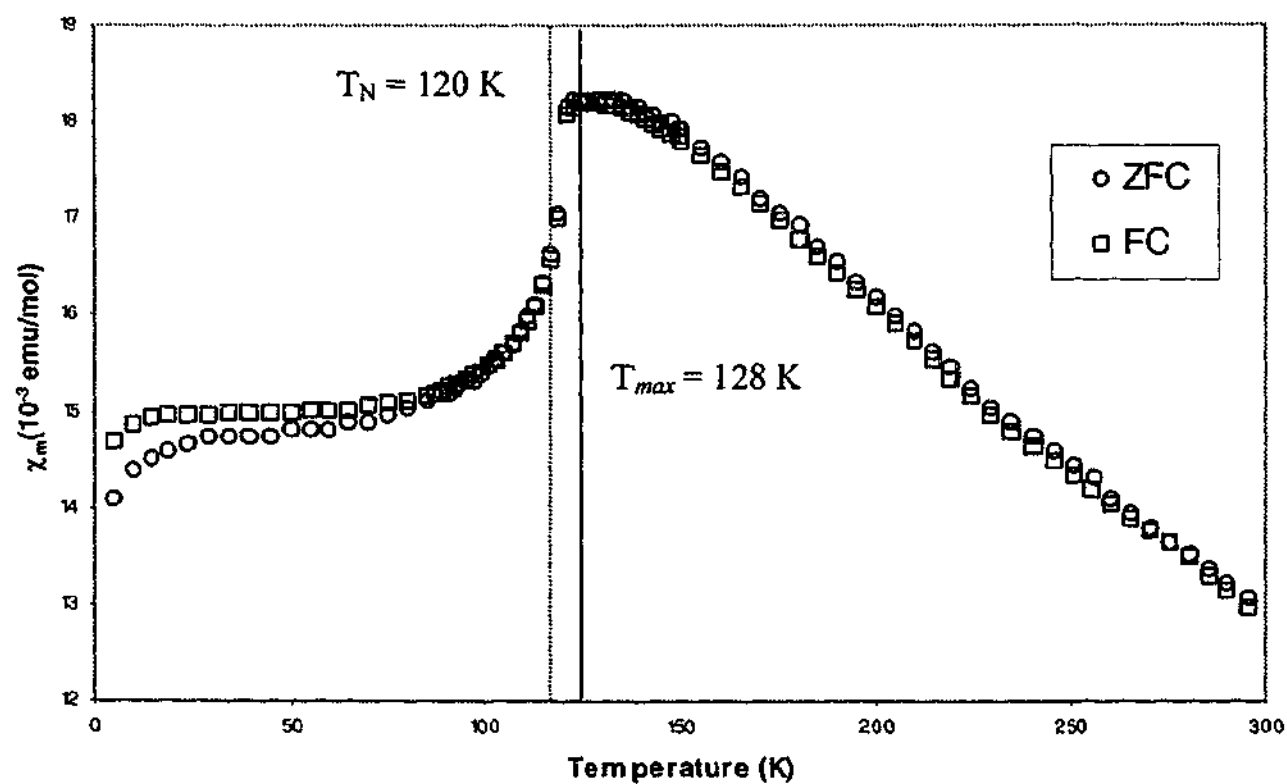


Figure 5.1: Field cooled (FC) and zero field cooled (ZFC) susceptibility measurements for a single crystal of $FePS_3$. The field of 0.06 T was applied perpendicular to the c^* -direction.

The FC susceptibility plots for the applied field parallel (\parallel) to the c^* -direction were also consistently lower than the ZFC plot at temperatures below 50 K, however the deviation was much less pronounced. This supports the supposition of a metastable state with the smaller deviation expected when the external field was applied along the moment's easy axis.

Figure 5.2 shows the comparison between the parallel and perpendicular susceptibility for the ZFC situation. The applied field was 0.6 T, and similar to Figure 5.1, the Néel temperature and maximum susceptibility have been displayed.

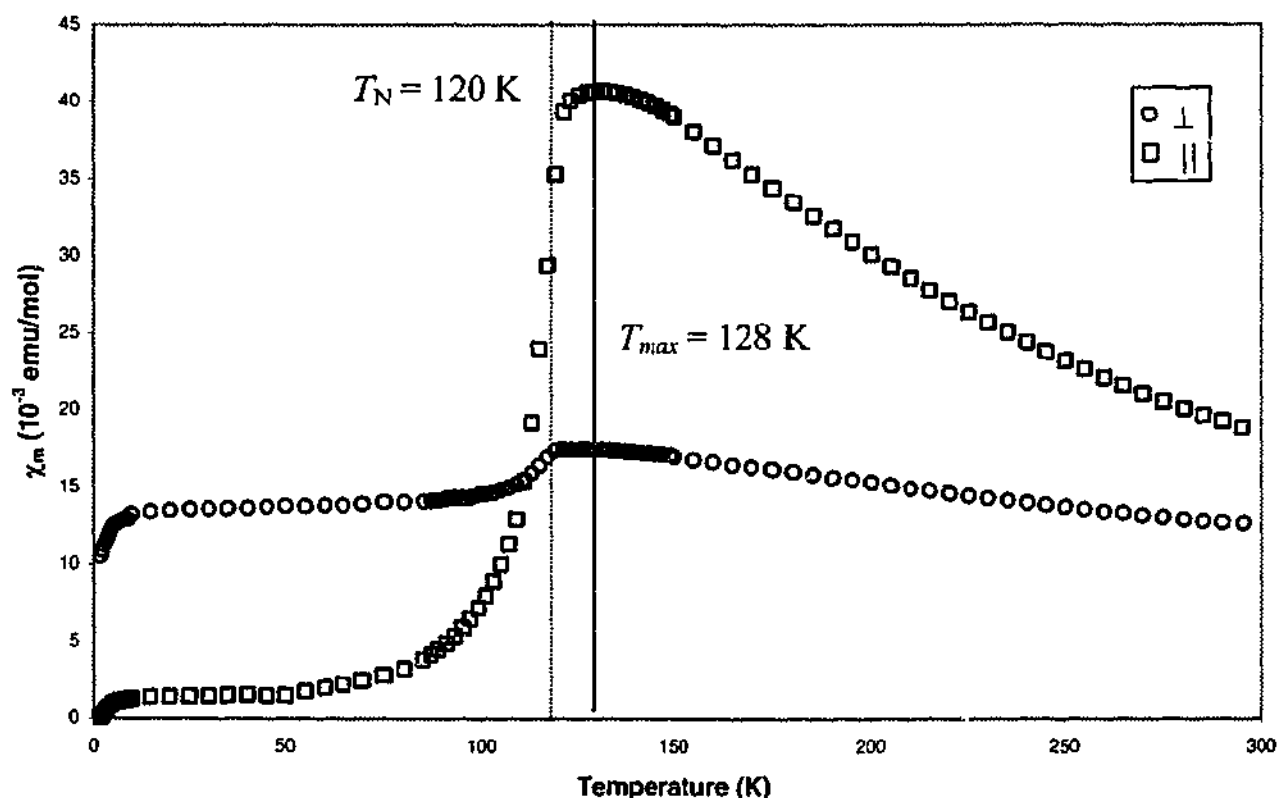


Figure 5.2: Parallel (\parallel) and perpendicular (\perp) susceptibility measurements for ZFC, with $B_{app} = 0.6$ T.

At very low temperatures, the susceptibility appears to decrease sharply in both the parallel and perpendicular sample alignments. The relative gradients for the two data sets were very similar which implies that the effect is not orientation dependent, and may not be related to the sample at all. The SQUID sample environment for both orientations involved a Teflon sample holder of approximately 3-4 cm long. Although the Teflon was chosen as an appropriate sample holder due to its low magnetic signal, it is believed that at low temperatures and such low applied

fields the Teflon signal may dominate over the FePS₃ signal. A susceptibility measurement using only the Teflon sample holder was not conducted to confirm this. However, susceptibility measurements of other samples with the same Teflon sample holders, exhibited a very similar dip, supporting this proposition. Thus it is most likely that the dip at low temperatures is not a product of the material but of the sample environment, and thus can be neglected in the analysis of FePS₃.

The maximum signal for the parallel susceptibility was much larger than that of the perpendicular susceptibility however both sets of data appear to follow the Curie Weiss law in the paramagnetic region, above 200 K. As the value of the crystal field splitting, Δ , is sufficiently large for FePS₃ ($\Delta > 4000$ K), it was considered that the Van Vleck paramagnetism does not play a significant role in the shape of the susceptibility curves. Thus it was not included in the following calculations that arose from the susceptibility data. When the magnetic field was applied parallel to the c^* -direction, and thus parallel to the preferred orientation of the moment, the SQUID measured a stronger response. At these paramagnetic temperatures, the moments are random so the effect of the small, applied field on each moment depends on the interaction with its neighbours. This interaction is the exchange interaction and is strongest in the ab -plane.

As can be seen from Figure 5.2, the point of maximum gradient, indicated as the Néel temperature, was found to occur at 120 K with the peak of the susceptibility at 128 K. This agrees favourably with the previous susceptibility data (Jernberg et al., 1984; Joy & Vasudevan, 1992a; Rao & Raychaudhuri, 1992). The maximum susceptibility is larger than that at the Néel temperature, due to strong intraplanar order persisting after any three-dimensional (3D) order breaks down at T_N . Between 120 K and the maximum susceptibility at 128 K, strong 2D short-range order is still present between the metal ions in the ab -plane. However, beyond 120 K, there is no remaining long-range magnetic order. As the dimensionality of a material is reduced, the susceptibility peak typically becomes broader. Thus the broadness of the susceptibility peak is an indication of the low dimensionality of FePS₃. At temperatures higher than 128 K, the 2D short-range order deteriorates enough that the susceptibility decreases with increased temperature. At around 200 K the susceptibility begins to follow the Curie-Weiss relationship for paramagnets, as described in Equation 1.13.

Extrapolation of these results below 4 K revealed that the parallel susceptibility becomes zero at approximately 1.7 K while the perpendicular susceptibility remains at some non-zero value.

These results followed the expected trend for an antiferromagnet. For a collinear antiferromagnet, the parallel susceptibility is expected to go to zero as T approaches 0. As the field is aligned at angles of 0° and 180° to each of the moment sublattices, it cannot produce a torque on the antiparallel spins. If the field were aligned at some other angle with respect to the moments, then there would be some degree of torque, which could rotate the antiparallel spins, resulting in a non-zero susceptibility.

When the field was applied perpendicular to the moment sublattices, the moments had the freedom to rotate towards the direction of the applied field. A small, applied field may cant the moments towards the applied field direction, giving an overall magnetisation along that same direction. Thus the susceptibility was not expected to reach zero at zero temperature when the field was applied orthogonal to the magnetisation axis. The extrapolated susceptibility for an external field applied perpendicular to the magnetisation axis was determined to be approximately 9.5×10^{-3} emu/mol at 0 K.

It is interesting to note the differences between the susceptibility plots of FePS_3 and MnPS_3 . For comparison, the results of Okuda et al., (1986) for a single crystal of MnPS_3 are shown in Figure 5.3.

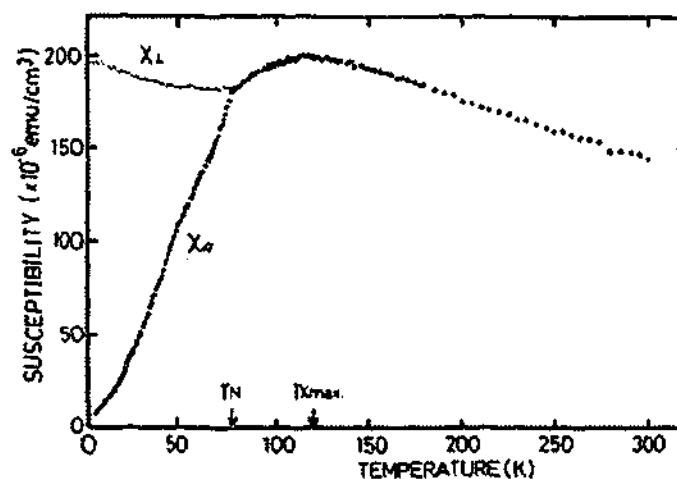


Figure 5.3: Single crystal susceptibility measurements of MnPS_3 taken from Okuda et al., (1986)

In FePS_3 , the peak susceptibility for applied fields parallel to the magnetisation axis reached more than twice that of the perpendicular susceptibility. Above the Néel temperature, the parallel and perpendicular susceptibilities then followed different curves, as opposed to the two

susceptibilities in MnPS_3 , which were identical at temperatures above the Néel temperature. This can be attributed to the anisotropy differences between the two metal ions in the thiophosphate compounds. The Fe^{2+} ion has a much greater anisotropy than Mn^{2+} , due to the extra d -shell electron. Because of this, more energy is required to rotate the Fe^{2+} moments away from their preferred magnetization axis than for the Mn^{2+} ions. Thus the moments are less susceptible to rotate when the applied field is perpendicular to the axis of magnetisation, resulting in a lower overall susceptibility.

5.2 EXCHANGE INTEGRALS IN FePS_3

A plot of the thermal variation of reciprocal susceptibility was created using the data points above 200 K from Figure 5.2. This was considered the paramagnetic region of FePS_3 where the Curie-Weiss law fits the data. For paramagnetic materials, as described by the Curie-Weiss law, the critical temperature occurs at $T = \Theta$, when the susceptibility goes to infinity. This is seen as the temperature intercept of an inverse susceptibility curve. Straight-line inverse susceptibility fits to the FePS_3 data were used to determine the g -factors for both the parallel and perpendicular susceptibilities, according to the method outlined in Niira and Oguchi (1954). These plots can be seen in Figure 5.4.

The inverse susceptibility for the parallel and perpendicular fields have different gradient magnitudes, which are directly related to the Curie constant, C , and therefore the spectroscopic splitting factor, g , according to Equations 1.14 and 1.15. Differing gradients are not unusual for the inverse susceptibilities of an antiferromagnetic material (Niira & Oguchi, 1954). From the slopes of Figure 5.4, the spectroscopic splitting factors for the parallel and perpendicular applied fields were calculated as 2.52 and 3.00 respectively, indicating a significant combined spin and orbital contribution to the angular momentum. However it is interesting to note that the intercepts of the temperature axis are more than 250 K apart, highlighting the extreme anisotropy in this material. The value of the Weiss characteristic temperature, when the field was applied parallel to the magnetisation direction, was $\Theta_{\parallel} = 44.5$ K and $\Theta_{\perp} = -236.5$ K when the field was applied perpendicular to the magnetisation direction. The value of Θ is affected by both antiferromagnetic exchange and single-ion anisotropy, suggesting that the large variation in Θ is probably caused by crystal field effects from the trigonal distortion of the FeS_6 octahedra.

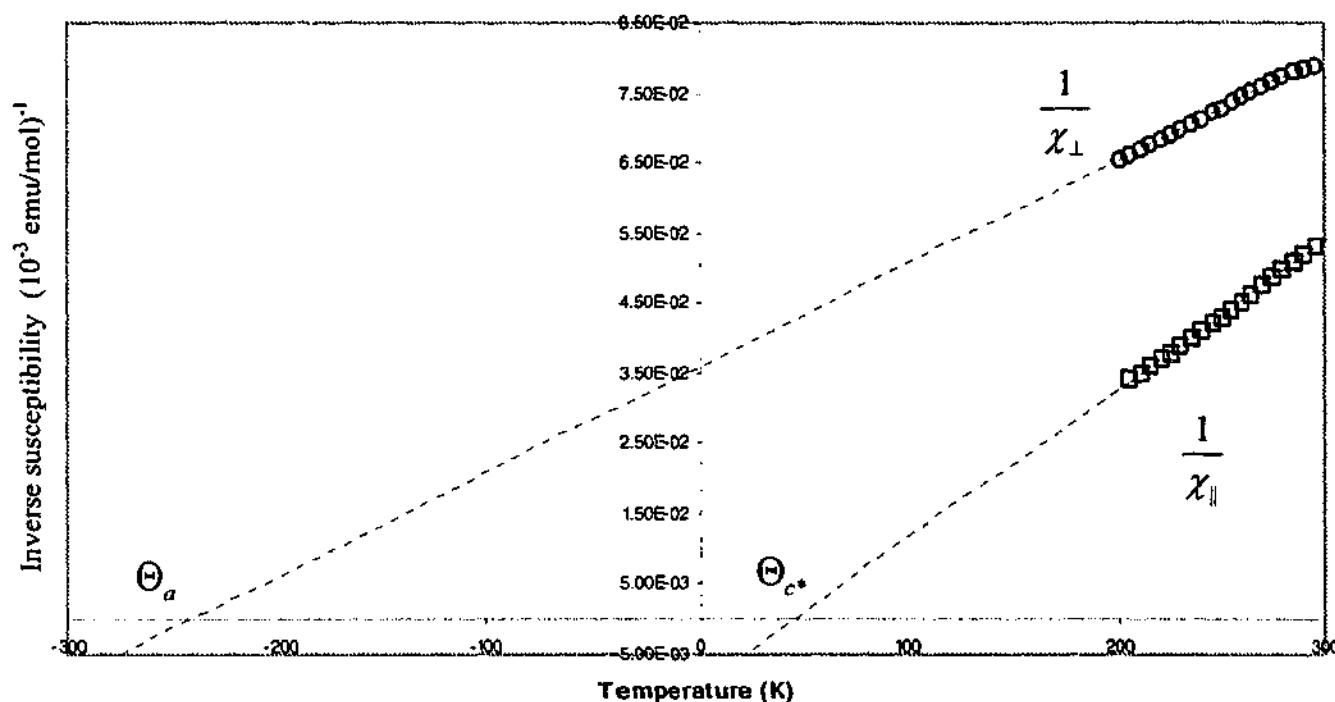


Figure 5.4: Inverse susceptibility plots for temperatures above 200 K and an applied field of 0.6 T. A linear trend line for this data intercepts the temperature axis at $\Theta_a = -236.5$ K and $\Theta_{a^*} = 44.5$ K for the perpendicular and parallel susceptibilities respectively.

Joy and Vasudevan (1992a) have calculated the exchange integrals from the susceptibility plots of FePS_3 using equations based on Equation 1.19 with thermally varying g -factors. However, on closer inspection of their paper, the equations used were discovered to be incorrect. Thus, using the current data from Figure 5.4, and updating the equations, the nearest neighbour interactions of FePS_3 , were calculated. To simplify the calculations, the g values used were 2.52 and 3.00 calculated previously for the parallel and perpendicular susceptibilities, rather than the thermally varying g . In this method, the first nearest neighbour interactions were calculated for two situations: when the external field was applied perpendicular, and parallel, to the moment magnetisation. Both should give the same value for the first nearest neighbour exchange interaction.

In this method the Weiss characteristic temperature, Θ , was taken from the intercepts of the plot of $1/\chi$ for the parallel and perpendicular data. Calculating this for $S = 2$, the exchange

integrals were $\frac{J_{\perp}}{k} = 13.9$ K and $\frac{J_{\parallel}}{k} = -19.7$ K respectively. The equivalent parameters

calculated by Joy and Vasudevan (1992a) were $\frac{J_{\perp}}{k} = 8.1 \text{ K}$ and $\frac{J_{\parallel}}{k} = -12.4 \text{ K}$, which are similar to the current calculated values despite remarkably different values of Θ between studies. The difference in the values may be partially due to the thermal variation of g used by Joy and Vasudevan (1992a) in their calculations. This correction would be responsible for reducing the overall difference between the exchange parameters measured parallel and perpendicular to the applied field direction. These values should be identical, and thus a smaller variation between them would be desired. The difference between the two calculated first neighbour exchange interactions is 33.6 K in the current data, while the difference in the values obtained by Joy and Vasudevan (1992a) is 20.5 K.

The difference in the sign of the two exchange parameters, as found above, was attributed to the different types of exchange; ferromagnetic for a positive exchange and antiferromagnetic for a negative exchange. The values obtained above would imply that the first neighbour exchange was ferromagnetic when the external field was applied perpendicular to the magnetisation axis, and antiferromagnetic when the external field was applied parallel to the magnetisation axis. This is clearly unphysical, as the magnetic interactions can not vary from ferromagnetic to antiferromagnetic under such small applied fields (Okuda et al., 1983). Thus these exchange integrals cannot be attributed to the same first neighbour interaction. At such low fields, the exchange integral obtained from the parallel field data should be approximately the same as the exchange integral taken from the perpendicular field data. It is believed that the exchange coupling between antiparallel moments is much stronger than the applied field of 0.6 T. Thus this method of finding exchange parameters of different signs for the applied field parallel and perpendicular to the planes is erroneous. Even by correcting the equations outlined by Joy and Vasudevan (1992a), the current data does not show equal values for the parallel and perpendicular exchange constants.

In the above analysis, Joy and Vasudevan (1992a) had to force the exchange constants and the spin-orbit coupling constant to impossible values to obtain a suitable fit to their data. It was assumed that the value of the trigonal splitting parameter, Δ/k , was much larger than the spin-orbit coupling constant, λ/k . The difference in the sign of these exchange interactions implies an unphysical situation, which was realised during the re-analysis of Joy and Vasudevan's (1992a) data by Chandrasekharan and Vasudevan (1994).

The results of Joy and Vasudevan (1992a) were reanalysed (Chandrasekharan & Vasudevan, 1994) using the correlated effective field approximation (CEF), first developed by Lines (Lines, 1974). The CEF is a good model for describing low dimensional magnetic behaviour, and it was for this reason that it was considered appropriate for FePS₃. This approximation requires that the excited orbital crystal field energies have the same order of magnitude as the exchange energies (J) and thermal energies (kT). From this reanalysis, different values of the exchange and crystal field parameters were found. The values found by Chandrasekharan and Vasudevan (1994), for the first and second nearest neighbour interactions within the plane were 27.2 K and -2.3 K respectively. These values came from the simultaneous CEF fitted to both the parallel and perpendicular susceptibilities, with slightly different temperature dependent correlation parameters.

The exchange integrals have also been found using high field magnetisation results in which FePS₃ underwent metamagnetic phase transitions from antiferromagnet to ferrimagnetic and then to paramagnetic (Okuda et al., 1983). The applied fields at which these transitions occurred were used to determine the exchange parameters using the following equations.

$$H_{C1} = -(4J_2 + 6J_3) \langle S \rangle / g\mu_B, \quad H_{C2} = -(4J_1 + 12J_2 + 6J_3) \langle S \rangle / g\mu_B \quad (5.1)$$

$$\Theta = (2/3)S(S+1)(3J_1 + 6J_2 + 3J_3) / k \quad (5.2)$$

The value of H_{C1} and H_{C2} are the applied fields at which FePS₃ changes from antiferromagnet to ferrimagnetic and ferrimagnetic to paramagnetic respectively. The value of Θ is the Weiss temperature for a polycrystalline sample. During a combined analysis of the susceptibility data of Kurosawa et al., (1983) with high field magnetisation results, Okuda et al., (1983) found the three nearest neighbour exchange constants to be $J_1/k_B = 19.6$ K, $J_2/k_B = -10.3$ K and $J_3/k_B = 2.2$ K.

The results were similar to those of the CEF theory in that the first nearest neighbour interactions are ferromagnetic, while the second nearest neighbour exchange constant is negative indicating antiferromagnetic interactions. The sign of the third nearest neighbour interaction is questionable if the in-plane magnetic structure of Le Flem et al., (1982) is considered. In this structure, each of the third nearest neighbour interactions should be antiferromagnetic. Thus a positive value for J_3 is unlikely. However the magnitude of this exchange is relatively small and insignificant when compared with J_1 and J_2 .

The positive first nearest neighbour interaction in all the above results indicates that the exchange between first nearest neighbours is ferromagnetic. Most of the magnetic models proposed for FePS₃ do not have all first nearest neighbours aligned ferromagnetically with respect to each other. In fact, the structure of Le Flem et al., (1982) had two ferromagnetic interactions with the third antiferromagnetic. The orientation of the third spin could be due to the influence of the second neighbour interaction. If all first nearest neighbour moments were ferromagnetically coupled, then the entire system would be ferromagnetic rather than antiferromagnetic. This would indicate that for an antiferromagnetic material with a ferromagnetic exchange between first nearest neighbours, the system must be frustrated for at least one nearest neighbour moment. This also appears to be the only way to satisfy the condition of antiferromagnetic exchange interactions between the second nearest neighbours and in the material as a whole. The high field method for calculating the exchange parameters has been conducted in Section 5.4 for the current data.

From the above investigations, the CEF model has shown the most accurate correspondence with the high temperature susceptibility data, as it takes into account spin fluctuations and short-range correlations as well as the thermal variation of the g factors. The first neighbour interactions calculated with this method, from the parallel and perpendicular susceptibilities, are identical, leading to just one value for the first neighbour interactions as expected. More simply though, high, applied field magnetisation data, was combined with powder susceptibility data to calculate reasonable exchange interactions for 1st, 2nd, and 3rd nearest neighbour interactions. However this method, outlined by Okuda et al., (1983) relies on complete randomisation of a polycrystalline sample. Due to the strongly preferred orientation in FePS₃, crystallites within the powdered samples may stack, yielding a wrongly averaged Θ value. Thus the CEF method as outlined by Chandrasekharan and Vasudevan (1994) appears to be the most accurate method for determining the exchange integrals of the highly oriented FePS₃.

5.3 THE SPECTROSCOPIC SPLITTING FACTOR

Joy and Vasudevan (1992a) also made some calculations for the spectroscopic splitting factor, g , and found different values for both the parallel and perpendicular susceptibility. This indicates that the g -factors are related to the anisotropy of the material, which differs for the applied field parallel and perpendicular to the moment direction. The spin-orbit coupling

constant, λ , has also been related to the spectroscopic splitting factor, g , indicating that the g -factors are temperature dependent. From their data, Joy and Vasudevan (1992a) have found the spin-orbit coupling coefficient for FePS_3 to be -92.8 cm^{-1} (-132.9 K) for the susceptibility parallel to the applied field and -89.8 cm^{-1} (-128.8 K) for the susceptibility perpendicular to the applied field. The original equations that were presented in their paper were missing a factor of μ_B^2 , which resulted in calculated values of g less than 2. Correcting for this factor gave values of around 2.5 for both g -factors at 200 K. The g -factors have been calculated in Table 5.1 below, from the current data using the different methods as outlined in each of the references in the source column.

Table 5.1: Spectroscopic splitting factor for Fe^{2+} calculated from the spin-orbit coupling constants from a variety of sources. A is from Chandrasekharan & Vasudevan (1994), B is from Joy & Vasudevan (1992a), both for FePS_3 , and C is the free ion case, from Abragam & Bleaney (1986). Source D (Niira & Oguchi, 1954) was used to calculate the thermally independent values for FePS_3 .

λ (K)	Temperature (K)	g_{\parallel}	g_{\perp}	g_J	Source
166.5	200	2.54	2.51		A
	400	2.60	2.73		A
132.9	200	2.53			B
	400	2.65			B
128.8	200		2.61		B
	400		2.76		B
106	200			1.89	C
	400			1.97	C
-	-	2.52	3.00		D

Different values for the spin-orbit splitting parameter have been obtained from different sources, according to the different models of analysis used. Source A is from Chandrasekharan and Vasudevan's (1994) CEF model, while source B relates the factor to the anisotropy dependent model of Joy and Vasudevan (1992a). Thus in source A, the spin-orbit coupling coefficient is independent of the anisotropy, while for source B, it varies for g_{\parallel} and g_{\perp} . These can be compared with the free ion value of λ found from source C.

As can be seen, the g -factors increase by less than 10 % as the temperature doubles. The susceptibility is proportional to g^2 . The effect is greater for g_{\perp} . It appears that the temperature variation of g may be partially responsible for the greatly different values of the Weiss temperature obtained from the inverse susceptibility plots. Taking the variation of g_{\parallel} and g_{\perp} from source B and rectifying the inverse susceptibility from Figure 5.4, the Weiss temperatures became $\Theta_{c^*} = 72$ K and $\Theta_a = -151$ K. In Figure 5.4, where a constant g factor was considered for simplicity, the difference between Θ_{c^*} and Θ_a was 281 K, whereas a difference of 223 K was observed when the temperature dependent g factor was considered. A reduced difference in Θ values could also affect the magnitude of the exchange interactions.

The only real similarity between the values in Table 5.1 and the non-temperature dependent g -factors calculated using the method of Niira and Oguchi (1954), is that the general trend sees $g_{\parallel} < g_{\perp}$. It is likely that g is temperature dependent with a constant spin-orbit coupling constant, λ , due to the repopulation of the spin-orbit coupling energy levels as the temperature increases. This can be seen in Equation 1.19. If the g factors were temperature dependent, as indicated above, then similarly the magnetic moment would also have a thermal variation according to Equation 1.4.

5.4 HIGH FIELD MAGNETIZATION MEASUREMENTS

The magnetization was measured as a function of applied field up to 7 T at 35 K for a single crystal of FePS_3 . The field was applied parallel to the magnetic moments – that is, parallel to c^* . It was observed from this measurement that the magnetisation followed a linear trend as the applied field was increased (Figure 5.5). No noticeable phase changes such as a spin flop were observed from this particular measurement. Thus it was assumed that any magnetic phase changes for this compound exist at applied fields greater than 7 Tesla.

The magnetization was then measured by A. M. Mulders, using a pulsed magnetic field at the University of Amsterdam with applied fields of up to 40 T. The applied field was aligned parallel to the c^* -direction, which was also the orientation of the moment sublattices. The aim of this study was to observe the fields and temperatures at which the ordered state changes from antiferromagnetic to some other magnetic state.

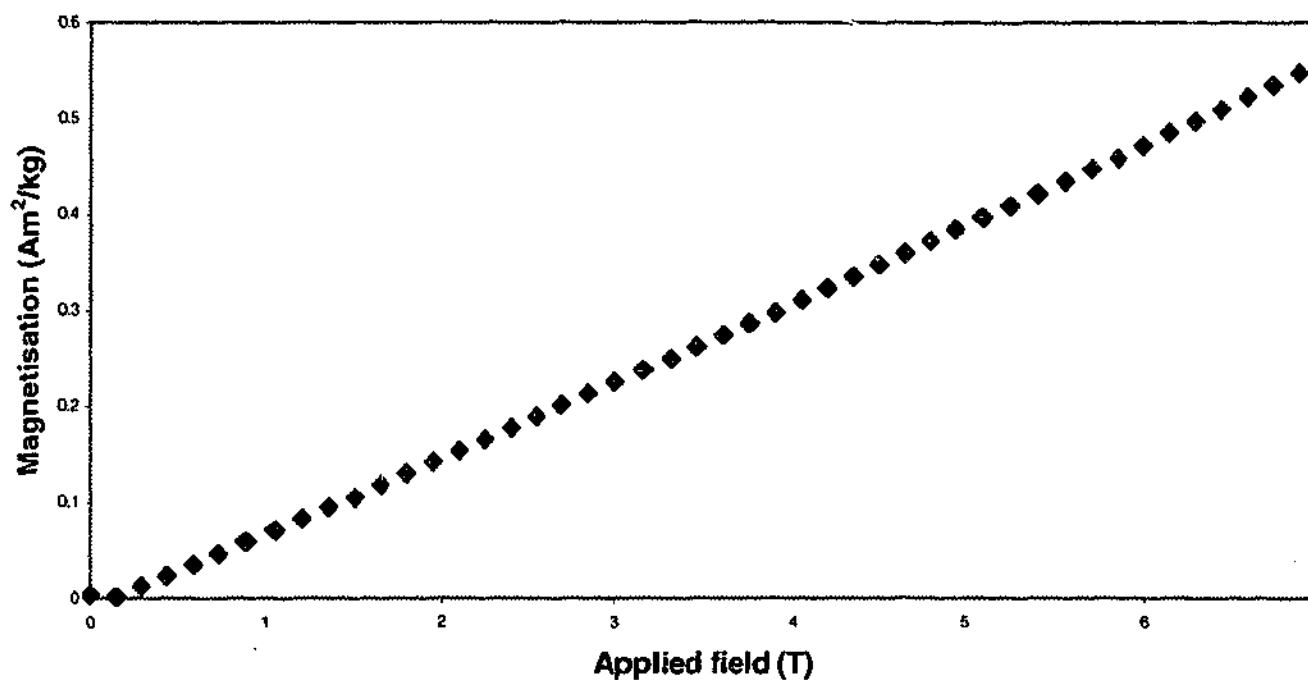


Figure 5.5: Magnetisation as a function of applied fields for FePS_3 . The linear trend indicates that there are no phase changes or spin flips occurring for applied fields up to 7 T.

A hysteresis of the magnetization was observed as the applied field was increased and then decreased through fields from 32 to 38 T. This can be seen for the data taken at 8.5 K in Figure 5.6. In this region, as the field was increased, approximately half the antiparallel moments appeared to flip, aligning with the field direction. As the internal moment of FePS_3 is close to $5 \mu_B$, flipping half the moments would increase the magnetisation by around half this value, which was observed at approximately $2.44 \mu_B$. Thus the sample was ferrimagnetically ordered with approximately 75% of the spins aligned along the field direction and 25% remaining antiparallel. The moments that flipped were observed to remain in that orientation until the field dropped below 34 T. Below this field, they gradually rotated back to the original antiferromagnetic order. This is an indication that the anisotropy energy is greater than the exchange forces between the moments.

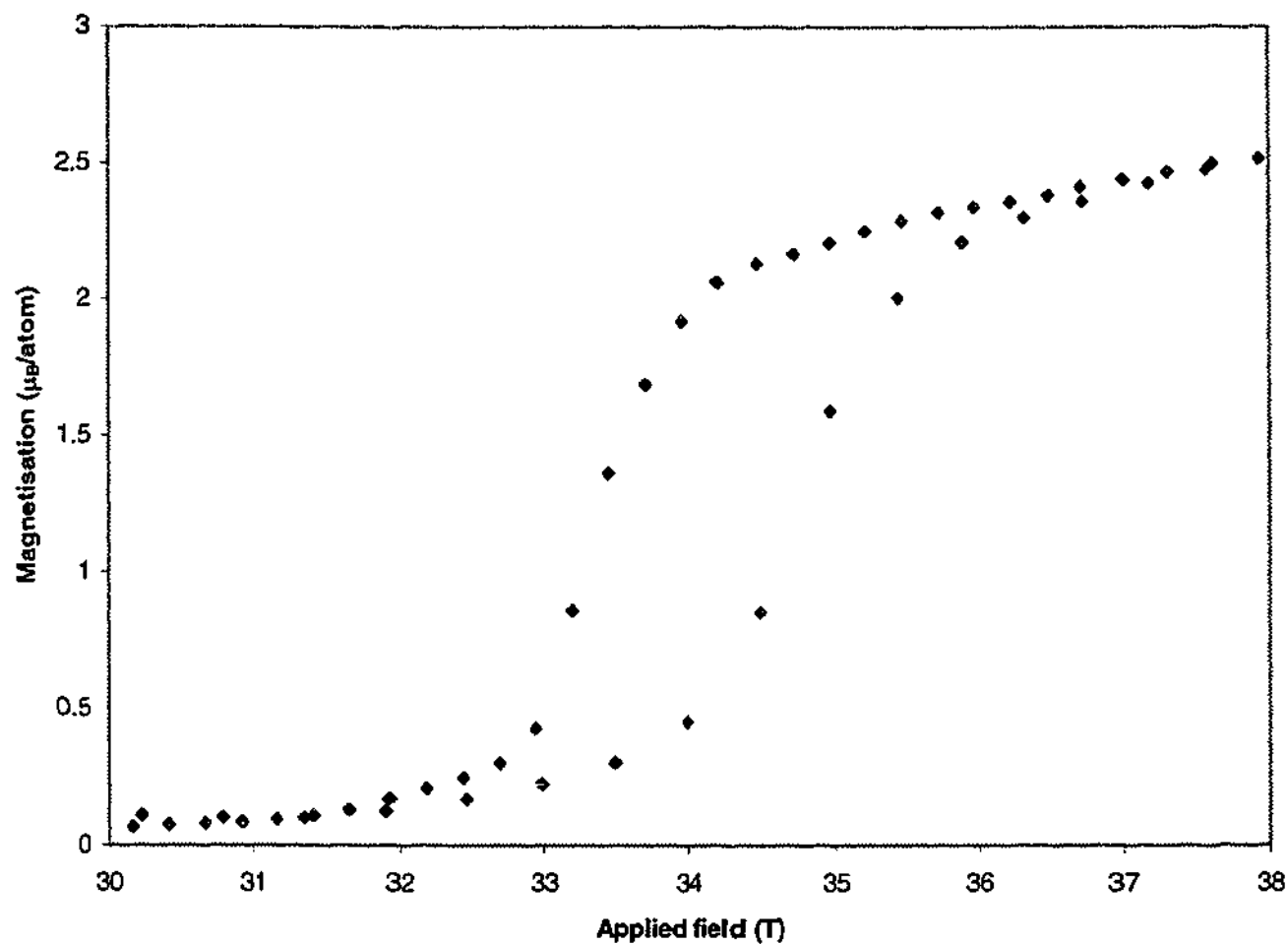


Figure 5.6: Hysteresis observed in the magnetization for applied fields between 32 and 38 T. This data was taken at 8.5 K.

At temperatures between 10 and 70 K, the sample showed two magnetic phase changes in increasing fields as seen in Figure 5.7. At fields below 30 T, the sample remained in its original antiferromagnetic state. Between 30 and 35 T, about half of the antiparallel magnetic moments flipped parallel with the applied field such that a ferrimagnetic state was reached. Beyond about 38 T, at temperatures greater than 30 K, the magnetic moments moved into their final orientation where all spins pointed along the direction of the applied field. This has been termed a paramagnetic state (Taylor et al., 1973). This can be seen in Figure 5.7, where the phase changes occurred at 32.4 T and 37.6 T at 30 K and at 31.2 T and 35.0 T at 59 K.

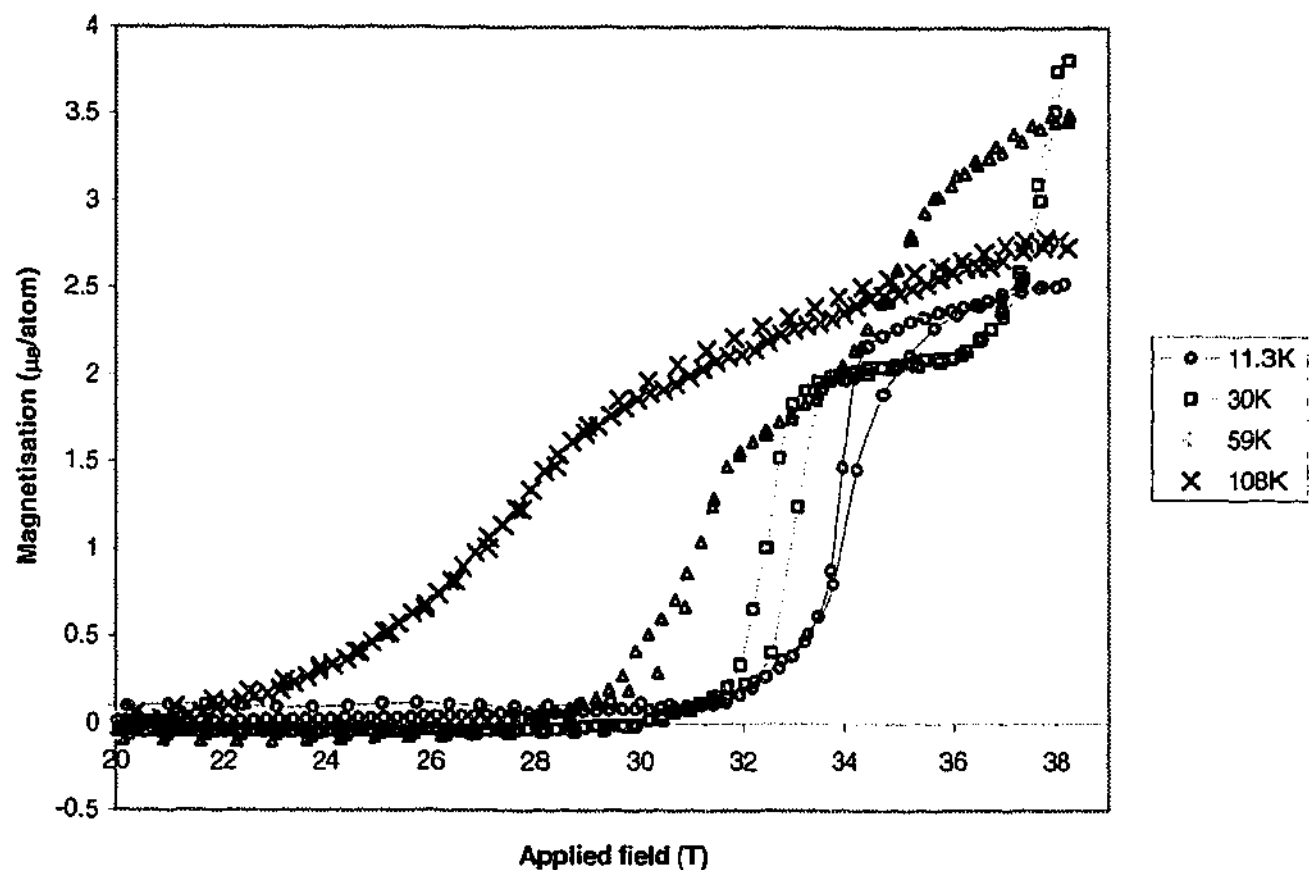


Figure 5.7: Changes in magnetization with applied field for temperatures ranging from 11.3 K to 108 K. Field applied parallel to the c^* -direction.

Table 5.2: Temperature dependence of the magnetic moment, taken from Figures 5.6 and 5.7.

Temperature (K)	Magnetisation of plateau (μ_B /atom)	Effective magnetic moment (μ_B)
8.5	2.44	4.88
11	2.38	4.76
30	2.06	4.12
59	1.78	3.56

The magnetic moment can be found from the plateaus in both Figures 5.6 and 5.7 indicating the transition from antiferromagnetic to ferrimagnetic. The magnetisation of the plateau can be

seen to decrease with increased temperature in Table 5.2, indicating that the magnetic moment is indeed temperature dependent. Full saturation to ferromagnetic was not achieved, so the moment can be taken as twice the magnetisation of the plateau if it is assumed that the plateau exists when half of the antiferromagnetic moments are flipped.

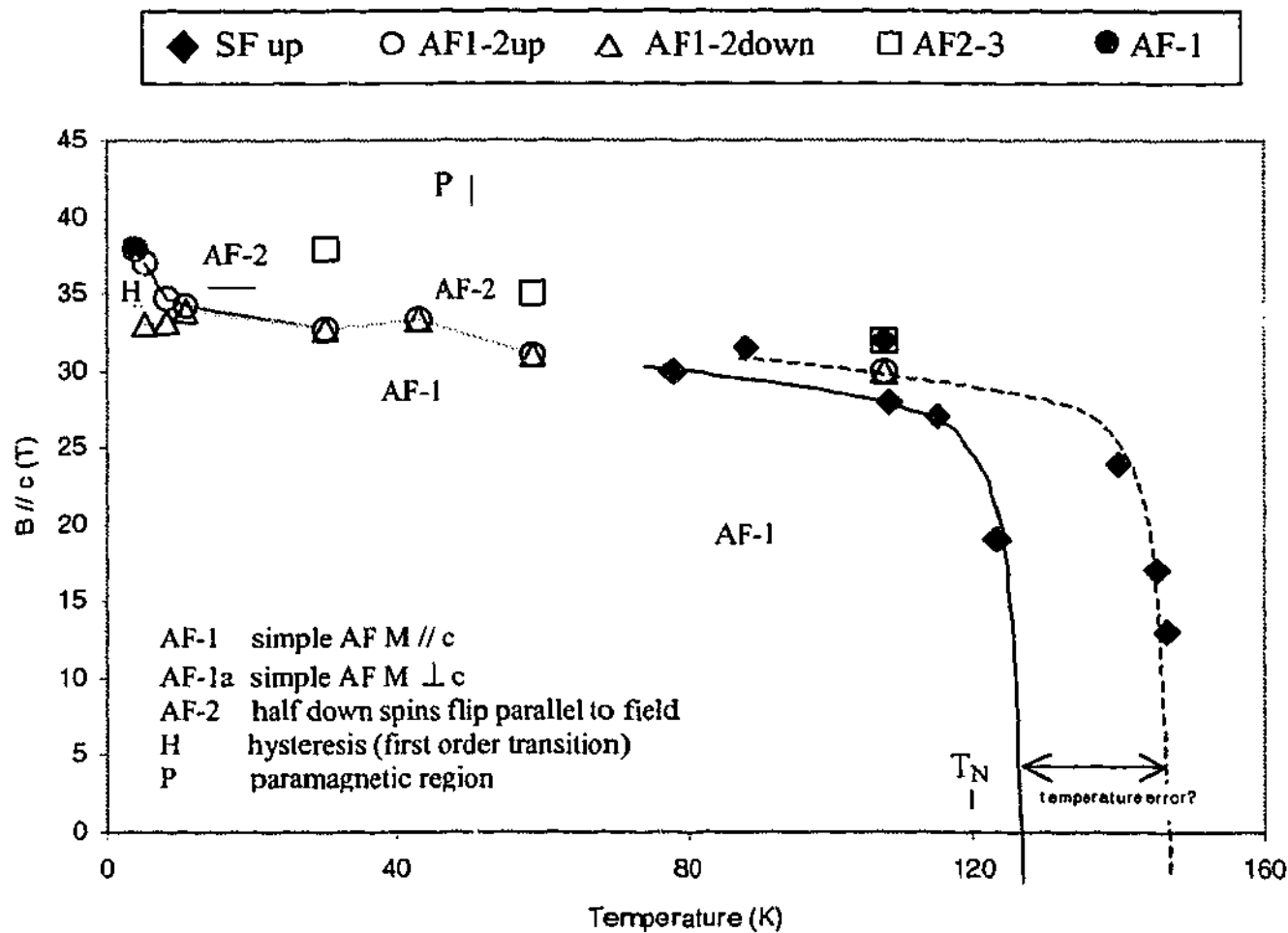


Figure 5.8: Change in magnetic phase with applied field and temperature. AF1-2 shows the phase change between antiferromagnet and ferrimagnetic with increasing field (up) and decreasing field (down). AF2-3 shows the phase change between ferrimagnetic and paramagnetic.

Figure 5.8 shows the applied fields at which phase changes occurred for a variety of temperatures. Information from Figure 5.7 is repeated here along with data taken at temperatures between 4.2 K and 147 K. Only the applied fields that gave the steepest gradients are displayed as these correspond to the phase changes from antiferromagnetic to ferrimagnetic (AF1-2) and ferrimagnetic to paramagnetic (AF2-3). As can be seen only the two data sets taken at 30 K and

59 K showed the transition into the paramagnetic state. At 4.2 K, the applied field of 38 T was not strong enough to change the magnetic ordering of the moments. There was a slight hysteresis below 11.3 K between the data taken in increasing field (AF1-2up) and that taken in decreasing field (AF1-2down), as displayed in Figure 5.6.

At temperatures above 70 K, there was some uncertainty as to the exact temperature displayed. The high temperature data in Figure 5.8 can be split into two groups as shown by the dashed and full lines that intersect the temperature axis at around 145 K and 125 K respectively. It was thought that there was a reading error in the variable temperature insert used to take the data, such that the temperature measurements from the dashed curve were all larger than the true sample temperature by around 20 K. The data following the dashed curve should therefore be shifted to the left and would follow the full curve. This being the case, the results would indicate that as the temperature approached the Néel point, the magnetic ordering became weaker, and the applied field required to flip the moments decreased to around zero at 125 K, when the sample was truly paramagnetic.

The high field magnetisation measurements were used to determine the exchange parameters according to the method outlined in Okuda et al. (1983) and Equations 5.1 and 5.2. Taking the critical field as the applied field at which the magnetisation changes most rapidly, the exchange constants were determined for the 30 K data. Initially the value of Θ used was the powder-averaged value of the Weiss characteristic temperature, which, for these calculations was taken as equivalent to $1/3 \Theta_{\parallel} + 2/3 \Theta_{\perp} = -142.8$ K. Solving for the simultaneous equations gave values of the exchange integrals as $J_1/k_B = -19.7$ K, $J_2/k_B = 9.28$ K and $J_3/k_B = -10.77$ K. The signs of the first and second neighbour interactions were opposite those of Okuda et al., (1983) as well as the expected values, and thus the values were deemed improbable. It was thought that the extremely large, negative value of Θ was responsible for the unreasonable values.

By assuming the third nearest neighbour interaction to be zero, similar to Chandrasekharan and Vasudevan (1994), the value of Θ and therefore Equation 5.2 was not necessary to solve for J_1 and J_2 . Solving for Equation 5.1 gave more reasonable values of $J_1/k_B = 6.9$ K, $J_2/k_B = -0.4$ K. The signs of these values indicate a ferromagnetic first neighbour interaction and an antiferromagnetic second neighbour interaction as expected, and would suggest that the third nearest neighbour interaction is weak when compared with the first and second neighbour interactions.

5.5 MÖSSBAUER SPECTROSCOPY OF THE SINGLE CRYSTAL SAMPLE

Initial Mössbauer spectroscopy measurements were taken using a large single crystal of FePS_3 . Room temperature results can be seen in Figure 5.9. This plot exhibits an asymmetric doublet with the left absorption line shorter than the right. The left line represents the $m_I = \pm 1/2$ to $\pm 1/2$ transitions, ($\Delta m = 0$), and the $m_I = \pm 1/2$ to $\mp 1/2$ transitions, ($\Delta m = \mp 1$), while the right line represents the $m_I = \pm 3/2$ to $\pm 1/2$ transitions ($\Delta m = \pm 1$). The solid line represents the least squares fit to the data calculated by solving the full Hamiltonian and applying Lorentzian line shapes to the peaks.

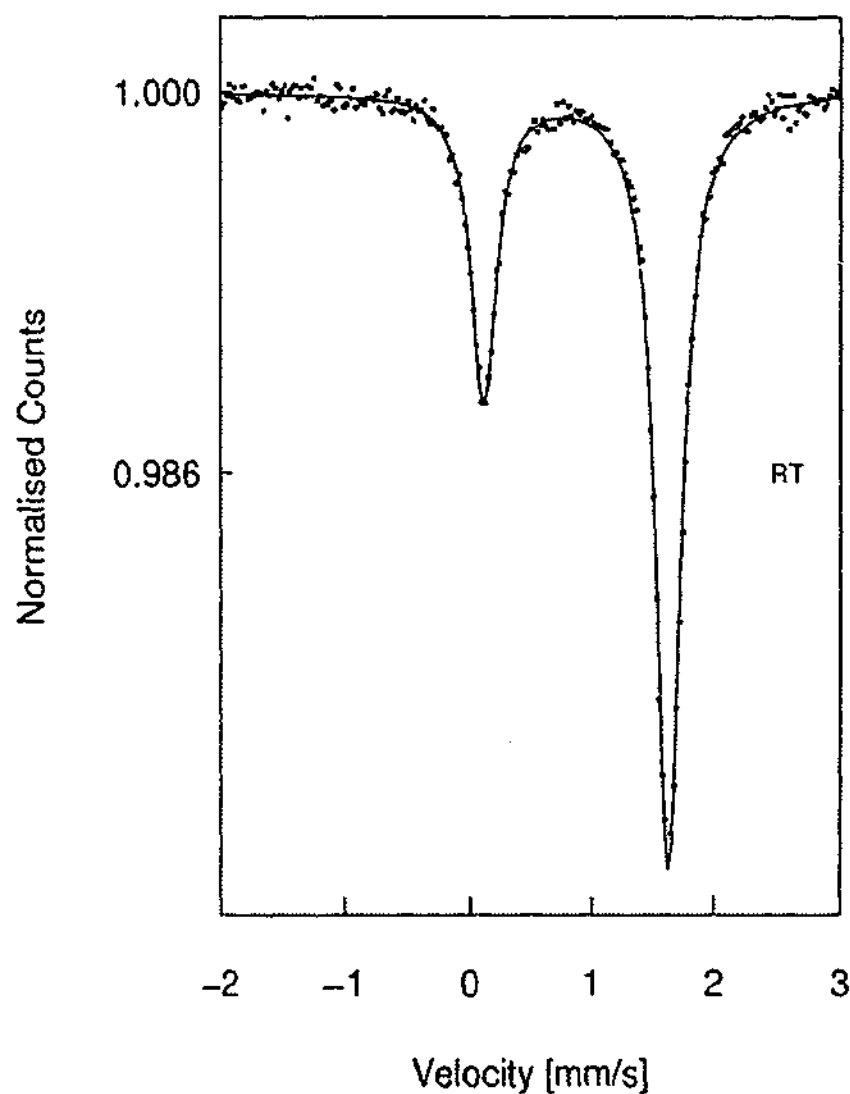


Figure 5.9: RT Mössbauer spectrum of single crystal sample. The γ -ray was directed parallel to the c^* -direction and the velocity scale is in mm/s with respect to α -Fe.

Although the room temperature spectra were fitted using Lorentzian line shapes, the low temperature data had much larger intensity peaks. The Lorentzian peak shapes did not give the best fit to the data around the baseline and the tip of each dip. For thick absorbers, or strongly overlapping lines, non-Lorentzian profiles must be used (Bancroft, 1973). Thus, Voigtian line shapes were used to fit the low temperature data, and account for the thickness effects in the low temperature, single crystal spectra. A Voigtian line shape can be considered as a Gaussian distribution of Lorentzian lines and provides a better fit to absorption peaks with a broader and more rounded dip. In this type of analysis, the lines were fitted with a smooth Gaussian distribution of four Lorentzian lines having different positions and relative areas (Rancourt, 1996). Voigtians were constrained such that the line width of the four Lorentzian profiles fitted the natural line width of Fe, 0.196 mm/s. Voigtians were only necessary for the low temperature data, as the percentage absorption increased due to the increase in recoilless fraction. Room temperature spectra with an absorption dip of around 3 % were adequately fitted with Lorentzian line shapes.

Figure 5.10a shows the same single crystal sample in the magnetically ordered state, at 10 K. Three lines are clearly visible in Figure 5.10a, with the central line largest in intensity. It appears that the hyperfine field and quadrupole splitting are in opposite directions such that lines 1 and 6 have shifted to the right of the spectrum while lines 2, 3, 4 and 5 have shifted to the left. Because of this, lines 4 and 1 overlap as seen in Figure 5.10b. When considering the 6 absorption lines of a magnetic hyperfine interaction, it becomes clear that at least two have zero intensity. In fact transitions 2 and 5 of the magnetically split spectrum have zero intensity which indicates that the internal magnetic moments are along the gamma-ray direction according to Equation 3.11.

The magnetically ordered hyperfine spectrum of FePS₃ has a small hyperfine field compared with the typical α -iron hyperfine field of 33 T (Gonser, 1975). In fact the internal hyperfine field at 10 K is 9.75 ± 0.06 T. This hyperfine field was similar to that of FePSe₃, which may indicate that the Fe²⁺ in each compound is within a similar magnetic environment. Jernberg et al., (1984) favoured this idea to describe the similarities between the Mössbauer spectra of each compound. The relatively small hyperfine field at the Fe nucleus can be attributed to the degree of covalent bonding in FePS₃ as well as the lattice magnetic dipole field and the 3d orbital moment contribution. It has been shown that the factors that reduce the hyperfine field from the free ion case include charge transfers, covalent bonding and crystal field effects (Watson & Freeman, 1961). Covalent bonding has been found responsible for reducing the hyperfine field of other

compounds, such as ilmenite (FeTiO_3) which has an internal field of only 4.3 T (Grant et al., 1972). It was also noted in this paper, that lattice contributions to the charge felt at the nucleus also play a significant role in the reduction of the hyperfine field.

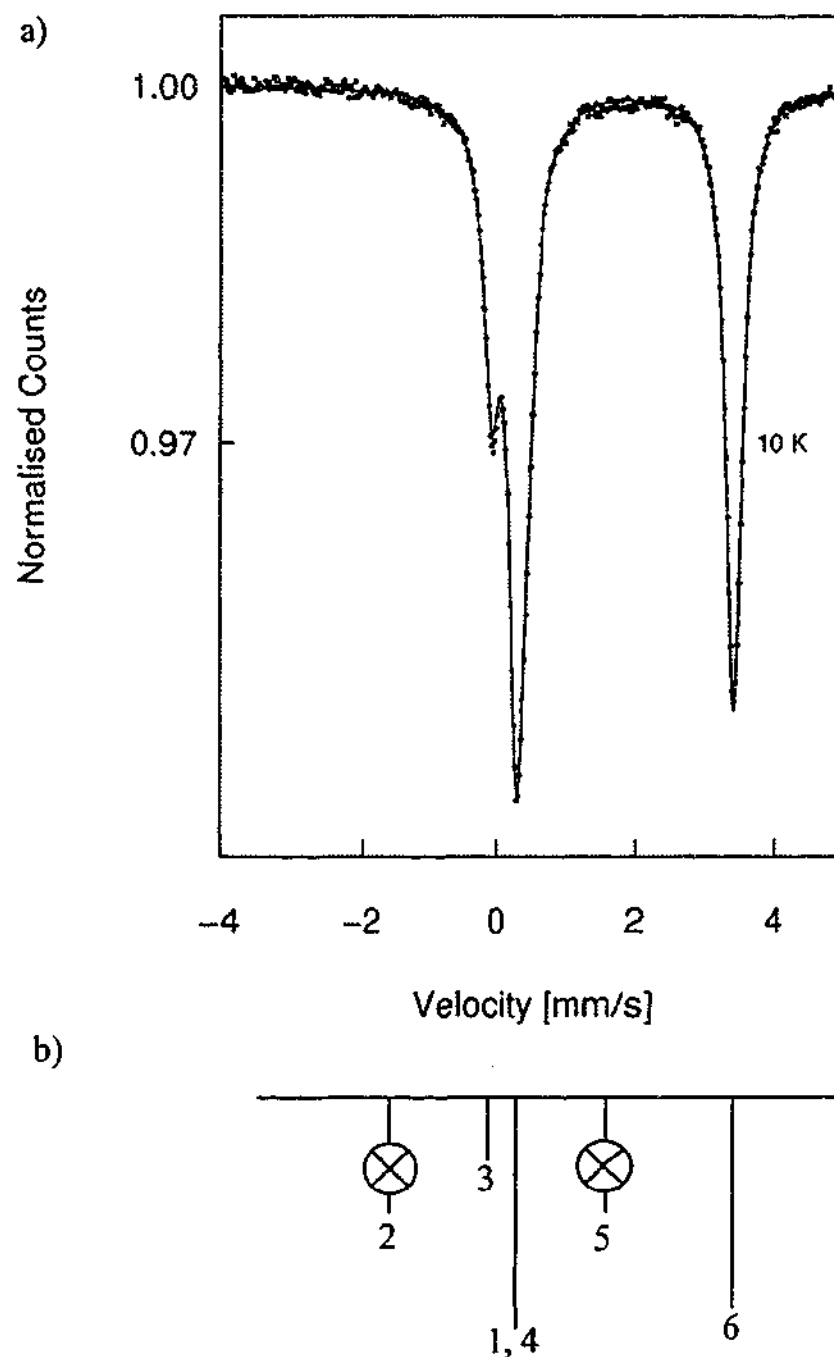


Figure 5.10: Single crystal Mössbauer spectrum taken at 10 K (a). The relative line positions for the magnetically ordered spectrum (b). Lines 2 and 5 have zero intensity.

Table 5.3 shows the hyperfine parameters for the single crystal Mössbauer spectra taken at room temperature as well as temperatures below the magnetic ordering temperature. The Q.S.

value in Table 5.3 for the quadrupole split spectra is $\frac{1}{2}eQV_z$. It can be seen that as the temperature of the sample decreased, the isomer shift and the quadrupole splitting increased. The hyperfine field was also larger at 10 K than 96 K as expected. The line width for the room temperature measurement was taken as the full width at half the maximum intensity (FWHM).

Table 5.3: Mössbauer parameters for the single crystal sample. These values were obtained by diagonalising the full Hamiltonian and fitting a Lorentzian line shape to the room temperature spectrum and Voigtian profiles to the low temperature spectra. The values in the parentheses indicate the uncertainty in the last figure.

T (K)	Fitting profile	I.S. (mm/s)	Q.S. (mm/s)	HF field (T)	Γ (mm/s)	χ^2
295	Lorentz	0.87(1)	1.50(3)	-	0.25(2)	1.27
96	Voigt	1.01(1)	1.54(3)	9.26(6)	-	1.46
10	Voigt	1.03(1)	1.61(3)	9.75(6)	-	1.81

The relative intensities of the quadrupole split absorption lines in Figure 5.9 were calculated from the ratio of the lines, $R_q = \frac{I_{\Delta m=\pm 1}}{I_{\Delta m=0}}$. Room temperature spectra were fitted with singlet Voigtian lines using the CERN Minuit fitting program such that the ratio of the areas was found to be 2.58 (Litterst & Stieler, 2003). This value is much larger than the asymmetry obtained by Taylor et al. (1973), of 1.78. This discrepancy may be due to the quality of the sample used by Taylor et al., (1973), as the ratio of 2.58 was repeatable with different crystals from the current samples. The low temperature Mössbauer data of Taylor et al., (1973) showed 6 absorption peaks which conflicts with the current results of 4 lines. It has been claimed by many that the magnetic moments are oriented along the c^* -direction which corresponds to the γ -ray direction in these Mössbauer spectroscopy experiments (Le Flem et al., 1982; Kurosawa et al., 1983; Okuda et al., 1983). Thus misalignment or stacking faults in the single crystal sample may have been responsible for the presence of lines 2 and 5 in Taylor's magnetically ordered spectrum. In a magnetically ordered spectrum, the relative line intensities are governed by Equation 3.11

$$3(1 + \cos^2 \theta) : 4 \sin^2 \theta : (1 + \cos^2 \theta) \quad (3.11)$$

which suggests that lines 2 and 5 should have zero intensity when the angle between the internal magnetic field, the EFG and the γ -ray direction, θ , is zero. Thus a ratio of 3 between the $\Delta m = \pm 1$ and $\Delta m = 0$ transitions would indicate that the EFG direction was parallel with the γ -ray direction, and that the asymmetry parameter, η , was zero. The recently obtained ratio of 2.58 is much closer to this value than that obtained by Taylor et al., (1973) however, neither set of data would imply that the EFG direction is along the c -axis. Discrepancies between the experimental and theoretical values can be attributed to the directions of the EFG tensor. These will be discussed later.

Another effect that may alter the relative line intensities in a single crystal absorber is polarisation. As mentioned in Chapter 3, incident gamma rays may be polarised by single crystal absorbers, depending on the thickness of the absorber. The low temperature spectra of a thick crystal will be affected more by polarisation effects than the high temperature spectra, due to the reduced amplitudes of lattice vibrations at low temperatures. Similarly polarisation effects will affect absorption lines with greater intensity more than the less intense lines of the spectrum. That is, the percentage reduction in the line intensity is greatest for the larger absorption peak. Thus it would appear that the room temperature absorption line for the $\Delta m = \pm 1$ transition (the right hand peak for FePS_3) would be more greatly affected by polarisation effects than the $\Delta m = 0$ transition. The effect of polarisation in the sample is to reduce the intensity of the absorption dip from that of a non-polarising sample. Therefore, it can be assumed that the intensity of the $\Delta m = \pm 1$ transition would be greater in the absence of a polarising sample, bringing the intensity ratio closer to the expected value of 3. The degree to which the polarisation alters the intensity ratio is not known, however it is not believed to be responsible for the entire deviation of the intensity ratio from 3 to 2.58. The impact of the polarisation present in FePS_3 will be discussed later in Section 5.9.

5.6 MÖSSBAUER SPECTROSCOPY OF THE POWDER SAMPLE

Mössbauer spectra of the powdered pattern taken at room temperature and 96 K can be seen in Figure 5.11. Although this sample was supposed to be completely random, there was some texture provided by the stacking of the crystallites in the sample holder. This can be seen by the

still significant asymmetry in the room temperature spectrum (Figure 5.11a). However a degree of randomisation was achieved which is evident by the appearance of lines 2 and 5 in the magnetically ordered spectrum (Figure 5.11b).

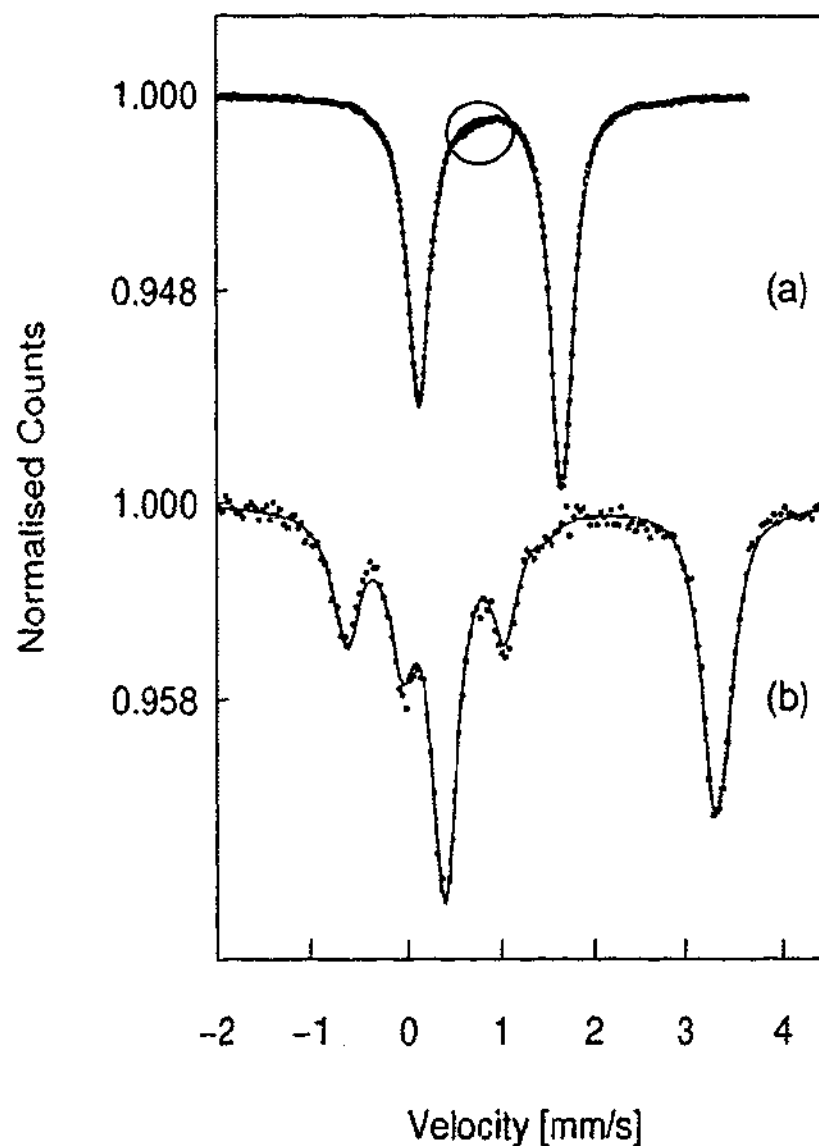


Figure 5.11: Powdered sample Mössbauer spectra taken at room temperature (a) and 96 K (b). The circle represents the region of incompatibility between the data and the fit.

The asymmetry of the room temperature lines gives an area ratio close to $R/L = 1.25$ which can be compared to both a completely random sample with equal line intensities ($R/L = 1$) and the single crystal data ($R/L = 2.58$). These comparisons indicate that the crystallites within the powdered sample have a preference to stack with a common c^* -direction. This is comparable with other Mössbauer spectra taken using powdered samples with incomplete randomisation.

Sakai found the intensity ratio of their powdered material was approximately 1.2, and 7 months later, another powdered sample had an asymmetry of 1.5 (Sakai et al., 1999a; Sakai et al., 1999b). The deviation from a completely randomised sample in these reports is significantly large enough that other effects such as GKE and polarisation cannot be held solely responsible for the asymmetry of the peaks. Thus, although steps were taken both in previous studies as well as the current investigation to completely randomise the powdered sample, some preferred orientation remained, creating a textured sample.

Both the room temperature and magnetically ordered spectra were fitted with Lorentzian line shapes as the powdered sample was considered to be sufficiently thin. The Mössbauer parameters for these fits can be seen in Table 5.4 below. Again, the Q.S. value in Table 5.4 for the sextets is $\frac{1}{2}eQV_{zz}$. The uncertainty in the last digit is represented by the parentheses after each value. It can be observed that the hyperfine parameters for the powdered patterns are the same, within error, to the single crystal parameters in Table 5.3. The uncertainty in the fit can be described by χ^2 which according to statistical measures equals unity for a perfect fit. The room temperature spectrum has a large uncertainty with $\chi^2 = 5.79$, indicating that the fit to the data is not adequate.

Table 5.4: Temperature dependent Mössbauer spectroscopy data for powdered FePS_3 .

T(K)	I.S. (mm/s)	Q.S. (mm/s)	HF field (T)	Γ (mm/s)	χ^2
295	0.877(2)	1.52(7)	-	0.291(7)	5.79
96	1.02(3)	1.6(1)	9.3(3)	0.32(7)	1.09

It must be noted that the room temperature fit to the powder spectrum does not pass through the data points at around 0.8 mm/s near the base line. This bump is an indication of an unknown impurity in the powdered sample, whether from deterioration of the crushed sample, or from the mixing process with boron nitride. This small intensity absorption profile was fitted with either a doublet or a singlet to observe how this unknown impurity affected the hyperfine parameters. The fit to this data with a singlet absorbing the foreign intensity can be seen in Figure 5.12. The profiles for both FePS_3 and the impurity, along with the overall fit can be seen in this plot. The

overall fit to the data within the circle appears to be more accurate than the fit in Figure 5.11. The impurity was responsible for less than 2% of the area and did not appear to affect the hyperfine parameters of the FePS_3 absorption lines. The parameters for each fit can be seen in Table 5.5. The parameters of the fits to the impurity, listed in Table 5.5, are very unlikely unless the sample had oxidised, since they would typically indicate the presence of Fe^{3+} .

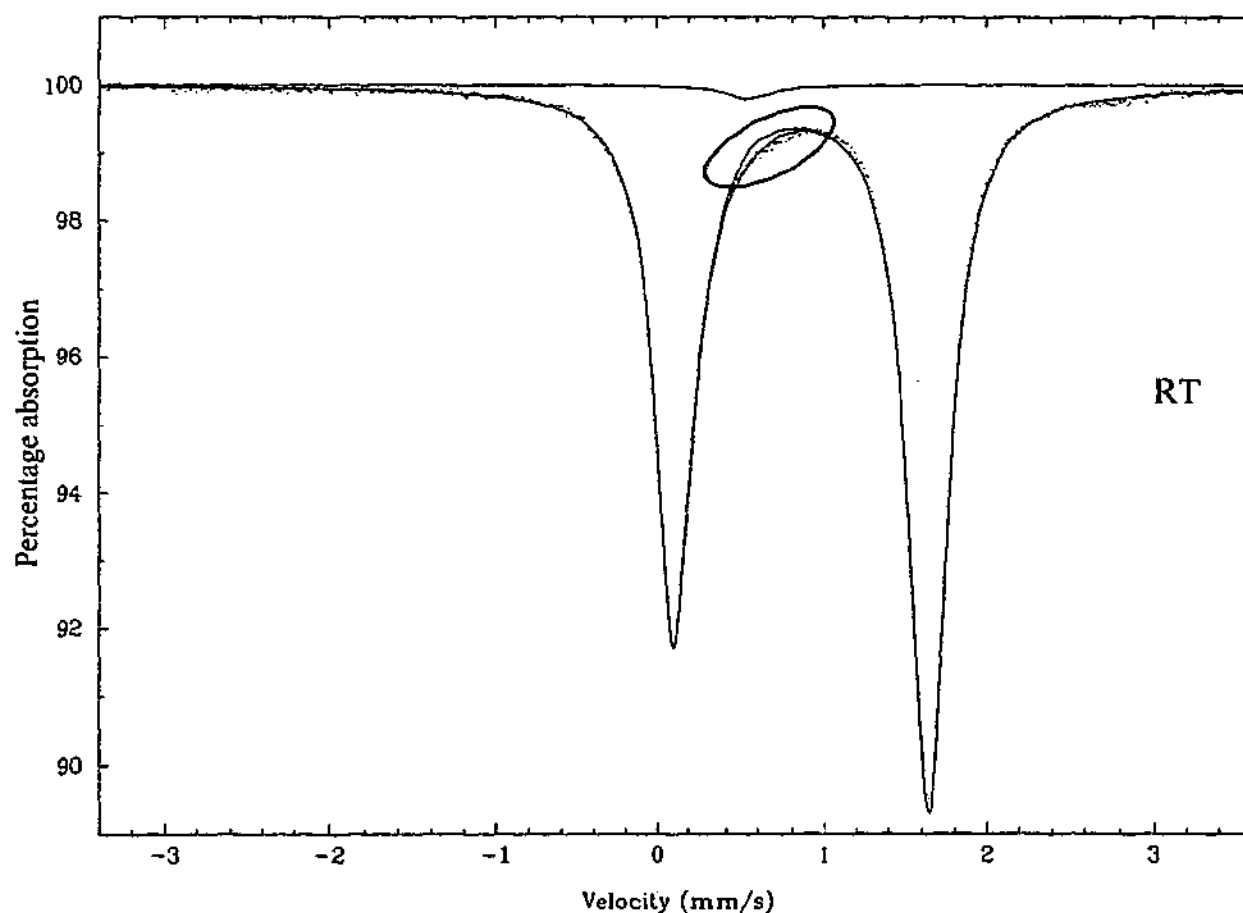


Figure 5.12: Powder Mössbauer spectrum fitted with a small singlet line to absorb the impurity. The circle highlights the region that is better fitted with the singlet line.

The impurity was not fitted into the low temperature spectrum for two reasons. First, the statistics in the low temperature data were not as good as the room temperature data. Thus the small impurity was not obvious in the spectrum and was considered to have a minimal effect. Secondly, as the nature of the impurity was unknown, any variation with temperature was also unknown. It can be seen by the goodness of fit parameter in Table 5.5 that adding another profile for the impurity would have had only a slight impact on the overall fit. Thus it was deemed better to fit the low temperature spectrum with only one magnetic spectrum from FePS_3 .

Table 5.5: Comparison of hyperfine parameters after fitting with no impurity and with the impurity absorbed by a doublet or singlet. The singlet fit to the impurity appeared to give the most reasonable fit to the region in the circle of Figure 5.12

Fit	I.S. (mm/s)	Q.S. (mm/s)	Area (%)
No impurity	0.877(2)	1.52(7)	100
Impurity as a doublet	0.877(1)	1.53(2)	99.48
	1.03(1)	1.00(3)	0.52
Impurity as a singlet	0.876(1)	1.53(1)	98.78
	0.54(1)	-	1.21

5.7 APPLIED MAGNETIC FIELDS

The single crystal sample was also investigated in applied fields of 10.0 (± 0.2) T and 14.3 (± 0.2) T. The raw data plots can be seen in Figure 5.13 with the zero applied field spectrum at 10 K for comparison. The applied field was aligned with the γ -ray direction.

Many absorption dips are visible in these spectra, which indicate the presence of two sublattices in which the moments are parallel and antiparallel to the applied field. This confirms that the sample is indeed antiferromagnetically ordered at low temperatures. Applying the magnetic field along the moment direction boosts the internal field felt by the nucleus with its moment antiparallel to the field, and reduces the internal field felt by the nucleus with its moment parallel to the field. This is observed by the increase and decrease of the respective magnetic hyperfine fields. Thus as the applied field was increased, the subsequent difference in the two hyperfine fields also increased.

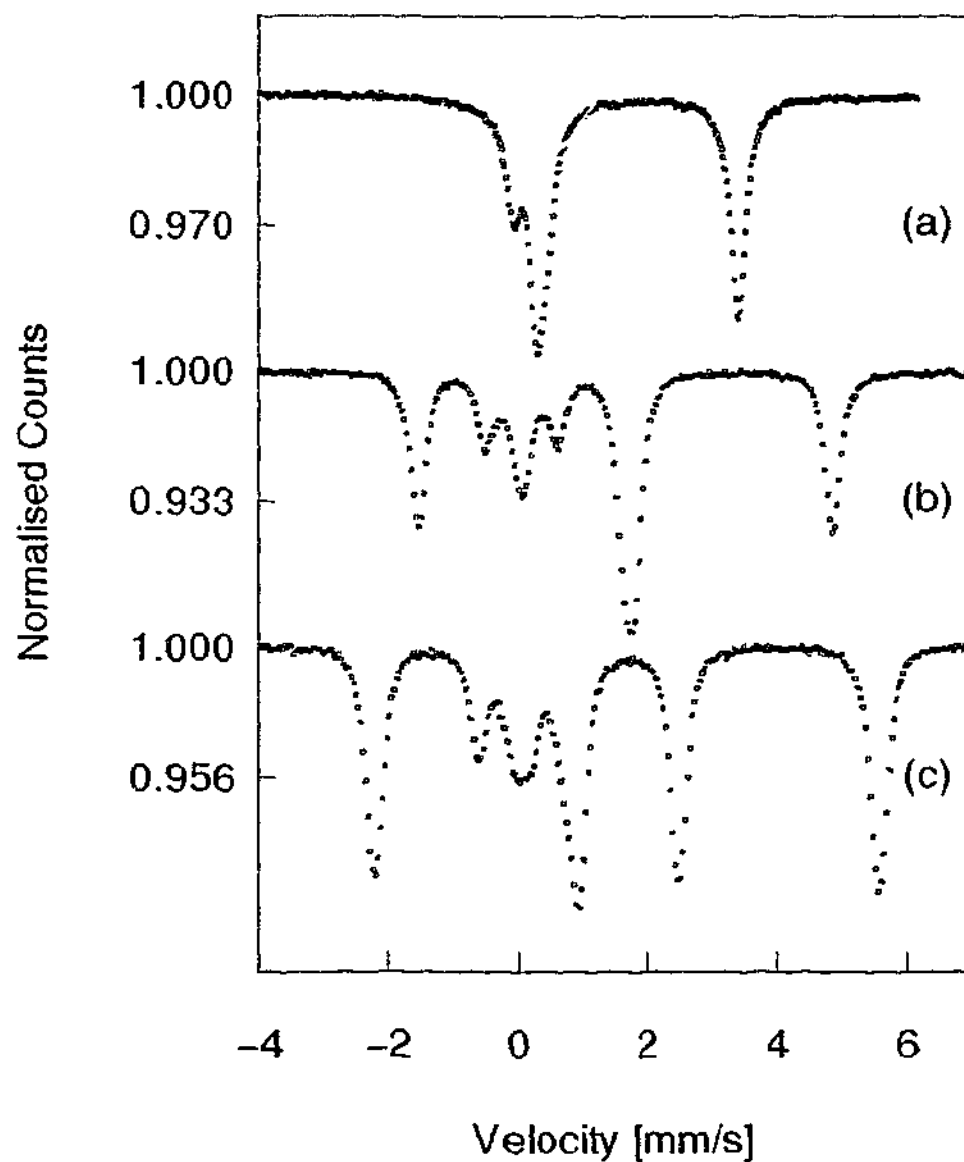


Figure 5.13: Mössbauer data for the applied field spectra. Taken at 10 K with no field (a), 10.0 T (b), and 14.3 T (c) respectively.

The Mössbauer spectrum taken in an applied field of 10.0 T exhibited interesting features with regards to the spread of the absorption peaks. Lines 1 and 6 of the smaller hyperfine field overlapped one another in the centre of lines 1 and 6 of the larger hyperfine field. This can be seen in Figure 5.13b where the peak at around 2 mm/s is broadened by the two dips. As the applied field of 10.0 T is almost equal to the measured hyperfine field of $9.75 (\pm 0.06)$ T (Table 5.3), the field at the parallel Mössbauer nucleus is reduced to almost zero. For an applied field of 10.0 T, with two sublattices each with an opposite internal hyperfine field of 9.75 T, the two measured hyperfine fields should be close to 0.25 T for opposing fields and 19.75 T for adding

fields. Fitting two sextets to the data revealed that the hyperfine fields were indeed close to these values as seen in Figure 5.14 and Table 5.6.

Table 5.6: Mössbauer parameters for the applied field spectra. The value in the parentheses indicates the uncertainty in the last figure.

Sample	IS (mm/s)	QS (mm/s)	HF (T)	Relative area %
10 T (1)	0.89(2)	1.58(6)	19.93(7)	48.1
10 T (2)	0.89(2)	1.58(6)	0.47(7)	51.9
14 T (1)	0.87(1)	1.60(3)	4.91(7)	50.9
14 T (2)	0.87(1)	1.60(3)	24.16(6)	49.1

For an applied field of 14.3 T, the sublattice with an opposing internal hyperfine field of 9.75 T, should be measured as approximately 4.6 T and the cooperative fields would be measured as approximately 24.1 T. These are very similar to the measured hyperfine fields which were equal to 4.90 (± 0.07) T and 24.16 (± 0.06) T respectively.

Fitting Lorentzian profiles to the absorption dips in the applied field spectra did not appear to fit the line shape successfully around the base of each peak. Thus the Voigtian profiles were again employed to fit the applied field data. It can be seen that line broadening occurred in the applied field spectra in Figure 5.13. After looking at these spectra in both unfolded and folded format, it was noted that the line broadening occurred along both ends of the velocity scale. It was considered that the line broadening is not a property of the material but of the drive device used in the Mössbauer set up.

The goodness of fit parameter, χ^2 , was minimised to 5.75 for the 10.0 T fit and 5.49 for the 14.3 T fit. These values are still quite large, however from Figure 5.14, the positions for each sub-spectrum appear to be correct. It is not clear why the profiles of the applied field data are not as well fit as the other Mössbauer spectra of FePS₃, however, the parameters obtained from the current fits appear to be correct. From this data it can be seen that the two moment sublattices in FePS₃ have equal and opposite internal hyperfine fields of approximately 9.8 T.

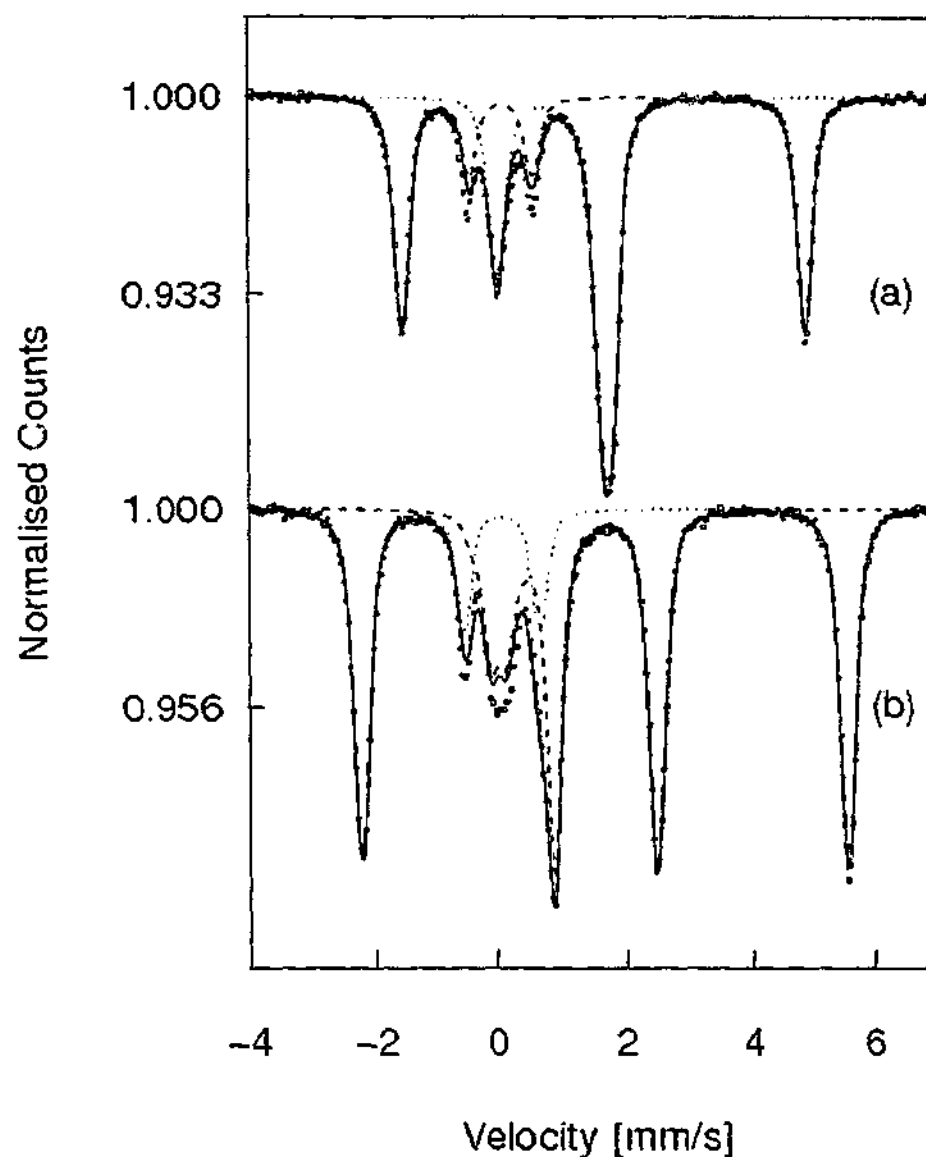


Figure 5.14: Mössbauer spectra taken at 5 K with applied fields of (a) 10.0 T and (b) 14.3 T directed parallel with the internal moment direction – the c^* -direction. The two different dashed lines indicate the two subspectra in the fit.

A plot of the internal hyperfine fields measured at each sublattice for both applied fields can be seen in Figure 5.15. The two lines on the plot indicate the trend for each sublattice as the applied field was increased. The gradients for these lines are 1.01 and -1.02, as marked on the plot. The similarity between these values is a good indication that the moments within the sublattices remain perpendicular to the ab -plane, and don't tilt in applied fields up to 14.3 T. Thus, although there are regions that appear to be under fit in the Mössbauer spectra of both the 10.0 T and 14.3 T data, the conclusions that can be made by fitting the Voigtian profiles remain the same.

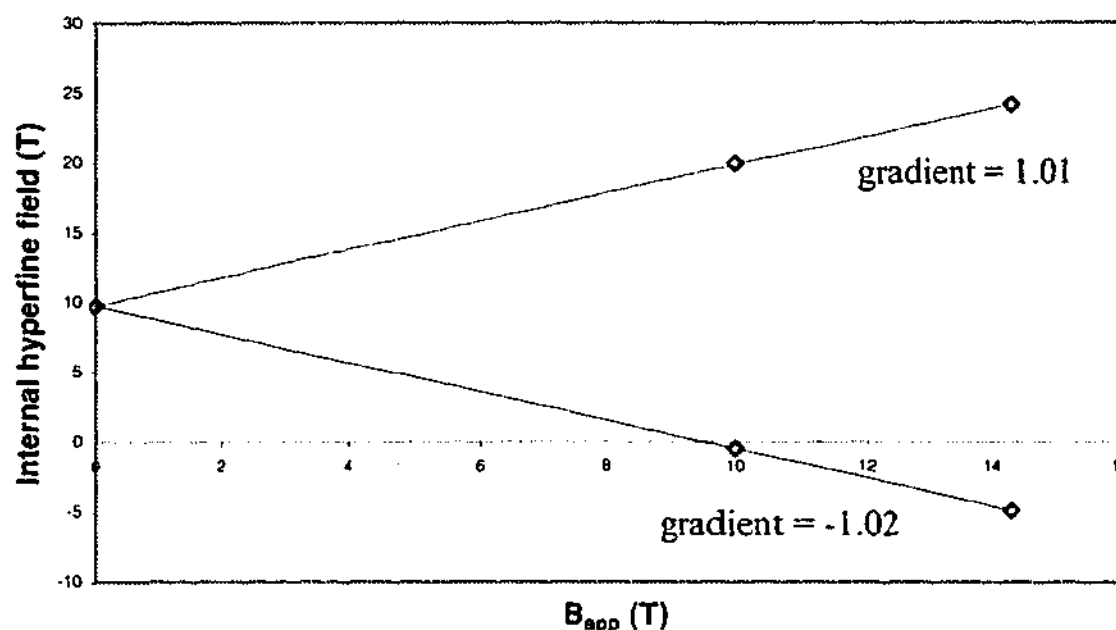


Figure 5.15: The variation of the internal hyperfine field measured for each sublattice at applied fields of 10.0 T and 14.3 T.

5.8 THE GOLDANSKII-KARYAGIN EFFECT

The effects of texture and the Goldanskii-Karyagin effect (GKE) were initially investigated using a powdered sample of FePS_3 mixed with boron nitride. Both texture effects and lattice vibrational anisotropy can affect the relative line intensities of a quadrupole split spectrum to different degrees. In general, the asymmetry due to texture is much larger than that from the GKE. Due to the extreme preferred orientation of the crystallites, the texture of the powdered sample was considerable, and had to be eliminated before testing the GKE of FePS_3 . To remove the texture, the sample was placed such that the normal to the plane of the sample holder was at the "magic angle" of 54.7° to the γ -ray direction (Ericsson & Wäppling, 1976; Grenèche & Varret, 1982). Four spectra were taken, rotating the sample by 90° in the plane of the sample holder between each measurement. This had the effect of averaging the intensities of the $\Delta m = 0$ and $\Delta m = \pm 1$ lines. The remaining asymmetry in the lines was found to be $(\text{right line}/\text{left line}) = 0.96$

± 0.02 which agrees favourably with previous results describing the GKE for powdered FePS_3 as 0.97 (Chandra & Ericsson, 1979).

The GKE experiment was repeated using the large single crystal sample. The single crystal sample was used to measure the lattice vibrational anisotropy, as the purity of the powdered sample was questionable. As mentioned in Section 5.5, the crushed sample showed evidence of an impurity, from either the crushing process, oxidation from exposure to the atmosphere, or even by some other means. Any contamination in the sample would significantly effect the highly sensitive measurements of the GKE. According to theory, by rotating the sample around 90° step wise in the plane of the "magic angle", four sets of data can be produced where the sum of these spectra should be completely randomised (Grenèche & Varret, 1982). Thus four separate GKE measurements were taken with the single crystal, ensuring that approximately the same number of counts was taken for each run. It was envisaged that the sum of the four spectra collected with the single crystal should look very similar to that obtained from the powdered sample. Each of the four spectra taken can be seen in Figure 5.16a - d with the summed spectrum in 5.16e.

The "magic angle" method will completely randomise the powdered sample and the single crystal by the same process. Any slight discrepancy between the intensity ratios may be attributed to the presence of an impurity remaining in the powdered sample. Although Chandra and Ericsson (1979) verified that texture was absent from their powdered sample, they did not mention the possibility of an impurity. As the impurity in the current powder sample was responsible for less than 2 % of the entire absorption, it is possible that impurities may not be immediately obvious in the spectra. However these impurities may affect the sensitive measurements of the GKE.

It can be seen from Figure 5.16 that there are slightly different intensity ratios between the absorption dips in each of the separate plots, however when summed, all the asymmetry due to texture should be eliminated. Two plots (b and c) showed no marked asymmetry while spectra (a) and (d) showed significant and opposite asymmetry (i.e. $R < L$ and then $L < R$). Taking the average asymmetry of all four plots, the total intensity ratio was found to be $(R/L) = 0.96$, which is the same as the asymmetry found in the powdered sample, as well as that found by Chandra and Ericsson (1979).

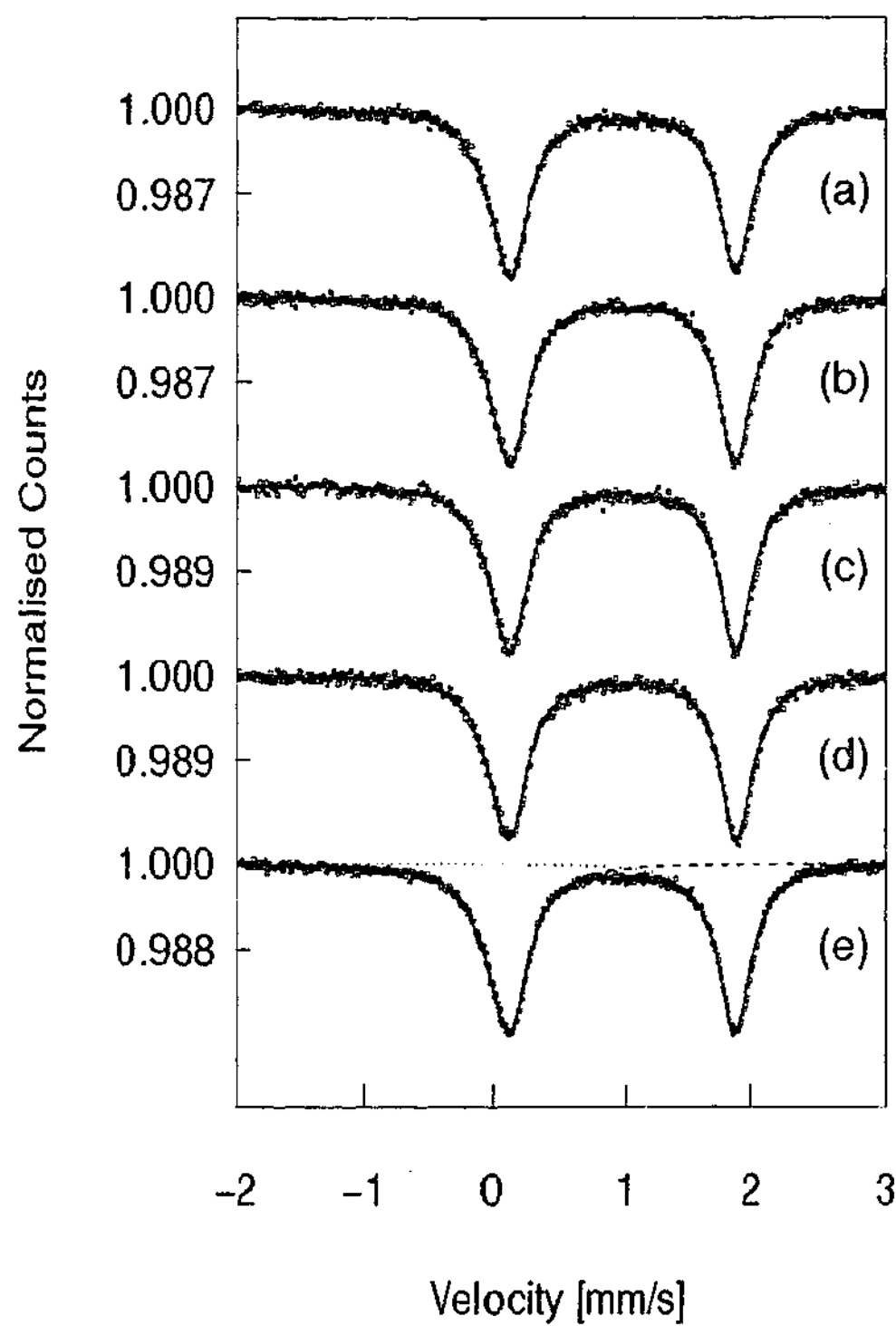


Figure 5.16: Four Mössbauer spectra taken with a 90° rotation in the plane between each plot (a-d). The fifth plot (e) is the summed spectra from (a) to (d). The summed spectrum was fitted with singlet lines to determine the asymmetry from the intensity ratio of the lines.

Two methods for sample randomisation have been discussed. The powdered cube method outlined by Chandra and Ericsson (1979) and the “magic angle” method have both been used to investigate the GKE of FePS_3 . From both studies, the vibrational amplitude was found to be

greatest along the z -direction. However, it must also be noted that although the results of these two studies gave the same result, the method of grinding a material into a powder may lead to impurities in the sample and stacking preferences in the powder, which could affect the sensitive measurements of the GKE. The "magic angle" technique is also a non-destructive way to randomise a single crystal sample. Thus it is believed that the "magic angle" technique of randomising a textured sample for GKE investigations is a better method than the powdered cube method outlined in Chandra and Ericsson (1979).

5.9 SEARCH FOR THE EFG DIRECTION

Previous research into the direction of the EFG, has found that V_{zz} is parallel to the hyperfine field (Taylor et al., 1973; Ericsson & Wäppling, 1976; Chandra & Ericsson, 1979; Bjarman et al., 1983; Jernberg et al., 1984). This corresponds to the crystallographic c^* -direction and was based on calculations from the intensity ratio of the quadrupole split lines of FePS_3 . The major assumption made by each group was that the asymmetry parameter $\eta = 0$. This assumption is not entirely correct as it does not account for the observed intensity ratio of the $\Delta m = \pm 1$ and $\Delta m = 0$ transitions in either their published or the current data. For any ratio less than 3 with $\eta = 0$, the EFG cannot be along the gamma ray direction.

The ratio of the line intensities in the RT single crystal data can be used to determine the angle between the γ -ray and the principal axis of the EFG. Keeping with the popular assumption that the asymmetry parameter, η , was equal to zero, the formula for the line intensity ratios were simplified. Equation 3.11 can be re-written with these assumptions (Equation 5.3), and the relative line intensities can be used to determine the angle between the EFG and the gamma-ray direction, θ . In this situation it has also been assumed that the principal axis of the EFG lies in the mirror plane (so $\phi = 0$).

$$\frac{I_{(\Delta m=\pm 1)}}{I_{(\Delta m=0)}} = \frac{\text{Right}}{\text{Left}} = \frac{1 + \cos^2 \theta}{\frac{5}{3} - \cos^2 \theta} \quad (5.3)$$

Using this relation, with the diagonalised Hamiltonian intensity ratio of 2.58 for the single crystal, the angle between the normal to the ab -plane and the principal axis of the EFG was

calculated to be approximately $17 \pm 2^\circ$. This angle of $17 \pm 2^\circ$ is equal within error to the angle between the c and c^* crystallographic axes of $107.1^\circ - 90^\circ = 17.1^\circ$. Knowing that V_{ZZ} must be either along the b -axis or in the mirror plane, this result implies that V_{ZZ} lies in the mirror plane. The angle indicates that it is either along the c -axis, or else at around 17° from the c^* -axis, on the opposite side to c^* (c' in Figure 5.17), if the asymmetry parameter is zero.

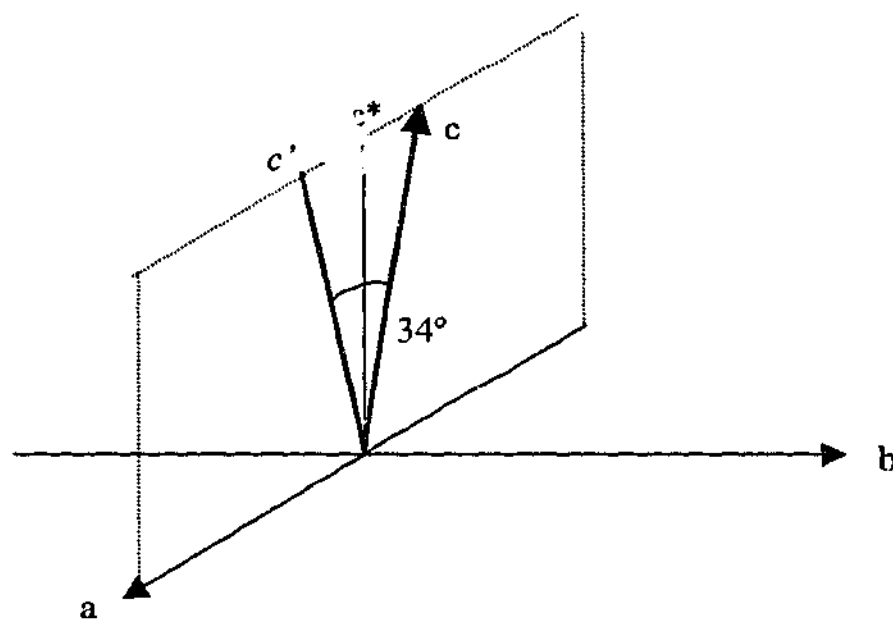


Figure 5.17: According to initial analysis, the principal direction of the EFG is aligned either along the crystallographic c -direction or along the other bold direction, x , located at 17° from the c^* direction in the ac -plane.

Each of these calculations has involved the assumption that $\eta = 0$ which is not necessarily the case for FePS_3 . By diagonalising the full Hamiltonian this parameter could be varied and fitted to the data using a variation of the fitting program CERN Minuit (Litterst & Stieler, 2003). To clarify the direction of the EFG, Mössbauer spectroscopy was performed on the same single crystal mounted in two different orientations to the original, flat sample. This ensured that the direction of the EFG changed with respect to the incident γ -ray for each spectrum. Thus with three Mössbauer spectra, there would be three intensity ratios with which to find η and θ , the angle between the γ -ray and V_{ZZ} .

The large single crystal was oriented on a 17° wedge in a sample holder such that the crystallographic $+a$ direction was facing down the slope (to within $\pm 5^\circ$). Mössbauer spectra

were taken at both room temperature and below the Néel temperature, at around 96 K. The second orientation consisted of the same sample rotated such that the $-a$ direction was facing down the slope. Corresponding high and low temperature spectra were also taken for this arrangement. The angle of 17° was chosen to coincide with the previously calculated angle between the EFG and the γ -ray when $\eta = 0$. If the EFG were indeed parallel to the c^* -direction, the intensity ratio of the two absorption dips should be 3 for the crystal oriented with the $+a$ crystallographic axis down the slope.

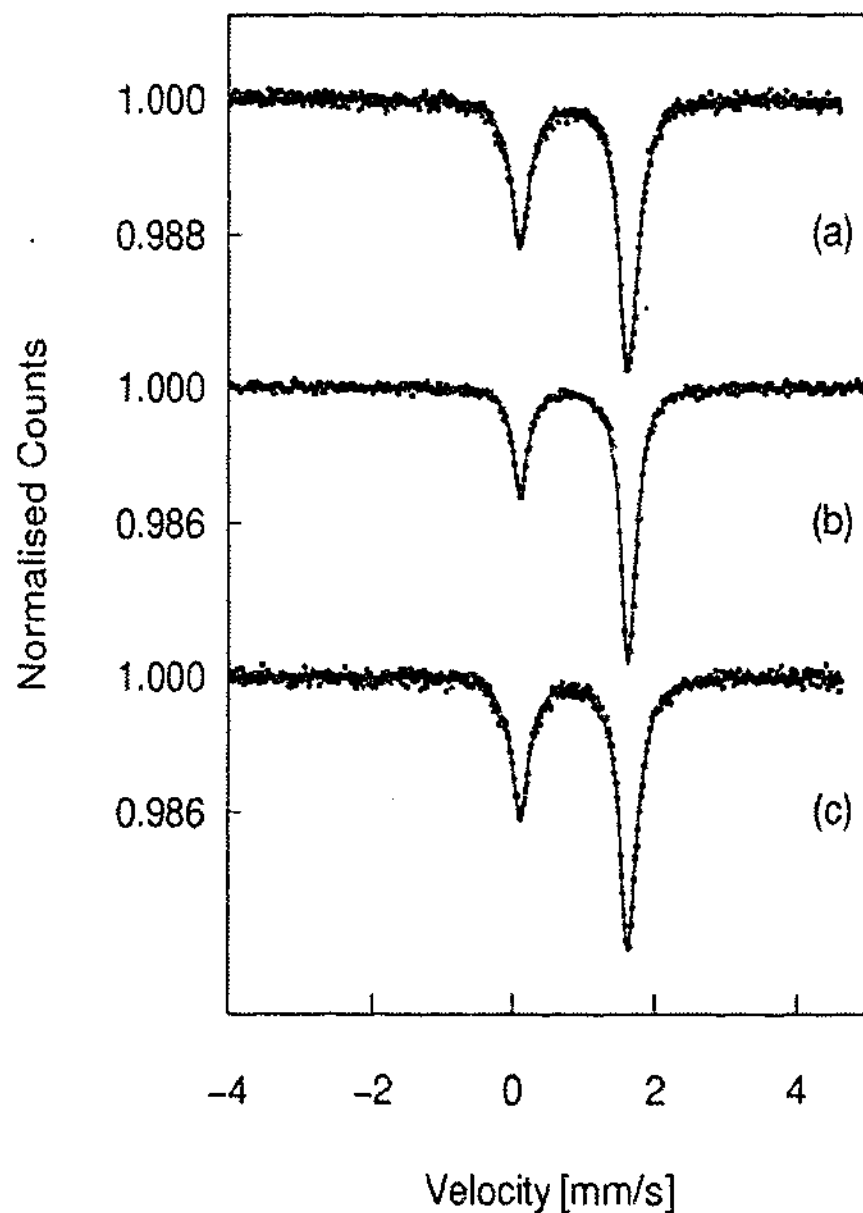


Figure 5.18: Room temperature spectra: (a) with the crystallographic $+a$ down the slope, (b) with the sample flat in the sample holder and (c) with $-a$ down the slope. These were fitted with singlets to determine the intensity ratios from the relative areas.

The three room temperature spectra can be seen in Figure 5.18 fitted with a doublet of Lorentzian line shapes. Each individual absorption dip in the spectra was also fitted with a singlet line such that the intensity ratio could be calculated from the relative areas. The linewidths of each singlet line was constrained to be the same in these fits. The asymmetry in the quadrupole split lines was found to be 2.58 for the non-tilted sample, 2.02 for the c -axis oriented parallel to the γ -ray and 1.97 for the c -direction oriented at 34° from the γ -ray beam. From this it can be seen that the original estimation of the EFG direction oriented parallel to the c -direction is incorrect as none of the intensity ratios have values close to 3. Thus V_{zz} cannot be oriented along the crystallographic c -direction.

It is also interesting to note that the intensity ratios of the $\Delta m = \pm 1$ and $\Delta m = 0$ transitions for both tilted samples are very similar. When the crystal was tilted $\pm 17^\circ$ in the ab -plane, the intensity ratios were within 0.05 of each other. This indicates that, as the value of η is constant for the crystal, the angle, θ , between the EFG and the γ -ray must be very similar for each tilt. If the intensity ratios of the two tilted orientations were the same, it could be concluded that the EFG lay parallel to the c^* -direction. Although the intensity ratios for the two tilted samples were very similar (taken as the ratio of the relative areas of each peak), they were sufficiently different to indicate that V_{zz} was not oriented along the c^* -direction. Thus it can be assumed from these results that the EFG is very close but not quite aligned to the c^* -direction.

Using Equation 3.12, the intensity ratio was calculated for a variety of θ and ϕ values with $0 \leq \eta \leq 1$. Two situations were investigated – for the V_{zz} in the mirror plane, and for V_{zz} perpendicular to the mirror plane. For each situation, the range of possible angles tested can be seen in Table 5.7.

$$\frac{I_{(\Delta m=\pm 1)}}{I_{(\Delta m=0)}} = \frac{I_{\pm 3/2}}{I_{\pm 1/2}} = \frac{\left(1 + \frac{\eta^2}{3}\right)^{1/2} + (3 \cos^2 \theta_q - 1 + \eta \sin^2 \theta \cos 2\phi)/4}{\left(1 + \frac{\eta^2}{3}\right)^{1/2} - (3 \cos^2 \theta_q - 1 + \eta \sin^2 \theta \cos 2\phi)/4} \quad (3.12)$$

Table 5.7: Possible orientations for the principal axis of the EFG

Variables	Range for θ	Range for ϕ
V_{ZZ} in ab -plane	$\theta = 90^\circ$	$0 \leq \phi \leq 90^\circ$
V_{ZZ} in bc -plane	$0 \leq \theta \leq 90^\circ$	$\phi = 90^\circ$
V_{ZZ} in ac -plane	$0 \leq \theta \leq 90^\circ$	$\phi = 0^\circ$
V_{ZZ} perpendicular to mirror plane	$\theta = 90^\circ$	$\phi = 90^\circ$

Figures 5.19a, b and c show the calculations of the situation where V_{ZZ} is in the mirror plane; when $\phi = 0^\circ$. The value of θ is the angle that V_{ZZ} makes with the x -direction. Extrapolating from these plots, the Mössbauer measurements taken with the flat sample, and that tilted at $+17^\circ$ appear to have the similar values of $\theta \approx 12^\circ$ when $\eta = 0.68$. The value of the third Mössbauer intensity ratio when the sample was tilted at -17° did not correspond to these values of θ and η . In fact only for large angles of θ , close to 45° , did the -17° tilt calculations give intensity ratios similar to the observed ratio.

It was not possible to calculate the observed intensity ratios corresponding to all three orientations of the sample for a single value of η less than one. The intensity ratios as measured from the line areas in the Mössbauer spectra are considered correct within a few percent. Other influences, which may attenuate the measured intensity ratios, include polarisation effects and thickness effects, however these influences are not significant enough to account for the mismatch in all three data sets. The sample used was noted to contain two crystallites offset from one another by approximately 60° in the ab -plane. Misalignment of the two crystallites within the single crystal sample may also have affected the intensity ratios of the two absorption lines, however, this was considered to be a small effect.

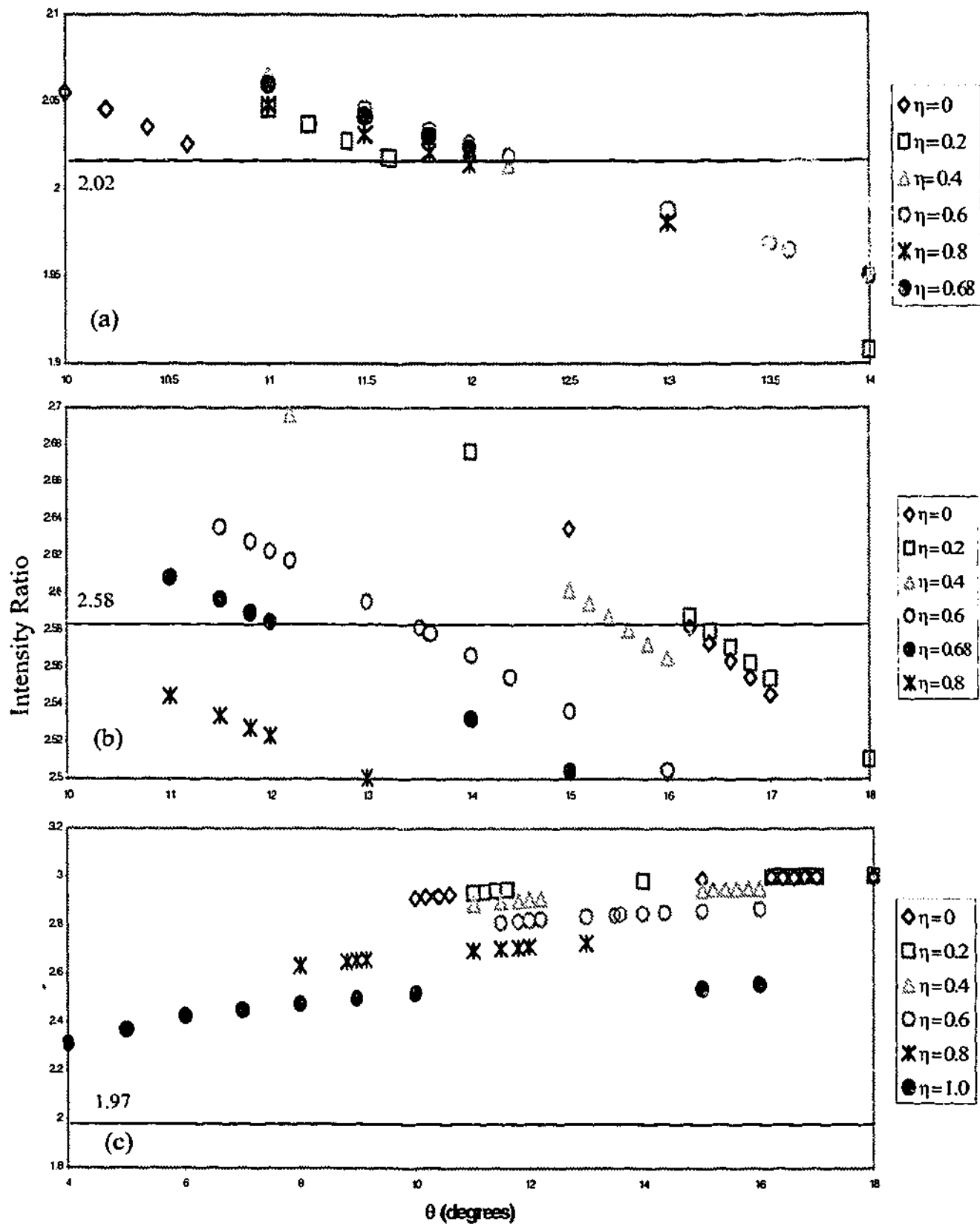


Figure 5.19: The variation of intensity ratios from the three Mössbauer spectra: (a) taken with an angle of $+17^\circ$, (b) with no tilt and (c) with an angle of -17° . The full circles in (a) and (b) represent the η value that is similar to both intensity ratios at $\theta \approx 12^\circ$.

One possible influence that may have affected the relative line intensities was polarisation. The effect of the γ -ray polarisation from the single crystal was estimated from Equation 5.4. In this equation the first factor of $1/2$ represents the amount of the beam that cannot be absorbed by the crystal because it has the wrong polarisation. For the remaining $1/2$ intensity of the γ -ray beam, the exponential describes the amount that is transmitted. The ax represents the exponent corresponding to a percentage absorption. For instance, 0 % absorption would be described by $ax = 0$, and the entire γ -ray would have been transmitted. A γ -ray transmission of 95 % would have $ax = 0.1$, which indicates that the absorption dip is around 5 %.

$$\frac{1}{2} + \frac{1}{2} \exp(-ax) \approx \frac{1}{2} + \frac{1}{2} - \frac{ax}{2} + \frac{(ax)^2}{4} + \dots \quad (5.4)$$

Calculating this approximation showed approximately 1 – 2 % increase in the intensity ratios when compared with the ratios with polarisation accounted for. Keeping this in mind, this estimation did not take into account the thickness effects of the single crystal. In the tilted crystal sample, the γ -ray would have to pass through slightly more material, allowing for more absorption. As the degree of absorption in the two dips is different, this would affect the relative line intensity ratio. Again, this would account for less than 5 % difference in the peak asymmetry. It is not clear why the calculations for the -17° tilt sample did not produce reasonable results, however the experimental results cannot be ignored, and would suggest that the most probable orientation of the principal axis of the EFG, was in the mirror plane, within a few degrees of the c^* -axis.

The principal axis of the EFG has also been found using the computer-modelling program WIEN2k (Blaha et al., 2001). By creating the atomic positions in the monoclinic crystal structure, the effects of the electron charge density close to the Fe atom could be calculated. Calculations made by Dr A. E. Smith for the Fe^{2+} ion could then be related to the experimental Mössbauer results from above.

When setting up the monoclinic cell structure in WIEN2k, the preferred centring of the crystallography was b -centring rather than c -centring which has been used throughout this dissertation. Thus the unit cell parameters had to be changed to meet with these requirements of WIEN2k. For a c -centred structure, the cell dimensions are $a = 5.93 \text{ \AA}$, $b = 10.28 \text{ \AA}$, $c = 6.72 \text{ \AA}$

with an angle of $\beta = 107.1^\circ$ (Klingen et al., 1968). In WIEN2k, the *b*-centred structure had dimensions $a = 5.934 \text{ \AA}$, $b = 7.57 \text{ \AA}$, $c = 10.28 \text{ \AA}$ with an angle of $\gamma = 121.3^\circ$. The calculated magnitude for the principal axis of the EFG felt at the Fe nucleus was $2.503 \times 10^{21} \text{ Vm}^{-2}$. This value corresponds to a quadrupole splitting of approximately 0.57 mm/s , which is close to $1/3$ of the value of the measured quadrupole splitting of 1.53 mms^{-1} . The large discrepancy between these values may be partially due to the assumptions made by WIEN2k about the electron distribution in the lattice. The asymmetry parameter found by the WIEN2k program was $\eta = 0.272$. This does not correspond to the asymmetry parameter of 0.68 that was found from the intensity ratios for two of the three sample orientations in the Mössbauer spectra. This is another indication that the calculations from the intensity ratios do not describe all 3 sets of observed data sufficiently. The angle of the EFG when compared to the *c*-centring lattice was calculated to be approximately 10° from the *c**-axis.

Taking a broad overview of the results obtained from both Mössbauer spectroscopy measurements and calculations from WIEN2k, it appears that the principal axis of the EFG lies close to the *c**-axis. This general view is taken from the results of two Mössbauer measurements taken at $\pm 17^\circ$ to the *c**-direction, which gave very similar intensity ratios. This would suggest that the EFG lay along the mirror plane, somewhere in between the two tilted sample orientations. However in a more detailed investigation, if the EFG did lay parallel to the *c**-direction, the intensity ratio of the flat sample should be 3, rather than 2.58. The WIEN2k calculations appear to support the general overview and not the more detailed investigation. It is not known why FePS₃ does not have an intensity ratio of 3, similar to FePSe₃, as polarisation and thickness effects do not play a significant role. The multi-crystallite structure of the FePS₃ sample may affect the measurements from the Mössbauer spectra, as although the crystallites have a common *c**-axis, the *ab*-planes do not coincide. However it is not known to what degree this will affect the results. Thus there appears to be a degree of inconsistency in the results from various Mössbauer spectra and calculations. Therefore, from the results obtained in this investigation, the direction of the EFG cannot be determined more accurately than the broad overview above.

5.10 CONCLUSIONS

The SQUID magnetisation data indicated a slight difference between field cooled and zero field cooled measurements, which implies that in the presence of an applied field, a metastable state is retained in the ordering of the third dimension. This is responsible for the increases in susceptibility at low temperatures and implies that the magnetic sublattices are not strongly correlated. From the high field magnetisation data it was found that the anisotropy energy of the Fe ions is larger than the exchange between them such that spin flops do not occur at low temperatures.

From Mössbauer spectroscopy measurements, it was found that the magnetic moments are aligned within a couple of degrees, parallel and antiparallel to the crystallographic c^* -axis. The iron nucleus experiences a hyperfine field of only $9.75 (\pm 0.06)$ T, which, due to covalency effects, is much lower than the hyperfine field of α -Fe of 33 T. This was confirmed with applied field Mössbauer spectra in which two moment sublattices exhibited different hyperfine fields dependent upon the magnitude of the applied field. The average hyperfine field from these measurements was 9.8 ± 0.1 T.

From GKE measurements, the lattice vibrational amplitude is greatest along the z -direction. It was shown that a well randomised powder sample may contain impurities, and that the method of the "magic angle", when applied to a single crystal, is sufficient to completely average out the intensities of the $\Delta m = \pm 1$ and $\Delta m = 0$ transitions. The "magic angle" technique is also a non-destructive method of randomisation ideal for single crystal measurements.

Finally, the general direction of the EFG was found to be close to the c^* -direction, however not aligned with it exactly. The results could not be determined more definitely as there were internal inconsistencies between the observed and calculated data. Polarisation, thickness effects and sample quality were the most probable explanation for the discrepancy between these results.

CHAPTER SIX

6: Results and Discussion of Neutron Diffraction Techniques

Neutron diffraction was considered an excellent tool for investigating the magnetic properties of FePS_3 and thus a variety of neutron diffraction techniques were employed. Scans were taken with powdered and single crystal samples, in environments both above and below the magnetic ordering temperature. Comparisons between the scans taken in different environments could therefore reveal information about the magnetic structure of FePS_3 . Although each neutron scattering technique gave unique information, it was only through combining all of the results that a complete picture of the magnetic structure could be devised.

6.1 POWDER DIFFRACTION OF FePS_3

The powder diffraction scans taken at various temperatures with MRPD can be seen in Figures 6.1 and 6.2. The wavelength of the neutrons for each of these scans was 1.666 Å. Figure 6.1 shows the data taken at room temperature while 6.2 shows the emergence of magnetic Bragg peaks at temperatures below 130 K. Each plot within Figure 6.2 has been adjusted by a value of 0.6918° along 2θ to account for the instrumental zero shift of MRPD. This value was obtained by initial fitting of the room temperature spectrum using the analysis program FullProf (Rodriguez-Carvajal, 1998). All observed Bragg peaks were offset from the calculated positions by this value.

The nuclear peaks in the room temperature data were fitted using two fitting programs based on the Rietveld method, FullProf (Rodriguez-Carvajal, 1998) and Rietica (Howard & Hunter, 1996). The parameters from the best fit can be seen in Table 6.1 below. The goodness of fit can be seen in the two factors Bragg R and χ^2 . For a perfect fit, both of these values go to 1.

Table 6.1: Cell and refinement parameters from the Rietica refinement of FePS_3 at room temperature. The plot of this fit is seen in Figure 6.1.

a (Å)	b (Å)	c (Å)	β	Bragg R	χ^2
5.9469	10.2981	6.7152	107.05°	5.896	5.066

The best-fit pattern from Rietica can also be seen in Figure 6.1 below. The crosses indicate the data points, while the line through these points indicates the calculated fit. The small markers below the plot indicate the positions of expected Bragg peaks, while the pale line at the base of the plot shows the difference between the data points and the fit.

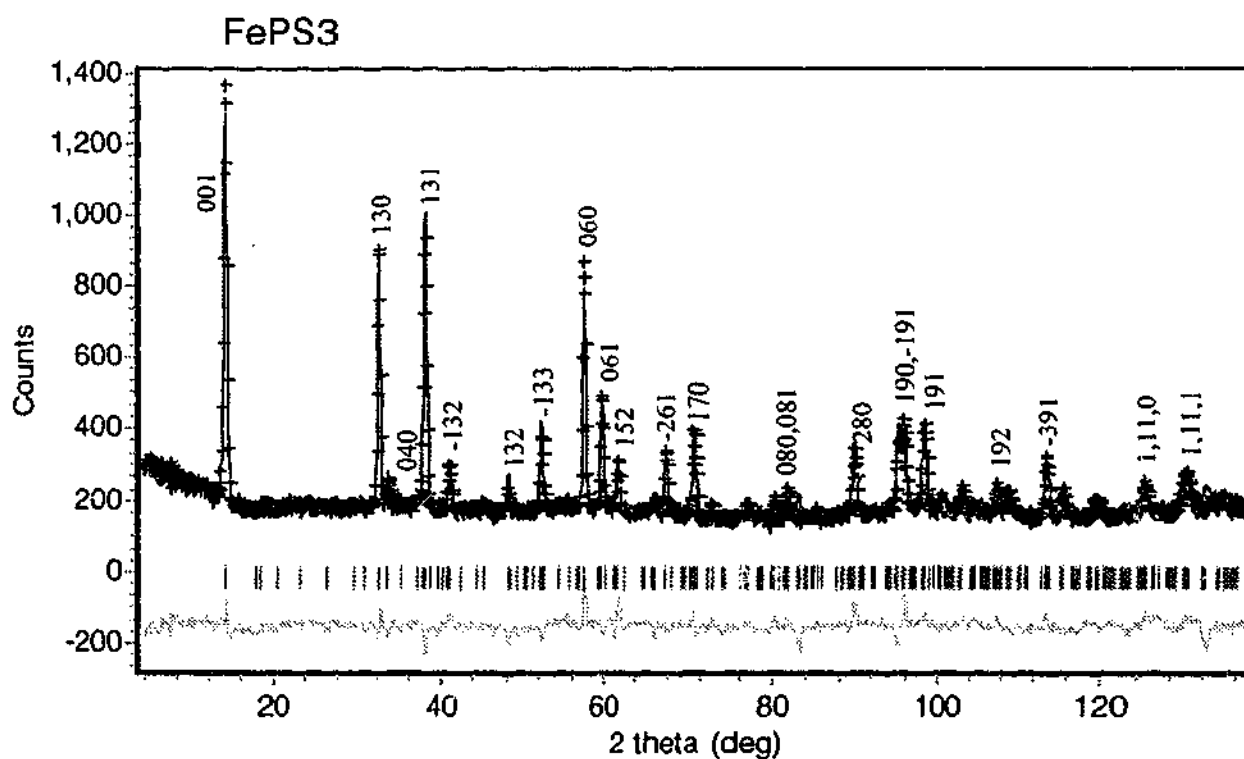


Figure 6.1: Refinement of FePS_3 using the Rietica analysis program. The line through the crosses indicates the fit to the data. The pale line at the bottom of the plot is the difference between the data and the fit.

Although the goodness of fit parameters in Table 6.1 do not indicate a perfect fit, the pale difference line in Figure 6.1 appears quite flat with only a few bumps indicating a mismatch between the observed and calculated patterns. By observing the peak shape in the difference plot,

the type of mismatch can be determined. For some peaks the observed intensity was smaller than the calculated intensity and for some, it was larger. The mismatches appeared to be random with scattering angle, however the peaks that were over-fit with the calculated pattern were mostly reflections with l not equal to zero (eg 131, 132, -133, 081, -191), and those that were under-fit occurred at positions where l was equal to zero (eg 130, 060, 280, 190). This is an indication that the major difference between the calculated and observed peaks is due to the preferred orientation of the crystallites within the powder sample.

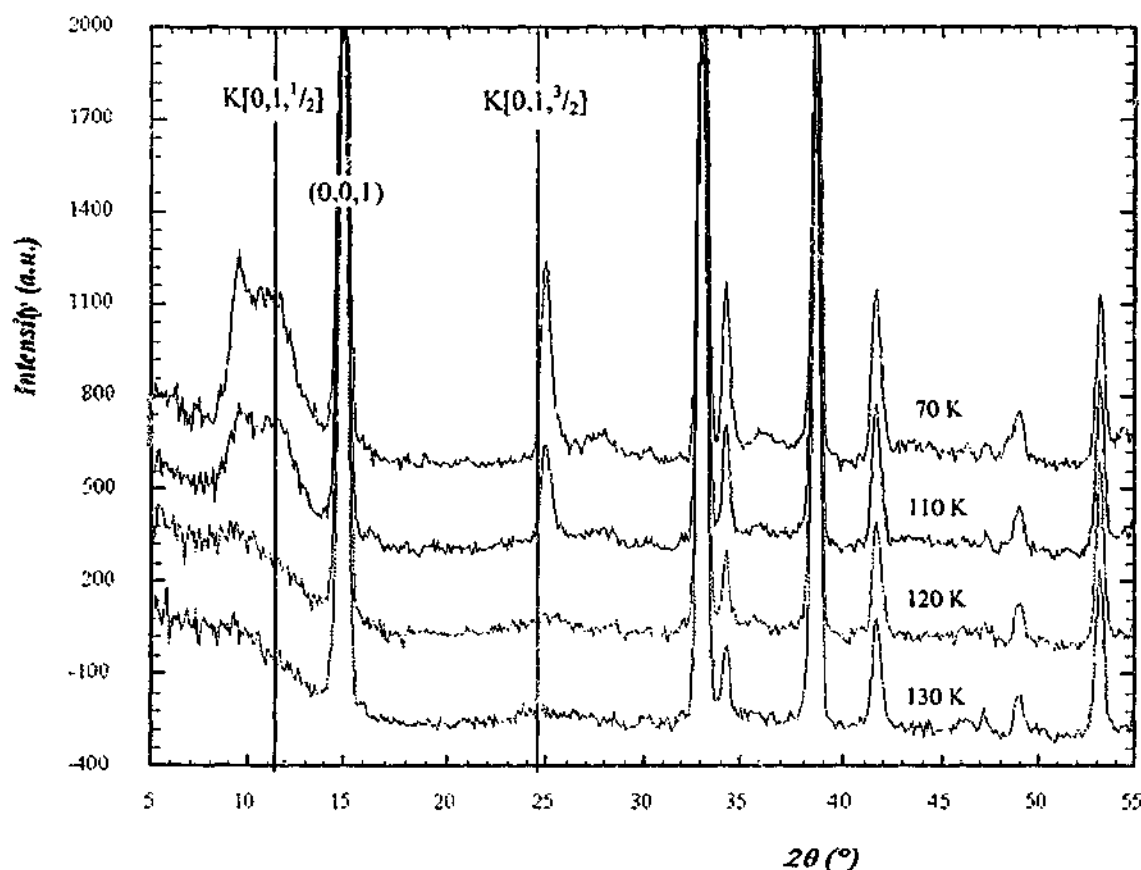


Figure 6.2 Neutron powder diffraction scans of FePS_3 at 1.666 \AA . Scans were taken at temperatures above and below $T_N = 120 \text{ K}$. Each spectrum is shifted up 300 counts from the previous spectrum for clarity. The two lowest magnetic Bragg peaks from Kurosawa et al. (1983) are labelled with K .

In Figure 6.2, magnetic peaks are seen to emerge around 120 K with well-defined peaks at 70 K indicating increased magnetic order with decreasing temperature. The most obvious magnetic peak occurs at a scattering angle of around 25° in 2θ . In the spectra taken below the ordering temperature at scattering angles between 8° and 12° in 2θ , a diffuse set of peaks was observed.

Clearly magnetic in nature, the unresolved peaks remained diffuse at lower temperatures rather than becoming sharper with increased magnetic order. Initially the hump was thought to consist of three or more magnetic Bragg peaks, overlapping to create an apparently diffuse band.

It was interesting to note that Kurosawa et al. (1983) did not observe these peaks below 12° in 2θ . In fact the lowest magnetic peak observed by Kurosawa et al. (1983) was labelled $(0, 1, \frac{1}{2})$ at 12.1° in 2θ . The two lowest magnetic Bragg peaks obtained from this study can be seen in Figure 6.2 labelled with a K. The $(0, 1, \frac{3}{2})$ peak also appears to be misaligned with the current data.

Kurosawa et al. (1983) used a pseudo-single crystal containing about 100 single crystals, which were rotated within the neutron beam to calculated hkl positions. It is not surprising then that the low scattering angle peaks were missed. The presence of these peaks in Figure 6.2 is therefore an indication that the magnetic structure defined by Kurosawa et al. (1983) is incorrect. It would not be possible, with the propagation vector of $[0, 0, \frac{1}{2}]$, to obtain magnetic reflections below a scattering angle of 12° . A magnetic structure that encompasses these low angle peaks would have to involve a doubling of the crystallographic unit cell along more than one direction. For instance a doubling along the a direction as well as their proposed doubling along the c direction. Thus there is strong experimental evidence to suggest that the proposed propagation vector is not $[0, 0, \frac{1}{2}]$.

From the discrepancies between the current data and that of Kurosawa et al. (1983), it was decided that the key to determining the true magnetic structure of FePS_3 lay in those reflections below a scattering angle of 12° in 2θ . The sample was again mounted in the cryofridge on MRPD and measured with 1.98 \AA and 5.0 \AA neutrons at 5 K. As the wavelength of the neutrons was increased the resolution in Q -space also increased, although the intensity of the reflections decreased significantly. The pattern taken with a wavelength of 5.0 \AA can be seen in Figure 6.3 (a) along with the 5 K data taken with 1.98 \AA (b) and 1.666 \AA (c) neutrons.

The dotted line in Figure 6.3 defines the same magnetic Bragg peak at low scattering angles in each scan. The slight increase in wavelength to 1.98 \AA did not appear to resolve the diffuse hump sufficiently to expose any structure. The 5 \AA data appears disjointed with breaks in the background corresponding to steps of 4° in 2θ . The regularity of these steps indicates a possible detector problem. The background was calibrated using the available computer package (*smooth*,

(Kennedy, 1994)) as well as a least squares fitting technique. Neither calibration technique removed the steps from the background as can be seen in Figure 6.4. Thus these instrumental errors made observations of the low scattering angle peaks very difficult.

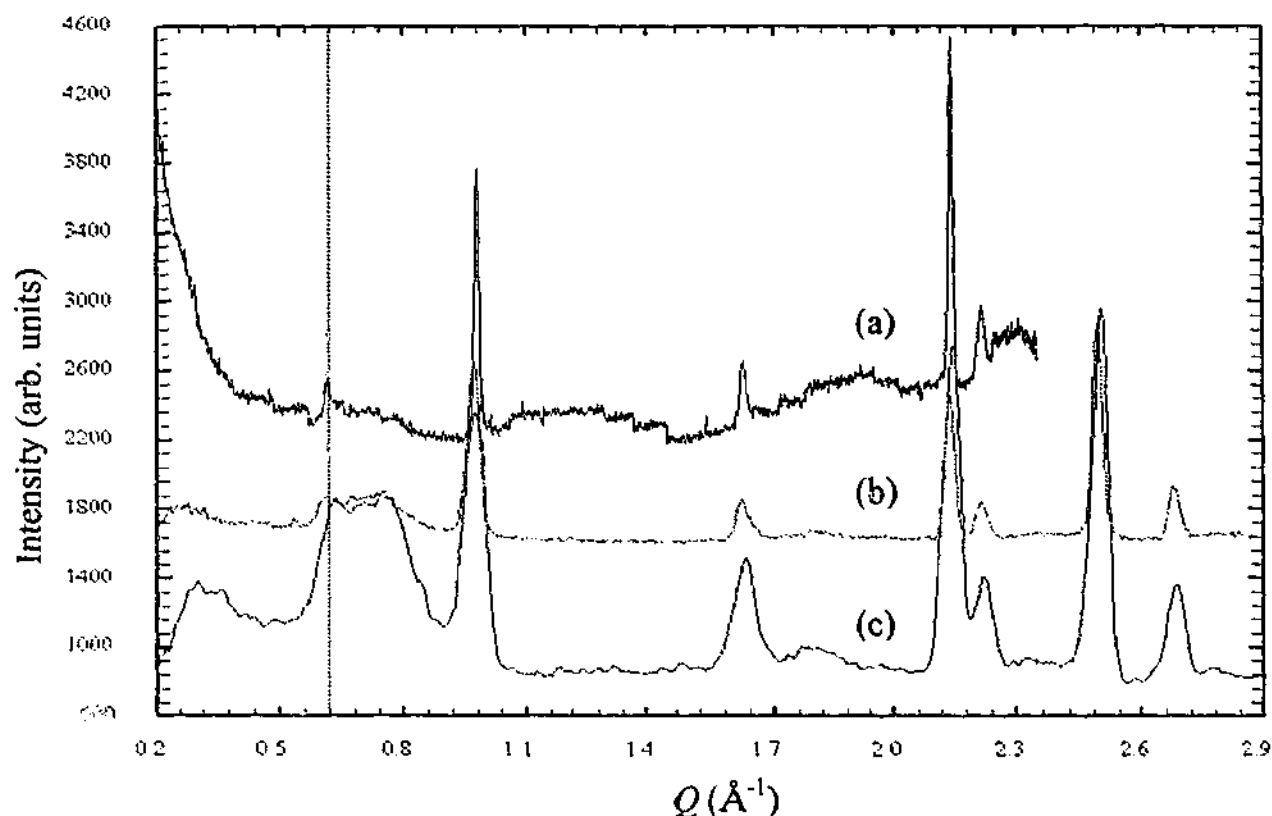


Figure 6.3: Powder neutron diffraction data taken at 5 K with (a) 5.0 Å, (b) 1.98 Å and (c) 1.66 Å neutrons. The position of the dotted line indicates the position of the first magnetic peak in each spectrum. Each plot has been shifted along the Intensity axis for clarity.

The strong peak in the 5 Å data at around 0.98 \AA^{-1} in Q -space corresponds to the 1st nuclear Bragg peak, while the first magnetic peak can be seen around 0.61 \AA^{-1} in Q -space. The diffuse magnetic peaks on the high angle scattering side of the first magnetic Bragg peak appeared to have far less intensity in the 5 Å data, when compared to either the 1.98 Å or 1.666 Å data. Due to low intensities and the relative step height in the background, it was difficult to confirm how well resolved the diffuse magnetic peaks were.

From this result, two possibilities were present. One idea was that the diffuse magnetic peaks were still present at 5 Å, but not easily seen with the detector resolution difficulties. The other possibility was that there was only one magnetic Bragg peak at 0.61 \AA^{-1} . The loss of magnetic

intensity in the diffuse peak at high wavelengths could be an indication of an energy dependent magnetic event, such as magnon scattering.

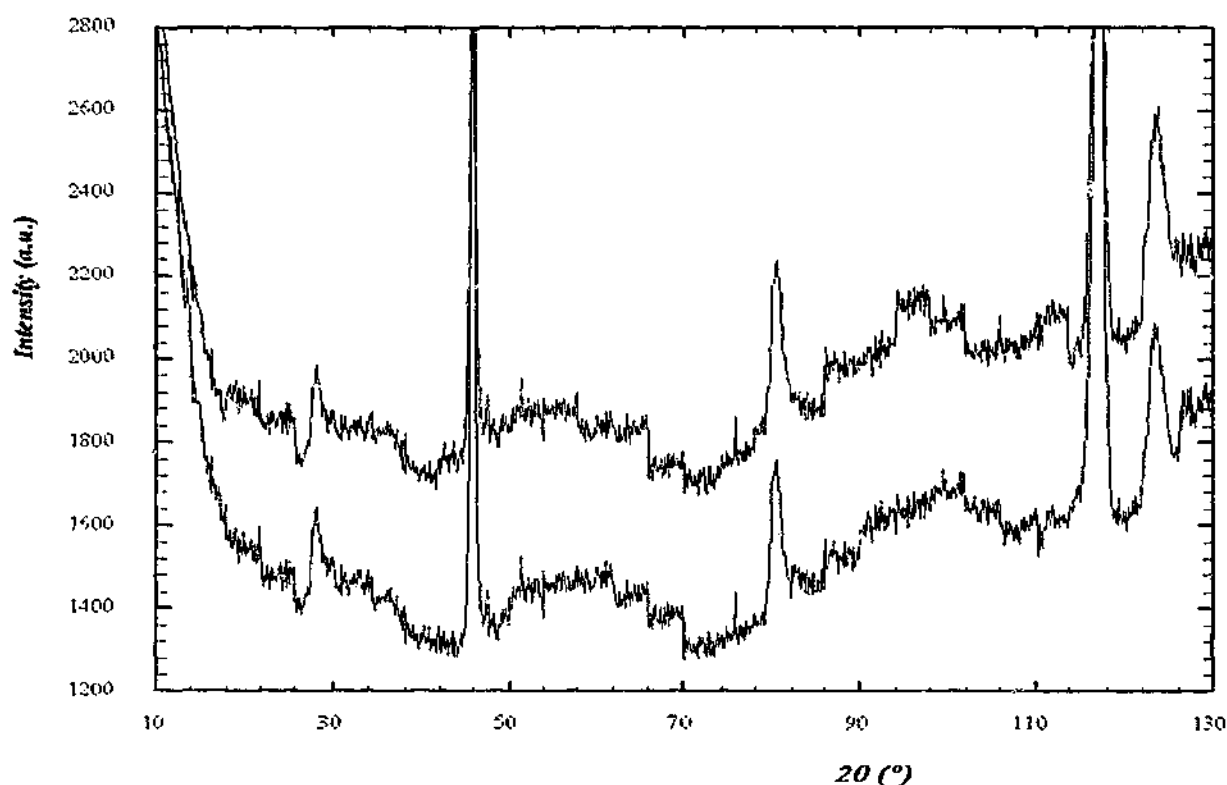


Figure 6.4: MRPD data taken at 5 Å. The top plot includes background correction using "smooth" (Kennedy, 1994) while the lower plot shows the corrections from the least squares fitting. The two plots have been separated by 350 units.

6.2 ENERGY ANALYSIS OF FePS_3 USING LONGPOL

From the powder diffraction patterns of MnPS_3 , the magnetic peaks were heralded by distinctive trailing edges on the high scattering angle side of the magnetic peaks. The trailing edges only occurred below the ordering temperature and represent a rod-like scattering profile in reciprocal space. These trailing edges were thought to have resulted from one of two possibilities; incomplete long-range order, or spin waves in the lattice.

The exchange interactions between the Mn layers in MnPS_3 have been found to be very weak due to the small single-ion anisotropy from the spherical symmetry of the half full d -shell (Wildes et al., 1998). For manganese, the 3-dimensional magnetic order relies on the small interplanar exchange interaction and magnetic dipole-dipole interaction. The calculations of the

anisotropy of the magnetic dipole interaction corresponded well to the anisotropy measured in the spin-flop field (Goossens et al., 2000). Thus the long-range order in MnPS_3 is not well-established perpendicular to the planes. This could result in the rod-like profiles in reciprocal space. Thus for the MnPS_3 , the trailing edges in the neutron diffraction data could be a result of the short-range order perpendicular to the plane. However, the static structure may not be the cause of the trailing edges. Another popular theory lies with spin wave excitations in the lattice.

Magnons were considered as a possible energy dependent event that could cause trailing edges in the MnPS_3 diffraction pattern as well as the diffuse magnetic reflections at low scattering angles in FePS_3 . Wildes, Roessli, Lebeck and Godfrey measured the magnon dispersion relation for MnPS_3 in 1998. They found that the magnon band gap at reciprocal lattice positions was 0.5 meV. The plot of this can be seen below in Figure 6.5. For wave vectors oriented along the crystallographic c^* -direction, there is little increase in the magnon energy. This reflects the small exchange interactions between the layers of Mn ions. Neutrons with a wavelength of 1.666 Å, corresponding to an energy of 29.6 meV, have sufficient energy to excite magnons in the magnetic lattice, even at the lowest temperatures. This would result in magnetic intensity around each of the magnetic reciprocal lattice positions directed perpendicular to the ab -plane.

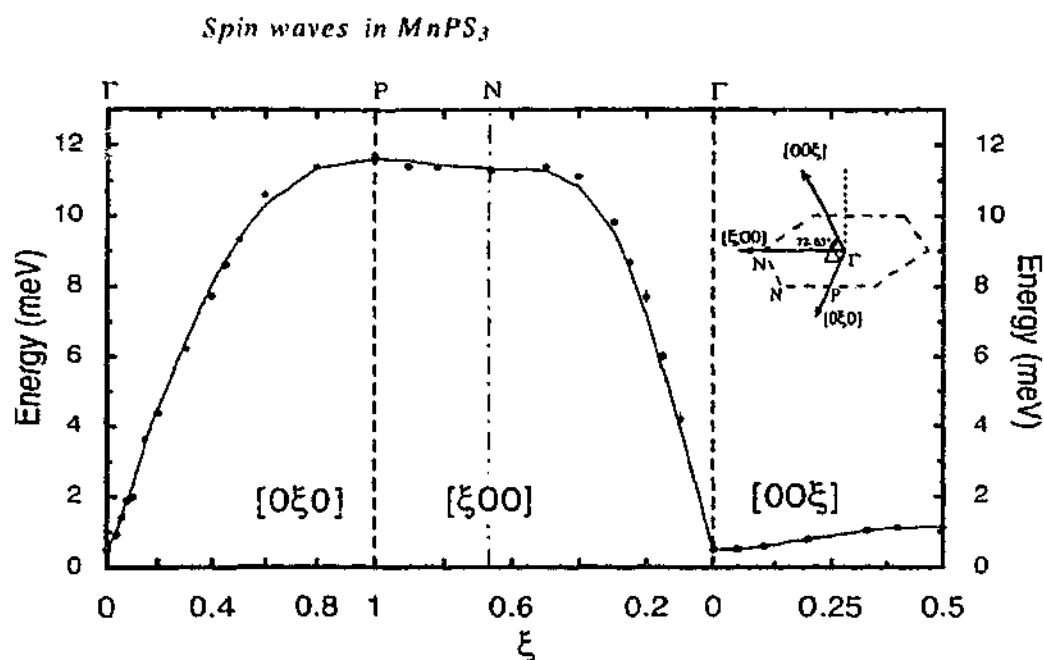


Figure 6.5: Band gap calculations for MnPS_3 calculated by Wildes et al. (1998)

However one great difference between MnPS_3 and FePS_3 is the relative strength of the single-ion anisotropy of the metal ions. Trailing edges were not immediately obvious in the powder

diffraction pattern of FePS₃, which could have been an indication of the increased single-ion anisotropy of Fe compared with Mn. This indicates that the magnon band gap is indeed much larger in Fe, and therefore less likely to be observed.

The energy of the magnon band gap was investigated for FePS₃ by comparing the MRPD spectra taken at different wavelengths. The diffuse peaks at low scattering angles were visible for 1.98 Å neutrons with an energy of 20.6 meV, but not apparent for 5.0 Å neutrons with only 3.2 meV energy. It was thus believed that the excitation energy lay somewhere between these energies, such that diffuse scattering due to magnons was observed at 1.98 Å but not 5.0 Å. Thus the magnon band gap, otherwise known as the energy required to set up spin-waves through the lattice, must be greater than 3.2 meV but less than 20.6 meV.

Initially the magnon band gap for FePS₃ was calculated by comparing it with the known energy for the MnPS₃ band gap. The band gap energy was related to the exchange field between moments for Fe and Mn. From the high field susceptibility measurements taken in Amsterdam (Section 5.3), the field required for spin flop in FePS₃ was greater than 40 T. The spin flop field for MnPS₃ at 4 K was about 4.7 T – around an order of magnitude difference. Thus, if the spin flop field was directly related to the magnon energy, then the band gap energy for FePS₃ would be expected to be at least 10 times greater than the accepted value of 0.5 meV found for MnPS₃ (Wildes et al., 1998). This rough estimate placed the magnon band gap within the range observed in the MRPD data.

To verify this estimate for the magnon band gap, previous Raman spectroscopy results were also examined. A peak that was attributed to magnons was observed in the Infrared spectra of FePS₃, at a frequency of 122 cm⁻¹ at 21 K (Sekine et al., 1990a). This corresponds to an energy of 15 meV. This peak was attributed to a magnon, as the position of the peak shifted to higher frequencies as the temperature was decreased. It was also noted that the peak only occurred at temperatures below the Néel temperature. The energy required to excite magnons within a magnetic lattice also increases as the sample temperature decreases, due to the increasing sublattice moment within the material. Thus extrapolation of the Raman spectra gave a magnon band gap energy of greater than 13 meV at 100 K. This was slightly different to the rough estimate obtained from comparisons with MnPS₃, however it still lay within the range of 3.2 meV to 20.6 meV. The initial estimate was based on the assumption that the magnon band gap energy was proportional to the exchange interactions, however this is not entirely true. In FePS₃ the

magnon energy gap is very much greater than for MnPS_3 due to the much larger single-ion anisotropy. For neutrons with a wavelength of 5 Å, the maximum energy available is well below the excitation energy of 13 meV for the magnons. On the other hand, neutrons with wavelengths of 1.666 Å and 1.98 Å have sufficient energy to excite spin waves. Thus the loss of diffuse intensity at long wavelengths may be due to the large magnon band gap.

An energy analysis was conducted using LONGPOL to observe any energy changes in the scattered neutrons. The sample and detectors were set up to observe time of flight data for known magnetic Bragg peaks and for the diffusely scattered peaks at scattering angles between $Q \sim 0.7$ - 0.82 \AA^{-1} . The sharp magnetic peaks at $Q = 0.61 \text{ \AA}^{-1}$ and $Q = 1.65 \text{ \AA}^{-1}$ were considered to be Bragg reflections. The polarisation was oriented along the scattering vector for the middle of the eight detectors in the ^3He detector bank. Energy analysis was conducted at temperatures within 1 K of 100 K. This temperature was chosen as it was suitably below the Néel temperature for the sample to be magnetically ordered, yet high enough in energy to thermally excite magnons in the magnetic lattice. It was considered that 100 K would be sufficient for a large magnon population such that the polarised neutrons would scatter with an energy gain. No decrease in energy would be observed, as the incident neutron energy of 6 meV (3.6 Å) is too low to excite magnons.

Data was collected in the centre of each of the eight detectors, which were separated by around 7° in 2θ . The detectors were rotated by around 1° between each data set such that data points were obtained for a continuous range in Q space. The raw data was initially examined using a cross-correlation analysis program called Nucros2 (Kennedy, 2001).

Cross correlation involves relating the pseudo random sequence fed to the flipper with that appearing in the detectors after polarisation analysis. For elastic scattering, the input and measured signals are separated by τ , the time of flight of the incident beam. A non spin-flip (NSF) event will give a signal identical to the spin flipper signal while a spin-flip (SF) event will be opposite in magnitude (Figure 6.6). Inelastic scattering will be obvious from the position of the correlated peak, produced from the overlapping signal of the spin flipper.

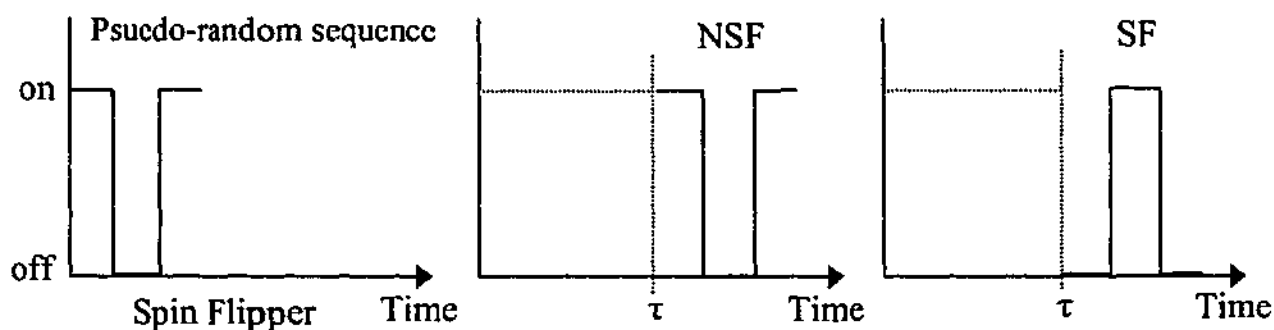


Figure 6.6: Relative signals for a non-spin flip and spin flip neutron with respect to the original spin flipper orientation. The output signal is separated from the input by the time of flight, τ .

The cross correlation analysis displays the output spectrum of NSF minus SF. If the polarisation of the neutrons is oriented along the scattering vector, then all magnetic scattering will be SF. If the polarisation is orthogonal to the scattering vector, the magnetic scattering will be half spin flip and half non-spin flip. Thus there will be no magnetic output from the orthogonal cross correlation spectrum. By subtracting the orthogonal cross correlation outputs from the aligned spectrum, the true order of the magnetic peaks can be found.

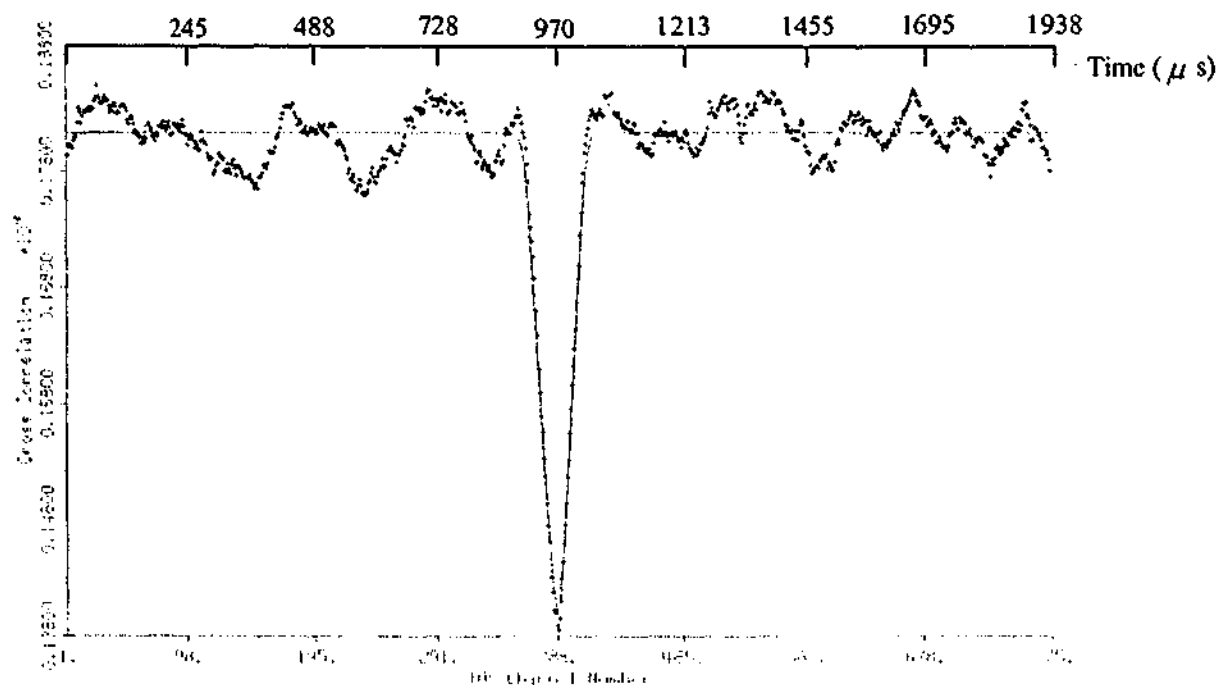


Figure 6.7: Data cross-correlated using Nucros2 (Kennedy, 2001). The negative dip indicates that the neutron spin has been flipped, and is therefore magnetic. This plot was collected in the detector at a scattering angle of 25° in 2θ .

This information was used to differentiate between the magnetic and nuclear scattering, depending on the orientation of the polarisation with the scattering vector. The peaks were also classified as either elastic or inelastic in the first instance by the position in the time of flight data. A peak observed in channel number 388 was considered to be elastically scattered, while peaks at a higher channel number indicated that the neutrons scattered with an energy loss and those in lesser channels scattered with an energy gain. This can be seen in the cross-correlated data in Figure 6.7.

6.3 MAXIMUM ENTROPY ANALYSIS

The peak in Figure 6.7 appears to be quite broad, as the cross-correlation analysis did not remove any of the instrumental uncertainties. Therefore, the peak width is not a true representation of energy dependent scattering in the material. A maximum entropy package was used to de-convolute the instrumental resolution in the data.

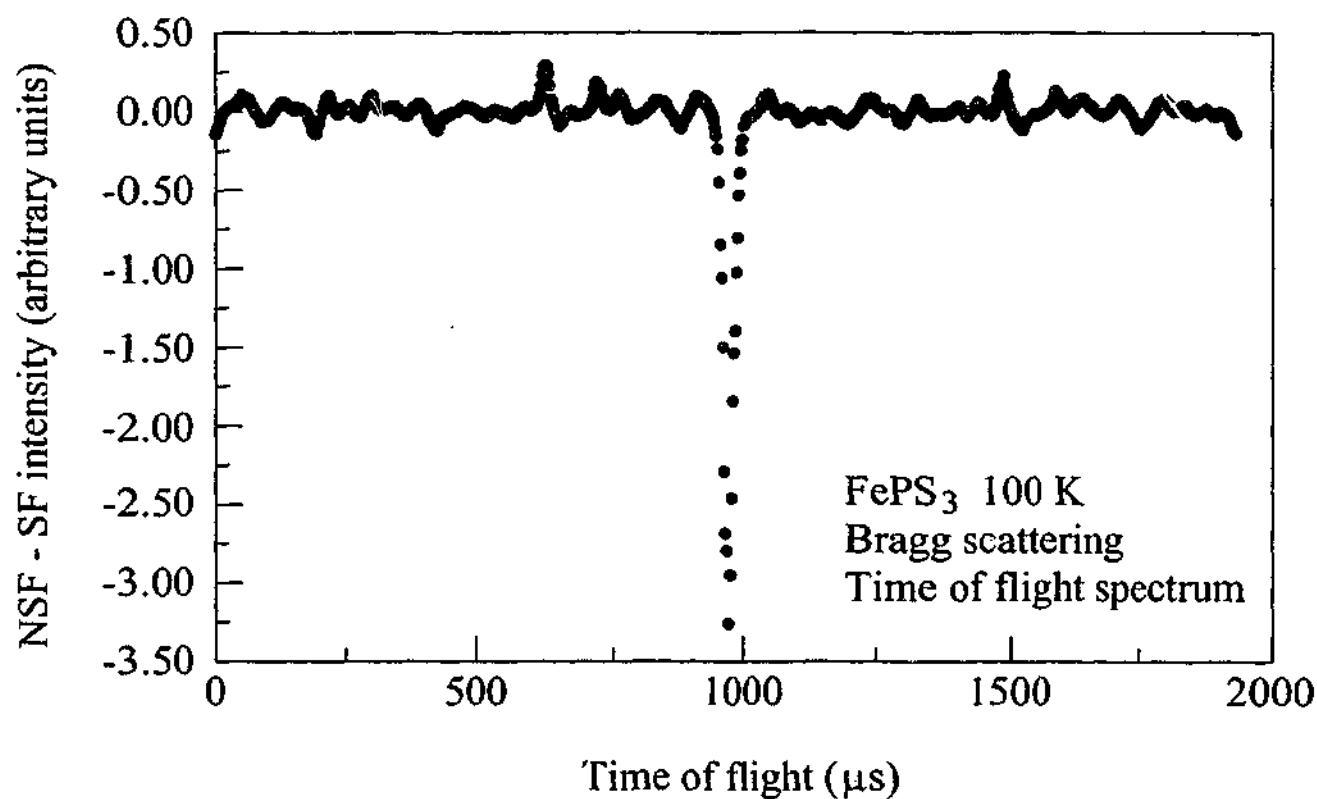


Figure 6.8: Time of flight measurements from the regions of known magnetic Bragg scattering at a scattering angle of 25° in 2θ .

Figure 6.8 shows a typical time of flight measurement taken for the known magnetic Bragg peak at 25° in 2θ . The spectrum shows the result of the spin-flip subtracted from the non-spin flip cross sections with the straight through incident beam (with no sample present) used as a point spread function for the de-convolution. The resultant peak is negative indicating that it arose from a spin flip, magnetic reflection. The peak is also situated at the time of flight position for elastic scattering confirming that it was produced by a magnetic Bragg reflection. This result is confirmed by the MRPD data indicating that the peak at 25° is indeed a magnetic Bragg peak.

Figure 6.9 shows the time of flight spectrum taken from the sum of the diffuse scattering at $Q \sim 0.7-0.82 \text{ \AA}^{-1}$. Again, the spectrum is proportional to the difference between the spin flip and non-spin flip cross sections. As the scattering vector was parallel with the polarisation of the neutrons, all spin flip scattering is magnetic, provided there is no nuclear incoherent scattering. Similar to Figure 6.8, the magnetic peak occurs at the elastic position in the time of flight spectrum. The position for the 13 meV neutron energy gain is also displayed on Figure 6.9. From this it is unlikely that the diffuse scattering between $0.7-0.82 \text{ \AA}^{-1}$ was caused by magnons, however the spectra were analysed for other indications of inelastic scattering.

From the de-convolution of the time of flight spectra, the energy resolution of the diffuse peak was found to be $200 \mu\text{eV}$, which was comparable to the resolution of the magnetic Bragg peak in Figure 6.8. This is an indication that the diffuse peaks and the magnetic Bragg reflections have around the same energy dependence. A more reliable energy comparison should have been made between the diffuse peaks and a nuclear peak, however, due to the preferred orientation in the sample, the intensity of the observed 001 nuclear peak was too low. Comparing the energy resolution of one magnetic peak to another is problematic, as there may be an energy dependent event that affects all magnetic peaks but not the nuclear peaks. The comparison was made, however, to highlight any differences between the diffuse and magnetic Bragg scattering.

The limits of the maximum entropy package were tested using the "straight through" (undiffracted) neutron beam on LONGPOL. Separate data sets were taken with gradually reduced neutron counts in order to discover the limit for de-convolution. For a counting rate of 0.25 seconds and 4850 counts, the de-convolution with the MEM package remained at maximum resolution. This indicates that even for very low counts, the de-convolution process is complete. Thus the resolution of $200 \mu\text{eV}$ was indeed a true energy representation of the known magnetic Bragg peak and the peaks between $\sim 0.7-0.82 \text{ \AA}^{-1}$ in Q . The width of the peak may indicate a

degree of inelasticity in the magnetic reflections on a scale much less than the resolution of $200 \mu\text{eV}$ measured here.

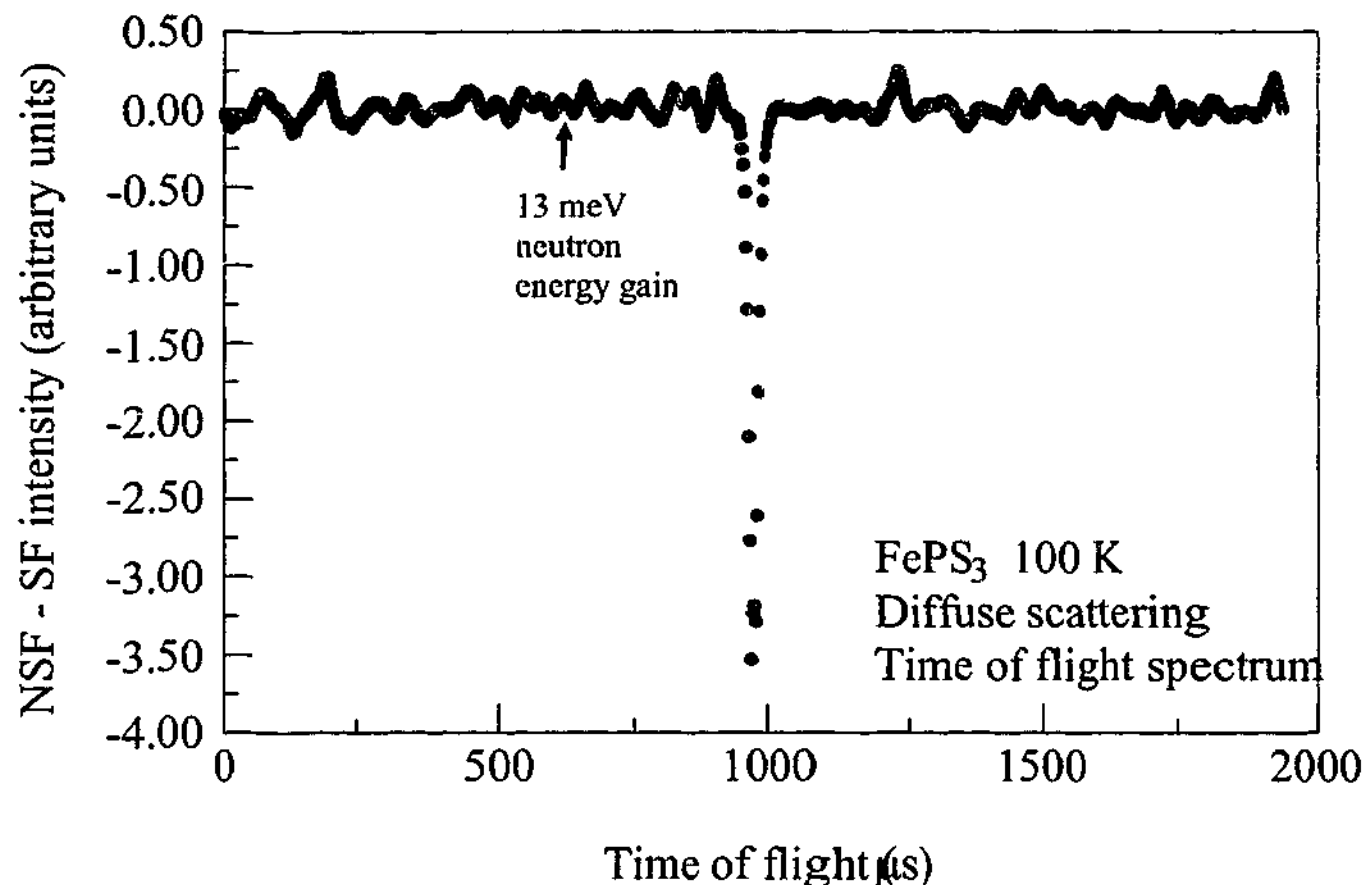


Figure 6.9: The sum of the diffuse scattering at 'elastic' scattering vectors 0.7 , 0.73 , 0.76 and 0.82 \AA^{-1} indicate that they are truly elastic scattering events. The arrow indicates the position at which a 13 meV energy gain caused by magnon de-excitation, would appear.

One effect that is not removed by the de-convolution process is the finite size of the sample. Scattering from different parts of the sample resulted in different path lengths and therefore different flight times, which were absent in the straight through beam. The size of the sample gave a range of neutron detection flight times of around $22 \mu\text{s}$ however, this spread in the time of flight data is within the peak width of $30 \mu\text{s}$ and is therefore not explicitly observed in Figures 6.8 and 6.9. As there was no apparent position shift or peak width change in the diffuse scattering spectrum when compared with the magnetic Bragg peaks, it can be concluded that the diffuse peaks were not caused by magnon excitations in the lattice. Thus if the diffuse reflections

at low scattering angles were indeed Bragg reflections, a more appropriate magnetic structure would be needed to describe the unknown number of magnetic peaks within the broad hump.

To choose an appropriate magnetic structure, a clear indication of the number of peaks in the diffuse band, as well as their scattering angles was needed. This was not immediately possible, as seen in Section 6.1, and so only the first defined peak at around 9.6° in 2θ was considered. The scattering angle of this magnetic reflection corresponded to a d -spacing of 10.3 \AA which is equivalent to the unit cell dimension b . Thus a propagation vector of (010) was investigated as it conveniently placed the first magnetic Bragg peak from the $0,0,0$ nuclear position at the required scattering angle of around 9.6° in 2θ . The in-plane moment orientations of this magnetic structure followed that of Kurosawa et al., (1983) and can be seen in Figure 6.10.

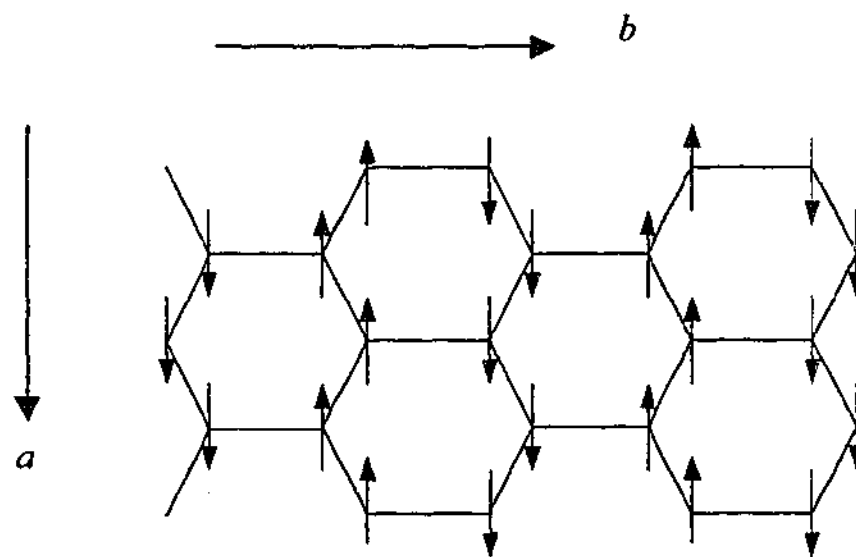


Figure 6.10: The in-plane moment structure predicted for FePS_3 with a propagation vector of (010) . This structure is similar to that found by Kurosawa et al. (1983).

Structure factor calculations were conducted to discover the scattering angles of the other magnetic peaks for this structure. The predicted positions can be seen labelled on the MRPD scan in Figure 6.11. The magnetic structure with a propagation vector of (010) was able to predict magnetic intensities for each of the observed peaks. However, many more magnetic peaks were also calculated, and these can be seen in Figure 6.11 highlighted with dashed markers. It is obvious from the positions of these markers that there are no magnetic intensities at the predicted positions. The effect of other factors such as the magnetic form factor, multiplicity and

preferred orientation were considered to influence the intensity of the peaks, however, none of these could be responsible for removing all intensity at these reflections.

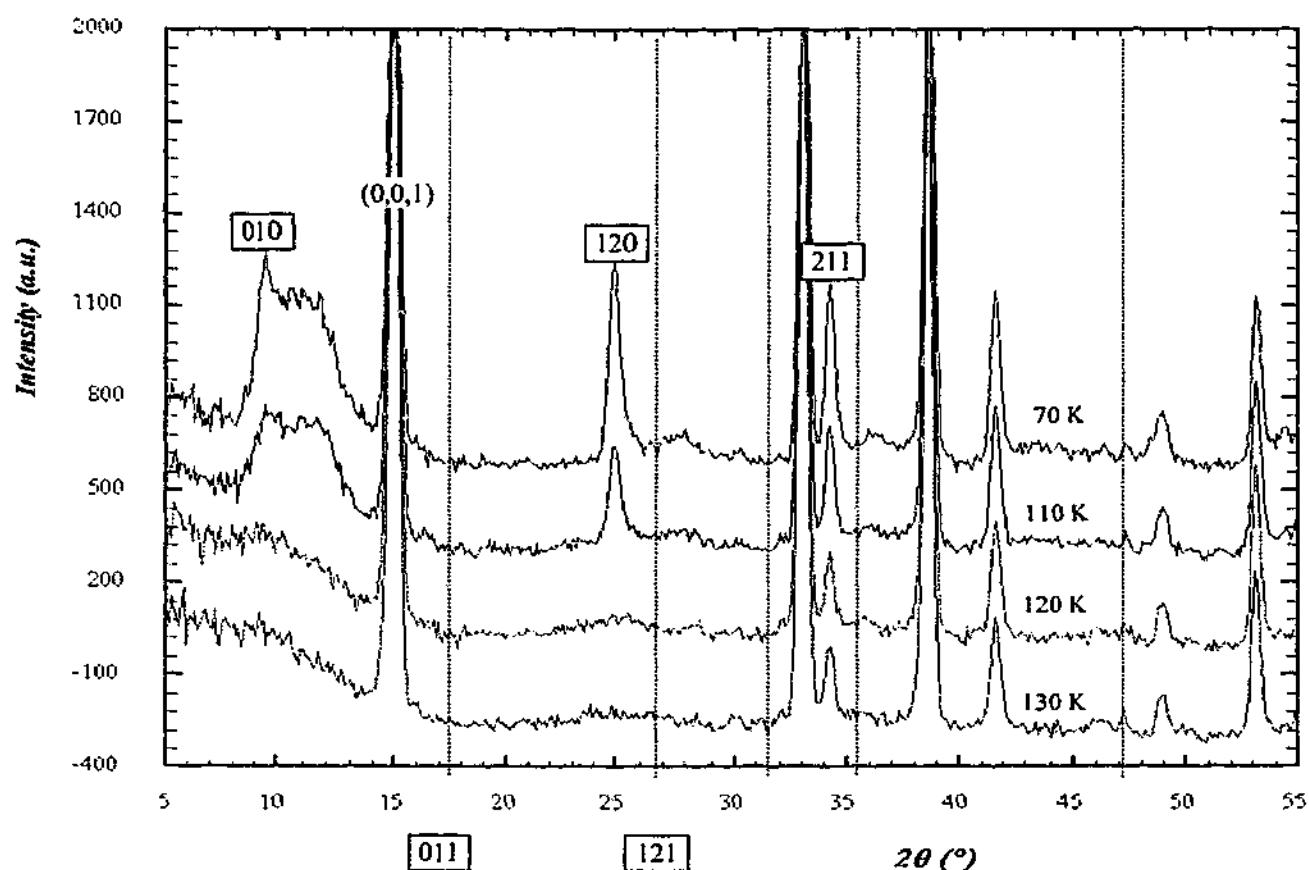


Figure 6.11: The magnetic peaks in the MRPD data, labelled according to the propagation vector of (010). The dashed lines indicate the positions of magnetic reflections expected from this structure, but missing from the data.

Although this model included unexplained, missing reflections, it was the most accurate at predicting the scattering angles of the observed magnetic peaks. The in-plane moment structure of this model was identical to that proposed by Kurosawa et al. (1983), however, the planes were coupled ferromagnetically rather than antiferromagnetically. Not satisfied with the missing magnetic reflections, single crystal neutron diffraction was conducted to test the model and determine a more accurate and acceptable magnetic structure for FePS_3 .

6.4 LAUE NEUTRON DIFFRACTION

A single, hexagonal shaped sample of FePS_3 was used for the single crystal neutron scattering techniques (Figure 6.12). The VIVALDI data for this sample can be seen in Figure 6.13a and b below. Both plots were taken with the crystal in the same orientation with respect to the incident neutron beam, however Figure 6.13a shows the data taken at 140 K and Figure 6.13b shows the data taken at 5 K. The black spot in the centre is the beam stop for the straight through, non-diffracted neutron beam. The dull grey streaks emanating from the central position are artefacts of the cryostat that encased the sample. These features do not influence the crystallographic information from the sample and so have been disregarded during peak analysis.

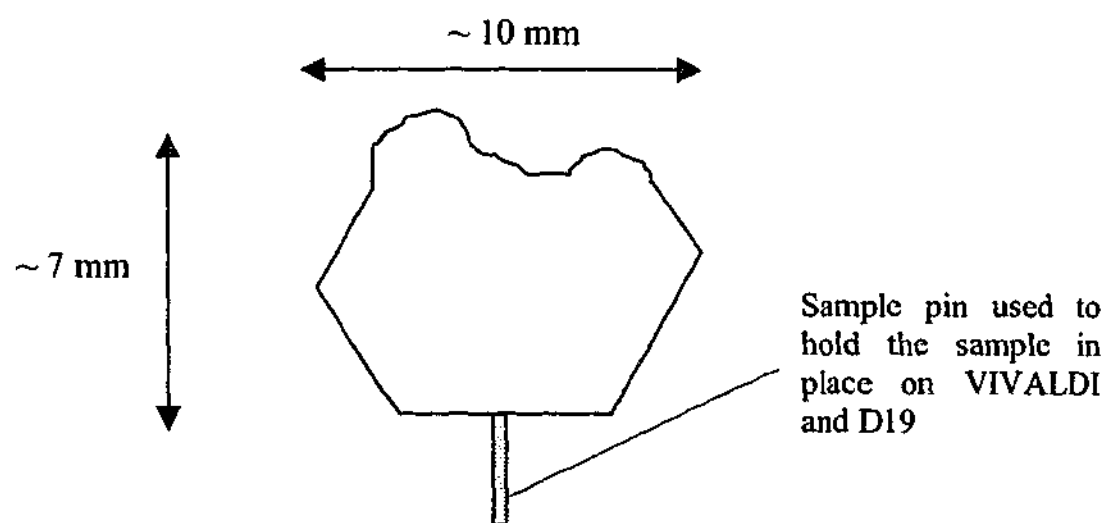


Figure 6.12: Sketch of the single crystal sample used for the neutron diffraction experiments at ILL, France.

The strong white peaks observed at identical positions in each spectrum are nuclear in origin and were used to classify the orientation of the crystal using the analysis program, Lauegen (Campbell, 1995). This program was able to superimpose a monoclinic unit cell structure onto the data for peak matching. From the spectra in Figure 6.13, the lone white peak on the right-hand black stripe was labelled as the 001 peak.

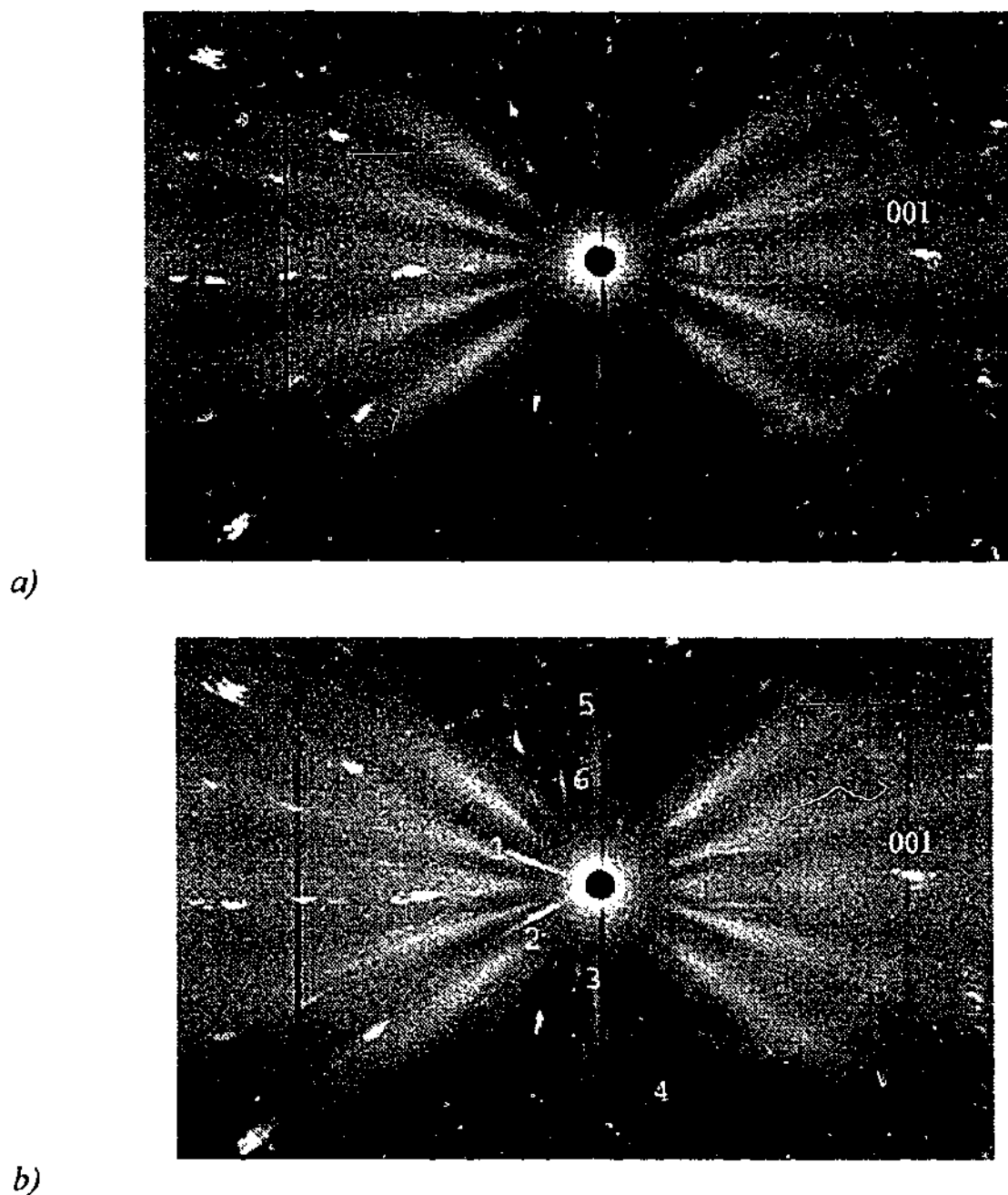


Figure 6.13: Laue neutron diffraction patterns from VIVALDI at a single sample orientation. The nuclear spectrum (a) was taken at 140 K and the magnetically ordered spectrum (b) was taken at 5 K.

The nuclear peaks also displayed some broadening, unusual for a perfect single crystal with long-range order. These were attributed to a twined growth structure within the sample. It was not possible to fit all the reflections with one monoclinic structure using Lauegen, however two identical structures rotated 60° from each other were able to predict every observed reflection. For the two domains within the sample, one (Crystallite B) was around twice as large as the other (Crystallite A) and they shared a common c^* -axis. The rotation of 60° between the crystallites

corresponds well with the observed shape of the sample. The sample was chosen for its hexagonal shape with almost 5 straight sides and only one with damage as seen in Figure 6.12. Thus a second crystallite had to be a multiple of 60° rotated from the first. The two crystallites within the single crystal sample were present due to screw dislocations that had come about during crystal growth. This type of crystal defect is not uncommon in these layered materials, and was first recorded in 1973 (Klingen et al., 1973a). It has also been observed in x-ray diffraction patterns (Ouvrard et al., 1985).

The most prominent magnetic peaks were labelled 1 to 6 in Figure 6.13b and these were observed to be very streaky when compared with the nuclear peaks, even accounting for the two crystallites. Lauegen was again used to predict the peak positions for a magnetic structure by following zones in the pattern as seen in Figure 6.14. This was done by creating a magnetic unit cell that was twice as large as the nuclear unit cell along a and b and three times as large along c . Black markers were observed to occur at each of the magnetic peaks for a combination of the two crystallites in the sample.

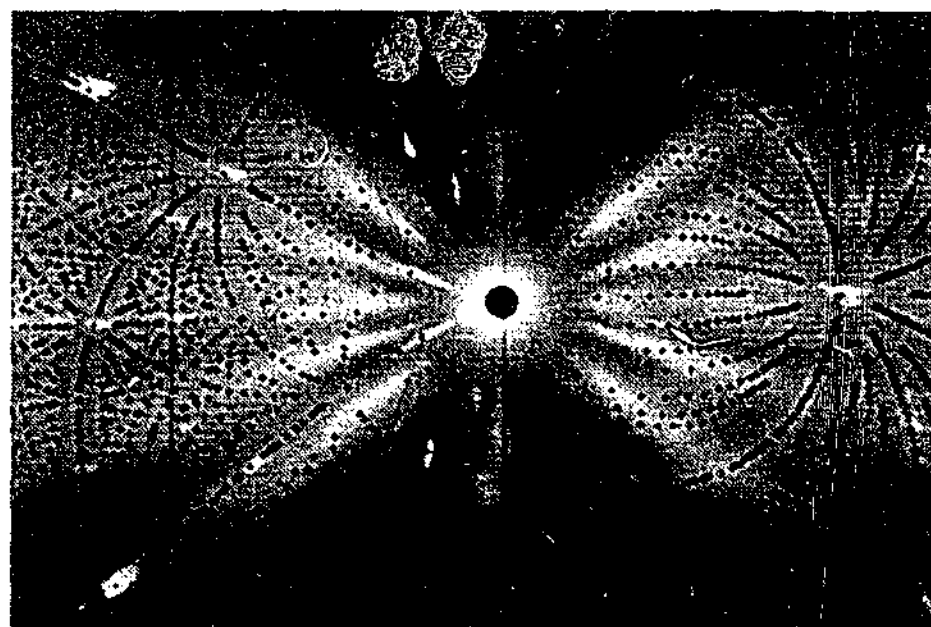


Figure 6.14: Positions of diffraction peaks for a monoclinic structure twice the size of FePS_3 along the a and b directions and three times as long in the c direction.

The classifications of the magnetic peaks labelled 1 to 6 in Figure 6.13b can be seen for both crystallites in Table 6.2. It is evident from this table that Crystallite B was more dominant, as the

monoclinic structure for this crystallite was able to fit magnetic peaks to each of the observed reflections, while the structure for Crystallite A produced less peaks.

Table 6.2: VIVALDI magnetic peak classifications for Figure 6.13b.

Peak number	1	2	3	4	5	6
Crystallite A	$\frac{1}{2} \frac{1}{2} \frac{1}{3}$	-	-	$\frac{3}{2} \frac{5}{2} \frac{1}{3}$	$\frac{3}{2} \frac{1}{2} \frac{2}{3}$	$\frac{3}{2} \frac{1}{2} \frac{1}{3}$
Crystallite B	$\frac{1}{2} \frac{1}{2} \frac{1}{3}$	$\frac{1}{2} \frac{1}{2} \frac{1}{3}$	$\frac{1}{2} \frac{5}{2} \frac{1}{3}$	$\frac{1}{2} \frac{7}{2} \frac{1}{3}$	$\frac{1}{2} \frac{5}{2} \frac{1}{3}$	$\frac{1}{2} \frac{5}{2} \frac{2}{3}$

From these results, the magnetic reflections appeared to correspond to a magnetic unit cell which was doubled along the a and b directions and tripled along the c direction. This was a rough estimate of the unit cell based on the peak correspondence in the Lauegen fit. The size of the magnetic unit cell implied a propagation vector of $\frac{1}{2} \frac{1}{2} \frac{1}{3}$. The simplest and most common magnetic structures usually have a single propagation vector. This tends to minimize the magnetic energy of the system with the ground state wave function described by $\psi_j^k e^{-2\pi k r}$ where ψ_j^k is the basis vector, and $e^{-2\pi k r}$ is the incident plane wave (Wills, 2000). The basis vector indicates the size and direction of the magnetic moment on the atom site j . Multiple propagation vectors are also possible in magnetic systems and tend to be associated with a magnetic domain such that some reflections fitted within the $+k$ domain and the rest fitted in the $-k$ domain. For FePS_3 , a collinear structure could be described by either propagation vector, $\frac{1}{2} \frac{1}{2} \frac{1}{3}$ and $-\frac{1}{2} -\frac{1}{2} -\frac{1}{3}$. For more accurate investigations of the magnetic peaks, the single crystal was measured using the four-circle diffractometer, D19.

6.5 D19 OBSERVATIONS

Using the same single crystal sample as VIVALDI, the 4-circle diffractometer, D19, was calibrated. The nuclear peak positions with the greatest intensity were used to find the crystallographic axes of the crystal. Using the predicted magnetic peaks from the Lauegen model, magnetic reflections were investigated in the region of $h \pm \frac{1}{2}$, $k \pm \frac{1}{2}$, $l \pm \frac{1}{3}$ taken from

the nuclear peaks in reciprocal space. Due to time constraints, a complete set of reflections was not possible, so only a limited data set was available for analysis.

Magnetic peaks were readily found at the lattice positions of $h \pm 1/2$ and $k \pm 1/2$ however, the intensity of the peaks appeared to be smeared along the l direction. The intensities of most magnetic peaks were found to be maximum at positions where $I_{\text{mag}} = I_{\text{nuc}} \pm 0.34$, however magnetic intensity was also found within ± 0.15 of these positions. A table of the most intense magnetic peaks for each crystallite can be seen in Table 6.3. The strongest magnetic peaks appear to lay predominantly in the xy -plane, close to the origin along z . Neutrons will scatter with a maximum intensity when the magnetic moments are aligned perpendicular to the scattering vector. Thus if the peaks with a maximum intensity lie in the xy -plane, then the moments will be perpendicular to this – along the z -axis of the crystal. This result supports the Mössbauer spectroscopy data, which also indicated that the moments were oriented along the z -direction, perpendicular to the ab -plane.

Table 6.3: The most intense magnetic peaks as found on D19 for the two crystallites in the sample, A and B.

Crystallite A		Crystallite B	
hkl	Intensity (a.u)	hkl	Intensity (a.u)
$\frac{3}{2} \frac{7}{2} 0.34$	26.0 ± 1.0	$\frac{1}{2} \frac{1}{2} 0.66$	45.5 ± 0.5
$\frac{1}{2} \frac{1}{2} 0.66$	25.1 ± 0.3	$\frac{3}{2} \frac{1}{2} 0.66$	30.7 ± 0.7
$\frac{1}{2} \frac{11}{2} 0.66$	23.5 ± 1.1	$\frac{3}{2} \frac{1}{2} 1.34$	28.9 ± 0.6
$\frac{1}{2} \frac{1}{2} 0.35$	18.6 ± 0.4	$\frac{1}{2} \frac{1}{2} 0.68$	24.9 ± 0.3
$\frac{1}{2} \frac{11}{2} 0.34$	18.3 ± 1.3	$\frac{3}{2} \frac{1}{2} 0.34$	13.5 ± 0.6
$\frac{1}{2} \frac{5}{2} 0.34$	16.1 ± 0.8	$\frac{5}{2} \frac{1}{2} 1.66$	9.9 ± 0.9
$\frac{1}{2} \frac{7}{2} 0.34$	10.6 ± 0.9	$\frac{5}{2} \frac{1}{2} 0.66$	9.0 ± 1.0
$\frac{1}{2} \frac{3}{2} 0.34$	6.8 ± 0.5	$\frac{5}{2} \frac{1}{2} 0.66$	8.5 ± 0.9

The intensity profiles for some of the magnetic reflections were plotted from the integrated D19 data. The data was also fitted using a Voigtian profile consisting of multiple Lorentzian lines convoluted with a narrow Gaussian distribution. This combination of profiles was chosen to constrain the peak shape, which was required for a suitable fit. For short-range ordering along l , the peak shapes follow a Lorentzian profile, and the Gaussian distribution was chosen to describe the instrumental resolution function of D19. The halfwidths of the Lorentzian profiles were constrained to remain consistent for all peaks in a given scan and the background was similarly constrained to be flat. The intensity profile along l for Crystallite B taken at $h = 3/2$ and $k = 1/2$ can be seen in Figure 6.15, where the spots represent the data points and the continuous line represents the best fit to the data. Figure 6.16 shows a similar plot for Crystallite B with $h = 1/2$ and $k = 1/2$.

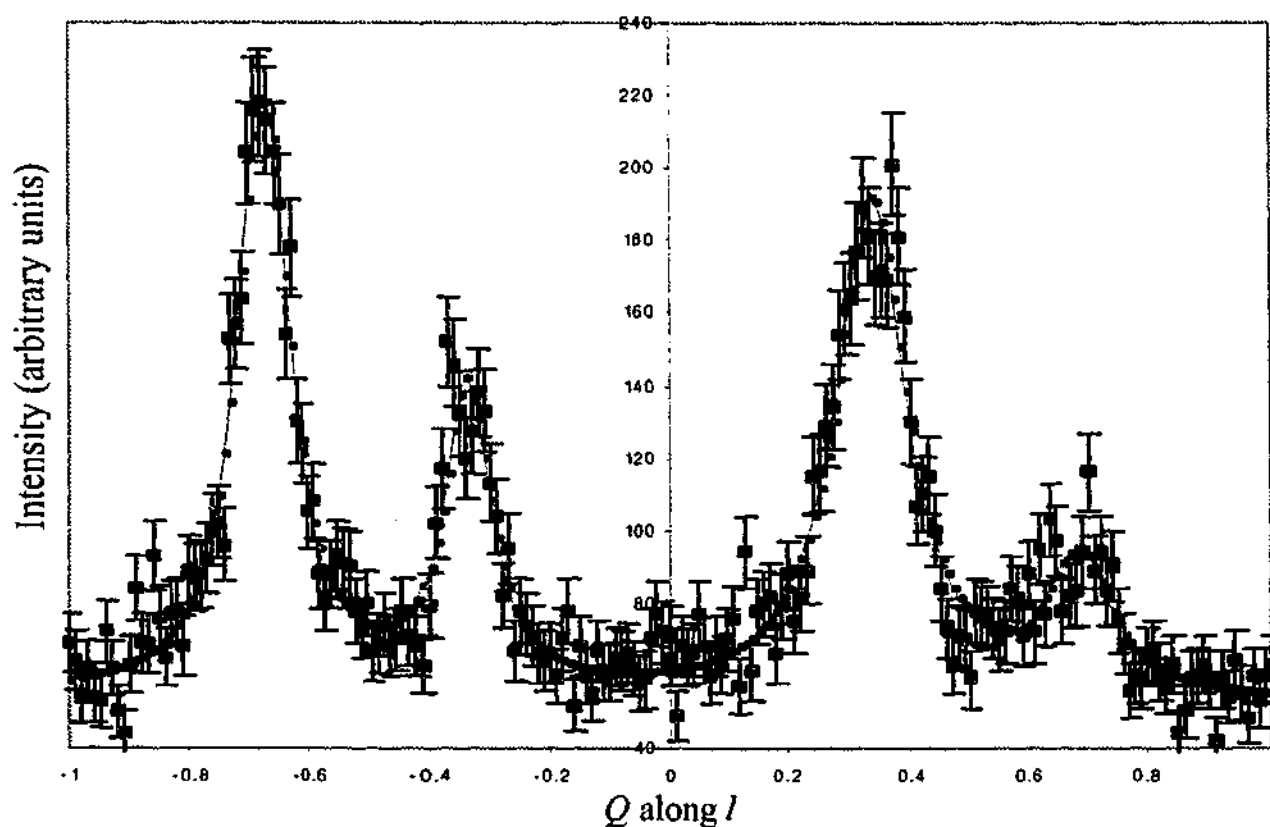


Figure 6.15: Intensity profile along the reciprocal lattice vector, l , for Crystallite B at $h = 3/2$ and $k = 1/2$. The line represents the fit to the data.

From Figure 6.15, the intensity of the peaks at $l = +0.34$ and -0.66 is about twice as large as the intensity of the peaks at $l = +0.66$ and -0.34 . These correspond to two domains within the hk rod-like structure of $3/2 \ 1/2$ in Crystallite B, with one domain about twice the size of the other.

This gave peaks centred at 0.34 and -0.66 ($0 + \frac{1}{3}$ and $-1 + \frac{1}{3}$) a larger intensity than those at 0.66 and -0.34 ($1 - \frac{1}{3}$ and $0 - \frac{1}{3}$). The relative intensities of the two peaks are around 2:1, which indicates that the $+\frac{1}{3}$ domain is about twice as large as the $-\frac{1}{3}$ domain. The intensity profile in Figure 6.16 exhibited only one set of peaks at $0 + \frac{1}{3}$ and $-1 + \frac{1}{3}$, indicating the presence of only one domain in this hk plane. Both crystallites showed similar domain structures for both the $\frac{3}{2} \frac{1}{2}$ plane, and the $\frac{1}{2} \frac{1}{2}$ plane.

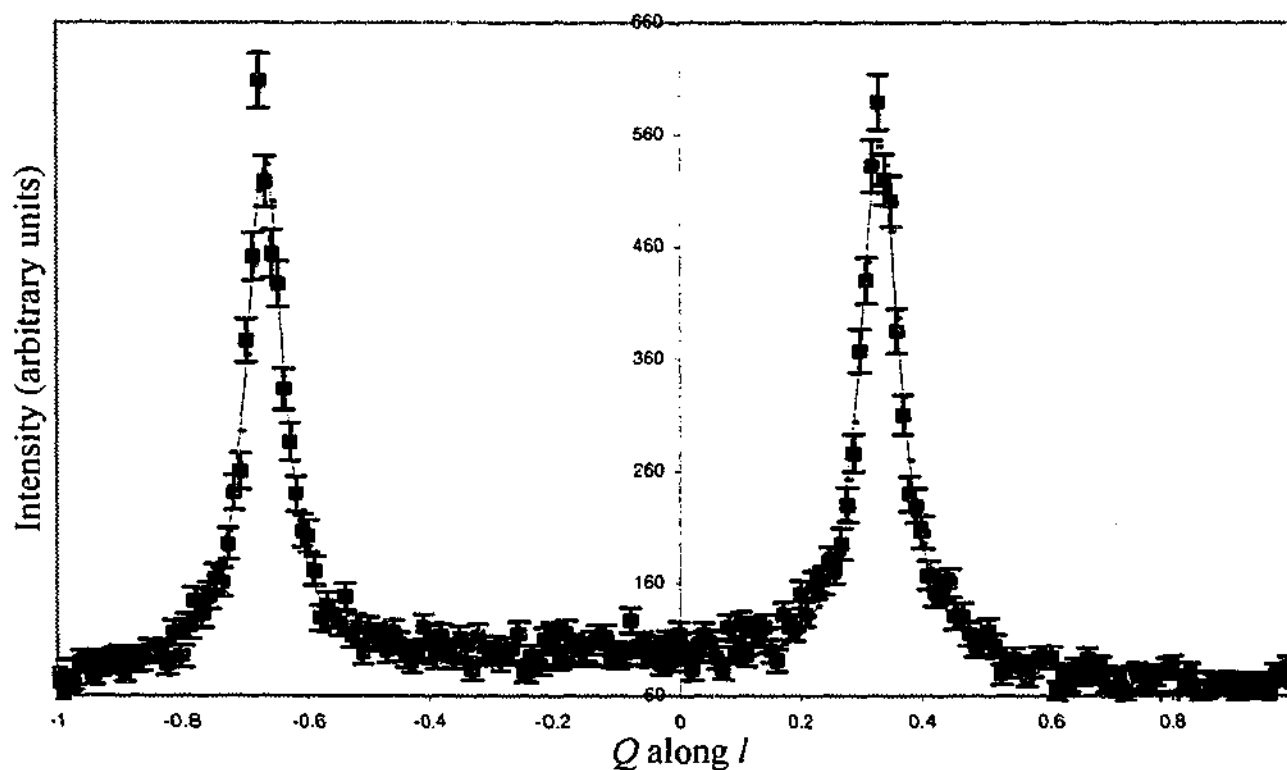


Figure 6.16: Experimental data taken from D19 showing the intensity profile of the magnetic peaks along the c^* direction. This was taken at $\frac{1}{2} \frac{1}{2} l$ for Crystallite B.

From this data, it appears that the hk plane of $\frac{1}{2} \frac{1}{2}$ has only one domain, while the plane of $\frac{3}{2} \frac{1}{2}$ has two. This is not physically possible, however the multi-crystallite structure of the single crystal sample may have provided the basis for this observation.

Intensity profiles of the other magnetic reflections have been integrated along l from the D19 data. Table 6.4 shows the full width of the peaks at half the maximum intensity for both Crystallite A and Crystallite B. The value of l indicates the position of maximum peak intensity. The width of each peak at half the maximum height can be seen in the final column, with an average width of 0.121 units along l .

Table 6.4: Values indicating the width of the profiles along c , at half the total intensity. The FWHM indicates the width of the peak at half the maximum intensity.

Crystallite	hk	l	FWHM
A	$\frac{1}{2} \frac{\sqrt{1}}{2}$	0.35	0.172
A	$\frac{3}{2} \frac{\sqrt{1}}{2}$	0.312	0.138
		0.65	0.200
A	$\frac{3}{2} \frac{1}{2}$	0.34	0.100
		0.67	0.115
B	$\frac{3}{2} \frac{1}{2}$	0.34	0.13
		0.68	0.06
		-0.34	0.09
		-0.68	0.10
B	$\frac{1}{2} \frac{1}{2}$	0.33	0.085
		-0.68	0.070

The thermal variation of the reduced magnetic moment was also observed from the integrated D19 data. A plot of the magnetic intensity as a function of temperature can be seen in Figure 6.17. As can be seen, the magnetic intensity drops to around zero at the Néel temperature. The shape of this plot indicates that the magnetic intensity remains at a constant maximum value for temperatures below 100 K, and decreases sharply between 100 and 120 K. This square-like profile is an indication of the strong anisotropy of FePS₃ as well as the possible 2D magnetic ordering and will be discussed in more detail in Section 7.4.

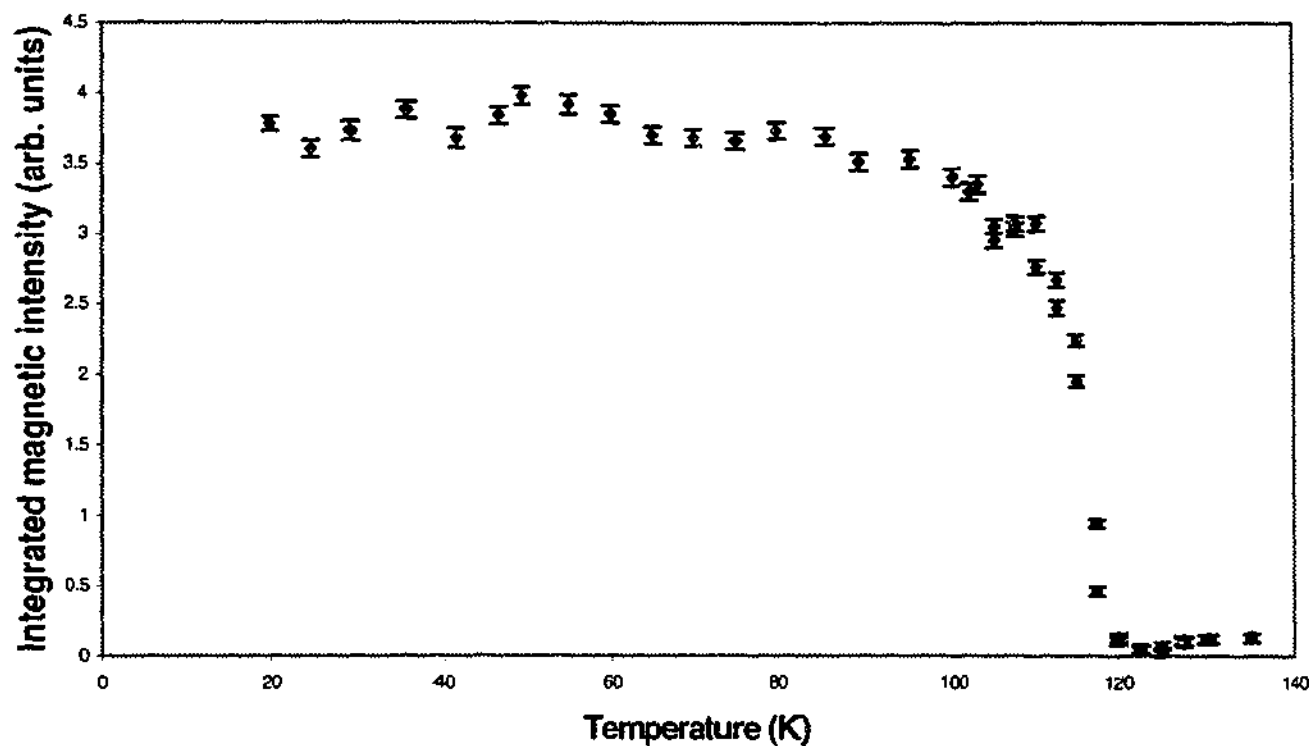


Figure 6.17: The thermal variation of the reduced magnetic moment for FePS_3 . Taken from integration of the D19 data.

6.6 CONCLUSIONS

The results from each of the neutron scattering techniques outlined in this chapter have assisted in creating a model for the magnetic structure of FePS_3 . Separately, these techniques would not have revealed as much information about the crystal and magnetic unit cell structures in real and reciprocal space.

The initial powder diffraction scans indicated that the previously accepted magnetic structure was incorrect. The appearance of diffuse magnetic peaks at low scattering angles were evidence that the propagation vector of $00^{1/2}$ was insufficient to describe the magnetic structure and that the magnetic unit cell needed to be larger than this propagation vector described. The low scattering angle peaks were also found to be true, elastic Bragg reflections with magnons not contributing significantly to the diffuse scattering.

Single crystal neutron diffraction scans showed that the magnetic unit cell structure was more likely to be of the order $1/2 \times 1/2 \times l$ where l is a value around $1/3$ or 0.34. This indicates that the magnetic unit cell structure is twice as large as the crystallographic unit cell in both the a and b -directions and around three times as large in the c -direction. The discrepancy in the l direction was attributed to the streaky patterns of the neutron scans, which were observed as broad scattering profiles in reciprocal space. The cause of this discrepancy lies in the strength of the magnetic ordering and the anisotropy in FePS_3 . The various magnetic models arising from these results shall be discussed further in the following chapter.

CHAPTER SEVEN

7: The Magnetic Structure of FePS₃

In order to obtain a magnetic structure model to accurately describe the moments in FePS₃, all of the magnetic evidence was considered. Only by combining the results obtained from Mössbauer spectroscopy, SQUID magnetometry and neutron scattering, could a true model be developed and investigated. Each individual technique was not sufficient to reveal the magnetic structure, however when constraints from all data were taken into account, the number of possible magnetic structures was reduced.

7.1 INITIAL MAGNETIC STRUCTURES OF FePS₃

Kurosawa et al. (1983) performed pseudo-single crystal neutron diffraction experiments and claimed to uncover the magnetic structure of FePS₃. It was found with recent powder neutron diffraction that their structure was incorrect, however the true magnetic structure was not easily revealed. To find the true magnetic structure, the results from both the magnetometry and Mössbauer spectroscopy experiments were combined with the data from the powder and single crystal neutron diffraction experiments.

Mössbauer spectroscopy results and susceptibility measurements were both considered important tools for the magnetic structure determination. In the single crystal Mössbauer spectroscopy experiments, the magnetically ordered spectrum displayed 4 absorption lines. Typical hyperfine spectra have 6 absorption lines when the moment orientation is random within the sample. The absence of lines 2 and 5 from this spectrum indicated that, for a static structure or for a structure existing longer than the Larmor precession period of the Fe nucleus, the moments were directed perpendicular to the *ab*-plane.

Susceptibility measurements have been taken at temperatures close to absolute zero for applied fields both parallel and perpendicular to the trigonal axis, that is, the *z*-direction. Results indicated that for fields applied parallel to *z*, the susceptibility dropped to around zero. This also supports the Mössbauer spectroscopy data indicating that the moments are indeed oriented along the *z*-direction, perpendicular to the *ab*-plane.

The magnetic reflections from both VIVALDI and D19 were compared with the low temperature MRPD data. The predicted peak classifications for the MRPD peaks can be seen in Table 7.1, taken as the nuclear peaks \pm the propagation vector of $1/2 \ 1/2 \ 1/3$. The most intense peaks from the VIVALDI data corresponded well with the lowest scattering angle peaks from the MRPD data. Equivalent magnetic peaks with high intensity were also found in the D19 data. These peaks are also displayed in Table 7.1 with the *d*-spacing values for each technique displayed to highlight the similarities and differences between the observed data from the three different observations. The MRPD data was taken from the first 5 intense, magnetic peaks in the diffraction pattern, and due to the magnetic intensities being stronger in the *ab*-plane, the classifications were constrained to low *l* values. The absence of data from the VIVALDI and D19 results in the final two magnetic peaks is due to insufficient resolution in the VIVALDI data and an incomplete set of results taken with D19.

Table 7.1: Relative *d*-spacings (\AA) for the low scattering angle magnetic peaks from MRPD, VIVALDI and D19.

MRPD <i>d</i> -space (\AA)	Expected <i>hkl</i> from $\tau = 1/2 \ 1/2 \ 1/3$	VIVALDI peak (<i>hkl</i>)	VIVALDI <i>d</i> -space (\AA)	D19 peak (<i>hkl</i>)	D19 <i>d</i> -space (\AA)
10.12	$-1/2 \ -1/2 \ -1/3$	$-1/2 \ -1/2 \ -1/3$	9.95	$-1/2 \ 1/2 \ -0.34$	9.92
3.86	$1/2 \ 5/2 \ 1/3, \ 3/2 \ 1/2 \ 1/3$	$-1/2 \ -5/2 \ 1/3$	3.73	$-1/2 \ 5/2 \ -0.34$	3.87
2.82	$3/2 \ 5/2 \ 1/3$	$-3/2 \ 5/2 \ -1/3$	2.85	$3/2 \ 5/2 \ 0.66$	2.85
2.34	$3/2 \ 7/2 \ 1/3, \ 5/2 \ 5/2 \ 1/3$	Out of range		Not measured	
1.86	$5/2 \ 7/2 \ 1/3$	Out of range		Not measured	

From this table it can be seen that the peak classifications from VIVALDI and D19 are very similar. In devising possible magnetic structures in real space, previous results were considered as either supporting or contradictory to each model. The magnetic fit to the VIVALDI plots

indicated that the propagation vector was $(\frac{1}{2} \frac{1}{2} \frac{1}{3})$, as each of the reflections could be labelled with reciprocal lattice vectors of this sort. The D19 data on the other hand, also found magnetic intensity at $(\frac{1}{2} \frac{1}{2} \frac{1}{3})$, but it was clear that the maximum intensity occurred around $(\frac{1}{2} \frac{1}{2} 0.34)$. These two propagation vectors open the paths of very different magnetic structures in real space with issues involving incommensurability, collinearity and magnetic moment alignment.

7.1.1 Modulated moment structure

The first magnetic model that was considered was a collinear, modulated moment structure. In this situation, all of the moments could be oriented parallel and antiparallel to c^* with different magnitudes. This would imply a static magnetic structure in which there are multiple moment sublattices within the crystal structure. This was considered briefly as a means for tripling the nuclear unit cell along the c -axis, while remaining consistent with a propagation vector of $(\frac{1}{2} \frac{1}{2} \frac{1}{3})$. It was also consistent with the susceptibility measurements and the low temperature Mössbauer spectroscopy results, which implied that the moments were aligned along the c^* -direction. This structure was deemed improbable however, as the applied field Mössbauer spectroscopy data indicated the presence of only two sublattices. Thus the Mössbauer data contradict the possibility of multiple moment intensities throughout the lattice.

7.1.2 Helical moment structure

Although the propagation vector of $(\frac{1}{2} \frac{1}{2} \frac{1}{3})$ allows for a relatively simple, commensurate structure such as the modulated moments, the D19 data indicated that the reciprocal lattice positions with $I_{\text{magnetic}} = (I_{\text{nuclear}} \pm 0.34)$ are more accurate. A closer inspection of the magnetic peaks from the powder diffraction data also indicated that $l = 0.34$ is more accurate than $l = \frac{1}{3}$. In most cases from the D19 data, the position $(l \pm \frac{1}{3})$ had some magnetic intensity, but due to the elongated scattering profile in reciprocal space, the centre of the peaks was more commonly found at $(l \pm 0.34)$.

A propagation vector of $h \pm \frac{1}{2}, k \pm \frac{1}{2}, l \pm 0.34$ would indicate an incommensurate structure, such as a helical arrangement. In this type of structure, the moments could be either static or dynamic, rotating about a common z -axis. In a helical structure the moments would have a

component that was not along the z -axis. This initially seems to contradict the Mössbauer spectroscopy results that show, by the absence of lines 2 and 5, that all the moments are aligned along z . However, for a dynamic helical structure, the Mössbauer results merely constrain the speed of the moment rotation to some value greater than the Larmor precession frequency of the iron nucleus. In this way, the time-averaged moment, as measured in the Mössbauer spectra, will be along z . The Larmor precession period of the Fe nucleus in a hyperfine field is around 4×10^{-8} seconds (Cohen, 1976), while the energy resolution of the neutrons corresponds to a wave period of around 2×10^{-11} seconds. So the helical moment structure relies on that fact that the moments fluctuate faster than the iron precession frequency yet slower than the time of interaction with the neutrons from D19. Thus the neutrons may see a 'snapshot' of the Fe moment rotation, whereas the Mössbauer measurements don't. This could result in inelastic magnetic scattering, which may have been contained within the $200 \mu\text{eV}$ line width observed in the time-of-flight LONGPOL experiment. However any inelastic scattering could have been beyond the resolution of the time of flight experiment. This is one instance where a comparison of the magnetic peak width with a nuclear peak width may have revealed more information.

A helical moment structure may also be partially responsible for the low hyperfine field felt at the Fe nucleus in FePS_3 . The measured hyperfine field was found to be $9.75 \pm 0.06 \text{ T}$ at 10 K from the Mössbauer spectroscopy results, which is only about $1/3$ of the hyperfine field for α -Fe. A helical structure would have a component of the moments perpendicular to the c^* -direction, which could assist in reducing the hyperfine field in the z -direction. This however would not be sufficient to reduce the hyperfine field felt at the nucleus by a factor of three. In fact it is the distortion from cubic symmetry and the covalent bonding that are primarily responsible for the low hyperfine fields in both FePS_3 and FePSe_3 as discussed in Section 5.5. The applied field Mössbauer spectra indicate that a dynamic helical arrangement is unlikely, as the applied fields would alter the rotation dynamics. Thus, the variation in the internal hyperfine field in Figure 5.15 would not be linear for a dynamic helical arrangement.

7.1.3 Collinear magnetic structure

As there was some uncertainty to the true classification of the l coordinates in the magnetic reflections, a collinear, commensurate structure was also considered to describe the magnetic

structure. This structure incorporated a propagation vector of $\frac{1}{2} \frac{1}{2} \frac{1}{3}$ to describe the reflections with the VIVALDI classifications of $l = \frac{1}{3}$ rather than the D19 value of $l = 0.34$. This structure required a doubling of the crystallographic unit cell along the a and b directions and a tripling along the c^* -direction. One constraint to this structure is that the magnetic unit cell must be antiferromagnetic. This can be achieved by ensuring that each layer of Fe atoms in the cell is antiferromagnetically ordered, such that by stacking three layers the overall magnetisation will remain zero. Thus by observing a corresponding spin in each layer, the order may go in repeatable units such as "up-up-down" in Figure 7.1.

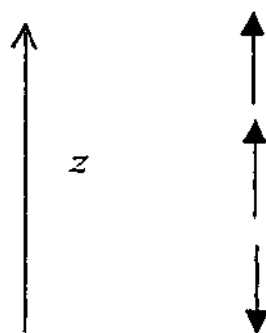


Figure 7.1: A collinear structure can have different arrangements with a magnetic cell repeating every 3 crystallographic unit cells along z . Each plane is antiferromagnetically ordered such that the net magnetic moment is zero.

This structure corresponds favourably with the Mössbauer spectroscopy and susceptibility data such that all the moments are oriented either parallel or antiparallel to the z -direction, however it does not explain the broad distribution of the data along l taken with D19.

A variety of in-plane moment orientations within this structure were tested using the fitting program FullProf and the powder neutron diffraction data. This included the structures proposed by Le Flem et al. (1982) and Kurosawa et al. (1983). From the analysis of the VIVALDI and D19 data, the in-plane moment structure was constrained to be twice the size of the crystallographic unit cell in both the a and b directions. Thus it was obvious that the in-plane structure chosen by Kurosawa et al. (1983) was not a possible moment structure. Although Kurosawa et al. (1983) claimed that their moment structure was identical to that of Le Flem, they failed to realize that they had imposed a 60° rotation of the cell, such that the structure published by Kurosawa was not doubled along either the a or b directions (Figure 2.9). The magnetic peaks

were fitted across a scattering range of 0 to 60° in 2θ . Figure 7.2 shows the fit for the in-plane structure that was considered the best representation of the moments.

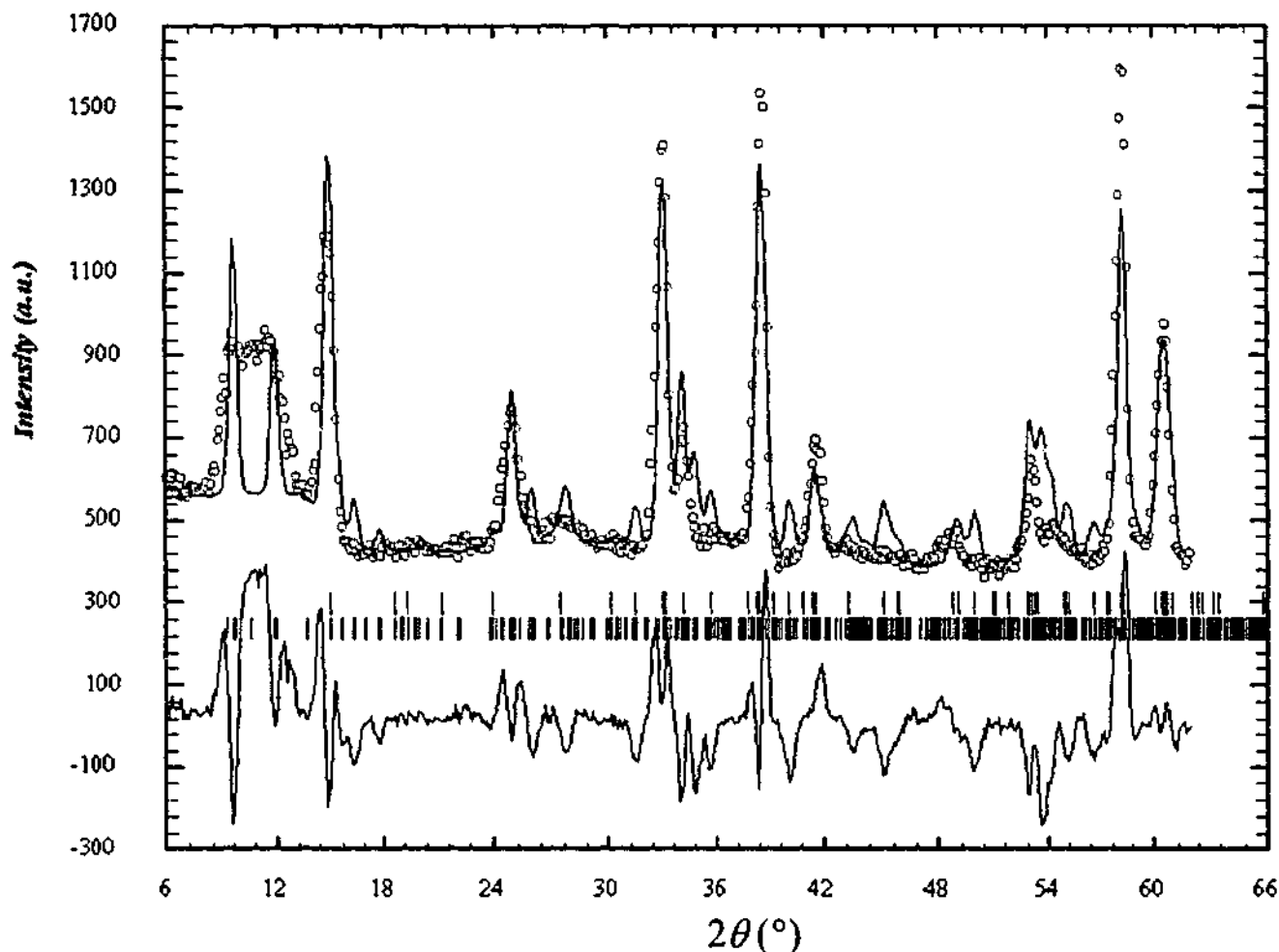


Figure 7.2: FullProf fit of the powder neutron diffraction data taken at the Lucas Heights Research Reactor, using MRPD. The red circles represent the data points and the line through these points represents the fit. The small, green markers below the data indicate the calculated reflections for this model and the blue line at the bottom of the figure is the difference between the data and the fit.

The red circles in Figure 7.2 represent the data points taken from MRPD at 4 K, while the line through the data points represents the fit to the data. Below the data and fit are two sets of green markers. These represent the predicted nuclear and magnetic peaks respectively. From this it can be seen that there are many more possible magnetic reflections than nuclear reflections, although not all the magnetic reflections have strong enough intensity to be clearly observed. This is especially noticeable at the higher scattering angles when the magnetic form factor significantly reduces the magnetic intensity. The magnetic form factor will reduce the intensity of the magnetic peaks to about 30 % of the original height by 60° in 2θ . Thus it is not surprising

that the magnetic reflections are observed most strongly at low scattering angles. Other factors, which may reduce the intensity of some magnetic peaks and enhance others, include the preferred orientation effects relating the orientation of the moments in the powdered sample with respect to the scattering vector and wavelength related effects.

The magnetic moment orientation that was used to calculate the fit in Figure 7.2 was that of Le Flem et al. (1982) and can be seen in Figure 7.3. Although many other moment structures were tested, this one appeared to give the best fit to the observed data.

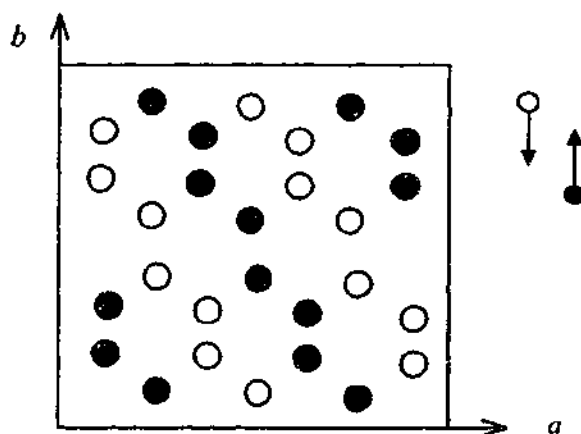


Figure 7.3: The in-plane moment structure used to obtain the best fit to the magnetic structures in the powder neutron diffraction pattern. This structure, with the black circles representing spin up and the white representing spin down, is equivalent to the structure proposed by Le Flem et al. (1982).

This in-plane structure appeared to predict magnetic reflections at scattering angles corresponding to the observed peaks. The diffuse, low scattering angle peaks were fitted with two strong magnetic Bragg peaks, labelled as $^{-1/2} \ ^{-1/2} \ ^{1/3}$ and $^{-1/2} \ ^{-1/2} \ ^{-1/3}$ with corresponding scattering angles of 9.66° and 11.91° respectively. However due to the extreme preferential stacking in the powdered sample, a suitable fit to each peak was not obtained, as can be seen by the blue difference line in Figure 7.2. One common inaccuracy in each peak was the profile shape used to fit the data. The pseudo-Voigt line shape employed by FullProf did not appear to successfully model the shape of the data, especially around the diffuse peak on the high scattering angle side of the first magnetic Bragg peak, at around 10° in 2θ . It was also noted that the peak height on the nuclear peaks did not correspond well with the data, indicating the effects of preferred orientation on the fitting process.

This in-plane moment structure was also used to calculate the exchange field in FePS_3 using a combination of Equations 1.6 and 1.9

$$H_{\text{ex}} = \frac{k_B T}{g \mu_B} \quad (7.1)$$

With the 1st, 2nd and 3rd nearest neighbour exchange interactions taken from Okuda et al. (1983), the exchange field was calculated to be approximately 32 T. This is comparable to the exchange field of 33 T, observed experimentally in Figure 5.7, indicating that the in plane structure of Le Flem et al., (1982) closely resembles the moment structure of FePS_3 .

7.2 LOW DIMENSIONAL MAGNETIC STRUCTURE

As the FullProf fit to the data was not very accurate, the magnetic peaks were investigated separate from the nuclear peaks. Figure 7.4 shows the magnetic peaks removed from the neutron powder diffraction scan by subtracting the nuclear peaks from the magnetically ordered scan taken at 70 K. It was observed that on the high scattering side of each strong magnetic peak, there is a small hump, which is also magnetic. These have been highlighted with arrows in Figure 7.4. The diffuse humps could be due to either magnetic Bragg peaks of lesser intensity at these scattering angles, or they could indicate incomplete long-range order in the quasi-2D material. The FullProf analysis program originally attempted to fit these features with sharp peaks, as in Figure 7.2, yet the fit was insufficient to describe the width and shape of the peaks.

It is believed that these diffuse magnetic peaks at the high scattering angle side of the sharp magnetic peaks may be an indication of the short-range correlations between the moments along the z-direction. If these features do represent incomplete long-range order between the Fe ions, then they must correspond to elongated, rod-like scattering profiles in reciprocal space.

The powder neutron diffraction patterns of MnPS_3 also revealed rod-like structures in reciprocal space. These were in the form of trailing edges on the high scattering-angle side of the magnetic peaks (Goossens, 1999). This elongation, or rod-like behaviour in reciprocal space, is a result of the two-dimensional structure of these materials. These rods appear to travel along the l -direction in reciprocal space, which corresponds to low dimensional order along the z-axis in real space. Although the powder diffraction pattern of FePS_3 does not show obvious trailing edges on

each of the magnetic peaks, it is possible that the diffuse humps are equivalent features representing the short-ranged order.

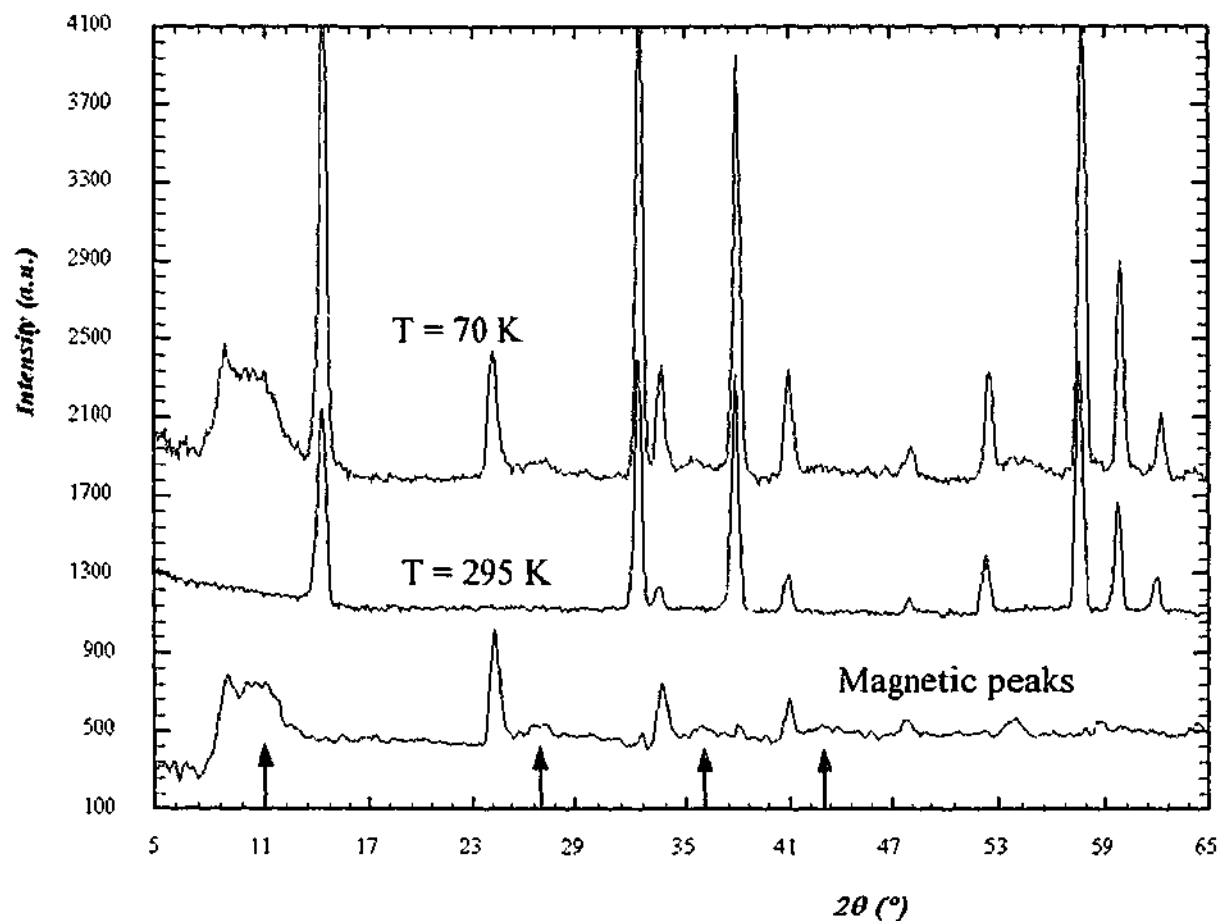


Figure 7.4: Magnetic peaks separated from the combined nuclear and magnetic spectrum at 70 K. The arrows indicate the pattern of a diffuse magnetic hump on the high scattering side of the sharp magnetic Bragg peaks.

The rod-like structures in reciprocal space are different between FePS₃ and MnPS₃, which may be due to the relative anisotropies of the two transition metal ions. The trailing edges are more pronounced in the powder pattern for MnPS₃, which would initially suggest that the rods in reciprocal space are more elongated than for the FePS₃. The D19 results supported this theory, as the magnetic rods originating at reciprocal lattice positions of $l_{\text{nuclear}} \pm 0.34$ had zero intensity within around ± 0.15 of the central maximum.

The difference in the observed short-ranged features between the Fe and Mn compounds can be attributed partially to the relative anisotropies between the two transition metals. The Fe in FePS₃ has a larger single-ion anisotropy due to the extra *d*-shell electron when compared with

Mn. Although the iron compound has a much larger anisotropy than the manganese compound, this does not necessarily imply that the ordering is longer ranged in FePS_3 than for MnPS_3 . The rod-like structures in reciprocal space may also be related to the exchange interactions or the magnetic dipole interactions between the layers. In MnPS_3 , the anisotropy is nearly negligible, and the exchange interactions between the planes of metal ions are up to 400 times less than the interactions within the layers (Wildes et al., 1998). In FePS_3 , the anisotropy is much larger and the exchange interactions between the layers are also possibly larger. However, the exchange interactions between the metal layers are related to the spin of the moment only.

The short-ranged order between the metal layers may not be related to the anisotropy or the exchange interactions, but due entirely to the magnetic dipole interactions. The magnetic dipole interactions are related to the total moment, which is much larger for MnPS_3 than FePS_3 . The relative strength of the effective moments in FePS_3 and MnPS_3 are $5.00 \mu_B$ and $5.97 \mu_B$ respectively. The smaller moment in the iron compound may lead to a smaller interaction between the planes. Thus it may be that the interactions between the transition metal layers are only dipole related, which would correspond to shorter ranged correlations along z for the FePS_3 .

For such short-ranged correlations along l , producing a truly 2-dimensional magnetic structure, the magnetic ordering temperature can be considered a phase transition from paramagnetic to 2D order rather than paramagnetic to weakly 3D order. This then gives rise to discussions about the fluidity of the moments along the z -direction.

7.2.1 *Static versus Dynamic order along z .*

It appears as though FePS_3 has no long-range order along the c^* -direction, however the magnetic order within the ab -plane is long-ranged and antiferromagnetic. This is obvious from the sharpness of the Bragg reflections in the a and b directions. Thus in the c^* -direction the lack of long-range order can be termed *paramagnetic* or *frozen paramagnetic*. Paramagnetic suggests that the order along the c^* -direction is dynamic and proportional to the temperature dependent susceptibility whereas frozen paramagnetic indicates that there is a temperature at which the moment planes freeze and become static, however there are no long-range correlations along c^* .

It is not yet known which process occurs in FePS₃, however either situation is possible. If the structure is static, the spins remain frozen below the magnetic ordering temperature. For a dynamic structure, entire planes of moments flip, such that the relative in-plane antiferromagnetic structure remains constant due to the relatively strong intraplanar exchange interactions. For the dynamic structure, the flipping may proceed until some equilibrium state such as long-range order is reached, however this is not always the case.

If the structure were dynamic, a change in temperature may induce a change in the position or distribution of the elongated streaks, as seen in the VIVALDI and D19 results, below the magnetic ordering temperature. In this case, the correlations would be thermally activated below T_N . Over time, the relative orientations of the moment planes would vary, however, given enough time, the structure may settle into long-range 3-dimensional order. This would require entire planes of moments to spontaneously flip, keeping their relative antiferromagnetic structure. Turning entire planes over would be difficult, as it would require many times the anisotropy energy, relative to the number of atoms within the plane. As the anisotropy energy in the plane is equal to the anisotropy energy per atom multiplied by the number of atoms, the system may eventually relax into some equilibrium state.

Achieving a state of equilibrium does not necessarily mean that the planes will find some 3D order. In fact, there is a strong possibility that there will never be 3D long-range order in FePS₃ as the moments are Ising objects with only two possible orientations (up and down). A chain of these Ising objects in the z -direction does not order at any temperature above $T = 0$ K. If FePS₃ orders in the ab -plane first, and then tries to order in the c -direction, the process can be described as a two dimensional Ising ordering followed by a one dimensional Ising ordering in which the units of the chain are the two dimensionally ordered planes themselves.

If the structure were static, there would be no change in the correlations as the temperature was lowered below the Néel temperature. In this case the moments would be frozen in place and the structure can be considered as glass-like with a glass temperature most likely coinciding with the Néel temperature. If a sample of FePS₃ was cooled towards its Néel temperature of 120 K, the interactions within the ab -plane would become long-ranged and the anisotropy of the Fe²⁺ would align the moments parallel and antiparallel to the c^* -direction in the structure described by Le Flem et al. (1982). However, as the interactions within the plane are so much stronger than those between the Fe layers, the moments order preferentially in the plane at higher temperatures.

Then as the temperature is reduced still further, the weak interactions between the planes try to order the moments along c^* . However as the anisotropy of the moments is so strong, and the in-plane interactions are long-ranged, the inter-planar interactions do not have enough energy to flip the planes of moments to form long-range correlations along c^* . Thus for a static structure in FePS_3 it appears as though the anisotropy hinders the correlations in this direction.

The state of the moments along c could possibly be measured as static or dynamic via inelastic neutron diffraction experiments or AC susceptibility measurements. In principle, the line widths from inelastic neutron scattering at temperatures just below the Néel temperature may indicate a static behaviour, however this depends on the relaxation time of the moment planes. If the frequency of the planes flipping is too low, the neutrons may not detect it. Another possible measurement technique is AC susceptibility, which may pick up slow relaxation times. These measurements could detect the flipping rate of the planes.

7.3 SIMULATIONS

7.3.1 Simulation of the powder neutron diffraction data

The magnetic structures proposed in section 7.1 were reassessed with consideration given to the streaky magnetic reflections observed in each of the neutron scattering techniques. The MRPD data appeared to have diffuse features on the high scattering angle side of the strong magnetic peaks, similar to the trailing edges observed in the MnPS_3 powder diffraction data. The Laue plots from VIVALDI also exhibited elongated magnetic peaks that extended beyond the effects of twinning in the crystal. Finally the intensity profiles taken along l from the D19 data showed rod-like profiles in reciprocal space. The rod-like behaviour observed in the VIVALDI and D19 data implied that long-range order was incomplete along the c^* -direction. This information was used to calculate possible diffuse, low-dimensional trailing edges for the low scattering angle magnetic peaks in the FePS_3 powder neutron diffraction pattern.

There was much debate as to the true centre of the magnetic peaks in each result, however, it was later realized that the streakiness in both the D19 data and the VIVALDI data was a result of the short-range correlations between metal atoms along the z -direction. The helical and collinear structures discussed in Section 7.1 differed in their classification of the magnetic unit cell as

either incommensurate or commensurate. A commensurate magnetic unit cell can be defined by a simple, exact multiple of the nuclear unit cell, whereas an incommensurate structure is not an exact multiple of the nuclear cell. Both structures involve long-ranged ordering which results in sharp magnetic Bragg peaks either at positions directly related to the nuclear cell, or at positions that are not exact multiples of the nuclear cell respectively. The propagation vector of $\frac{1}{2} \frac{1}{2} l$ for FePS₃ is neither an exact multiple nor fractional multiple of the nuclear unit cell due to the elongated magnetic reflections along l . Thus all evidence suggests that neither a commensurate nor an incommensurate structure can successfully describe the magnetic moments in FePS₃ as both structures imply that long-range order is present.

A simulation was set up to model the magnetic reflections from a randomised powder with short-ranged correlations. The magnetic peaks were calculated from the pair of propagation vectors that best fit the in-plane moment structure in Figure 7.3, with moments parallel and antiparallel with c^* . These propagation vectors, $\frac{1}{2} \frac{1}{2} l$ and $-\frac{1}{2} -\frac{1}{2} l$, modelled magnetic peaks taken from the 000, 130, and 200 nuclear positions. Thus the simulated magnetic reflections were at 9.6° in 2θ for the $\frac{1}{2} \frac{1}{2} l$ lines and centred around a scattering angle of 25° in 2θ for the $\frac{1}{2} \frac{5}{2} l$ and $\frac{3}{2} \frac{1}{2} l$ lines. The line shapes were approximated with Gaussian profiles and the peak intensity was adjusted according to the angular dependent magnetic form factor. The magnetic form factor curve for Fe²⁺ can be seen in Figure 7.5.

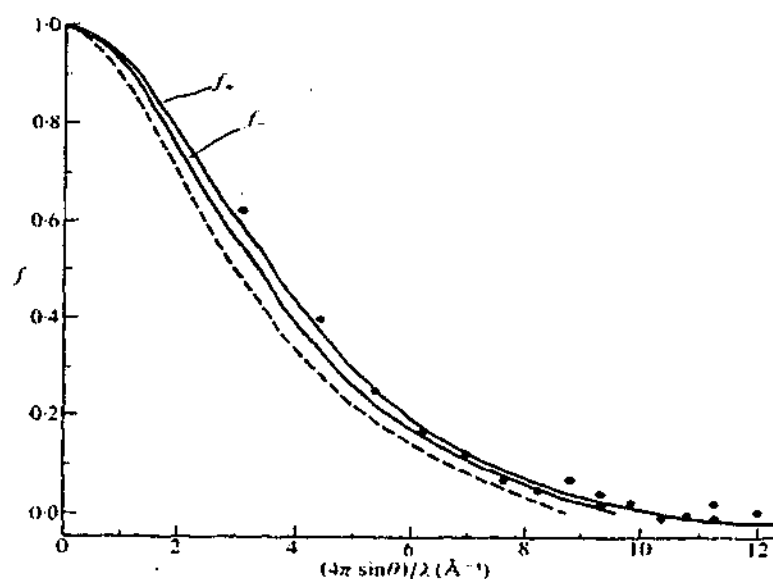


Figure 7.5: Magnetic form factor of Fe²⁺ (Bacon, 1975). A Gaussian line shape was used to model the data points shown in the simulation of the magnetic peaks for FePS₃.

In Figure 7.5, the points were taken from the work of Shull and Yamada (Shull & Yamada, 1962) and the full and dashed lines represent calculations for a free iron atom and Fe^{3+} respectively.

In the D19 data, the intensities of the magnetic reflections were found to be strongest for the reflections closest to the origin along l . Thus each peak in the simulation was created from the sum of the peaks with $l = \pm 0.34, \pm 0.66, \pm 1.34, \pm 1.66$. An instrumental half-width of 0.025 was assumed for each peak, with broadening taken from the qualitative spread of the magnetic reflections in the D19 intensity profiles. As the intensity of the magnetic peaks ranged between ± 0.15 of the central maximum, the simulated peaks also covered the range of $l \pm 0.15$. The peaks were also constrained to have the same areas, such that the simulation contained a series of Gaussian peaks centred at the wave vector for each point, but each with progressively increasing widths and therefore decreasing peak heights. This can be seen in the subspectra in Figure 7.6.

The only factor that was not included in this simulation was a preferred orientation factor, relating the texture in the powder sample to the simulated peak heights. As the exact degree of preferential stacking in the sample was not known, the best preferred orientation factor was also not known. This factor was not considered vital for the simulation as it affects mainly the peak intensities, while the peak shapes are the key indicators of short-ranged correlations. If the magnetic order were long-ranged along z , the peaks would be sharp, or at least only broadened by the instrumental resolution. If there is a uniaxial preference for the crystallites in the sample to align with a common 001 direction, then the reciprocal lattice points off the plane would be more probable leading to an enhancement of the diffuse part of the first peak, and possibly also for the second peak.

Comparing Figure 7.6 with the observed powder neutron diffraction pattern in Figure 7.7, it can be seen that the trailing edges did not sufficiently describe the intensity of the diffraction peaks at around 0.85 \AA^{-1} . This could be an indication of the effects of preferred orientation.

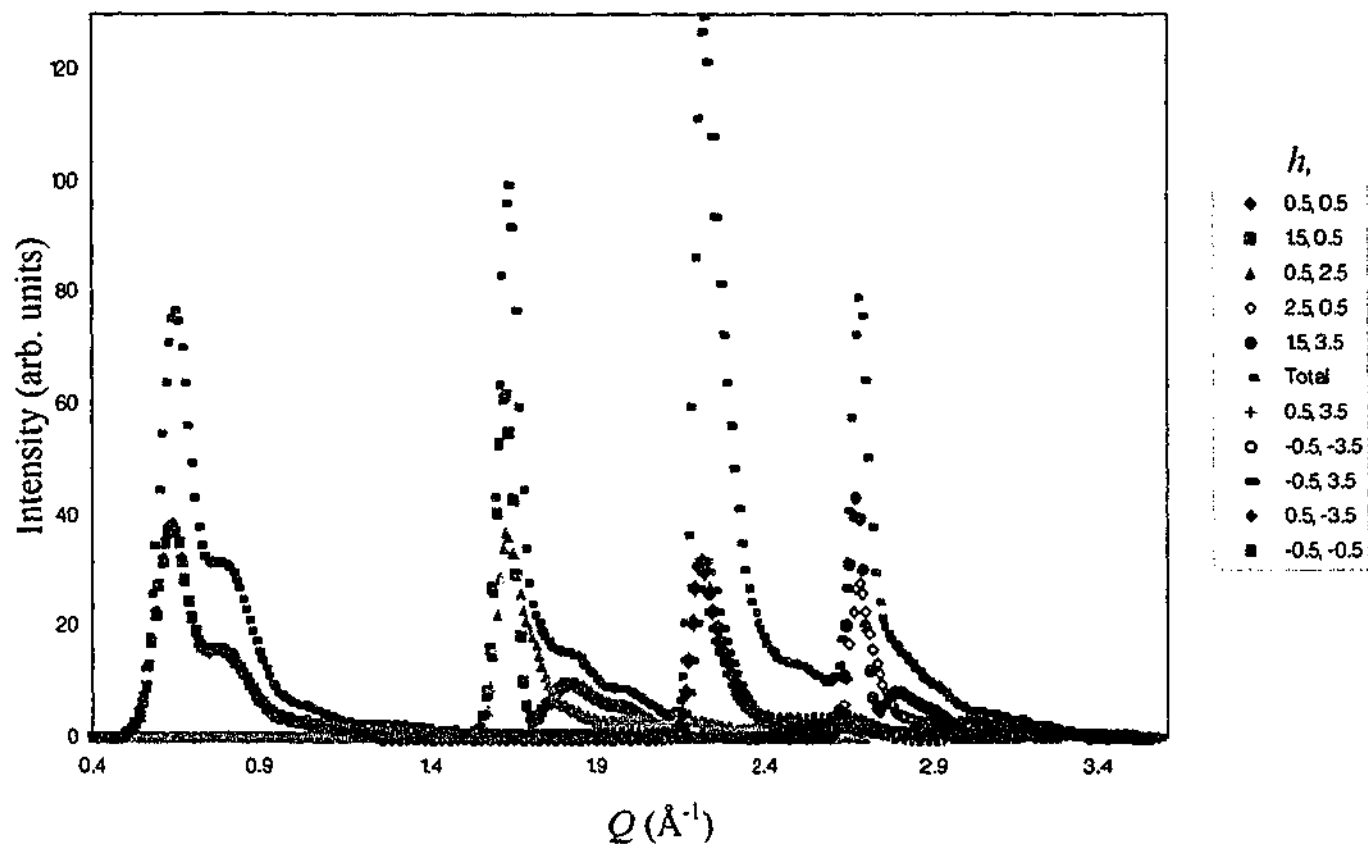


Figure 7.6: Simulation of the magnetic peaks with propagation vectors of $1/2, 1/2, 1$ and $-1/2, -1/2, 1$ taken from the 000, 130, and 200 nuclear positions. This simulation includes magnetic peaks below a scattering vector of 2.9 \AA^{-1} .

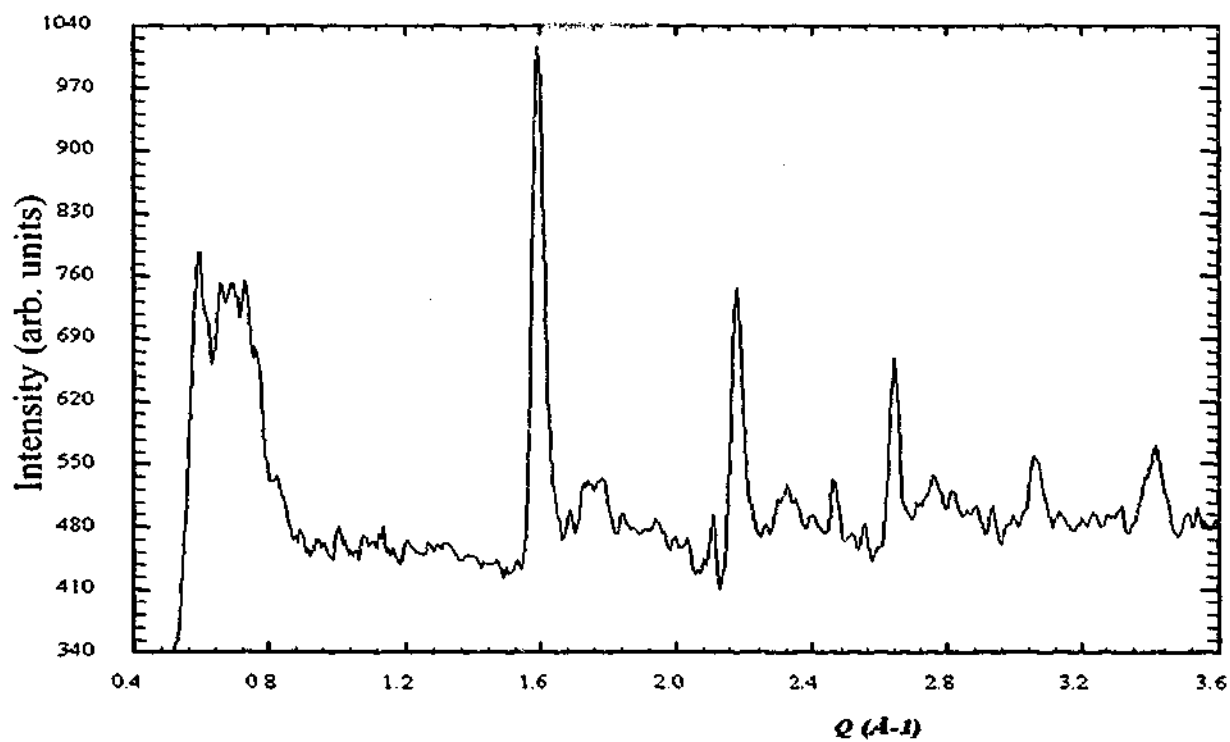


Figure 7.7: The corresponding MRPD diffraction pattern of the same region as in Figure 7.6.

7.3.2 Simulation of the peak intensity along l

Due to the broadness of the peaks along l from the D19 data, a simulation was carried out to model the intensity distribution of a one-dimensional (1D) magnetic lattice in the paramagnetic region. Short-ranged order can be estimated using the paramagnetic Curie Weiss relationship, based on the mean field theory as in Equation 1.15.

$$\chi = \frac{Ng^2\mu_B^2S(S+1)}{3k_B T(1+\Theta/T)} \quad (1.15)$$

The susceptibility arising from short-ranged order correlations can be related to the neutron scattering intensities via the exchange interactions, J , from first, second and more distant nearest neighbours. This exchange integral, $J(\kappa)$, is dependent on the scattering vector, κ , which is a non-zero wave vector in reciprocal lattice units. Thus the value of the Weiss characteristic temperature, Θ , in Equations 1.15 can be replaced by this variable, to give Equation 7.2 below.

$$\chi(\kappa) = \frac{Ng^2\mu_B^2S(S+1)}{3k_B T(1+J(\kappa)/T)} \quad (7.2)$$

Here $J(\kappa)$ is the Fourier transform of the exchange integral, which is influenced by the anisotropy and magnetic dipole interactions. The magnetic dipole interaction acts to align the spins in the lattice. For simplicity, it can be assumed that there are two exchange interactions between the planes, J_1 and J_2 . Thus the scattering vector dependent exchange can be approximated by the periodic functions as in Equation 7.3.

$$J(\kappa) = J_1 \cos(2\pi\kappa) + J_2 \cos(4\pi\kappa) \quad (7.3)$$

The susceptibility is directly proportional to the intensity of the profile along l , and thus the intensity of the peaks can be defined by Equation 7.4. In this Equation, the constant terms from Equation 7.2 have been removed and $C_i \propto J_i/T$, thus the absolute values of C_1 and C_2 vary with temperature.

$$I \propto \frac{1}{1 + C_1 \cos(2\pi\kappa) + C_2 \cos(4\pi\kappa)} \quad (7.4)$$

For this model, only the first two planar interactions were considered and the function was constrained to peak at $\kappa = 0.34$, which corresponds to a ratio of the first to second neighbour plane interaction of $C_1/C_2 = 1.927$. The graph in Figure 7.8 has $C_1 = 1.25$ and $C_2 = 0.65$. The absolute values of C_1 and C_2 vary with temperature in a dynamic situation as $C \propto J/T$, however the ratio stays the same for the peak position of $\kappa = 0.34$. The current model of FePS_3 is probably not dynamic for short time scales, as the correlations are frozen below T_N . The intensity above 120 K is proportional to the generalised susceptibility and appears to peak at the positions at which Bragg peaks appeared in the D19 data. For antiferromagnetic exchange interactions, between the first and second nearest neighbours, the ratio of the two interactions describes the position of the peaks, and the width is controlled by the magnitude of C_1 and C_2 . Thus by maintaining the ratio between the exchange interactions, J_1 and J_2 , the peak positions in the simulation will remain constant. A change in the absolute values of these parameters will result in a peak shape change.

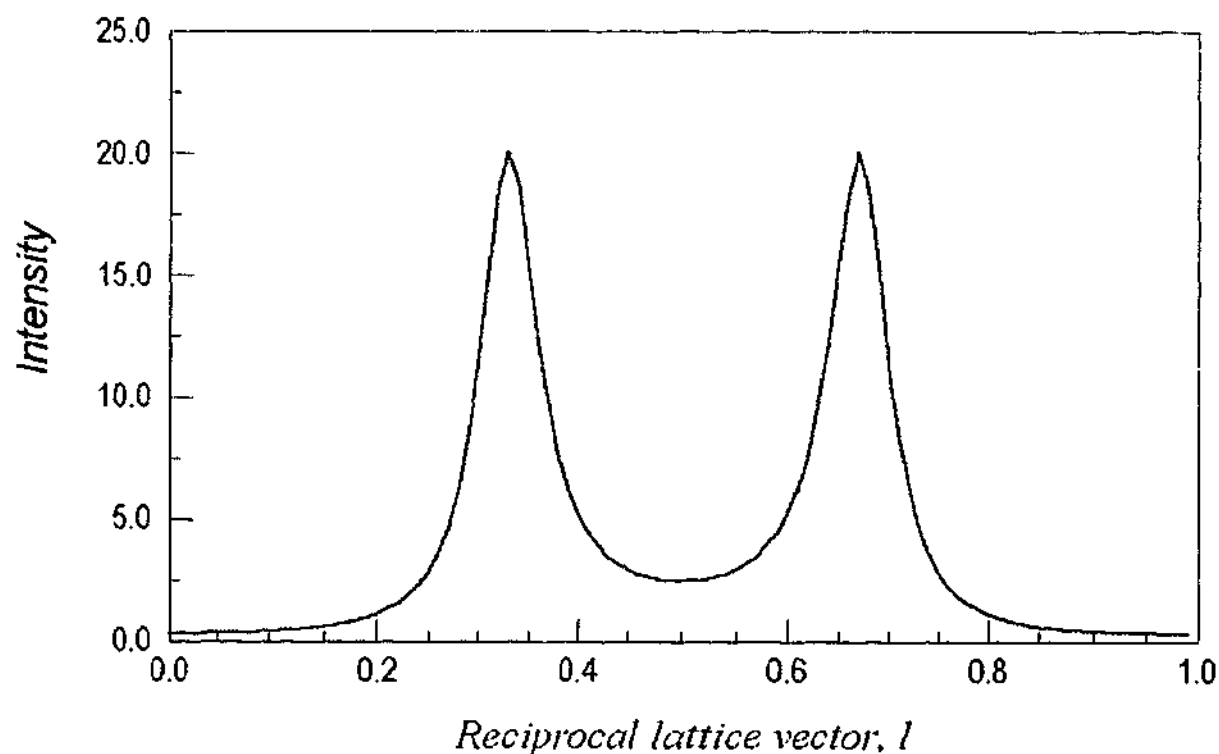


Figure 7.8: Theoretical prediction of the intensity along the reciprocal lattice vector, l .

The model outlined above assumes that the crystallographic c -axis is perpendicular to the ab -plane. In this simulation the scattering vector of the 1D system was taken to be perpendicular to the ab -plane, rather than along the monoclinic angle, β . The susceptibility in this model relies on the Curie Weiss law and a Fourier transform of the exchange integrals. As these exchange integrals are symmetric and can be applied in one direction as easily as another, the Fourier transforms must be even. This gives rise to the symmetric peak shape seen in the model where peaks are observed at the same position in $\pm l$. This is why the intensities of both peaks are equal, rather than unequal as seen in the results.

With this model, it was assumed that the reflections would occur at both hkl and $hk\bar{l}$ sites, however this was not true in all of the D19 results. It was also assumed for these calculations that these sites were equivalent, leading to equal intensities for both $+l$ and $-l$ reflections. These assumptions lead to discrepancies between the modelled and observed intensity profiles. Each peak at either $+l$ or $-l$ represents a magnetic domain within the sample. Thus a plot showing peaks at only the $+l$ positions implies that there is one magnetic domain in the crystal, whereas peaks at both the $+l$ and $-l$ reflections would indicate the presence of two domains. In the true crystal structure, one domain will most likely be preferred over the other, and thus the relative intensities of the two peaks should differ.

It must also be noted that the results in Figures 6.15 and 6.16 were taken well below the magnetic ordering temperature of 120 K, such that the system was antiferromagnetically ordered. This model presents what should be seen in the paramagnetic phase as a function of Q along the c^* -direction. In the paramagnetic phase a peak will occur at every reciprocal lattice vector, and thus this model predicts peak positions at both $\pm l$. In the antiferromagnetic phase, this is only true for multiple domains. If long-range order were present, then a propagation vector of $\frac{1}{2} \frac{1}{2} 0.34$ would imply that reflections occur at $\frac{1}{2} \frac{1}{2} 0.34$ and $-\frac{1}{2} -\frac{1}{2} -0.34$, but not at $\frac{1}{2} \frac{1}{2} -0.34$ or $-\frac{1}{2} -\frac{1}{2} 0.34$.

It was noted in section 6.5 that a single peak occurred in both crystallites at the $+l$ position for the peaks scanned at $\frac{1}{2} \frac{1}{2} l$ while the peaks scanned at $\frac{3}{2} \frac{1}{2} l$ showed peaks at both $\pm l$. This would suggest that at $\frac{1}{2} \frac{1}{2} l$ there is only one domain and for $\frac{3}{2} \frac{1}{2} l$ there are two. This unexpected result does not fit with the current understanding of the sample. It is possible for two domains to be present in one crystallite, however, peaks should be observed at both $\pm l$ in all hk rods, rather than only one. The fact that two peaks, indicating the presence of two domains, were

observed in both crystallites for the same hk plane of $3/2 \ 1/2 \ l$ is puzzling. It is still unclear why this might be possible.

This model clearly indicates that although there are magnetic interactions between the interplanar moments, these correlations are very weak such that there is no apparent long-ranged order along the c -axis. Thus the variation of the intensity along c^* can be described by a disordered but correlated set of magnetic planes with the moment directions along c^* . One such model that could describe this structure is the 1D-Ising model.

The 1D Ising model describes a single dimensional chain of magnetic moments that interact via short-ranged correlations only. In this model, interacting magnetic spins that form a one-dimensional linear chain do not exhibit long-range order at any temperature above absolute zero Kelvin. Even when there is extreme anisotropy, as in the case of an Ising system, these one dimensional chains display no phase transitions (Lines, 1969).

In FePS_3 , as the temperature is reduced below the ordering temperature, the magnetic moments in the ab -plane order two dimensionally. Once these planar interactions within the 2D lattice have formed, the weaker interactions along the c^* -direction attempt to order, such that along the z -direction, the moments planes form a chain. As there can be no magnetic order in a 1D Ising system above 0 K, there will be no long-range order along c^* . This clearly describes FePS_3 as a truly 2D magnetic system, with ordering in the plane only.

7.4 TEMPERATURE DEPENDENCE OF THE 2D MAGNETIC BRAGG PEAKS

The magnetic Bragg peaks from the powder neutron diffraction scans appeared to be sharp and well defined in the a^*b^* -plane, yet smeared and elongated along the c^* -direction. Thus there is long-range order within the planes, and only short-range correlations between the planes. From the D19 profiles, the thermal variation of the short-range order was examined in terms of the change in the sublattice moment. This temperature variation of the peak position can be seen in Figure 7.9. This plot shows how the peak positions varied along l with increased temperature. It is obvious from this plot that the peak positions do not deviate from their initial values of 0.34 and 0.66 up to and beyond the Néel temperature.

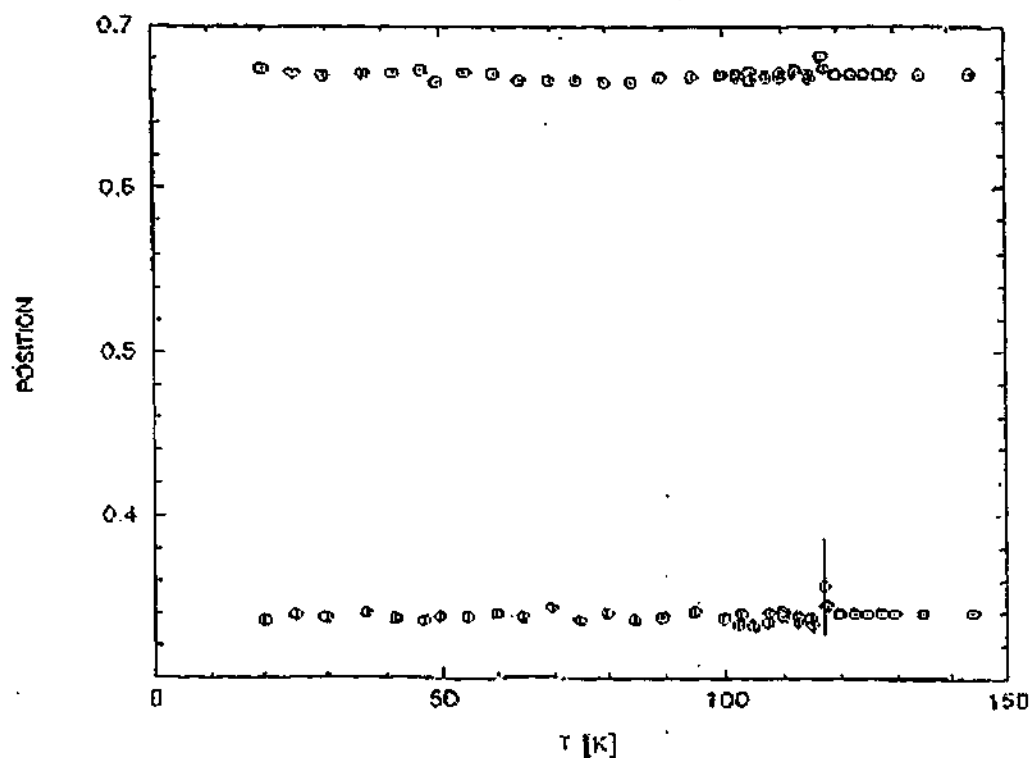


Figure 7.9: The thermal variation of the peak position as taken from D19. This plot was taken for the $3/2, 1/2$ position with the two peaks at $l = 0.34$ and 0.66 .

From the discussion above, it can be seen that FePS_3 is well described by a 2D Ising model in the ab -plane and a 1D Ising chain with no long-range order perpendicular to the planes. Wiedenmann et al. (1981) and Kurosawa et al. (1983) have both shown evidence of the 2D in-plane structure of the MPX_3 compounds ($M = \text{Mn}$ and Fe , $X = \text{S}$ and Se) from their neutron diffraction studies, however neither has commented on the significance of their results. Each study displayed plots of the temperature dependence of the reduced magnetic moments, superimposed with a modelled Brillouin function for different spin values ($S = 1/2, 5/2$). These can be seen in Figure 7.10.

As can be seen in these figures, the data for the Mn compounds fitted the Brillouin curve of $S = 5/2$ very well, as expected for a material with very little single-ion anisotropy and three dimensional order. The data from the Fe compounds appear to remain at a constant level in T/T_N up to approximately 0.7, beyond which the magnitude of the moment falls sharply as T approaches T_N . This sharp decrease can be attributed to the strong anisotropy of the Ising type system and may also describe the two-dimensionality of the interactions.

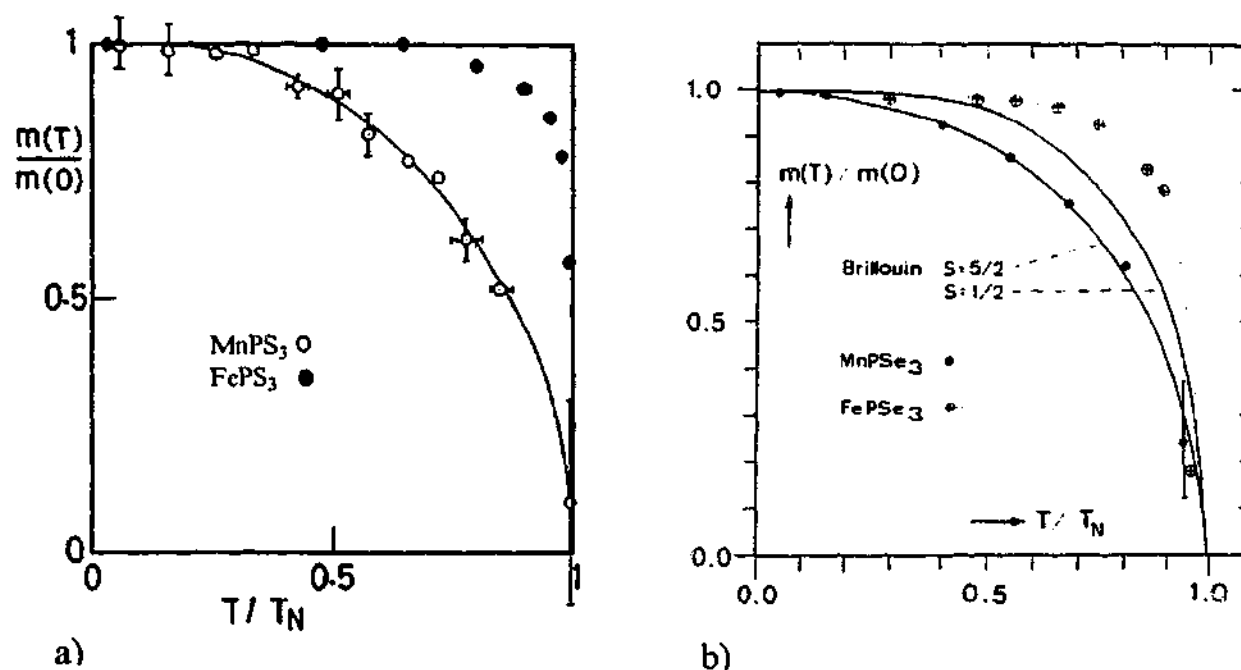


Figure 7.10: The thermal variation of the reduced magnetic moment for (a) MnPS_3 with FePS_3 (Kurosawa et al., 1983) and (b) MnPSe_3 with FePSe_3 (Wiedenmann et al., 1981).

The temperature variation of the reduced magnetic moment can be described by the following equation, which describes the spontaneous magnetisation of the Ising square lattice. It is valid for all temperatures in the range from 0 K to the critical temperature (Fisher, 1967).

$$M_0(T) = \left\{ 1 - \left(\sinh 2K_x \sinh 2K_y \right)^{-2} \right\}^{1/8} \quad (7.5)$$

$M_0(T)$ is the thermal variation of the sublattice moment and K_x and K_y represent the isothermal compressibility in both the x and y directions. For a square lattice, the compressibility is equal in each direction and $K = J/k_B T$. When $T = T_c$, the spontaneous moment reduces to 0, and when T is close to 0 K, the moment is at its maximum value. As this equation describes the model for a 2D square lattice, the true model will differ for the honeycomb lattice of FePS_3 .

Equation 7.5 can be approximated for all lattice types with Equation 7.6, however this holds true only for temperatures close to the critical temperature.

$$M_0(T) \cong B \left(1 - \frac{T}{T_c} \right)^\beta \quad (7.6)$$

Here, $\beta = 1/8$ for an Ising system with a dimensionality of 2 (Fisher, 1967). The parameter B is a scaling constant representing the amplitude of the magnetic moment and T_c is the critical temperature defining the transition from magnetic order to disorder. The value of B is dependent on the lattice structure and differs for a square, triangular or honeycomb lattices. These have been found to equal 1.222410, 1.203270 and 1.264904 respectively for the Ising model (Fisher, 1967). For an antiferromagnet, the critical temperature is equivalent to the Néel temperature.

The 2D Ising model for a honeycomb lattice has been calculated by Burley (1960) and these results along with the square and triangular 2D lattices as well as some 3D models can be seen in Figure 7.11. It can be seen that the exact solution for each of the 2D lattices are less curved than the 3D models with the honeycomb structure showing the most square-like profile. It can also be seen that the 2D square lattice, as described by Equation 7.5 closely resembles the 2D honeycomb lattice. Thus Equation 7.5 was used as a first approximation of the 2D honeycomb lattice.

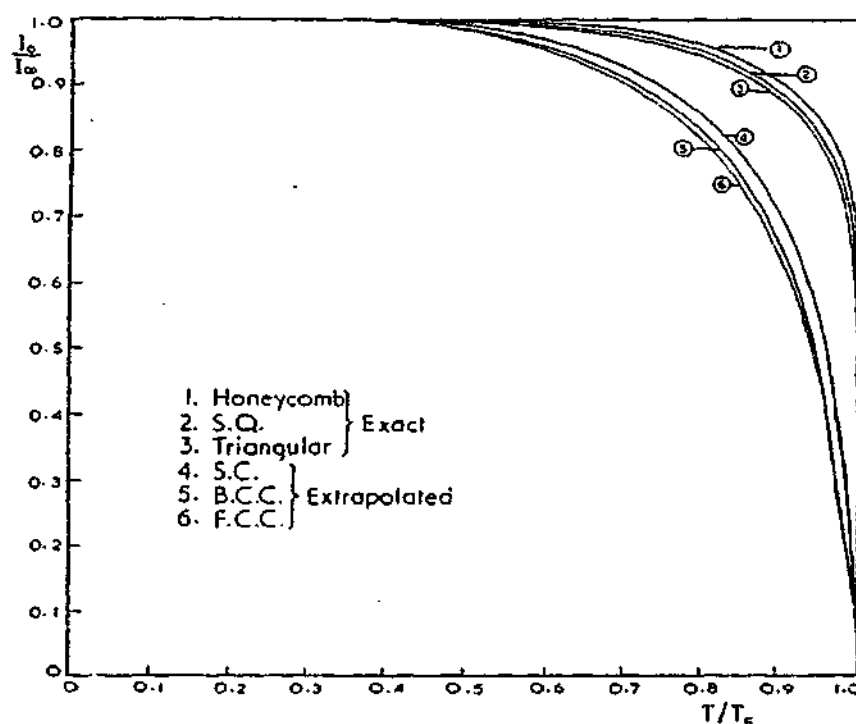


Figure 7.11: The spontaneous magnetization as a function of reduced temperature plotted for the 2D honeycomb, square and triangular lattices as well as the 3D cubic models (Burley, 1960).

The temperature dependent magnetic intensity of the current sample of FePS_3 was produced from the D19 results and can be seen in Figure 7.12. This data has been fitted with a 2D, square-lattice, Ising curve (Equation 7.5). The curve for the three dimensional, $S = 1/2$ mean field approximation has also been drawn for reference. The $S = 1/2$ Brillouin function was chosen to represent the simplest model for a 3D Ising system with only two states; spin up and spin down. This does not appear to represent the data well at temperatures just between 80 and 120 K. This is another indication that the interactions must be weaker in one direction compared with the other two.

The two curves have been calculated for nearest neighbour interactions only, and it is clear from this plot how well the 2D model fits the data, even though it is based on a square lattice rather than honeycomb.

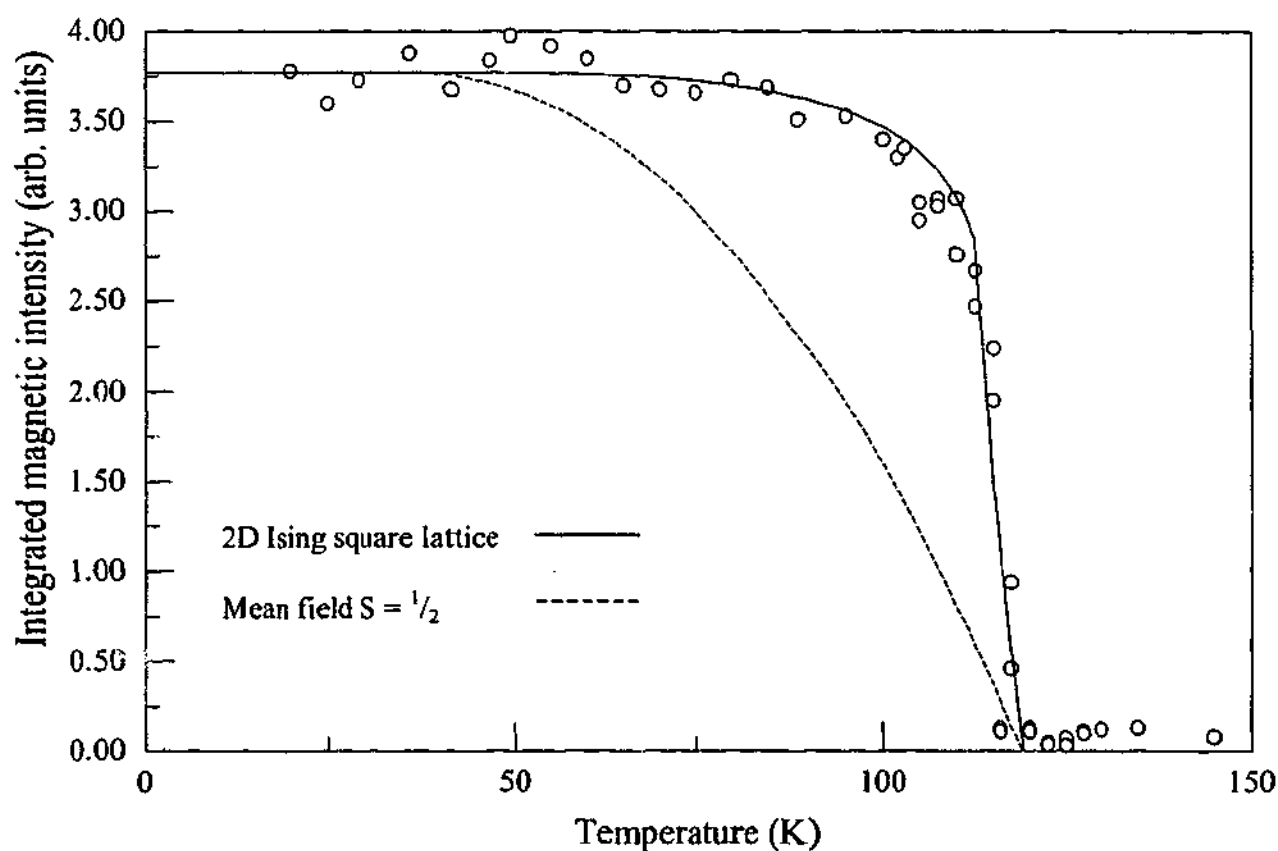


Figure 7.12: The variation of magnetic intensity in FePS_3 with temperature. This data was taken from the variation of the $^{3/2} 1/2 0.6 \dots$ intensity in the D19 data. The fit to the data is taken from the square lattice 2D Ising model and the other curve represents the spin $1/2$ mean field approximation for a 3D material.

Although the 2D square lattice model was used to fit the FePS_3 data in Figure 7.12, the calculations of Burley (1960) indicate that the curves for the 2D square and honeycomb lattices

are very similar. As the variation in the sublattice moment for the honeycomb lattice closely resembles the shape of the 2D square lattice, it is considered more likely that the structure of FePS₃ is 2D, rather than 3D. From the fit to the current data, the value of the first neighbour interaction was $J_1/k_B = 50.7$ K. This appears to be much larger than the calculated values for the first neighbour interactions due to the fact that all other interactions were neglected. The Néel temperature from this fit was found to be 119.1 K.

7.5 COMPARISONS WITH OTHER MAGNETIC STRUCTURES

From the current data, it appears as though the magnetic structure of FePS₃ is truly two-dimensional. Analysis of this data has shown that it is well modelled as a 2D Ising antiferromagnet. Only two other materials fitted this description as completely as FePS₃; Rb₂CoF₄ and K₂CoF₄. Thus the structure and magnetic properties of these three materials can be compared to each other and to the similar materials Rb₂FeF₄ and FePS₃.

7.5.1 Other 2D Ising antiferromagnets

The structure of Rb₂CoF₄ (and similarly Rb₂FeF₄ and K₂CoF₄) consists of square antiferromagnetic planes with a large separation between the magnetic atoms caused by the interposition of two mixed Rb and F planes. The two dimensionality of this structure results from the extreme separation of the antiferromagnetic Co planes, with around 13.7 Å between each layer (Samuelsen, 1973).

Due to the antiferromagnet coupling of the moments in the planes, and the offset of the magnetic planes, the exchange interactions between nearest neighbours in adjacent planes appear to be zero (Birgeneau et al., 1970). The structure of Rb₂FeF₄, which is very similar to Rb₂CoF₄ can be seen in Figure 7.13.

Interestingly, the antiferromagnetic compound Rb₂FeF₄, which is similar in structure to Rb₂CoF₄, does not show characteristics of 2D behaviour. Mössbauer absorption spectra of Rb₂FeF₄ indicated that long-range order appears at around $0.6T_{\chi \max}$ (the temperature at which maximum susceptibility occurs), while neutron diffraction studies showed sharp magnetic Bragg

peaks at temperatures less than the Néel temperature (Wertheim et al., 1968; Birgencau et al., 1970). The neutron scans for Rb_2FeF_4 can be seen in Figure 7.14.

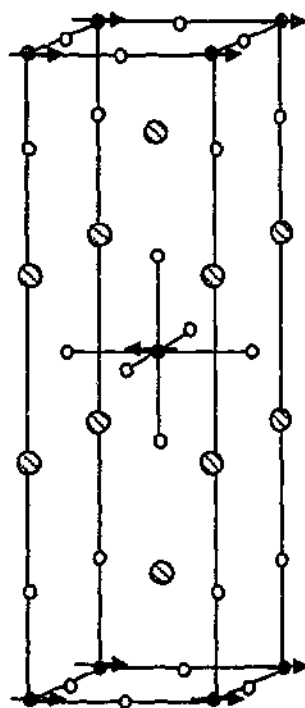


Figure 7.13: The crystal structure of Rb_2FeF_4 . The closed circles represent the Fe atoms, (moments lie in the plane). The open circles are F and the hatched circles are Rb.

In contrast to this, neutron diffraction studies of Rb_2CoF_4 have shown rod-like profiles in reciprocal space for the magnetic peaks below the Néel temperature. This indicates that it does not order along the z -direction, similar to FePS_3 . Scans taken along the $00l$ direction showed broad magnetic intensity indicating the presence of only short-ranged correlations along the l direction. A plot of the neutron scans taken along c^* can be seen in Figure 7.15. The speed of quenching was noted to affect the degree of ordering in Rb_2CoF_4 such that rapid cooling produced a broader magnetic peak characteristic of 2D ordering.

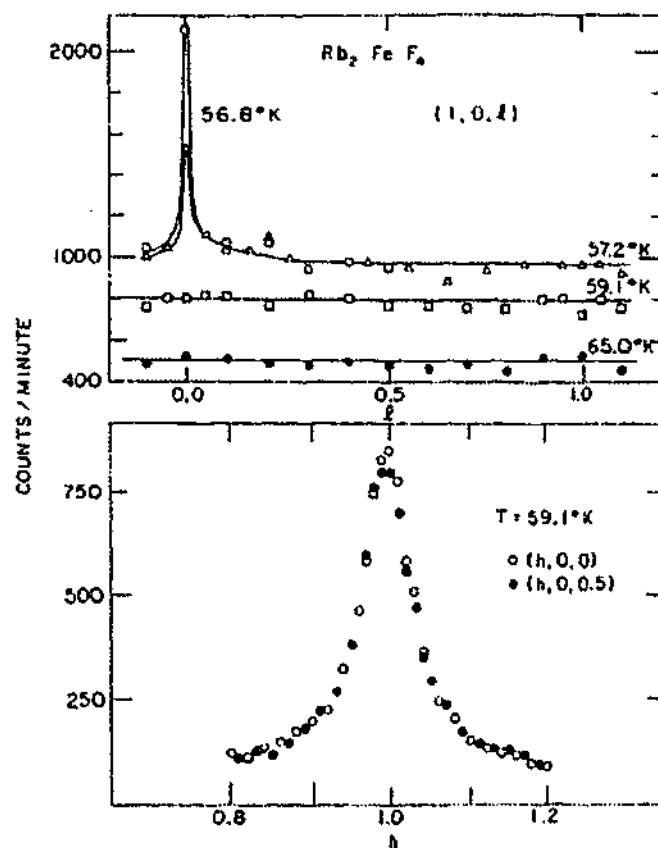


Figure 7.14: Neutron diffraction scans taken along the rods of intensity at temperatures above and below the Néel temperature of 57 K. A sharp magnetic Bragg peak appears at (100) below T_N in the top picture, while the bottom picture shows the cross sectional profile of the rod in reciprocal space at two different positions (Birgeneau et al., 1970).

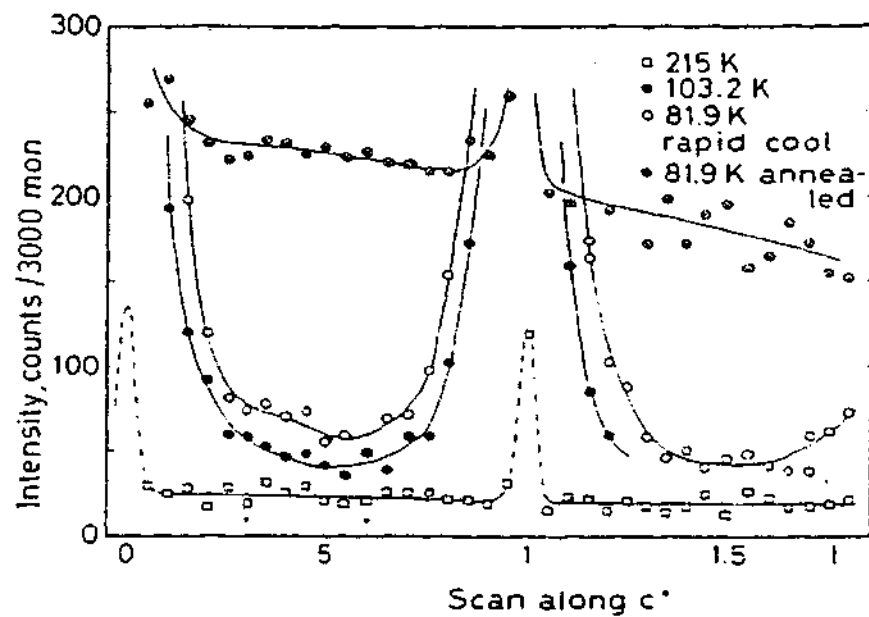


Figure 7.15: Neutron scans of Rb_2CoF_4 taken along c^* for four different temperature cases. Rapid cooling through T_N produced a broad Bragg peak indicating that the ordering may be incomplete long-ranged (Samuelsen, 1973).

From these neutron scans, the plot of the thermal variations in the reduced sublattice magnetisation was plotted for Rb_2CoF_4 , and fitted with a similar expression to Equation 7.4. From least squares fitting, the parameters B and β were found to be 1.16 ± 0.03 and 0.119 ± 0.008 respectively which were close to the theoretical values of 1.22 and 0.125 for a square lattice, 2D Ising antiferromagnet (Samuelsen, 1973). In this situation, the variation of the reduced magnetic moments also fell sharply at temperatures close to the Néel temperature. This was attributed to the absence of long-range order in the 3rd dimension. Thus both Rb_2CoF_4 and FePS_3 fall into the same category of true two-dimensional antiferromagnetic materials with only short-ranged correlations in the 3rd dimension.

Both neutrons diffraction results and susceptibility measurements of these two compounds showed similar features, which indicated the magnetic dimensionality was similar in each case. The rod-like scattering profiles in reciprocal space were a strong indication of incomplete long-range order, while the temperature dependent sublattice moment closely resembled the 2D Ising model. Thus as Rb_2CoF_4 is a well known 2D Ising antiferromagnet, so too may FePS_3 fitted into this category.

7.5.2 Comparison between the magnetic order of FePS_3 and FePSe_3

FePS_3 and FePSe_3 appear to be very similar compounds, with comparable internal hyperfine fields as observed in the Mössbauer spectra. The single-ion anisotropy is also very similar in each material due to the non-spherical Fe^{2+} in each compound. However the magnetic ordering is different in each compound with FePSe_3 displaying typically 3D features and FePS_3 exhibiting 2D features. The only difference between these compounds that may be responsible for the different magnetic ordering is the lattice structure.

The only major difference between the structures of FePS_3 and FePSe_3 is that the former has a monoclinic crystal structure and the later, a rhombohedral. The two corresponding unit cells are easily compared via simple shifts that translate the orthogonal a and b axes of the monoclinic system to the a and b axes at 120° to each other in the rhombohedral system. The layers of Fe in the FePSe_3 structure repeat three times within each unit cell, which is doubled along the z -direction in the magnetic unit cell. This corresponds to six Fe layers in their magnetic structure before the magnetic moment pattern repeats (Wiedenmann et al., 1981). Thus the FePSe_3 has

approximately twice the magnetic periodicity of FePS₃ in the z -direction. The interplanar interactions also appear to be considerably stronger in FePSe₃ such that the ordering is 3D.

7.6 CONCLUSIONS

The combination of results obtained from each of the analysis methods, indicated that the magnetic structure of FePS₃ is somewhat different to that of Kurosawa et al. published in 1983. The in-plane structure that best describes the magnetic moment arrangement was in fact the same structure of Le Flem et al. (1982), which consisted of ferromagnetic chains coupled antiferromagnetically at an angle of 60° to the a -axis. This magnetic unit cell was in fact twice the size of the crystallographic unit cell in both the a and b -directions.

Although neutron diffraction measurements initially pointed to a magnetic unit cell size three times as great as the nuclear cell along the c direction, it has more recently been discovered that this is not so. In fact, the ordering along the third dimension is short-ranged with only short-range correlations between the moments along c . Thus FePS₃ does not have long-range magnetic order and may not repeat exactly every third layer. It is not yet known if the ordering along z is static or dynamic, however, a static, random alignment is more probable. Fitting various models to the data has supported this theory, indicating that FePS₃ is truly a 2D Ising antiferromagnet, similar to Rb₂CoF₄.

It would appear from this that FePS₃ is rare as a truly 2D antiferromagnet, with no long-range order in the third dimension. It is not often that a perfectly 2D magnetic material is found, and thus FePS₃ is perfect for low dimensionality investigations, as described in Chapter 8.

CHAPTER EIGHT

8: Spin Diffusion through FEPS₃

In a magnetically ordered system, the spins on the magnetic atoms relate via exchange interactions in which the spin state of one atom will arrange itself according to the spin states of its neighbouring atoms. For long-range magnetic order, the exchange interactions are dependent on not only the nearest neighbours but also the more distant neighbour spins. Thus for ferromagnetic materials the moments align parallel, and for antiferromagnetic materials, they align antiparallel such that the overall magnetisation in the material is zero. Long-ranged magnetic order breaks down above the critical temperature as the correlations between distant neighbours decreases. In this paramagnetic phase, there is no overall magnetisation and the moments are aligned randomly throughout the structure. However even in the paramagnetic state, the spins can exchange information throughout the lattice. Thus the state of a spin can diffuse through the lattice over time. This is the basis of paramagnetic spin diffusion.

8.1 CONVENTIONAL SPIN DIFFUSION

The concept of spin correlations at high temperatures, and using inelastic neutron scattering to investigate them, has been around since Van Vleck's paramagnetic investigations in 1939 (Van Vleck, 1939). Bloembergen's investigation of the exchange interactions between nuclear spins revealed that they were inversely proportional to the time of spin-spin relaxation in the lattice, however this investigation was limited to single spin considerations only (Bloembergen, 1949). The mathematics describing the constraints of a spin diffusion model have been widely discussed with respect to physical conditions and theoretical limits (Liu, 1976; Müller, 1988; Lovesey et al., 1994; Ikeda et al., 1995; Lovesey, 1996).

The importance of this investigation is to enhance comprehension of the dynamical processes occurring in spin systems. Spin diffusion theory has been able to assist in the analysis and

interpretations of dynamical investigations such as NMR spin relaxations and electron spin resonance experiments (Boucher et al., 1976; Müller, 1988). The theory of statistical mechanics is the means by which the static and time-dependent features of magnetic spins within a lattice can be tested and understood. Especially when considering either short or long-range magnetic ordering. Low dimensional magnetic materials, such as Rb_2CoF_4 , have recently been considered in discussions of spin diffusion theory, as the short-ranged correlations in one or more directions changes the dynamics of the spin diffusion networks (Müller, 1988; Ikeda et al., 1995; Lovesey, 1996).

It has been proposed that under paramagnetic conditions, a spin state can diffuse through the crystal lattice, via the exchange interaction between neighbouring spins. The conventional spin diffusion model predicts that the rate for a spin state to diffuse through a lattice follows an exponential decay involving the dimensionality of the lattice (Lovesey et al., 1994). However recent theoretical investigations of Ising and Heisenberg materials suggest that a spin-diffusion event can be described by a spin autocorrelation function which indicates a power law decay (Lovesey et al., 1994; Lovesey, 1996). It is this mechanism that has developed the concept of time-dependent spin-diffusion.

Anomalous diffusion describes the concept of a single-particle or state diffusing through some structure, such as pure materials, or fractal (self-similar) structures, as observed by Ikeda et al. (1995). To measure this diffusion directly, the self-correlation function of the state must be measured (Ikeda et al., 1995). This time-dependent function correlates the spin states throughout the magnetic lattice and is often called the spin auto correlation function, $G(\kappa, t)$. This function combines the wave vector, κ , and the time of diffusion, t , in the paramagnetic material. The autocorrelation function can be described by the time evolution of the fluctuations in the total spin, $S(\kappa, t)$

$$G(\kappa, t) = \langle S(\kappa, t) \cdot S(-\kappa, 0) \rangle \quad (8.1)$$

There are currently two theories to describe the autocorrelation function with respect to temperature dependent spin interactions. The conventional theory of spin diffusion relates the autocorrelation function $G(\kappa, t)$ to Fick's Law of spin diffusion such that $G(\kappa, t)$ decays exponentially over time as in Equation 8.2.

$$G(\kappa, t) \approx \exp(-D\kappa^2 t) \quad (8.2)$$

Here D is the diffusion constant, κ is a sufficiently small wave vector and t is a sufficiently long time (Müller, 1988). The autocorrelation function correlates the spin state at a particular lattice site with itself over time via a Fourier transform involving all the spin states in the lattice. For instance the autocorrelation function will determine the way in which the spins change state from time $t = 0$ to time $t = t'$. Thus this function is the relationship between the initial state and the final spin state, whether it is an exponential change or a power-law change or some other change.

The most popular theory to date is the coupled mode theory of spin diffusion, which describes the paramagnetic spin fluctuations of both short and long wavelengths. It has been suggested that the conventional spin diffusion model fails to describe the decay at both intermediate *and* close to infinite time scales (Lovesey et al., 1994). Thus the coupled mode theory characterises the spin fluctuations for close to infinite times, by calculating the decay rates as a function of temperature and wave vector. This theory predicts a simple power-law to describe the diffusion rate and has been studied experimentally by Lovesey et al. (1994). Thus the coupled mode theory describes the spin diffusion according to the time and wave vector dependent spin state, as in Equation 8.3.

$$G(\kappa, t) = \left(\frac{1}{t}\right)^{\frac{d}{\theta}} \quad (8.3)$$

where $\theta = \frac{4+d}{2}$ for infinitely long times, d is the dimensionality of the lattice and $\theta = 1.88$ for intermediate times in a 2 dimensional lattice (Lovesey et al., 1994). For instance the coupled mode theory reveals for a 2 dimensional lattice that the decay rate follows $(1/t)^{2/3}$ for infinite times, while for intermediate times the decay is $(1/t)^{1.06}$. In contrast to this, the conventional spin diffusion model can be approximated by the coupled mode theory at relatively short time intervals such that the decay follows $(1/t)$ (Lovesey et al., 1994).

8.2 SPIN DIFFUSION IN FePS_3

Spin diffusion experiments on 2D Ising antiferromagnets have previously been carried out with $\text{Rb}_2\text{Co}_{0.6}\text{Mg}_{0.4}\text{F}_4$ (Ikeda et al., 1995). In this experiment, a large single crystal was used with magnetic scattering observed in only two of the 51 detectors of the IRIS spectrometer at ISIS, in the UK. Thus, although there was a wide range of scattering vector magnitudes from the range of wavelengths in the neutron beam, only two scattering vector directions were observed. The diffusion at only a single-spin site was observed which allowed for an investigation of the spin auto-correlation at each site. Their analysis revealed that the line shape of the inelastically scattered neutrons was best fit with a sum of Lorentzian and exponential features, where the Lorentzian profiles described the normal critical magnetic scattering, and the exponential profile was responsible for the long tailed decay of the spin diffusion. At temperatures close to the Néel temperature, the critical scattering was more dominant implying a larger contribution from the Lorentzian function (Ikeda et al., 1995). In this study, Ikeda et al., (1995) attributed the observed power law to the disordered nature of the sample whereas the theory of Lovesey et al., (1994) implied that the coupled mode power law can be obtained with a pure material

The current experiment involved the investigation of time dependent spin correlations at raised temperatures in the 2D antiferromagnet, FePS_3 . With three nearest neighbours, the spin on one Fe atom can transfer its spin state, via exchange interactions, to a neighbouring Fe atom within the plane. In the paramagnetic state, this occurs via super exchange with the adjacent sulphur ions. The interlayer interactions are much weaker due to the van der Waals gap between the sulphur layers. Neutron scattering measurements have shown the magnetic structure of FePS_3 to be truly 2D, similar to Rb_2CoF_4 , and thus these materials are ideal for studying 2D phenomena – including spin diffusion. Thus, in this investigation, the spin state of one iron site in FePS_3 is said to diffuse through the lattice over time. As the spin state diffuses away, the spin at the initial site is said to decay. Both terms, diffusion and decay, describe the same situation from different perspectives.

In the paramagnetic region the magnetic moments are randomly oriented. In neutron diffraction scans, the magnetic Bragg peaks becomes broader and flatter as the interactions between metal ions diminish. Even in the paramagnetic region however, the spins will influence each other to some degree. The aim of this experiment was to investigate the diffusion of a spin

state through a truly 2-dimensional lattice in the paramagnetic phase by using time of flight neutron scattering.

8.3 EXPERIMENTAL SET UP

LONGPOL at the Lucas Heights Laboratories was again employed for time of flight, inelastic neutron scattering. The sample consisted of two adjacent, crushed pellets of FePS₃ aligned with their central axes parallel to the initial polarisation of the incident neutrons. A polycrystalline sample was chosen as this allowed for magnetic scattering over a range of scattering vectors, in contrast to the single crystal experiment performed by Ikeda et al. (1995). The polycrystalline specimen allowed for a multitude of scattering vector directions for a single scattering angle. Thus for different scattering angles, a range of different scattering vector magnitudes were achieved. Thus there is a variety of scattering vectors which all contribute to the scattering. This allowed for the spin diffusion to be observed across a wide range of scattering vectors. The scans were taken at 150 K, 200 K and 250 K to observe the differences in the spin diffusion rates as the exchange interactions progressively weakened.

All eight detectors were used to scan for magnetically scattered neutrons, as the magnetic reflections were broadened in the paramagnetic region. As there is no long-range order present at high temperatures, sharp magnetic reflections were absent from the neutron diffraction pattern. However there were still some short-ranged magnetic correlations at temperatures close to the Néel temperature. Thus a good coverage of reciprocal space was achieved up to 2 \AA^{-1} . The sum over all detectors was then used to obtain the on-site spin autocorrelation function.

The energy profile of the scattering is the Fourier transform of the on-site spin autocorrelation function. Thus to follow the conventional model of spin diffusion, the inelastic neutrons would have a cross section proportional to a Lorentzian line shape, as the Fourier transform of this leads to an exponential decay.

8.4 RESULTS OF FEPS₃

The data from each detector was summed, with the main beam and any nuclear scattering removed. The time of flight data was cross-correlated, similar to the analysis of the low temperature energy scans in Chapter 7. The maximum entropy analysis was not applied to these results, as the current package was unable to deal with the errors involved in reconstructing inelastic neutron data. The cross-correlation analysis can be seen in Figure 8.1 below.

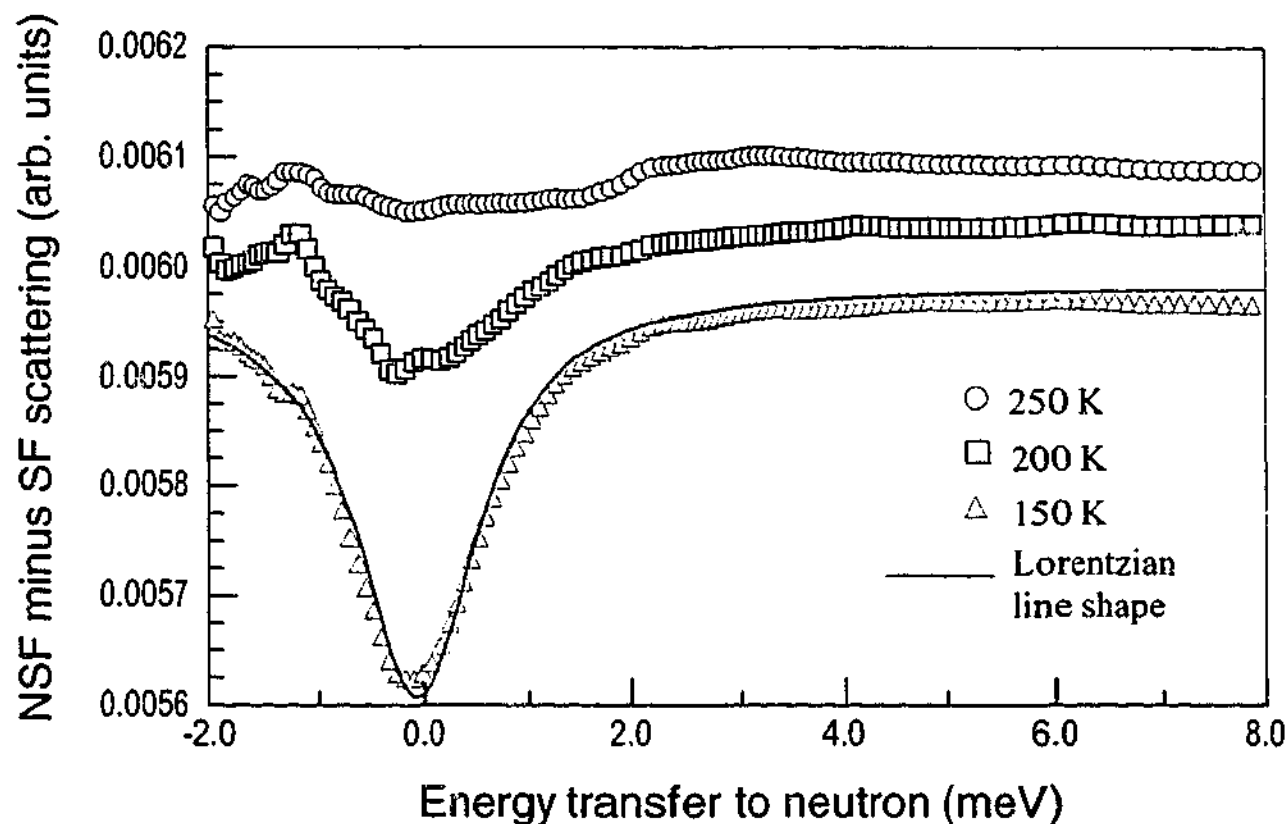


Figure 8.1: Cross correlation plot of the inelastic energy transferred to the neutron for increasing temperatures from 150 K to 250 K. The solid line represents a Lorentzian line shape fitted to the 150 K data.

As can be seen in Figure 8.1, each of the three temperatures follows a different energy transfer distribution. Each of the profiles is centred about the elastic position of 0 meV energy transfer. Thus, the width of the peaks is an indication of the inelasticity of the scattering. The plot shows the simple cross correlation data rather than the maximum entropy fit and so the instrumental resolution values have not been removed from this plot. This may be responsible for some peak broadening in Figure 8.1, however the general line shapes should remain consistent. It

is the shape of the inelastic neutron scattering profile that is directly related to the form of the single site decay due to spin diffusion.

The line shape that has been fitted to the 150 K data follows a Lorentzian profile with a constant background, and it is obvious that the line well describes the trend of the data. The half width at half maximum height of the Lorentzian profile corresponds to an energy of 0.66 meV which is equivalent to a frequency of approximately $2.4 \times 10^{11} \text{ s}^{-1}$. However the line shapes for the 200 K and 250 K are not so well determined. In fact the 250 K data appears to be approaching a square waveform with a peak energy width nearly the same size as the base width of the 150 K data.

These results are very similar to those obtained with $\text{Rb}_2\text{Co}_{0.6}\text{Mg}_{0.4}\text{F}_4$ at temperatures close to the Néel temperature. The distribution of inelastic neutrons followed a Lorentzian line shape close to T_N indicating an exponential decay similar to the conventional spin diffusion model. However, as the temperature of FePS_3 was increased, the line shape of the inelastic neutron distribution appeared to become more like a square wave function with rounded edges, indicating that the higher frequency components of the square wave may have been absent. There was also no indication of a power law variation with energy which may have implicated a disordered nature within FePS_3 as it did for the $\text{Rb}(\text{Co,Mg})_2\text{F}_4$ (Ikeda et al., 1995).

8.5 ANALYSIS OF THE SPIN DIFFUSION RESULTS

The dynamical spin correlation function is proportional to the inelastic neutron scattering cross-section, which, for a particular scattering vector, κ , and angular frequency, ω , can be given by the partial differential cross section in Equation 8.4 below. The differential cross section is proportional to the intensity of the neutrons detected in the solid angle, $d\Omega$, during the frequency interval $d\omega$.

$$\frac{d^2\sigma}{d\Omega d\omega} = \left(\frac{e^2 \gamma}{2m_e c^2} \right)^2 \sum_{\mathbf{R}, \mathbf{Q}} \exp^{-i\kappa \cdot (\mathbf{R} - \mathbf{Q})} \int \mathbf{S}_\perp(\mathbf{R}, t + t') \cdot \mathbf{S}_\perp(\mathbf{Q}, t') \exp^{-i\omega t} dt dt' \quad (8.4)$$

Here the first term in the brackets is a constant with e , the charge of an electron, γ , the gyromagnetic ratio of the neutron, m_e , the mass of an electron and c , the speed of light. $\mathbf{S}(\mathbf{R}, t$

$+t')$ and $S(Q, t')$ are the vector spin operators at position R at time $t+t'$ and at position Q and time t' . S_{\perp} is the vector component of the spin operator, S , perpendicular to the scattering vector κ . Although t is the difference in time between positions R and Q , the experiment is taking an average over the starting times t' . The time, t , represents the time for a particular spin state felt at R to diffuse to another position Q and this is the basis of the spin diffusion experiment.

In the current spin diffusion experiment the polycrystalline material was chosen such that an average was taken over all scattering vectors, κ , across a range of 2θ values. By taking counts from each of the eight detectors in LONGPOL, the summed values could be combined to find the average magnitude across all scattering vectors. This then gives the average behaviour of an individual spin for the on site autocorrelation function. The average cross-section over all scattering vectors is

$$\left\langle \frac{d^2\sigma}{d\Omega d\omega} \right\rangle_{\kappa} = \left(\frac{e^2\gamma}{2m_e c^2} \right)^2 \int d\kappa \sum_{R,Q} \exp^{-i\kappa(R-Q)} \int S_{\perp}(R, t+t') \cdot S_{\perp}(Q, t') \exp^{-i\omega t} dt dt' \quad (8.5)$$

By integrating over all scattering vectors, the exponential term will oscillate sinusoidally with κ unless $R-Q=0$. In this case, the exponent, $\exp^{-i\kappa(R-Q)}$ simplifies to 1. Thus for all $R-Q \neq 0$, the integral becomes zero due to the periodicity of the resulting wave, while the integral is non-zero only for $R-Q=0$. This then gives a factor of N number atoms in place of the summation with respect to κ , provided that $R=Q=0$. This indicates that the spin state that was at $R=0$ has diffused away through the lattice to some unknown position.

$$\left\langle \frac{d^2\sigma}{d\Omega d\omega} \right\rangle_{\kappa} = N \left(\frac{e^2\gamma}{2m_e c^2} \right)^2 \int S_{\perp}(0, t+t') \cdot S_{\perp}(0, t') \exp^{-i\omega t} dt dt' \quad (8.6)$$

This represents the time Fourier transform of the spin "self correlation" or "auto-correlation". Thus we can retrieve the way in which the spin information decays at each spin site by Fourier transforming the averaged κ data.

The simplest example is a spin for which the correlation with itself decays exponentially (which is what would be expected for the classical spin diffusion model). In this case, the x components of the vector spin operators perpendicular to the scattering vector can be taken as

$S_x(t+t') = Ce^{-\Gamma(t+t')}$ and $S_x(t') = Ce^{-\Gamma t'}$ where C is a constant and Γ represents the line width of the inelastically scattered peak. The variable Γ also represents the decay time in the time domain. When the time is restricted to $(t+t') > 0$ and $t' > 0$, the cross-section for the x components can be written as

$$\begin{aligned} \left\langle \frac{d^2\sigma}{d\Omega d\omega} \right\rangle_x &= N \left(\frac{e^2\gamma}{2m_e c^2} \right)^2 \int_0^\infty S_x(0, t+t') e^{-i\omega(t+t')} dt \int_0^\infty S_x(0, t') e^{i\omega t'} dt' \\ &= N \left(\frac{e^2\gamma}{2m_e c^2} \right)^2 \frac{iC}{\sqrt{2\pi}(\omega + i\Gamma)} \frac{-iC}{\sqrt{2\pi}(\omega - i\Gamma)} \\ &= N \left(\frac{e^2\gamma}{2m_e c^2} \right)^2 \frac{C^2}{2\pi(\omega^2 + \Gamma^2)} \end{aligned}$$

Similarly these can be evaluated for the other two Cartesian components to form $S_x^2 + S_y^2 + S_z^2 = \mathbf{S} \cdot \mathbf{S}$. Thus, the energy profile of the scattering is a Lorentzian with a width, Γ , which is also the decay rate of the correlation of each spin with itself as expected for classical diffusion. The Lorentzian line shape tells us that the spin orientation at the sites is decaying exponentially. If the spin state is not decaying exponentially, the line shape will not be Lorentzian, but follow some other function.

In the current results, the data taken at 150 K follows a Lorentzian profile (ignoring the slight Gaussian distribution from the instrumental resolution), while the data taken at 250 K looks similar to a square wave. The relaxation time, calculated from the frequency of $2.4 \times 10^{11} \text{ s}^{-1}$ was found to be $4.1 \times 10^{-12} \text{ s}$. The 250 K data may be reconstructed from the Fourier components of a square wave – ignoring the highest frequency harmonics due to the rounding of the edges in the data pattern. The spin diffusion theory takes a Fourier transform of the normalized correlation function to obtain the rate of the spin decay at each site. This is only true for the Lorentzian line shape, which is given by an exponential decay. For other line shapes the on site behaviour appears to be more complex, similar to a *sinc* function, which combines a decay with an oscillating component.

As the temperature increased, the shape of the inelastic neutron scattering cross section changed from a Lorentzian peak shape to something resembling a square waveform. Taking the

Fourier transform of the Lorentzian line shape would give an exponential diffusion rate similar to the conventional spin diffusion model. However the Fourier transform of the square waveform would result in a *sinc* function similar to that in Equation 8.7 below. Thus the on site auto-correlation function of the spins in the two dimensional antiferromagnet FePS₃ appears to follow a *sinc* function, which is interestingly not a diffusive motion.

$$f(\gamma) = \int \frac{\sin \gamma t}{\gamma} \cdot \exp(i \cdot \omega t) dt \quad (8.7)$$

8.6 CONCLUSIONS

Scans were taken of powdered FePS₃ to observe the inelastic neutron scattering in the paramagnetic region. At 150 K, the scattering profile followed a Lorentzian line shape, which corresponded to a relaxation time of approximately 4.1×10^{-12} s. According to the spin diffusion theory, the Fourier transform of this line shape would give the decay rate of the spin at each site throughout the lattice. Thus at 150 K, the decay rate followed an exponential decay, similar to that predicted by the conventional spin diffusion model. As the temperature increased and the material became more paramagnetic, the shape of the inelastically scattered peak also changed. At 250 K, the shape of the peak could be approximated by a square waveform. Taking the Fourier transform of the square wave function would suggest that the spin relaxation rate followed a *sinc* function.

Therefore it was found that as the quasi-two dimensional magnetic material, FePS₃ became more paramagnetic, the motion of a spin state through the magnetic lattice appeared to deviate from the conventional spin diffusion model. If the shape of the energy distribution at 250 K was more square wave like, the decay of each spin would have an oscillatory component. This method, involving a polycrystalline sample was preferred over the single crystal method of Ikeda et al. (1995), as it gave an average over all scattering vectors and magnetic sites in the lattice. More scattering vectors could be observed due to the polycrystalline sample in this case.

CHAPTER NINE

9: Conclusions and Further work

The magnetic structure and properties of FePS₃ have been investigated, using the techniques of Mössbauer spectroscopy, magnetisation measurements and neutron diffraction. It was revealed through the course of this study that the previously accepted model of the magnetic structure was incorrect. Many inconsistencies in the work by Kurosawa et al., (1983) have recently been discovered, and so the purpose of this investigation was to explore the magnetic structure of FePS₃ in more detail and to discover the true magnetic structure. Other aims of this study were to clarify the EFG direction of the Fe ion within FePS₃, and to experimentally test the theories of paramagnetic spin diffusion in low dimensional material.

The conclusions are as follows:

High field magnetisation measurements indicated that the anisotropy energy of the Fe atoms is much stronger than the exchange interactions at low temperatures. At applied fields of up to 38 T and temperatures up to 70 K, the anisotropy dominated the magnetic structure such that the magnetic structure changed from antiferromagnetic to ferrimagnetic and finally to paramagnetic.

From single crystal Mössbauer spectroscopy measurements, it was confirmed that the antiferromagnetic moments were aligned along the *c**-direction and were collinear, at least for frequencies less than the Larmor precession frequency of the Fe nucleus. This contradicted the results published by Taylor et al. (1973), in which absorption lines 2 and 5 were observed, which indicated that the moments were not oriented along the *c**-direction. By applying a magnetic field to the single crystal sample, the spectra of the two magnetic sublattices were separated and the hyperfine field was observed to be 9.8 ± 0.7 T.

Analysis of the GKE within FePS₃ indicated that the preferred direction of lattice vibrations was along the *z*-direction. The "magic angle" technique was non-destructive to the single crystal and was able to accurately replicate the results of Chandra and Ericsson (1979).

The direction of the EFG was investigated by multi-angle Mössbauer spectra, as well with the analysis program WIEN2k, which modelled the electron distribution for the monoclinic cell of FePS₃. It was found that the principal direction of the EFG of the Fe ions was most likely in the mirror plane, however was not aligned with the c^* -direction as previously thought. The asymmetry parameter of $\eta = 0$ published by Jernberg et al., (1984) did not appear to fit the Mössbauer spectroscopy data, or the WIEN2k model. Although the results contradicted the previously assumed values of these parameters, a true solution could not be found due to internal inconsistencies within the current data. In general, the results pointed towards an EFG within approximately 10° of the c^* -direction, in the mirror plane. It was not possible for the EFG to align with the c^* -direction as the line intensity ratio of 2.58 was much less 3. Discrepancies in the data could be partially, but not significantly, attributed to polarisation and thickness effects as well as the misalignment of the two crystallites in the single crystal sample.

Initial powder neutron diffraction scans of FePS₃ revealed the inconsistencies in the data from Kurosawa et al. (1983) that had remained unnoticed for 18 years. Because of the diffuse magnetic peaks observed at low scattering angles, the propagation vector of $[0,0,1/2]$ could not describe the structure. After taking long-wavelength neutron studies of the powdered sample, it was postulated that the diffuse scattering could be due to an energy dependent magnetic event such as magnons. An energy analysis using polarised neutrons in time of flight mode revealed that the diffuse peaks were in fact elastic Bragg reflections and not due to magnons.

Single crystal neutron measurements were undertaken at the ILL, using the Laue diffractometer, VIVALDI, and the 4-circle diffractometer, D19. VIVALDI photographs were used to classify the reciprocal lattice positions of the magnetic peaks. Although the magnetic peaks were quite streaky, the reciprocal lattice positions were fitted with a magnetic unit cell that was twice the size of the nuclear unit cell along the a and b directions and around three times along the c direction. These classifications were used in D19 to investigate the structure of the magnetic peaks in reciprocal space. Rod-like profiles were observed along the c^* -direction which indicated that there was no magnetic long-range order along that direction. This was confirmed by the streaky behaviour of the magnetic peaks in the VIVALDI patterns and by the broad peaks in the powder diffraction scans, which have been modelled by an interlayer paramagnetic response function along the c^* -direction. The Néel temperature was calculated from the D19 data to be 119.1 K.

Thus the true magnetic order for FePS_3 was the same in the ab -plane as that proposed by Le Flem et al., (1982), with ferromagnetic chains coupled antiferromagnetically. Between the layers long-range order is not well established, giving rise to a short-range ordering of moments along c even at low temperatures. Thus the propagation vector for FePS_3 is $\frac{1}{2} \frac{1}{2} l$.

By comparison, the features observed in the neutron diffraction results are similar to the compound Rb_2CoF_4 , which is a well known, square lattice, 2D Ising antiferromagnet. By association, FePS_3 has also been found to represent a true 2D Ising antiferromagnet, but with a honeycomb lattice.

The spin diffusion rate of the moments in the paramagnetic state was investigated using polarised neutrons. It was observed that at temperatures close to the ordering temperature, the distribution of energy transfers was a Lorentzian distribution, indicating an exponential diffusion rate of the moments in accord with the current theories. At higher temperatures the decay appeared to follow an almost square profile. This suggests that the decay of spins might follow a *sinc* function.

Recently, paramagnetic studies of FePS_3 have been performed at ISIS on HET. These results have not been included due to time constraints, however some interesting data was obtained. Cursory observations indicated that the splitting of the crystal field energy levels, Δ , was around 400 meV, which is equivalent to 3200 cm^{-1} .

As FePS_3 has been found to be a good example of a 2D Ising antiferromagnet, it would be fruitful to continue investigations into the spin-glass behaviour of the diluted material, as was an initial aim of this investigation. Dilution of the Fe with a non-magnetic transition metal, such as Zn, may form a species with frustrated exchange interactions and a different overall magnetic structure to that of pure FePS_3 . The spin glass ordering temperature of a truly 2D Ising system would make an interesting investigation. For Ising systems, this ordering temperature is finite for 3D materials, and theoretically 0 K for 2D materials. Ising systems have an advantage over Heisenberg systems in which the 2D Heisenberg magnets do not long-range order above 0 K. Thus with a truly 2D material, the spin glass characteristics may be tested.

BIBLIOGRAPHY

- Ables, G. J. (1974), *Astronomy & Astrophysics*, Supplement Series 15, 383-393.
- Abragam, A., Bleaney, B. (1986) *Electron Paramagnetic Resonance of Transition Metal Ions*. Dover Publications, Inc.: New York.
- Amsterdam. (2000), <http://www.science.uva.nl/research/mmun/40tindex.html> (7/2/00).
- ANSTO. (2003), <http://www.ansto.gov.au/ansto/bragg/hifar/long.html>.
- Aruchamy, A., Berger, H., Levy, F. (1988), *Journal of Solid State Chemistry* 72, 316-323.
- Ashcroft, N., Mermin, N. (1976) *Solid State Physics*. Saunders College: Philadelphia.
- Bacon, G. E. (1969) *Neutron Physics*. 1st edn.; Wykeham Publications (London) Ltd: London.
- Bacon, G. E. (1975) *Neutron Diffraction*. 3rd edn.; Clarendon Press: Oxford.
- Balcar, E., Lovesey, S. W. (1989) *Theory of Magnetic Neutron and Photon Scattering*. Clarendon Press: Oxford.
- Balkanski, M., Jouanne, M., Ouvrard, G., Scagliotti, M. (1987), *Journal of Physics C: Solid State Physics* 20, 4397-4413.
- Bancroft, G. M. (1973) *Mössbauer Spectroscopy*. Wiley: New York.
- Bernasconi, M., Marra, G. L., Benedek, G., Miglio, L., Jouanne, M., Julien, C., Scagliotti, M., Balkanski, M. (1988), *Physical Review B: Condensed Matter* 38 (17), 12089-12099.
- Bhowmick, A., Bal, B., Ganguli, S., Bhattacharya, M., Kundu, M. L. (1992), *Journal of Physics & Chemistry of Solids* 53 (10), 1279-1284.
- Birgeneau, R. J., Guggenheim, H. J., Sairam, T. N. (1970), *Physical Review B* 1 (5), 2211-2230.
- Bjarman, S., Jernberg, P., Wäppling, R. (1983) *Hyperfine Interactions*, 16 Switzerland, pp 625-628.
- Blaha, P., Schwarz, K., Madsen, G. K. H., Kvasnicka, D., Luitz, J. (2001); "WIEN2k An Augmented Plane Wave and Local Orbitals Program for Calculating Crystal Properties" Karlheinz Schwarz, Techn. Universität Wien, Austria.
- Bloembergen, N. (1949), *Physica* 15 (3-4), 386-426.

- Boucher, J. P., Ahmed-Bakheit, M., Nechtschein, M., Villa, M., Bonera, G., Borsa, F. (1976), *Physical Review B: Condensed Matter* **13** (9), 4098-4118.
- Brec, R., Ouvrard, G., Louisy, A., Rouxel, J. (1980), *Annales de Chimie (Paris)* **5**, 499-512.
- Brec, R., Schleich, D. M., Ouvrard, G., Louisy, A., Rouxel, J. (1979), *Inorganic Chemistry* **18** (7), 1814-1818.
- Burley, D. M. (1960), *Philosophical Magazine* **5**, 909-919.
- Byvik, C. E., Smith, B. T., Reichman, B. (1982), *Solar Energy Materials and Solar Cells* **7** (2), 213-223.
- Campbell, J. W. (1995), *Journal of Applied Crystallography* **28**, 228-236.
- Chandra, R., Ericsson, T. (1979), *Hyperfine Interactions* **7**, 229-239.
- Chandrasekharan, N., Vasudevan, S. (1994), *Pramana-Journal of Physics* **43** (1), 21-31.
- Chatterjee, I. (1995), *Physical Review B: Condensed Matter* **51** (6), 3937-3940.
- Chen, X. G., Yang, C. L., Qin, J. G., Inokuchi, M., Fujii, Y., Kinoshita, M., Yakushi, K., Ichimura, K., Liu, Y. Q. (2001), *Synthetic Metals* **121** (1-3 Special Issue SI), 1307-1308.
- Choi, W. K., Kneedler, E., Kevan, S. D. (1994), *Physical Review B: Condensed Matter* **50** (20), 15276-15286.
- Cohen, R. L. (1976) *Elements of Mössbauer Spectroscopy in Applications of Mössbauer Spectroscopy*; ed. Cohen, R. L.; Academic Press: New York, p 1-33.
- Cracknell, A. P. (1975) *Magnetism in Crystalline Materials*. Pergamon Press: Sydney.
- Crangle, J. (1991) *Solid State Magnetism*. Edward Arnold: London.
- Cullity, B. D. (1972) *Introduction to Magnetic Materials*. Addison-Wesley Publishing Company: Reading, Massachusetts.
- Dachs, H. (1978) *Principals of Neutron Diffraction in Neutron Diffraction*; ed. Dachs, H.; Springer-Verlag: Berlin, p 1-40.
- de Groot, H. J. M., de Jongh, L. J. (1986), *Physica B* **141**, 1-36.
- Ericsson, T., Wäppling, R. (1976), *Journal de Physique* **37** (12), C6 719-723.
- Fatseas, G., Evain, M., Ouvrard, G., Brec, R., Whangbo, H. (1987), *Physical Review B: Condensed Matter* **35** (7), 3082-3087.
- Fisher, M. E. (1967), *Reports on the Progress in Physics* **30**, 615-730.
- Foot, P. J. S., Suradi, J., Lee, P. A. (1980), *Materials Research Bulletin* **15** (2), 189-193.

- Gledel, C., Audiere, J. P., Clement, R., Cortes, R. (1989), *Journal de Chimie Physique* **86** (7/8), 1691-1698.
- Gonser, U. (1975) From a Strange Effect to Mössbauer Spectroscopy in *Mössbauer Spectroscopy*; ed. Gonser, U.; Springer-Verlag: New York, p 1-51.
- Gonser, U., Pfannes, H.-D. (1974), *Journal de Physique* **35** (12), C6 113-120.
- Goossens, D. J. (1999), PhD thesis; Monash University: Clayton.
- Goossens, D. J., Hicks, T. J. (1998), *Journal of Physics: Condensed Matter* **10**, 7643-7652.
- Goossens, D. J., Wildes, A. R., Ritter, C., Hicks, T. J. (2000), *Journal of Physics: Condensed Matter* **12**, 1845-1854.
- Grant, R. W., Housley, R. M., Geller, S. (1972), *Physical Review B: Condensed Matter* **5** (5), 1700-1703.
- Grasso, V., Neri, F., Patané, S., Silipigni, L., Piacentini, M. (1990), *Physical Review B: Condensed Matter* **42** (3), 1690-1695.
- Grasso, V., Santangelo, S., Piacentini, M. (1986), *Solid State Communications* **60** (4), 381-384.
- Greenwood, N. N. (1971) *Mössbauer Spectroscopy*. Chapman and Hall Ltd.: London.
- Grenèche, J. M., Varret, F. (1982), *Journal de Physique Lettres* **43**, L233-237.
- Griffith, J. S. (1971) *The Theory of Transition-Metal Ions*. Cambridge University Press: Cambridge.
- Gütlich, P. (1975) Mössbauer Spectroscopy in Chemistry in *Mössbauer Spectroscopy*; ed. Gonser, U.; Springer-Verlag: New York, p 52-96.
- Hahn, H., Klingens, W. (1965), *Naturwissenschaften* **52**, 494.
- Housley, R. M. (1969) Polarisation Effects in Mössbauer Absorption by Single Crystals in *Mössbauer Effect Methodology*; ed. Gruverman, I. J.; Plenum Press: New York City, p 109-121.
- Housley, R. M., Grant, R. W., Gonser, U. (1969), *Physical Review* **178** (2), 514-522.
- Howard, C. J. (1982), *Journal of Applied Crystallography* **15**, 615.
- Howard, C. J., Hunter, B. A. (1996) *A Computer Program for Rietveld Analysis of X-ray and Neutron Powder Diffraction Patterns*. Australian Nuclear Science and Technology Organisation, Lucas Heights Laboratories: Sydney.
- Ikeda, H., Itoh, S., Adams, M. A. (1995), *Physical Review Letters* **75** (24), 4440-4443.
- ILL-D19. (2003), <http://www.ill.fr/YellowBook/D19>.

ILL-VIVALDI. (2003), <http://www.ill.fr/YellowBook/VIVALDI>.

Ingalls, R. L. (1971) Application to Solid-State Physics in *An Introduction to Mössbauer Spectroscopy*; ed. May, L.; Plenum Press: New York, p 104-119.

Jernberg, P., Bjarman, S., Wäppling, R. (1984), *Journal of Magnetism & Magnetic Materials* **46** (1-2), 178-190.

Jiles, D. (1991) *Introduction to Magnetism and Magnetic Materials*. Chapman and Hall: Melbourne.

Joy, P., Vasudevan, S. (1992a), *Physical Review B: Condensed Matter* **46** (9), 5425-5433.

Joy, P., Vasudevan, S. (1992b), *Physical Review B: Condensed Matter* **46** (9), 5134-5135.

Joy, P., Vasudevan, S. (1993), *Journal of the Physics and Chemistry of Solids* **54** (3), 343-348.

Kamata, A., Nakai, S., Kashiwakura, T., Noguchi, K., Kozuka, N., Yokohama, T., Tezuka, H., Ohno, Y., Matsudo, O. (1996), *Journal of Electron Spectroscopy & Related Phenomena* **79**, 203-206.

Kennedy, S. J. (1994); "Smooth" Sydney.

Kennedy, S. J. (2001); "NUCROS" Sydney.

Khumalo, F. S., Hughes, H. P. (1981), *Physical Review B: Condensed Matter* **23** (10), 5375-5383.

Kittel, C. (1986) *Introduction to Solid State Physics*. 6th edn.; John Wiley & Sons, Inc.: Brisbane.

Klingen, W., Eulenberger, G., Hahn, H. (1968), *Naturwissenschaften* **55**, 229-230.

Klingen, W., Eulenberger, G., Hahn, H. (1970), *Naturwissenschaften* **57**, 88.

Klingen, W., Eulenberger, G., Hahn, H. (1973a), *Zeitschrift für Anorganische und Allgemeine Chemie* **401**, 97.

Klingen, W., Ott, R., Hahn, H. (1973b), *Zeitschrift für Anorganische und Allgemeine Chemie* **396**, 271-278.

Köseoglu, Y., Yilgin, R., Yakhmi, J. V., Qin, J. G., Chen, X., Aktas, B. (2003), *Journal of Magnetism & Magnetic Materials* **258-259**, 141-143.

Kreber, E., Gonsler, U. (1974), *Nuclear Instruments & Methods* **121**, 17-23.

Kündig, W. (1967), *Nuclear Instruments & Methods* **48**, 219-228.

Kurita, N., Nakao, K. (1989), *Journal of the Physical Society of Japan* **58** (2), 610-621.

- Kurosawa, K., Saito, S., Yamaguchi, Y. (1983), *Journal of the Physical Society of Japan* **52** (11), 3919-3926.
- Landau, D. P., Binder, K. (1981), *Physical Review B: Condensed Matter* **24** (3), 1391-1403.
- Le Flem, G., Brec, R., Ouvrard, G., Louisy, A., Segransan, P. (1982), *Journal of the Physics and Chemistry of Solids* **43** (5), 455-461.
- Leaustic, A., Audiere, J. P., Cointereau, D., Clement, R., Lomas, L., Varret, F., Constantmachado, H. (1996), *Chemistry of Materials* **8** (8), 1954-1961.
- Leaustic, A., Riviere, E., Clement, R., Manova, E., Mitov, I. (1999), *Journal of Physical Chemistry B* **103** (23), 4833-4838.
- Lines, M. E. (1969), *Journal of Applied Physics* **40** (3), 1352-1358.
- Lines, M. E. (1970), *Journal of the Physics and Chemistry of Solids* **31**, 101-116.
- Lines, M. E. (1974), *Physical Review B: Condensed Matter* **B9**, 3927.
- Litterst, J., Stieler, W. (2003); "CERN Minuit" Institut für Metallphysik und Nucleare Festkörperphysik, Braunschweig, Germany.
- Liu, S. H. (1976), *Physical Review B: Condensed Matter* **13** (7), 2979-2985.
- Long, G. J., Cranshaw, T. E., Longworth, G. (1983), *Mössbauer Effect Reference and Data Journal* **6** (2), 42-49.
- Lovesey, S. W. (1984) *Theory of Neutron Scattering from Condensed Matter*. Clarendon Press: Oxford.
- Lovesey, S. W. (1996), *Journal of Physics: Condensed Matter* **8**, L307-310.
- Lovesey, S. W., Engdahl, E., Cuccoli, A., Tognetti, V., Balcar, E. (1994), *Journal of Physics: Condensed Matter* **6**, L521-L526.
- Manriquez, V., Barahona, P., Peña, O. (2000), *Materials Research Bulletin* **35**, 1889-1895.
- Mattis, D. C. (1965) *The Theory of Magnetism*. Harper and Row: New York.
- Mc Elefresh, M. (1994) *Fundamentals of Magnetism and Magnetic Measurements: Featuring Quantum Design's Magnetic Property Measurement system*. Quantum Design: San Diego.
- Miyazaki, T., Fujimoto, H., Ichimura, K., Lee, K. P., Hasegawa, S., Inokuchi, H. (1995), *Chemical Physics* **201** (2-3), 539-546.
- Müller, G. (1988), *Physical Review Letters* **60** (26), 2785-2788.
- Niira, K., Oguchi, T. (1954), *Progress of Theoretical Physics* **11** (4-5), 425-436.

- Nitsche, R., Wild, P. (1970), *Materials Research Bulletin* **5**, 419-424.
- Ohno, Y., Nakai, S. (1985), *Journal of the Physical Society of Japan* **54** (9), 3591-3596.
- Okuda, K., Kurosawa, K., Saito, S. (1983) High Field Magnetization Process in FePS₃ in *High Field Magnetism*; ed. Date, M.; North-Holland Publishing Company, p 55-58.
- Okuda, K., Kurosawa, K., Saito, S., Honda, M., Yu, Z., Date, M. (1986), *Journal of the Physical Society of Japan* **55** (12), 4456-4463.
- Ouvrard, G., Brec, R., Rouxel, J. (1985), *Materials Research Bulletin* **20**, 1181-1189.
- Ouvrard, G., Prouzet, E., Brec, R., Dexpert, H. (1991), *Journal of Solid State Chemistry* **91** (2), 271-278.
- Pfannes, H.-D., Gonser, U. (1973), *Applied Physics* **1**, 93-102.
- Piacentini, M., Grasso, V., Santangelo, S., Fanfoni, M., Modesti, S., Savoia, A. (1984), *Solid State Communications* **51** (7), 467-471.
- Piacentini, M., Khumalo, F. S., Leveque, G., Olson, C. G., Lynch, D. W. (1982a), *Chemical Physics* **72**, 61-71.
- Piacentini, M., Khumalo, F. S., Olson, C. G., Anderegg, J. W., Lynch, D. W. (1982b), *Chemical Physics* **65**, 289-304.
- Puppin, E., Scagliotti, M., Chemelli, C. (1991), *Solid State Communications* **78** (10), 905-908.
- Pynn, R. (1990) *Neutron Scattering - A Primer in Neutron Scattering*; ed. Cooper, N. G.; Los Alamos Science: Los Alamos.
- Rancourt, D. G. (1996) Analytical Methods for Mössbauer Spectral Analysis of Complex Materials in *Mössbauer Spectroscopy Applied to Magnetism and Materials Science*; ed. Long, G. J.; Grandjean, F.; Plenum Press: New York, p 105-124.
- Rao, T. S., Raychaudhuri, A. K. (1992), *Journal of the Physics and Chemistry of Solids* **53** (4), 577-583.
- Rodriguez-Carvajal, J. (1998) *Short Reference Guide of the Program FullProf*. Laboratoire Leon Brillouin: Saclay.
- Rule, K. C., Kennedy, S. J., Goossens, D. J., Mulders, A. M., Hicks, T. J. (2002), *Applied Physics A: Materials Science and Processing* **74**, S811-S813.
- Sakai, H., Ukita, R., Machida, N., Shigematsu, T. (1999a), *Bulletin of the Chemical Society of Japan* **72** (10), 2249-2252.
- Sakai, H., Yamazaki, T., Machida, N., Shigematsu, T., Nakashima, S. (1999b), *Journal of Radioanalytical & Nuclear Chemistry* **239** (2), 241-244.

- Sakai, H., Yamazaki, T., Shigematsu, T., Nakashima, S., Hinomura, T., Nasu, S. (1997), *Chemistry Letters* (11), 1101-1102.
- Samuelsen, E. J. (1973), *Physical Review Letters* 31 (15), 936-938.
- Sanjuán, M. L., Kanehisa, M. A., Jouanne, M. (1992), *Physical Review B: Condensed Matter* 46 (18), 11501-11506.
- Scagliotti, M., Jouanne, M., Balkanski, M., Ouvrard, G. (1985), *Solid State Communications* 54 (3), 291-294.
- Scagliotti, M., Jouanne, M., Balkanski, M., Ouvrard, G., Benedek, G. (1987), *Physical Review B: Condensed Matter* 35 (13), 7097-7104.
- Schweika, W. (2002) Introduction to Polarized Neutron scattering in *Polarized Neutron Scattering: Lectures of the 1st Summer School held at the Forschungszentrum Jülich from 10-14 September 2002*; ed. Bruckel, T.; Schweika, W.; Forschungszentrum Jülich GmbH: Jülich, p 5-30.
- Schweizer, J. (2002) Magnetic Form Factors and Magnetisation Densities Investigated by Polarised Neutron Diffraction in *Polarized Neutron Scattering: Lectures of the 1st Summer School held at the Forschungszentrum Jülich from 10-14 September 2002*; ed. Bruckel, T.; Schweika, W.; Forschungszentrum Jülich GmbH: Jülich, p 291-231.
- Sekine, T., Jouanne, M., Balkanski, M. (1990a), *Journal of Magnetism & Magnetic Materials* 90-91, 315-317.
- Sekine, T., Jouanne, M., Julien, C., Balkanski, M. (1990b), *Physical Review B: Condensed Matter* 42 (13), 8382-8393.
- Shull, C. G., Smart, J. S. (1949), *Physical Review* 76, 1256.
- Shull, C. G., Yamada, Y. (1962), *Journal of the Physical Society of Japan* 17 (Suppl. BIII), 1-6.
- Silipigni, L., Calareso, C., Curró, G. M., Neri, F., Grasso, V., Berger, H., Margaritondo, G., Ponterio, R. (1996), *Physical Review B: Condensed Matter* 53 (20), 13928-13933.
- Smart, J. S. (1966) *Effective Field Theories of Magnetism*. W. B. Saunders Company: New York.
- Sourisseau, C., Forgerit, J. P., Mathey, Y. (1983), *Journal of Solid State Chemistry* 49, 134-149.
- Squires, G. L. (1978) *Introduction to the theory of Thermal Neutron Scattering*. Dover Publications, Inc: Mincola.
- Taylor, B., Steger, J., Wold, A. (1973), *Journal of Solid State Chemistry* 7, 461-467.
- Taylor, B., Steger, J., Wold, A., Kostiner, E. (1974), *Inorganic Chemistry* 13 (11), 2719-2721.
- Thompson, A. H., Whittingham, M. S. (1977), *Materials Research Bulletin* 12, 741-744.

- Travis, J. C. (1971) The Electric Field Gradient Tensor in *An Introduction to Mössbauer Spectroscopy*; ed. May, L.; Plenum Press: New York, p 75-103.
- Van Vleck, J. H. (1939), *Physical Review* **55**, 924-930.
- Vértes, A., Korecz, L., Burger, K. (1979) The physical bases of Mössbauer spectroscopy in *Mössbauer Spectroscopy*; ed. Vértes, A.; Elsevier Scientific Publishing Company: New York, p 13-122.
- Watson, R. E., Freeman, A. J. (1961), *Physical Review* **123** (6), 2027-2047.
- Wertheim, G. K., Guggenheim, H. J., Levinstein, H. J., Buchanan, D. N. E., Sherwood, R. C. (1968), *Physical Review* **173** (2), 614-616.
- Whangbo, H., Brec, R., Ouvrard, G., Rouxel, J. (1985), *Inorganic Chemistry* **24**, 2459-2461.
- Wiedenmann, A., Rossat-Mignod, J., Louisy, A., Brec, R., Rouxel, J. (1981), *Solid State Communications* **40**, 1067-1072.
- Wildes, A. R., Roessli, B., Lebeck, B., Godfrey, K. W. (1998), *Journal of Physics: Condensed Matter* **10** (28), 6417-6428.
- Williams, J. M., Brooks, J. S. (1975), *Nuclear Instruments & Methods* **128**, 363-372.
- Williams, W. G. (1988) *Polarized Neutrons*. 1st edn.; Clarendon Press: Oxford.
- Wills, A. S. (2000) JDN9 Ecole Magnétisme et Neutrons France.
- Zhukov, V., Alvarez, S., Novikov, D. (1996), *Journal of Physics and Chemistry of Solids* **57** (5), 647-652.

SUPPORTING PUBLICATIONS

Rule, K. C., Cashion, J. C., Mulders, A. M., Hicks, T. J. (2002), *Hyperfine Interactions* 141 (1-4), 219-222. "The orientation of the antiferromagnetic order in FePS₃"

Rule, K. C., Kennedy, S. J., Goossens, D. J., Mulders, A. M., Hicks, T. J. (2002), *Applied Physics A: Materials Science and Processing* 74, S811-S813. "Contrasting Antiferromagnetic order between FePS₃ and MnPS₃."

Rule, K. C., T., E., Kennedy, S. J., Hicks, T. J. (2003), *Physica B: Condensed Matter* 335, 6-10. "Identification of features in the powder pattern of the antiferromagnet FePS₃ using polarisation analysis with energy analysis."

Rule, K. C., McIntyre, G. J., Kennedy, S. J., Hicks, T. J. (2003) *Proceedings of the 27th Annual A&NZIP Condensed Matter and Materials Meeting. Wagga Wagga.* "The elusive magnetic structure of FePS₃." http://www.aip.org.au/wagga2003/WW03_14.pdf



The Orientation of the Antiferromagnetic Order in FePS₃

K. C. RULE, J. D. CASHION, A. M. MULDER and T. J. HICKS

School of Physics and Materials Engineering, Monash University, Clayton, VIC 3800, Australia

Abstract. Mössbauer spectroscopy was performed on FePS₃. Magnetic moments of a single crystal were found to be parallel to the *z*-axis at temperatures below 96 K. The internal hyperfine field was 9.64 T at 10 K. The EFG was calculated to be at an angle of 17(2)° to the *z*-direction.

Key words: antiferromagnets, iron thiophosphate, Mössbauer spectroscopy.

Iron thiophosphate is a member of the transition metal thiophosphate family, MPS₃ (where M = Mn, Fe, Co, Ni, etc.), and has been considered as quasi-two dimensional in both crystallographic and magnetic structure [4]. These thiophosphates form a layered structure with metal ions bonding in an hexagonal arrangement (Figure 1). Van der Waals gaps between sulphur layers are responsible for the weak bonding and thus the quasi-two dimensional characteristics of the compound. These crystals are monoclinic and belong to the space group *C2/m* [5, 7]. The lattice parameters for FePS₃ are given by Klingen *et al.* [5] as *a* = 0.593 nm, *b* = 1.028 nm, *c* = 0.672 nm and $\beta = 107.10^\circ$.

FePS₃ is antiferromagnetic below the Néel temperature of 120 K. In contrast to MnPS₃, which is essentially a Heisenberg antiferromagnet, FePS₃ moments have a significantly larger anisotropy [6] and the antiferromagnetic order is Ising-like.

Mössbauer spectroscopy has been performed on FePS₃ [1, 3, 8, 9]. Using a single crystal, Taylor *et al.* [9] found an asymmetric quadrupole doublet at room temperature (Figure 2a), while at 77 K, five lines were observed (Figure 2b). Lines 1 and 4 of the conventional hyperfine split spectrum are superposed resulting in

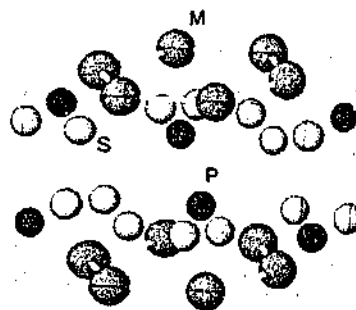


Figure 1. Crystal structure of MPS₃.

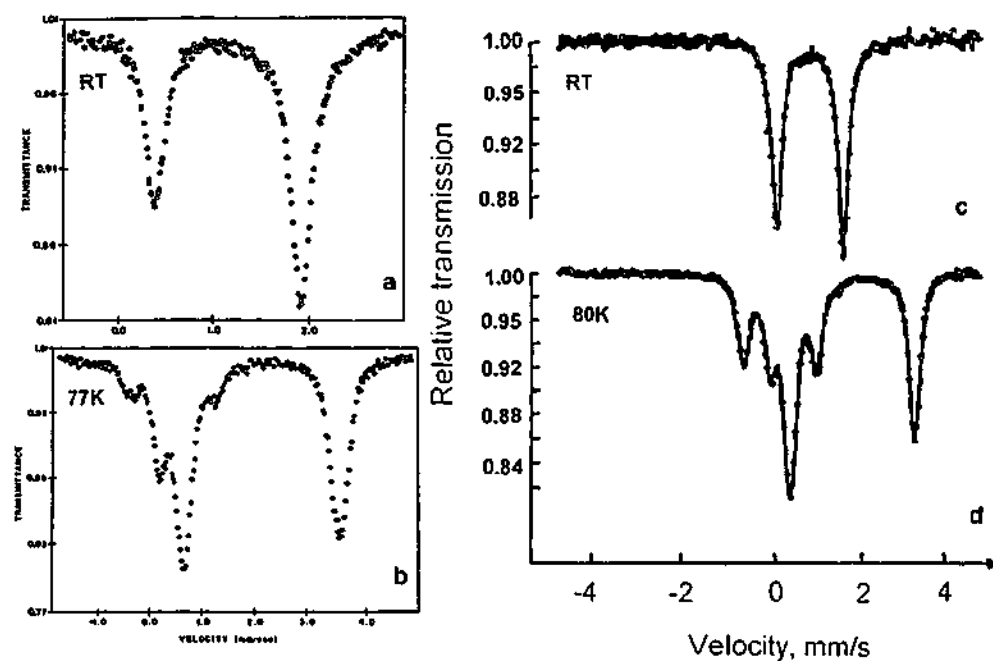


Figure 2. Previous Mössbauer spectra from Taylor *et al.* [9] (a and b) and Sakai *et al.* [8] (c and d).

five rather than six distinct lines. The results of Sakai *et al.* [8] on powdered FePS₃ were consistent with those of Taylor *et al.* [9] (Figures 2c,d). They found an internal magnetic field of 9.0 T.

Stoichiometric quantities of iron (99.998%), phosphorous (99.995%) and sulphur (99.99%) were combined in an evacuated quartz tube and heated across a temperature gradient of 690 to 630°C. Crystals of FePS₃ were formed via vapour deposition over 14 days. ⁵⁷Fe Mössbauer spectroscopy was performed using a single crystal of FePS₃ and a sample of finely crushed crystals mixed with boron nitride. The γ -rays from the ⁵⁷CoRh source were directed along the *z*-direction, perpendicular to the plane of the single crystal sample.

Mössbauer spectra of the single crystal sample were taken at temperatures above and below the Néel temperature (Figure 3a,c). Table I shows the parameters obtained by fitting these spectra.

At room temperature, the spectrum shows an asymmetric quadrupole doublet, similar to that of Taylor *et al.* [9] and Sakai *et al.* [8]. However, at 96 K and below, only three lines are obvious. Lines 2 and 5 are absent in the magnetic spectrum, in contrast to Figures 2b,d. For a simple magnetically split ⁵⁷Fe spectrum, the relative intensities of the outer : middle : inner pairs of lines are given by

$$3(1 + \cos^2 \theta) : 4 \sin^2 \theta : (1 + \cos^2 \theta), \quad (1)$$

where θ is the angle between the incident γ -ray and quantisation axis, in this case the hyperfine magnetic field. From this it can be seen that when $\theta = 0$, the γ -ray direction is parallel to the moments and the intensity of lines 2 and 5 becomes zero. Thus the moments in the single crystal are oriented perpendicular or close to

Table I. Temperature dependent Mössbauer spectroscopy data for FePS₃. The notation () means uncertainty in the last digit

Temp. (K)	<i>I</i> _{ratio} (Right line/Left line)	IS (mm/s)	QS (mm/s)	HF (T)
300	2.56	0.87(1)	1.53(2)	-
96 (crystal)	-	0.99(1)	0.83(1)	-8.65(8)
96 (powder)	-	1.01(1)	0.83(1)	-9.11(5)
10	-	0.88(1)	0.82(1)	-9.64(1)

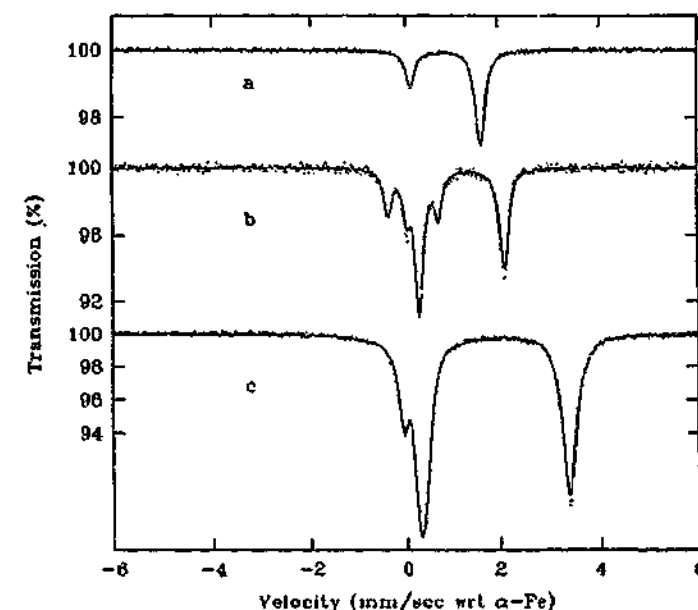


Figure 3. Mössbauer spectra for (a) a single crystal of FePS₃ at RT, (b) powdered sample at 96 K and (c) single crystal at 10 K.

perpendicular to the plane of the sample. Five lines were observed at 96 K in the powdered sample, indicating a random orientation of the magnetic moments with respect to the γ -ray direction. This result is consistent with that of Sakai *et al.* [8]. The QS value in Table I for the sextets is $\frac{1}{4}eQV_{zz}$.

In order to eliminate texture effects at room temperature, four spectra were taken of the powdered sample, which was oriented at 54.7° to the γ -ray direction and then rotated around this axis by 90° between each spectrum [2]. The resulting asymmetric doublet is due to the Goldanskii-Karyagin effect (GKE) and confirms the conclusions of Chandra and Ericsson [1] that the vibrational amplitude is greater along the *z*-direction.

have
magn

*Corres
(Fax: +

The relative line intensities of the single crystal spectrum (Figure 3a) can be used to determine the angular dependence of the EFG with respect to the gamma-ray direction. From Equation (1), the ratio of $I_{\text{right}}/I_{\text{left}}$ equals

$$\frac{1 + \cos^2 \theta}{5/3 - \cos^2 \theta} \quad (2)$$

Using this relation and our single crystal ratio of 2.56 for the asymmetry of the lines, we have obtained an approximate angle of $17(2)^\circ$ between the EFG and the normal to the ab -plane. The asymmetry parameter, η , was assumed to be zero.

The observation of three absorption lines in the magnetically ordered, single crystal spectra indicated that the antiferromagnetic moments are parallel to the z -axis in zero applied field and therefore are not parallel to the EFG direction.

We would like to thank T. Ericsson for helpful discussions. We also gratefully acknowledge the support of the Australian Research Council and the Australian Institute of Nuclear Science and Engineering for financial assistance in carrying out this research.

References

1. Chandra, R. and Ericsson, T., *Hyp. Interact.* **7** (1979), 239.
2. Grenèche, J. M. and Varret, F., *J. de Phys. Lett.* **43** (1982), L233.
3. Jernberg, P., Bjarman, S. and Wäppling, R., *J. Magn. Mater.* **46** (1984), 178.
4. Joy, P. and Vasudevan, S., *Phys. Rev. B* **46** (1992), 5425.
5. Klinge, W., Eulenberger, G. and Hahn, H., *Naturwiss.* **552** (1968), 29.
6. Okuda, K., Kurosawa, K. and Saito, S., In: M. Date (ed.), *High Field Magnetism*, North-Holland Publishing Company, 1983, p. 55.
7. Ouvrard, G., Brec, R. and Rouxel, J., *Mater. Res. Bull.* **20** (1985), 1181.
8. Sakai, H., Yamazaki, T., Machida, N., Shigematsu, T. and Nakashima, S., *J. Radioanal. Nucl. Chem.* **239** (1999), 241.
9. Taylor, B., Steger, J. and Wold, A., *J. Solid State Chem.* **7** (1973), 461.
10. Wildes, A. R., Roessli, B., Lebeck, B. and Godfrey, K. W., *J. Phys.: Condens. Matter* **10** (1998), 6417.

Contrasting antiferromagnetic order between FePS₃ and MnPS₃

K.C. Rule^{1,*}, S.J. Kennedy², D.J. Goossens², A.M. Mulders¹, T.J. Hicks¹

¹ School of Physics and Materials Engineering, Monash University, Clayton, Victoria, 3800, Australia

² Australian Nuclear Science and Technology Organisation, Private Mailbag 1, Menai 2234, Australia

Received: 25 July 2001 / Accepted: 8 January 2001 – © Springer-Verlag 2002

Abstract. Transition-metal thiophosphates, MPS₃ (M = Fe, Mn, etc.), make up a class of antiferromagnetic materials with quasi-two-dimensional magnetic behaviour. The metal atoms occupy a honeycomb lattice. In MnPS₃, the first-neighbour interaction is 400 times stronger than the exchange between the planes and the Mn moments show little anisotropy. The antiferromagnetic order is not well established perpendicular to the planes. Here we present the first powder neutron diffraction patterns of FePS₃. The absence of trailing edges on the magnetic Bragg peaks, such as have been observed in MnPS₃, indicates that the magnetic order is three-dimensional in FePS₃.

PACS: 75.25.+z; 75.30.Gw; 75.50.Ee

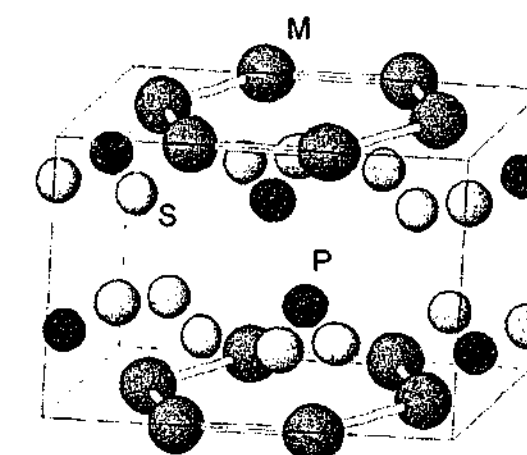


Fig. 1. Crystal structure of MnPS₃ and FePS₃

A great deal of research has previously been conducted in the area of two-dimensional antiferromagnetic structures, with numerous investigations of the transition-metal thiophosphate family, MPS₃ (where M = Mn, Fe, Co, Ni, etc.). These compounds are thought to be examples of two-dimensionality in both crystal and magnetic structure [1]. The transition-metal ions form a honeycomb lattice and each layer is isolated between two layers of sulphur and phosphorus atoms, which in turn are separated by a van der Waals gap (Fig. 1). The symmetry of these crystals is monoclinic with space group C2/m [2, 3]. The lattice parameters for FePS₃ given by Klinge et al. [2] are $a = 5.93 \text{ \AA}$, $b = 10.28 \text{ \AA}$, $c = 6.72 \text{ \AA}$ and $\beta = 107.10^\circ$.

These compounds are paramagnetic at room temperature and antiferromagnetic at low temperatures. The Néel temperature is 78 K for MnPS₃ and 120 K for FePS₃. For MnPS₃ the exchange interaction between metal atoms in adjacent planes is about 400 times less than that between first neighbours in the same plane [4]. In contrast to MnPS₃, which is essentially a Heisenberg antiferromagnet, FePS₃ moments have a significantly larger anisotropy [5] and the antiferromagnetic order is Ising-like.

*Corresponding author.
(Fax: +61-3/9905-3637, E-mail: Kirily.Rule@spme.monash.edu.au)

There have been few investigations of thiophosphates using neutron diffraction. However, MnPS₃ has been reasonably well investigated by Wildes et al. [6] using powder neutron diffraction over a range of temperatures above and below the Néel temperature. Results showed that MnPS₃ is a simple planar antiferromagnet for which long-range order is not well established along the direction perpendicular to the planes [6]. Distinctive trailing edges on the high-angle side of magnetic Bragg peaks, at temperatures well below the Néel temperature, indicate rod-like scattering profiles in reciprocal space (Fig. 2).

The only previous neutron-diffraction study to investigate FePS₃ was performed using stacked crystals to form a pseudo-crystal [8]. This study was limited in scattering angle, but also may have missed some magnetic Bragg peaks because of the necessity to explore all pseudo-crystal orientations. Kurosawa et al. [8] concluded that the magnetic structure was that proposed by Le Flem et al. [9], for which the structure is shown in Fig. 3. In contrast to MnPS₃, the planes are coupled antiferromagnetically rather than ferromagnetically. The magnetic propagation vector assigned by Kurosawa et al. [8] was $k_m = [0, 0, \frac{1}{2}]$, but this vector links the magnetic reflections to nuclear reflections of zero intensity. The vector which links magnetic reflections to nuclear reflections in the Kurosawa structure is $[0, 1, \frac{1}{2}]$.

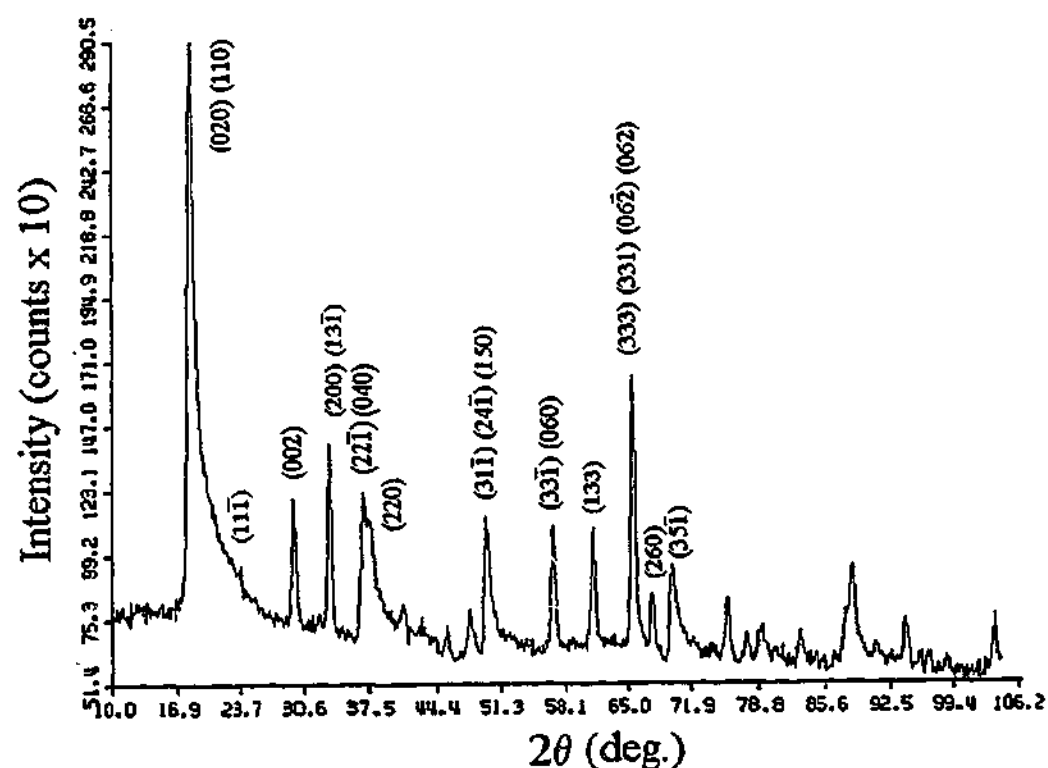


Fig. 2. Neutron powder diffraction data of MnPS_3 taken with 1.666-Å neutrons at 4 K [7]

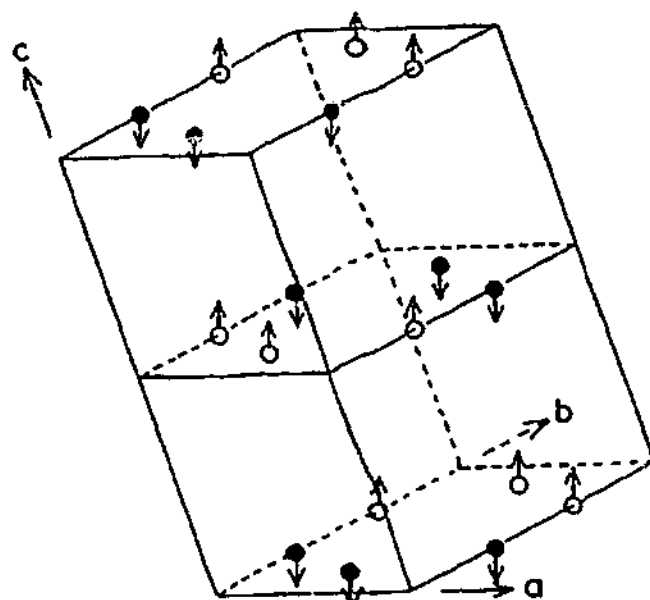


Fig. 3. Magnetic structure of FePS_3 taken from [8]

1 Experimental

The preparation of MnPS_3 for neutron powder diffraction has been described in earlier papers [10]. The preparation of FePS_3 was as follows. Stoichiometric quantities of iron (99.998%), phosphorus (99.995%) and sulphur (99.99%) were placed in a quartz ampoule under vacuum and heated for 14 days. Crystals were formed via vapour deposition over a temperature gradient from 690°C to 630°C. The crystals were then finely crushed and pressed into cylindrical pellets. These were then stacked with their axes mutually perpendicular to reduce the effects of preferred orientation. The sample was also rotated during data collection to further reduce the effects of preferred orientation. Data was collected using the medium-resolution powder diffractometer (MRPD) on the HIFAR research reactor at the Lucas

Heights Research Laboratories of ANSTO [11]. Spectra were taken over a wide range of temperatures with $\lambda = 1.666$ Å and some of these scans are shown in Fig. 4. The magnetic Bragg peaks, which appear below 120 K, are sharp with none of the trailing edges obvious in the MnPS_3 diffraction patterns. This indicates that the magnetic order is well established also in the direction perpendicular to the metal planes, and FePS_3 can be considered a three-dimensional magnet.

2 Discussion

It has been widely believed that MnPS_3 has a very small single-ion anisotropy due to the spherical symmetry of the half-full d -shell. A calculation of the anisotropy due to the magnetic dipole-dipole interaction accounts for the anisotropy as measured by the spin-flop field [12]. Without anisotropy, three-dimensional magnetic order would have to solely rely on the very small interplanar exchange interaction. It is therefore not surprising that long-range order may not be well established along the direction perpendicular to the planes, even though there is a strong interaction in the planes and this might give rise to the trailing edges seen even in the low-temperature diffraction patterns. Alternatively, the trailing edges may not be due to the static structure. Wildes et al. [4] have measured the magnon dispersion relations in MnPS_3 and have found a magnon band gap of 0.5 meV at magnetic reciprocal lattice positions. For wave vectors along the direction perpendicular to the planes, there is very little increase in the magnon energy, which reflects the very small exchange interaction between planes. With 28-meV energy, 1.666-Å neutrons are energetic enough to excite these magnons at even the lowest temperature. This would result in intensity around each magnetic reciprocal lattice point directed along the direction perpendicular to the planes. For FePS_3 the magnon band gap is very much bigger due to the

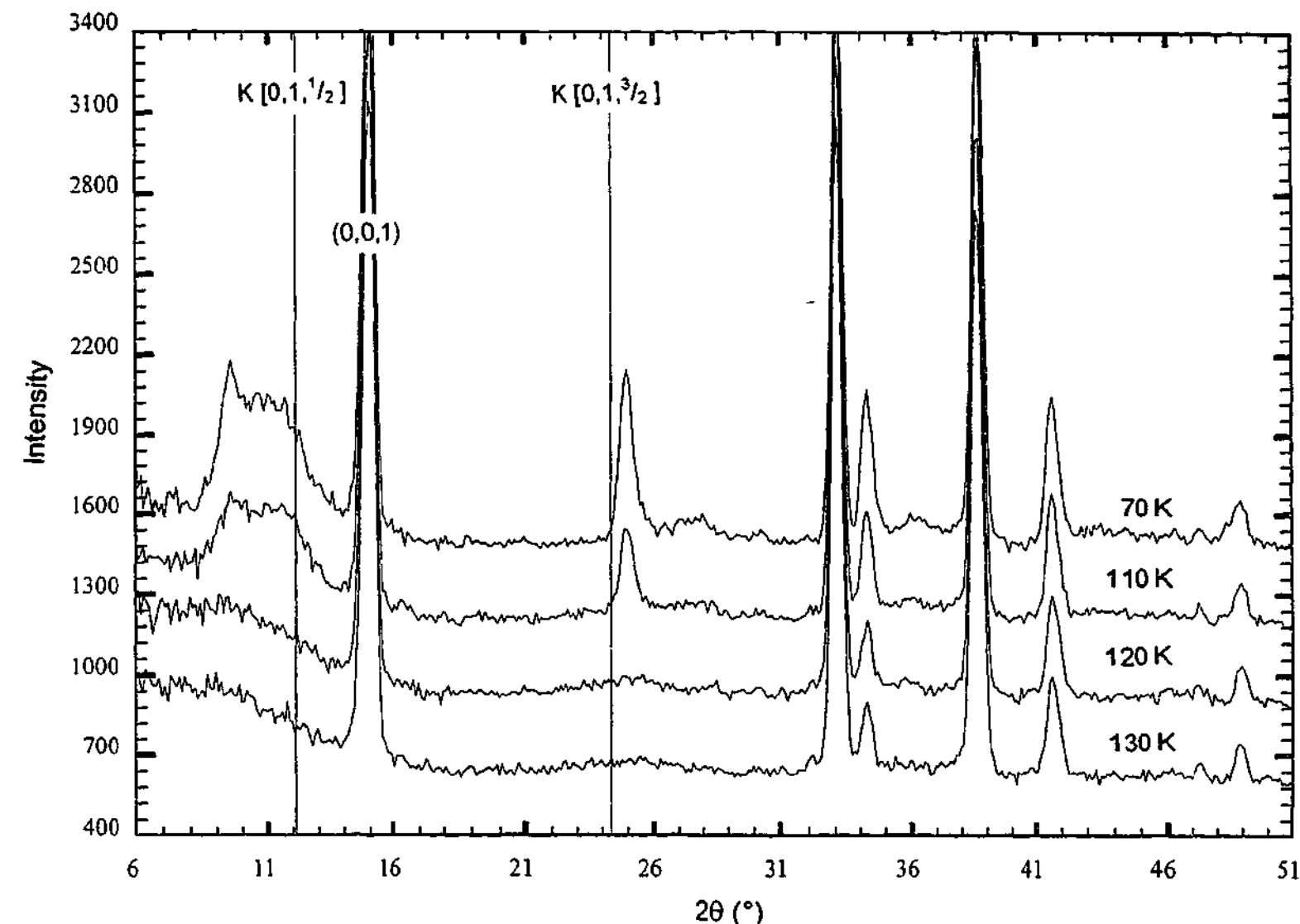


Fig. 4. Neutron powder diffraction scans of FePS_3 at 1.666 Å. Scans taken at $T > T_N$ (120 K, 130 K) and at $T < T_N$ (70 K, 110 K) shifted up 300 counts. $K[0, 1, \frac{1}{2}]$ and $K[0, 1, \frac{3}{2}]$ represent the two lowest magnetic peaks for the Le Flem et al. [9] and Kurosawa et al. [8] structure

much larger single-ion anisotropy and this magnon scattering is very much less likely.

One of the most striking features of the FePS_3 neutron powder patterns (Fig. 4) is the group of unresolved magnetic Bragg peaks at scattering angles between 8° and 13° in 2θ . The presence of these peaks suggests that there is at least a doubling of the unit cell by the antiferromagnetic structure in several directions, for example in the a direction as well as in the c direction. In contrast, the Le Flem-Kurosawa structure [8, 9] has a single Bragg peak at an angle less than that of the (0, 0, 1). This is indicated in Fig. 4, which also shows that the (0, 1, $\frac{3}{2}$) is misassigned.

In addition to the extra low-angle peaks arising from the extra doubling, the hkl and hkl peaks have different d -spacings due to the monoclinic structure. In these ways a number of low-angle magnetic Bragg peaks could be produced. It is clear from the present study that the particular structure suggested by Le Flem et al. and Kurosawa et al. [8, 9] is incorrect. The absence of trailing edges in the diffraction data indicates that long-range order is present in the direction perpendicular to the planes. This is in contrast to MnPS_3 , where either the magnetic correlation along the direction perpendicular to the planes is not long-ranged or it is so weak that it can be easily disrupted by the incident neutrons.

Acknowledgements. We would like to thank Dr. A. Studer for taking neutron scans on the MRPD. We are grateful to the Australian Research Council and the Australian Institute of Nuclear Science and Engineering (AINSE) for financial support. K.C. Rule holds an Australian Postgraduate Award with an AINSE Supplement.

References

- P. Joy, S. Vasudevan: *Phys. Rev. B: Condens. Matter* **46**, 5425 (1992)
- W. Klingenberg, G. Eulenberger, H. Hahn: *Naturwissenschaften* **55**, 229 (1968)
- G. Ouvrard, R. Brec, J. Rouxel: *Mater. Res. Bull.* **20**, 1181 (1985)
- A.R. Wildes, B. Roessli, B. Lebeck, K.W. Godfrey: *J. Phys.: Condens. Matter* **10**, 6417 (1998)
- K. Okuda, K. Kurosawa, S. Saito: *High Field Magnetism*, ed. by M. Date (North-Holland, Amsterdam 1983) pp. 55-58
- A.R. Wildes, S.J. Kennedy, T.J. Hicks: *J. Phys.: Condens. Matter* **6**, L335 (1994)
- D.J. Goossens: 'Magnetic Ordering in $\text{Mn}_x\text{Zn}_{1-x}\text{PS}_3$ ', PhD Thesis, Monash University, 1999
- K. Kurosawa, S. Saito, Y. Yamaguchi: *J. Phys. Soc. Jpn.* **52**, 3919 (1983)
- G. Le Flem, R. Brec, G. Ouvrard, A. Louisy, P. Segransan: *J. Phys. Chem. Solids* **43**, 455 (1982)
- D.J. Goossens, T.J. Hicks: *J. Phys.: Condens. Matter* **10**, 7643 (1998)
- S.J. Kennedy: *Adv. X-Ray Anal.* **38**, 35 (1995)
- D.J. Goossens, A.R. Wildes, C. Ritter, T.J. Hicks: *J. Phys.: Condens. Matter* **12**, 1845 (2000)



ELSEVIER

Available online at www.sciencedirect.com

SCIENCE @ DIRECT®

Physica B 335 (2003) 6–10

PHYSICA B

www.elsevier.com/locate/physb

Magnetic ordering in $\text{La}_{0.7}\text{Sr}_{0.3}\text{Co}_{1-x}\text{Mn}_x\text{O}_3$

J.S. Srikiran¹, A. Das^{1,*}, P.L. Paulose², S.K. Paranjpe¹¹Solid State Physics Division, Bhabha Atomic Research Centre, Trombay, Mumbai, 400 085, India²Division of Condensed Matter Physics, Tata Institute of Fundamental Research, Colaba, Mumbai 400 005, India

Received: 10 July 2001 / Accepted: 13 November 2001 – © Springer-Verlag 2002

Abstract. The structural and magnetic properties of the series of compounds $\text{La}_{0.7}\text{Sr}_{0.3}\text{Co}_{1-x}\text{Mn}_x\text{O}_3$ ($x = 0.1, 0.5, 0.75$, and 0.9) have been studied using DC magnetization and neutron powder diffraction techniques. All the samples crystallize in the rhombohedral structure. The values of T_C and the magnetic moment for $x = 0.1$ are significantly reduced from the reported values for $x = 0$. The results are discussed in terms of an increase in negative $\text{Co}^{3+}\text{-O-Mn}^{4+}$ interactions and a reduction in $\text{Co}^{3+}\text{-O-Co}^{4+}$ double-exchange interactions.

PACS: 75.25.+z; 75.30.Vn; 75.50.-y

The observation of large magnetoresistance in $\text{La}_{1-x}\text{Sr}_x\text{CoO}_3$ has generated a renewed interest in the study of these materials, and a comparison is made with isostructural manganates. In the case of manganates, since the exchange energy is larger than the crystal field energy, the high-spin (HS) state is always stable and a strong Hund's coupling of the spins in t_{2g} and e_g bands exists, which governs most of the observations. In the case of cobaltates, Co^{3+} in the low-spin (LS) state undergoes a LS to a HS transition in a wide temperature range. Substitution of Sr^{2+} in LaCoO_3 leads to the formation of intermediate-spin (IS) ferromagnetic (FM) clusters, consisting of LS Co^{4+} surrounded by IS Co^{3+} ions, which are stable at low temperatures. Thus, the metal-insulator transition observed in these systems corresponds to the formation of a percolation path between the growing FM clusters on Sr^{2+} substitution. On application of a magnetic field the growth of these clusters is enhanced, leading to a negative magnetoresistance.

In this paper, we discuss the effect of substitution of Co by Mn in the compound $\text{La}_{0.7}\text{Sr}_{0.3}\text{CoO}_3$ with $T_C = 242$ K [1].

*Corresponding author.

(Fax: +49-711/6891010, E-mail: a.das@fkf.mpg.de)

Present address: Max-Planck-Institut für Festkörperforschung, Heisenbergstraße 1, 70569 Stuttgart, Germany

1 Experimental details

Polycrystalline samples of the series $\text{La}_{0.7}\text{Sr}_{0.3}\text{Co}_{1-x}\text{Mn}_x\text{O}_3$ with $x = 0.1, 0.5, 0.75$, and 0.9 were prepared using a standard solid-state reaction route. Powders of starting compounds La_2O_3 , SrCO_3 , MnO_2 , and Co_3O_4 were dried at 800 celsius for 10 h and were fired in air at 1100 celsius for 3 days with intermediate grindings. Final sintering was carried out at 1130 °C for 24 h. All the samples are single-phase except for $x = 0.5$, in which a small impurity phase was observed. DC magnetization measurements were carried out using a commercial VSM and SQUID magnetometer. Neutron powder diffraction data were recorded on a powder diffractometer at Dhruva using a neutron beam of wavelength 1.24 Å.

2 Results and discussion

Figure 1 shows the variation of magnetization as a function of temperature for the series $\text{La}_{0.7}\text{Sr}_{0.3}\text{Co}_{1-x}\text{Mn}_x\text{O}_3$. All the samples indicate a paramagnetic-ferromagnetic transition. The value of T_C obtained from the derivative of $M(T)$ increases with x . At the Mn-rich end the transition is sharp and FM-like, whereas the transition is broad at the low-Mn end. A significant reduction of T_C for $x = 0.1$ is observed in comparison to the reported value of $T_C \sim 242$ K for $x = 0$ [1]. Since $T_C \propto J$, the magnetic exchange integral, the reduction in the value of T_C and the broad nature of the transition suggest a reduction of long-range ferromagnetic order. In addition, it is observed that for $x = 0.1$ and 0.5 the magnetization decreases on reducing the temperature below 40 K, indicating the presence of antiferromagnetic interactions.

Magnetization as a function of magnetic field has been measured at 5 K for all the samples and is shown in Fig. 2. For low values of x the magnetization does not saturate even in fields of 5 T. The value of $(1/M)(dM/dH)$ reduces from 0.14 for $x = 0.1$ to 0.0034 for $x = 0.9$. The values of the moment obtained from these measurements are 0.4, 0.81,

Identification of features in the powder pattern of the antiferromagnet FePS_3 using polarization analysis with energy analysis

K.C. Rule^{a,*}, T. Ersez^b, S.J. Kennedy^b, T.J. Hicks^a^aSchool of Physics and Materials Engineering, Monash University, P.O. Box 27, Victoria 3800, Australia^bNeutron Scattering Group, ANSTO, PMB1, Menai, NSW 2234, Australia

Abstract

Recent powder patterns of the antiferromagnet FePS_3 below its Néel temperature show unusual magnetic diffuse intensity in the Q range $0.5\text{--}0.8\text{Å}^{-1}$. This was initially thought to be a group of unresolved magnetic Bragg peaks. However subsequent powder patterns taken with longer wavelengths and better resolution have failed to resolve the peaks except to confirm the existence of a Bragg peak at $Q = 0.61\text{Å}^{-1}$. In particular the powder pattern taken with $\lambda = 5\text{Å}$ neutrons shows a marked diminution of the rest of the diffuse intensity with respect to this Bragg peak. To test whether the diffuse intensity is due to magnon scattering, the low Q region of the scattering from the powder sample of FePS_3 was measured on LONGPOL at 100 K with both polarization and energy analysis. The diffuse intensity was confirmed as magnetic but energy analysis showed that it is at least overwhelmingly elastic with no suggestion of scattering with an energy gain of 13 meV, the energy expected for the magnon band gap in this highly anisotropic antiferromagnet.

© 2003 Elsevier Science B.V. All rights reserved.

Keywords: Antiferromagnets; Neutron spectroscopy; Neutron polarization analysis

1. Introduction

Iron thiophosphate has come under much scrutiny over previous years because of its quasi two-dimensional character and possible applications in batteries [1,2]. FePS_3 is a member of the thiophosphate family of compounds MPS_3 (M = transition metal), with a monoclinic space group of $C2/m$ and cell parameters $a = 5.97\text{Å}$, $b = 10.29\text{Å}$, $c = 6.71\text{Å}$ and $\beta = 106.8^\circ$ [3]. One of

the most interesting features of these compounds lies in the structure perpendicular to the layers. Each iron and phosphorus layer is separated by two sulphur layers which are held together by relatively weak van der Waals forces. It is this feature which is responsible for the plate-like structure and two-dimensional characteristics of these compounds [4].

The magnetic structure for iron thiophosphate was proposed by Le Flem et al. in 1982 [4] and confirmed by Kurosawa et al. in 1983 [3]. This structure can be seen in Fig. 1 and was determined from neutron diffraction of a pseudo-single crystal of FePS_3 . However, after extensive examination of

*Corresponding author. Fax: +61-3-9905-3637.

E-mail address: krrily.rule@spme.monash.edu.au (K.C. Rule).

0921-4526/03/\$ - see front matter © 2003 Elsevier Science B.V. All rights reserved.

doi:10.1016/S0921-4526(03)00179-0

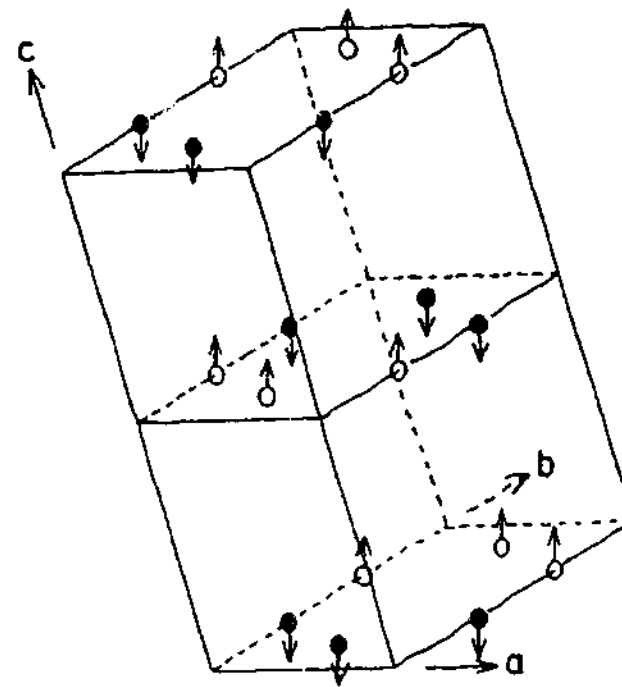


Fig. 1. Magnetic structure of FePS_3 proposed by Le Flem et al. [4] and Kurosawa et al. [3]. The arrows indicate the directions of the magnetic moments.

these results by Rule et al. [5], it was concluded that this structure, along with the proposed propagation vector of $[00\frac{1}{2}]$ is incorrect. In fact, the proposed propagation vector would not produce a magnetic Bragg peak at $01\frac{1}{2}$. The powder neutron diffraction pattern taken at 1.666 \AA by Rule et al. [5] can be seen in Fig. 2 with the positions of the lowest magnetic Bragg peaks found by Kurosawa et al. [3] labeled $K [01\frac{1}{2}]$ and $K [01\frac{3}{2}]$. These peaks do not correspond to peaks in the powder diffraction pattern, with more magnetic peaks appearing at angles less than that of $K [01\frac{1}{2}]$ at $Q = 0.8\text{ \AA}^{-1}$. The development of this diffuse band of peaks at lower Q with the lowest peak at about 0.6 \AA^{-1} eliminates the possibility of $[00\frac{1}{2}]$ as the propagation vector in this sample.

In this paper we focus on the diffuse, low Q , magnetic peaks in order to determine the relationship between the magnetic and nuclear unit cell sizes of FePS_3 . The peaks could be poorly resolved magnetic Bragg peaks from a complicated magnetic structure. They could be elastic diffuse scattering arising from massive defects in a simpler magnetic structure, or they could be magnetic

excitations, although the magnon band gap is large in FePS_3 due to the large anisotropy. The specific aim of this experiment was to test whether the diffuse intensity was inelastic.

2. Experimental

Crystals of FePS_3 were produced by the chemical vapour transport method as described earlier [5]. These plate-like crystals were crushed and pressed into cylindrical pellets with a diameter of around 1 cm.

Powder neutron diffraction was conducted on the medium resolution powder diffractometer (MRPD) at Lucas Heights Research Laboratories [6], using three pellets stacked with their central axes mutually perpendicular. The wavelengths of the neutrons ranged from 1.666 to 5.0 \AA at temperatures around 5 K —well below the ordering temperature for FePS_3 of 120 K .

Polarized neutron diffraction and spectroscopy was performed using the long-wavelength polarization-analysis diffractometer-spectrometer (LONG-POL) at Lucas Heights Research Laboratories [7]. Two FePS_3 pellets were stacked vertically, perpendicular to the scattering plane. The polarization was oriented along the scattering vector for the middle of the eight detectors in the ^3He detector bank. Energy analysis was conducted at temperatures below the Néel temperature, yet high enough to excite magnons. The temperature was maintained within 1 K of 100 K , for maximum occupancy of magnons such that the polarized neutrons would scatter with an energy gain.

3. Results and discussion

In an attempt to resolve the diffuse band of magnetic peaks found at low Q values, powder diffraction was carried out on MRPD using long wavelength neutrons. As the neutron wavelength increased, the resolution in Q improved, however the intensities of the magnetic peaks were dramatically reduced. The diffuse peaks remained unresolved at wavelengths less than 5 \AA , while at

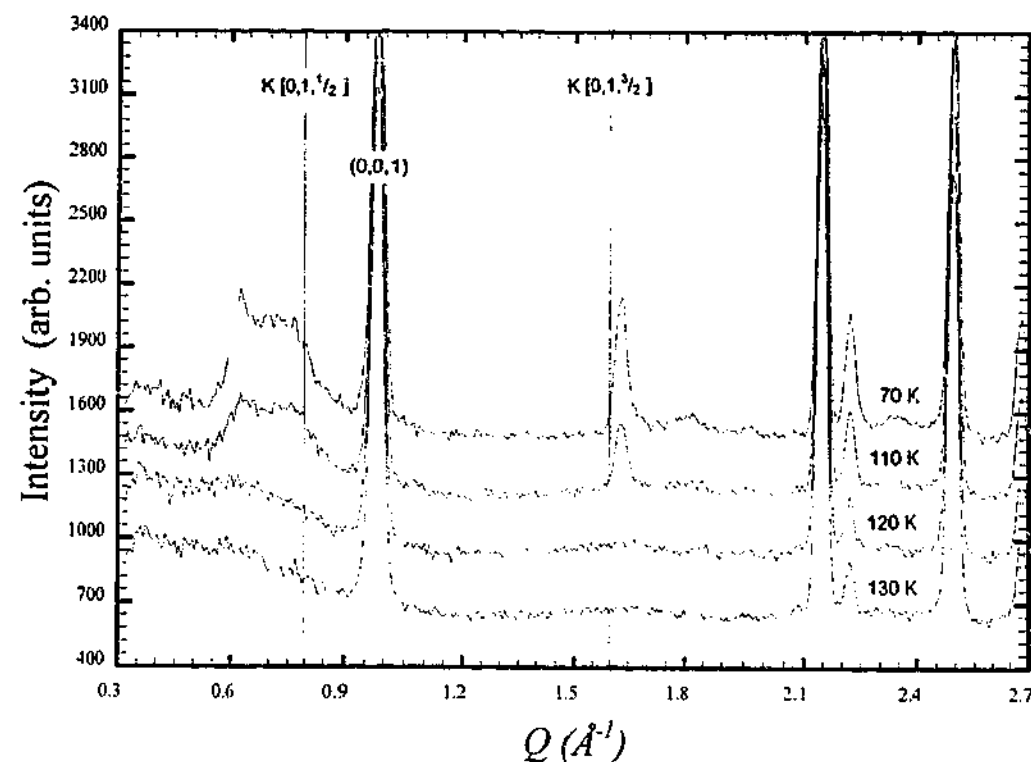


Fig. 2. Powder neutron diffraction scan taken at 1.666 \AA by Rule et al. [5] with the lowest magnetic Bragg peaks found by Kurosawa et al. [3] labeled $K [0, 1, \frac{1}{2}]$ and $K [0, 1, \frac{1}{2}]$.

5 \AA , the diffuse peaks appeared to have far less intensity with respect to the peak at $Q = 0.61 \text{ \AA}^{-1}$.

This loss of magnetic intensity at high wavelengths could be attributed to an energy dependent magnetic event, perhaps magnon scattering. Raman scattering has previously indicated that at 21 K the band gap energy of magnons in FePS_3 was 15 meV [8]. Extrapolation of this data to 100 K gave a magnon band gap greater than 13 meV . For neutrons with a wavelength of 5 \AA , the maximum energy available is 3.2 meV —well below the excitation energy for the magnons. Neutrons with a wavelength of 1.666 \AA have an energy of 29.6 meV , which is sufficient to excite spin waves. Thus the loss of diffuse intensity at long wavelengths might be due to the large magnon band gap.

To test this idea, neutrons scattered into the diffuse band of intensity of the FePS_3 diffraction pattern were energy analysed using time of flight on LONGPOL. An increase in neutron energy would indicate the absorption of energy from these magnons. No decrease in energy would be

observed, as the incident neutron energy of 6 meV (3.6 \AA) is too low to excite magnons.

Typical time of flight measurements can be seen in Fig. 3a and b for the known magnetic Bragg peaks at $Q = 0.61 \text{ \AA}^{-1}$ and the sum of the diffuse scattering at $Q \sim 0.7\text{--}0.82 \text{ \AA}^{-1}$. The spectrum is proportional to the non spin-flip minus the spin-flip cross-sections. The only feature at the elastic position is negative showing that it is spin-flip scattering. With the polarization along the scattering vector this means that, in the absence of nuclear spin incoherent scattering, the scattering is magnetic. This we have already inferred from the variation of intensity with temperature in the MRPD data. Deconvolution of the instrumental resolution was done with a maximum entropy package using a spectrum of the incident beam as point spread function. The energy resolution is $200 \mu\text{eV}$ at the elastic position in the spectrum from the Bragg peaks. This can be compared with an energy resolution of $20 \mu\text{eV}$ obtained from the spectrum of a magnetic diffuse feature from another material in which many more counts were

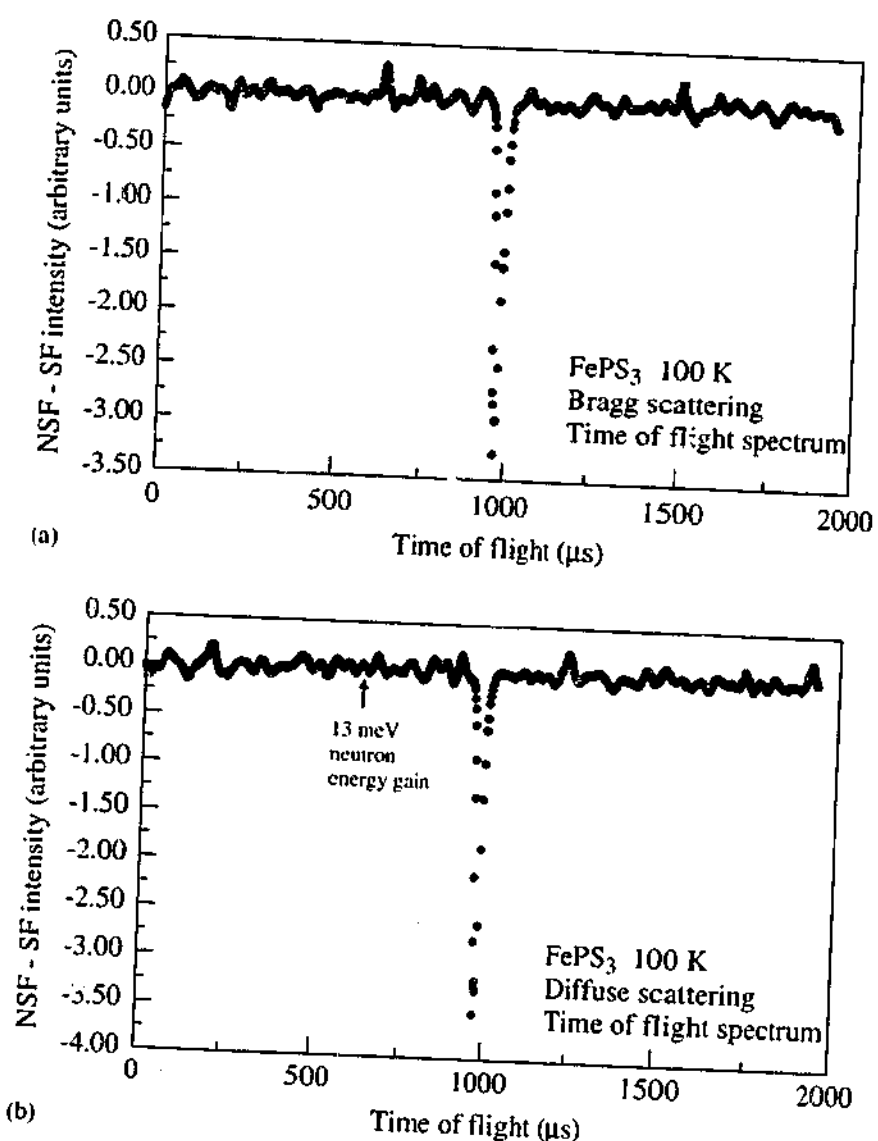


Fig. 3. Time of flight measurements from the regions of known magnetic Bragg scattering (a) and the sum of the diffuse scattering at 'elastic' scattering vectors $0.7, 0.73, 0.76$ and 0.82 \AA^{-1} . (b) indicate that both are elastic scattering events. The arrow in (b) indicates the position at which a 13 meV energy gain caused by magnon de-excitation, would appear.

gathered. This difference is probably due to the smaller total counts, which may lead to an incomplete deconvolution in this case. Nevertheless, as can be seen, there is no apparent position shift or peak width change in the diffuse scattering spectrum when compared with that from the Bragg peaks. This would suggest that the diffuse peaks are indeed as elastic as the Bragg peaks. Therefore the diffuse peaks cannot be caused by magnon excitation. The position for a 13 meV neutron energy gain is shown on the spectrum of the diffuse scattering. It may be that

the diffuse scattering is inelastic on a scale much less than $200 \mu\text{eV}$.

If the extra scattering is elastic and diffuse the large amount of scattering can only be due to faults in the magnetic structure. Whether these are in the form of stacking faults along the direction perpendicular to the layers or whether they are in the form of domain walls in the layers can only be determined by single crystal diffraction where the positioning of the scattering in reciprocal space and its morphology can be established.

4. Conclusion

Neutron powder diffraction data shows diffuse magnetic peaks at low scattering angles, between 0.5 and 0.8 \AA^{-1} , which do not fit with the previously accepted magnetic structure of FePS_3 . Long wavelength diffraction investigations reveal only one clearly defined magnetic Bragg peak in that region at $Q = 0.61 \text{ \AA}^{-1}$. Time of flight measurements taken with polarized neutrons indicate that both the Bragg and non-Bragg magnetic scattering are in fact elastic and therefore not due to magnetic excitations in the sample.

We would like to thank Dr. Andrew Studer for taking neutron scans on MRPD. We are grateful to the Australian Research Council and the Australian Institute of Nuclear Science and Engineering (AINSE) for financial support. Kirrily

Rule holds an Australian Postgraduate Award with an AINSE supplement.

References

- [1] W. Klingen, G. Eulenberger, H. Hahn, *Naturwissenschaften* 57 (1970) 88.
- [2] B. Taylor, J. Steger, A. Wold, *J. Solid State Chem.* 7 (1973) 461.
- [3] K. Kurosawa, S. Saito, Y. Yamaguchi, *J. Phys. Soc. Jpn.* 52 (1983) 3919.
- [4] G. Le Flem, R. Brec, G. Ouvrard, A. Louisy, P. Segransan, *J. Phys. Chem. Solids* 43 (1982) 455.
- [5] K.C. Rule, S.J. Kennedy, D.J. Goossens, A.M. Mulders, T.J. Hicks, *Appl. Phys. A* 74 (2002) S811.
- [6] S.J. Kennedy, *Adv. X-ray Anal.* 38 (1995) 35.
- [7] T. Ersez, S.J. Kennedy, T.J. Hicks, Y. Fei, T. Krist, P.A. Miles, in these Proceedings (PNCMI 2002), *Physica B* 335 (2003).
- [8] T. Sekine, M. Jouanne, M. Balkanski, *J. Magn. Magn. Mater.* 90–91 (1990) 315.

The Elusive Magnetic Structure of FePS_3

K. C. Rule^a, G. J. McIntyre^b, S. J. Kennedy^c and T. J. Hicks^a

^a School of Physics and Materials Engineering, Monash University, Victoria 3800, Australia.

^b Institut Laue-Langevin, BP156, 38042 Grenoble Cedex 9, France

^c Bragg Institute, ANSTO, PMB1, Menai, NSW 2234, Australia.

Laue diffraction patterns from a single crystal of FePS_3 were recorded at temperatures above and below the Néel temperature $T_N = 120 \text{ K}$ on the new thermal Laue diffractometer VIVALDI at the Institut Laue Langevin. Magnetic peaks were weaker and more extended than the nuclear peaks. The directions in reciprocal space of the magnetic reflections were found by reference to the nuclear peaks, and the magnetic reflections could then be readily located on the monochromatic diffractometer D19. The strongest magnetic peaks were found at 0.5 , -0.5 , 0.34 and 1.5 , -0.5 , 0.34 and symmetry related positions.

1. Introduction

Iron thiophosphate, FePS_3 is a member of the transition-metal thiophosphate group, MPS_3 , which has been a focus in recent years for two-dimensional investigations. It is the structure of these materials (see Fig. 1a) that makes them two-dimensional both crystallographically and magnetically. The transition-metal elements form a honeycomb lattice within the ab -plane, while two layers of sulphur and phosphorus atoms separate each pair of metal layers. The sulphur atoms in adjacent layers are in turn separated by a relatively weak van der Waals gap which is the basis for the low dimensionality.

A magnetic structure of the antiferromagnet FePS_3 has been accepted since 1983 [1]. First proposed by Le Flem et al. [2] this model has the moments collinear and perpendicular to the ab -plane and consists of ferromagnetic chains coupled antiferromagnetically within the plane as well as between planes, as seen in Fig. 1b. Kurosawa et al. [1] performed neutron diffraction on pseudo-single crystals of FePS_3 and claimed that their results supported Le Flem et al.'s proposed structure.

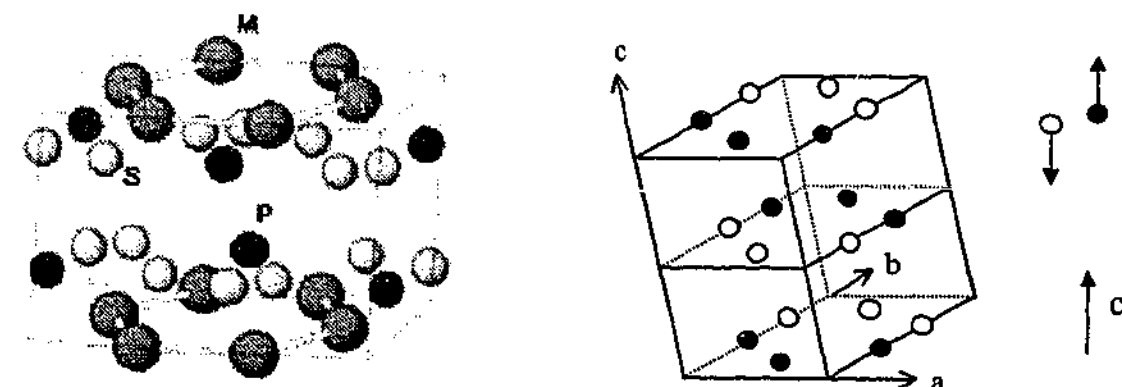


Fig. 1a) Crystallographic structure of MPS_3 and b) the previously accepted magnetic structure of FePS_3 [1]. Arrows represent magnetic moment directions parallel to c^* .

A recent review of this work found inconsistencies in Kurosawa et al.'s neutron diffraction data. The most recent neutron diffraction studies by Rule et al. [3] were

performed on powdered samples and displayed many more magnetic peaks at lower scattering angles than the data of Kurosawa et al. Furthermore, their magnetic propagation vector of $[0,0,\frac{1}{2}]$, did not link magnetic reflections to the observed nuclear reflections in either set of neutron diffraction data. The current research investigates the magnetic reflections of FePS_3 using two different, complementary neutron diffraction techniques. The aim was to find and classify magnetic peaks and determine possible propagation vectors.

2. Experimental Method

Crystals were produced via the vapour deposition method. Stoichiometric quantities of high purity starting materials were sealed in a quartz ampoule and heated for two weeks with a temperature difference of $690^\circ - 630^\circ\text{C}$. The crystals formed as thin platelets with maximum dimensions of about $10 \times 10 \times 0.1 \text{ mm}$. A large, well-formed crystal with a nearly hexagonal shape was used for both experiments conducted at the Institut Laue-Langevin.

The sample was mounted on a pin-like sample holder and placed in a He cryostat on VIVALDI (Very Intense Vertical Axis Laue Diffractometer). VIVALDI uses a white beam of neutrons in the wavelength range from $0.8 - 3.0 \text{ \AA}$. Laue diffraction patterns were collected at a variety of sample positions at both 5K and 140K to obtain a set of diffraction data below and above the Néel temperature of 120K.

The sample, on the same sample holder, was then transferred to D19, a monochromatic four-circle diffractometer. Using the data from VIVALDI, the orientation of the crystal was quickly verified and the sample was then re-cooled to below the ordering temperature. The magnetic peaks were found by scanning along the reciprocal space directions indicated in the Laue diffraction patterns.

3. Results

The Laue diffraction patterns of VIVALDI were recorded on an image-plate detector and analysed using the analysis program, Lauegen [4]. Fig. 2 shows Laue patterns taken at the same sample orientation at the two temperatures. Although much fainter than the nuclear peaks, streaky magnetic reflections can be seen at low scattering angles (especially close to the straight through beam in the centre of the pattern). A monoclinic reciprocal lattice for the space group $C2/m$ was superimposed on the pattern and refined until each nuclear reflection matched a predicted reflection. Two domains were observed in the sample with the second domain rotated 60° from the first. The two domains had a common c^* direction, perpendicular to the face of the sample.

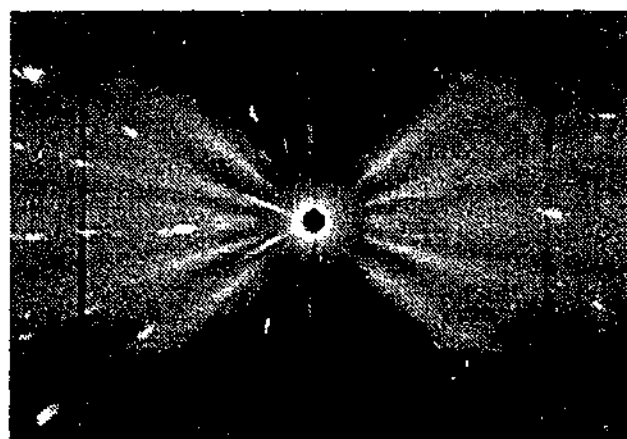
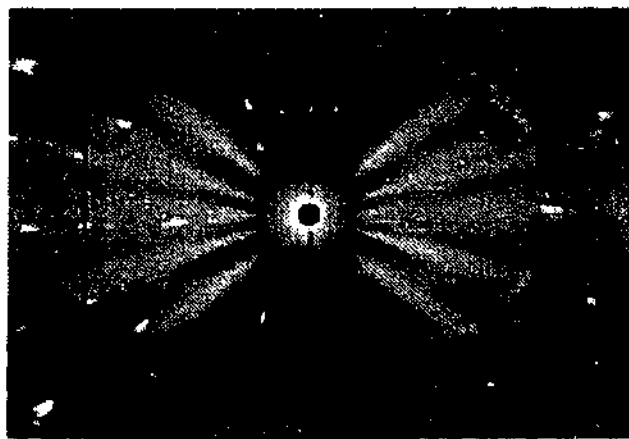


Fig. 2 Laue diffraction patterns from VIVALDI at 140 K (left) and 5 K (right).

The results from D19 were more quantitative yet complementary to those from VIVALDI. The presence of two crystal domains was confirmed and their orientations accurately determined. It was noted that the magnetic peaks observed on D19 were elongated along z . This corresponds to the streaky appearance in both the VIVALDI data and the recent MRPD data [3]. Peak intensities were found to be greatest at 0.5, -0.5, 0.34 and 1.5, -0.5, 0.34. Thus a general selection of peaks was measured at positions $h + 0.5, k \pm 0.5, l + 0.34$. The magnetic peaks from Kurosawa et al's [1] structure were also investigated in both domains, but gave zero intensity.

4. Discussion

Results from both VIVALDI and D19 were compared with the previously published MRPD data from Lucas Heights Research Laboratories in Sydney [3]. All predicted peak positions (for both nuclear and magnetic peaks) were generated by Lauegen and superimposed on the VIVALDI patterns. Each observed magnetic peak corresponded to at least one predicted reflections from one of the domains, with the more intense magnetic peaks often corresponding to two predicted reflections (one from each domain). The most intense peaks from the VIVALDI data corresponded to the lowest scattering angle peak from the MRPD data, labelled $(-\frac{1}{2}, \frac{1}{2}, -\frac{1}{3})$.

Although the propagation vector of $(\frac{1}{2}, \frac{1}{2}, \frac{1}{3})$ suggests a commensurate structure, the D19 data indicate that reciprocal lattice positions with $l_{\text{magnetic}} = (l_{\text{nuclear}} \pm 0.34)$ are more accurate, even though the elongation of the reflections does give intensity at the positions $(l \pm \frac{1}{3})$. Analysis of magnetic peak positions from the powder diffraction data also indicated that the $l = 0.34$ is more probable than $\frac{1}{3}$.

The powder neutron diffraction patterns of MnPS_3 also revealed rod-like structures in reciprocal space. These were in the form of trailing edges on the high scattering-angle side of the magnetic peaks [5]. This elongation, or rod-like structure in reciprocal space, is a result of the quasi-two-dimensional structure of these materials. These rods appear to extend along the l -direction in reciprocal space, which corresponds to incomplete long-range order along the z -axis in real space. Although the powder diffraction pattern of FePS_3 did not show such obvious trailing edges, it is possible that they are present to a lesser extent. The difference in extent of the two-dimensional scattering for FePS_3 and MnPS_3 is probably due to the different anisotropies of the two transition-metal atoms.

5. Conclusion

Although reciprocal space selection rules have been found for the magnetic peaks, a real-space magnetic structure has not yet been determined. The $(0.5, 0.5, 0.34)$ propagation vector implies that the structure is incommensurate, which allows several possible spin models. Mössbauer spectroscopy measurements on FePS_3 indicate that the magnetic moments must be oriented along the z -axis [6]. This would initially suggest a collinear structure, unless the moments rotate faster than the Larmor precession frequency. Current analysis is focusing on the possibility of a helical magnetic structure.

Acknowledgments

This work was supported by the Australian Research Council and the Australian Institute of Nuclear Science and Engineering (AINSE). Kirrily Rule holds an Australian Postgraduate award with an AINSE supplement.

References

- 1 K. Kurosawa, S. Saito, and Y. Yamaguchi, *J. Phys. Soc. Jpn.* **52**, 3919-3926 (1983).
- 2 G. Le Flem, R. Brec, G. Ouvrard, A. Louisy, and P. Segransan, *J. Phys. Chem. Solids* **43**, 455-461 (1982).
- 3 K. C. Rule, S. J. Kennedy, D. J. Goossens, A. M. Mulders, and T. J. Hicks, *Appl. Phys. A* **74**, S811-S813 (2002).
- 4 J. W. Campbell, *J. Appl. Crystallogr.* **28**, 228-236 (1995).
- 5 D. J. Goossens, PhD Thesis, Monash University, 1999.
- 6 K. C. Rule, J. C. Cashion, A. M. Mulders, and T. J. Hicks, *Hyperfine Interact.* **141**, 219-222 (2002).